

Integration of the sedimentological and petrophysical properties of mudstone samples

Julian K.S. Moore

Submitted in fulfilment for the degree of Doctor of Philosophy
in the Faculty of Science.

School of Civil Engineering and Geoscience
University of Newcastle upon Tyne

April 2005

NEWCASTLE UNIVERSITY LIBRARY

204 06433 0

Thesis L8025

Declaration

I hereby certify that this is my own work, except where otherwise acknowledged, and that it has not been submitted for a degree at this, or any other university.

Julian K. S. Moore

Acknowledgments:

Firstly, I would like to express my gratitude to Professor Andy Aplin for his advice, guidance, support and encouragement through out my time in Newcastle. Many thanks go to Dr Kuncho Kurtev for many interesting discussions and for his invaluable help on all things quantitative. I would also like to thank Dr Joe Macquaker for his help in the field, for his hospitality and for his help with the petrographic work carried out in this study. I thank BP exploration for access to sample data, and in particular Dr James Iliffle for his support and encouragement throughout my PhD. Thanks goes to all the staff at Newcastle University, in particular I would like to thank Trevor Whitfield for his help with the grain size, MICP analysis and petrographic preparation. I greatly enjoyed my time in Newcastle, and this was in large part due to the friends I made while there – so I would like to thank you all – you know who you are! Special thanks go to my mother, step-father and sister for their continued support throughout my time in Newcastle. Finally I would like to thank the Natural Environment Research Council who generously funded my PhD.

Abstract

Mudstones are of considerable scientific and economic importance as they are the dominant sedimentary rock type, forming the main repository of Earth history and having significance to numerous aspects of petroleum exploration and production, and many other industries. This study investigated the sedimentological characteristics of 150 diverse mudstone samples. The novel integration of grain size analysis combined with petrographic observations lead to a framework in which six mudstone grain size distribution (GSD) types are defined. The grain size types proposed are remarkably consistent in their form and characteristics and can be understood in terms of well constrained physical processes of deposition. The basis for this definition reflects largely the relative contributions of a flocculated, clay-rich component and an unflocculated silt/sand-rich grain size component. Integration of grain size data, pore size data and petrographic observations suggests a critical division between: (a) floc-dominated mudrocks whose structure is supported by the clay matrix; and (b) silt-rich mudrocks whose structure is supported by a silt/fine sand framework. Floc-dominated mudrocks with clay matrix support develop low permeabilities and become very good capillary seals at relatively shallow depths. In contrast, silt-rich mudrocks with framework support only become low permeability units and very good capillary seals at much greater levels of compaction. The framework proposed here can form the basis of predictive flow and seal capacity models for mudrocks. A combined PCA-cluster analysis approach to the grain size based classification of mudstones showed that of the six types defined in Chapter 2, types 1 – 4 (floc – silt mixtures) were consistently partitioned from types 5 – 6 (silt or sand rich mixtures). An attempt was made to quantify the distribution of key pore parameters, such as mean pore size, by grouping the data to reflect the matrix (grain size types 1 – 4) and framework (grain size types 5 – 6) support regimes and dividing into 5% porosity bins. The statistical distribution of pore network properties could not be verified, principally due to a combination of sparse sample numbers and highly variable nature of this data. This work illustrates that variability in mudstone pore size distributions is not constrained solely by lithology (support regime) and porosity, and thus that other factors must be taken into account if their evolution during compaction is to be understood.

Integration of the sedimentological and petrophysical properties of mudstone samples

Contents:

Chapter 1 Thesis Introduction:

1.0 Introduction.....	p. 1
1.1 Mudstone sedimentology.....	p. 2
1.2 Integration of sedimentology and physical property data for mudstones.....	p. 4
1.3 Flow properties of mudstones.....	p. 5
1.4 Significance of mudstones for the oil industry.....	p. 6
1.5 Dataset.....	p. 8
1.6 Thesis structure.....	p. 9

Chapter 2. On the nature of natural mudstone grain size distributions – characteristics, processes and typing

2.0 Introduction.....	p. 11
2.1. Background and previous work.....	p. 12
2.1.1 Behavior of fine grained sedimentary particles (<63µm) in aquatic environments.....	p. 12
2.1.2 Mudstone grain size parameters and their relationship to depositional processes.....	p. 13
2.1.2.1 Moment Statistics.....	p. 13
2.1.2.2 Sortable Silt.....	p. 15
2.1.2.3 Kranck model	p. 16
2.1.3 Grain size studies.....	p. 20
2.1.4 Integration of parameters and models.....	p. 23
2.2 Samples.....	p. 28
2.2.1 Iota Area.....	p. 28

2.2.2 Eta Area.....	p. 28
2.2.3 Jurassic sediments, North and Central Viking Graben, North Sea.....	p. 29
2.2.3.1 Lower Jurassic: The Viking Graben – Dunlin Group.....	p. 29
2.2.3.2 Middle Jurassic: The Viking Graben – Brent Group.....	p. 29
2.2.3.4 Late Jurassic – Humber Group.....	p. 30
2.2.4 Zeta Area.....	p. 30
2.2.5 Chi Area.....	p. 31
2.3 Methods.....	p. 31
2.3.1 Standard Techniques.....	p. 31
2.3.2 Moment Statistics.....	p. 33
2.3.3 Kranck model fitting.....	p. 33
2.3.4 Petrography.....	p. 34
2.4 Results.....	p. 34
2.4.1 Type 1 – floc dominated.....	p. 35
2.4.2 Type 2 – high concentration flocculated spectra.....	p. 43
2.4.3 Type 3 – floc silt mixture – floc dominated (silt $n \approx 0$).....	p. 52
2.4.4 Type 4 – floc silt mixtures.....	p. 58
2.4.5 Type 5 – floc silt mixture – silt dominated (silt $n \approx 1$).....	p. 65
2.4.6 Type 6 – sandy mudstones and siltstones.....	p. 74
2.5.6.1 Type 6a floc dominated sandy mudstones.....	p. 74
2.5.6.2 Type 6b floc – silt – sand mixtures.....	p. 79
2.5.6.3 Type 6c – clay-silt-sand mixture: Continuous distribution truncated by sieving.....	p. 83
2.4.7 Comparison of Types.....	p. 87
2.5. Discussion.....	p. 98
2.6. Chapter 2 Conclusions.....	p. 105

Chapter 3. Integrating detailed grain size distributions with the characteristics of natural mudstone pore throat size distributions at varying compaction states

3.0 Introduction.....	p. 107
3.1 Previous studies of the integration of grain size and pore size data.....	p. 108
3.1.2 Artificial slurries.....	p. 108
3.1.2 Soils and soil compaction.....	p. 113
3.1.3 Geological materials.....	p. 115
3.1.4 Synopsis – slurries to soils to ‘geological’ mudstones.....	p. 120
3.2 Methods.....	p. 122
3.2.1 Mercury Injection Capillary Pressure method – converting to pore size distribution.....	p. 122
3.2.2 Discussion of the Mercury Injection Capillary Pressure method.....	p. 123
3.3. Mudstone grain size distribution type characteristics.....	p. 125
3.4. Results.....	p. 128
3.4.1 Relationship between grain size and pore size distribution: Constant porosity.....	p. 128
3.4.2 Relationship between pore size distributions and porosity: Constant lithology (grain size type).....	p. 136
3.4.3 Behaviour of samples with intermediate grain size characteristics.....	p. 151
3.5 Discussion.....	p. 153
3.6 Chapter 3 Conclusions.....	p. 156

Chapter 4. Combined PCA-cluster analysis based classification of mudstone grain size data

4.0 Introduction.....	p. 159
4.1 Classification and clustering of geological data.....	p. 160
4.2 Dataset and Data Manipulation.....	p. 161
4.2.1 Moment statistics and sedimentary parameters dataset.....	p. 161
4.2.2 Whole phi bin dataset.....	p. 165

4.2.3 0.2 phi bin dataset.....	p. 165
4.2.4 Combined dataset.....	p. 165
4.3 Methodology: Combined PCA-k-means clustering of mudstone sedimentary parameters.....	p. 165
4.3.1 Cluster – Pore-throat size distribution (\approx flow properties) linkage.....	p. 167
4.4 Results.....	p. 168
4.4.1 Principal Component Analysis.....	p. 168
4.4.2 k-means clustering.....	p. 169
4.4.3 Cluster Population.....	p. 171
4.5 Discussion.....	p. 178
4.5.1 Relationship between clusters and petrophysical data.....	p. 179
4.6 Potential Application – defining mudstone ‘flow’ facies as building blocks in geological models.....	p. 184
4.7 Chapter 4 Conclusions.....	p. 186

Chapter 5 Investigation of the statistical distribution of pore network parameters of mudstones as a function of both support regime and porosity

5.0 Introduction.....	p. 187
5.1. Samples.....	p. 190
5.1.1 Sample Selection.....	p. 190
5.2 Methods.....	p. 193
5.2.2 Pore size distribution.....	p. 193
5.2.1 Statistical analysis.....	p. 193
5.2.2 Variability measures and sample support.....	p. 195
5.3 Results.....	p. 197
5.3.1 Group 1 (matrix supported samples – Grain size types 1 – 4).....	p. 197
5.3.2 Group 2 (framework supported samples – Grain size types 5/6).....	p. 210
5.4 Discussion.....	p. 221
5.4.1 Data distributions and sample support.....	p. 221
5.4.2 How different are Groups 1 and 2?.....	p. 223

5.4.3 Bimodality in the r mean and $r10\%$ pore size parameters.....	p. 224
5.4.4 Implications for techniques used to predict mudstone flow properties..	p. 227
5.4.4.1 Group 1 Porosity – grain size correlations.....	p. 231
5.4.4.2 Group 2 Porosity – grain size correlations.....	p. 234
5.4.4.3 Porosity – grain size – temperature.....	p. 235
5.4.4.3.1 Iota Area subset (Group 1).....	p. 236
5.4.4.3.2 North Sea Subset (Group 2).....	p. 239
5.5 Chapter 5 Conclusions.....	p. 241

Conclusions and future work

6.0 Conclusions and future work.....	p. 244
--------------------------------------	--------

Reference List

Chapter 2 list of Tables:

Table 2.1. Sedimentary parameters and moment statistics derived from Type 1 samples.....	p. 37
--	-------

Table 2.2. Kranck model parameters derived from the fitted floc-component of Type 1 sample grain size distributions.....	p. 38
--	-------

Table 2.3. Sedimentary parameters and moment statistics derived from Type 2 samples.....	p. 46
--	-------

Table 2.4. Kranck model parameters derived from the fitted floc-component of Type 2 sample grain size distributions.....	p. 47
--	-------

Table 2.5. Sedimentary parameters and moment statistics derived from Type 3 samples.....	p. 54
--	-------

Table 2.6. Kranck model parameters derived from the fitted floc-component and non-cohesive silt components of Type 3 sample grain size distributions.....p. 55

Table 2.7. Sedimentary parameters and moment statistics derived from Type 4 samples.....p. 60

Table 2.8. Kranck model parameters derived from the fitted floc-component and non-cohesive silt components of Type 4 sample grain size distributions.....p. 61

Table 2.9. Sedimentary parameters and moment statistics derived from Type 5 samples.....p. 68

Table 2.10. Kranck model parameters derived from the fitted floc-component and non-cohesive silt components of Type 5 sample grain size distributions.....p. 68

Table 2.11. Sedimentary parameters and moment statistics derived from Type 6 samples.....p. 76

Table 2.12. Kranck model parameters derived from the fitted floc-component and non-cohesive silt components of Type 6 sample grain size distributions.....p. 77

Chapter 3 list of Tables:

Table 3.1. Synopsis of the compactional behavior and relationship between the *lacunar* (or silt / sand) and clay fabric pore space in soils and fine grained sediments. Based upon the observations and results of Fiés (1992); Fiés and Bruand (1998); Yang and Aplin, (1998) and Dewhurst *et al.* (1998, 1999a).....p. 121

Table 3.2 (a) Physical property data and (b) grain size distribution data for samples with a porosity of ~26%. Grain size and pore size distributions shown in Figure 3.10.....p. 130

Table 3.3 (a) Physical property data and (b) grain size distribution data for samples with a porosity of 18 - 19%. Grain size and pore size distributions shown in Figure 3.11.....p.132

Table 3.4 (a) Physical property data and (b) grain size distribution data for samples with a porosity of 9 - 7%. Grain size and pore size distributions shown in Figure 3.12.....p. 134

Table 3.5 (a) Grain size data and (b) physical property data for Type 1 samples with a porosity of 9 - 30%. Grain size and pore size distributions shown in Figure 3.15.....p. 138

Table 3.6 (a) Grain size data and (b) physical property data for Type 2 samples with a porosity of 7 - 24%. Grain size and pore size distributions shown in Figure 3.17.....p. 140

Table 3.7 (a) Grain size data and (b) physical property data for Type 3 samples with a porosity of 9 - 26%. Grain size and pore size distributions shown in Figure 3.19.....p. 141

Table 3.8 (a) Grain size data and (b) physical property data for Type 4 samples with a porosity of 16 - 26%. Grain size and pore size distributions shown in Figure 3.21....p. 144

Table 3.9 (a) Grain size data and (b) physical property data for Type 5 samples with a porosity of 11 - 26%. Grain size and pore size distributions shown in Figure 3.23....p. 147

Table 3.10 (a) Grain size data and (b) physical property data for Type 6 samples with a porosity of 8 - 26%. Grain size and pore size distributions shown in Figure 3.25.....p. 150

Chapter 4 list of Tables:

Table 4.1. Sedimentary statistic and parameter dataset: Distribution of the grain size types proposed in Chapter 2 as a function of Cluster and the corresponding r^2 values for the porosity versus r mean regression [note cuttings were removed from this dataset]....p. 176

Table 4.2. Whole phi bin dataset: Distribution of the grain size types proposed in Chapter 2 as a function of Cluster and the corresponding r^2 values for the porosity versus r mean regression [note cuttings were removed from this dataset].....p. 176

Table 4.3. 0.2 phi bin dataset: Distribution of the grain size types proposed in Chapter 2 as a function of Cluster and the corresponding r^2 values for the porosity versus r mean regression [note cuttings were removed from this dataset].....p. 176

Table 4.4. Combined dataset: Distribution of the grain size types proposed in Chapter 2 as a function of Cluster and the corresponding r^2 values for the porosity versus r mean regression [note cuttings were removed from this dataset].....p. 177

Chapter 5 list of Tables:

Table 5.1. Interpretation of the p-values obtained when perform the AD and RJ test for normality; in both cases the null hypothesis is that the data have been drawn from a normal distribution (or log normal if the data have been transformed).....p. 194

Table 5.2. Normality test statistics for the pore network parameterizations of the samples with type 1 – 4 grain size distributions partitioned by porosity. The lowest AD values and the highest RJ values greater than the critical value (at 0.05), and their related *p*-values are in bold.....p. 208

Table 5.3. Coefficient of variation and N_0 estimates for the 5 porosity based data partitions of Group 1 (gsd types 1 – 4) for untransformed and log-transformed pore network parameterizations. [** = Iota subset].....p. 209

Table 5.4. Normality test statistic values for the pore network parameterizations of the samples with type 5 – 6 grain size distributions partitioned by porosity. The lowest AD values and the RJ values greater than the critical value (at 0.05) are in bold.....p. 219

Table 5.5. Coefficient of variation and N_0 estimates for the 5 porosity based data partitions of Group 2 (gsd Types 5 – 6) for untransformed and log-transformed pore network parameterizations [** = North Sea subset * = Zeta Area subset].....p. 220

Table 5.6. Summary table of regression results for the four Group 1 (gsd types 1 – 4) datasets.....p. 232

Table 5.7. Summary table of regression results for the four Group 2 (gsd types 5 – 6) datasets.....p. 234

Table 5.8. Summary table of regression results for the Iota subsets investigated comprising of Group 1 samples (gsd types 1 – 4).....p. 237

Table 5.9. Summary table of regression results for the Jurassic North Sea subsets investigated comprising of Group 2 samples (gsd types 5 – 6).....p. 239

List of Appendices:

Chapter 2:

Appendix A2.1: Moment Statistics (after Griffiths, 1967)

Chapter 4:

Appendix A4.1 Euclidean Sum of Squares (ESS), Cumulative Euclidean Sum of Squares (CESS) and Increase in Sum of Squares (ISS).

Appendix A4.2 PCA results

Appendix A4.3 k-means cluster statistics

Chapter 5:

Appendix A5.1 The Andersen-Darling Test Statistic

Appendix A5.2 The Ryan-Joiner (RJ) Test Statistic.

Appendix A5.3 Group 1 and Group 2 data tables.

Appendix A5.4 Ryan-Joiner normality test results

Appendix A5.5 Group 1 Regression Tables

Appendix A5.6 Group 2 Regression Tables

Appendix A5.7 Group 1 Iota Area Subset Regression Tables

Appendix A5.8 Group 2 Jurassic North Sea Subset Regression Tables

Definition of terms:

A number of abbreviations and parameters are referred to throughout this thesis, brief definitions of each are given as follows:

GSD – grain size distribution

Kranck grain size model terms:

C – is concentration (i.e. weight % or ppm) in a grain size class bin used to describe the grain size distribution

ΔQ – is the concentration at a reference settling velocity obtained when fitting the Kranck grain size model.

w – is the settling velocity of a sphere calculated using the empirical equation of Gibbs et al. (1971)

m – is hypothesized to be the slope of the size distribution present in suspension at time of deposition (i.e. the source suspension) obtained when fitting the Kranck grain size model.

n – controls the nature of the GSD model fit – i.e. flocculated or single grain obtained when fitting the Kranck grain size model.

k – describes the maturity of the depositional process (i.e. the extent to which the coarser grains have settled out) obtained when fitting the Kranck grain size model; k has units of ($s cm^{-1}$) as it multiplies the settling rate

D_f – intersection of the floc and single grain settle grain size components, estimates the grain size diameter at which particle behaviour changes from non-

cohesive to cohesive and thus estimates the maximum particle size which will be incorporated into flocs.

PSD – pore-throat size distribution

r_{mean} – mean pore size calculated numerically as a function of cumulative porosity distribution using the average of adjacent pore-throat sizes at each pressure step recorded by the MICP experiment.

$r_{10\%}$ - pore size at 10% non-wetting phase (mercury) saturation calculated numerically as a function of cumulative porosity distribution using the average of adjacent pore-throat sizes at each pressure step recorded by the MICP experiment.

CEP – critical capillary entry pressure

CEP_{Hg} – critical capillary entry pressure for the mercury – air system

CEP_{Hc} – critical capillary entry pressure for the oil – water system

Integration of the sedimentological and petrophysical properties of mudstone samples

Chapter 1 Introduction

“Possibly many may think that the deposition and consolidation of fine-grained mud must be a very simple matter, and the results of little interest. However, when carefully studied experimentally it is soon found to be so complex a question, and the results dependent on so many variable conditions, that one might feel inclined to abandon inquiry, were it not that so much of the history of our rocks appears to be written in this language.”

Henry Clifton Sorby, 1908

Mudstones are of considerable scientific and economic importance as they form the dominant sedimentary rock type, and as such are the main repository of earth history in the geological record (Schieber and Zimmerle, 1998). Mudstones also have significance to numerous aspects of petroleum exploration and production and many other industries (Aplin *et al.*, 1999; Slatt, 2003). The quote taken from Sorby (1908) eloquently describes the situation facing those who work with mudstones, and this situation has remained little changed over the century that has passed since Sorby’s day. Virtually all aspects of our understanding of this major sedimentary rock type are currently inadequate and lag behind that of less volumetrically significant sediment types. The terms mud and mudstone are used here in their most general sense to indicate clastic sediments and sedimentary rocks which are formed primarily from particles smaller than 1/16mm (62.5 μ m) following the definition of Aplin *et al.*, (1999). The term shale is avoided as it implies fissility.

The motivation for this work is focused around furthering the understanding of the sedimentology of mudstones, particularly the relationship between depositional process and grain size. The second motivation lies in attempting to gain a greater appreciation of the relationship between grain size distribution and pore-throat size distribution. This

work concentrates on understanding the nature of mudstone grain size distributions both in terms of their sedimentological significance and their importance with regard to understanding, constraining and predicting fluid flow properties. The aim is to establish a framework that will allow their sedimentological context to be understood and their fluid flow properties to be predicted. Therefore this work encompasses the sedimentological character of mudstones and the influence that grain size, along with porosity, has in controlling the pore-throat network properties of mudstones.

1.1 Mudstone sedimentology

One of the first quantitative studies of the lithological variability of mudstones was carried out by Blatt and co-workers in the late 1970's to early 1980's. For example, Blatt and Totten (1981) utilised the percentage and mean grain size of quartz as an indicator of distance from the shoreline in ancient mudstones (the Blaine Formation); the study made some broad generalisations about the composition of marine mudstones with distance from the shoreline. From the results of this study detrital quartz decreased from 57% (mean grain size 5.2 phi) at the sand-mud line to ~11% (mean grain size 6.9 phi) at ~270 km from the shore, indicating an approximate loss of 10% quartz per 60 km (Blatt and Totten, 1981). However, the degree to which these very generalised fining trends can be applied universally is questionable; Jones *et al.*, (1992) recorded silts and mudstones with mean grain sizes of up to 4.3 phi (silt content ~72%) at a water depth of ~5400m, indicating that in some situations (especially in settings that are or were close to sediment point sources) such generalisations may have little use, and indicates that mudstone variability will alter significantly in different settings.

Sedimentological studies of geological mudstone samples have principally utilised optical and/or electron microscope techniques (e.g. O'Brien and Slatt, 1990; Macquaker and Gawthorpe, 1993; Schieber, 1999; Macquaker and Howell 1999). These studies have provided significant insight, particularly with regard to the stratigraphic interpretation of mudstone sequences. However such findings are difficult to quantify, and thus lack a quantitative basis with which to link in physical measurements which further characterize

the sediment of interest. Investigations of the grain size characteristics of mudstones have largely been restricted due to difficulties associated with disaggregation. This problem was addressed by the gentle disaggregation technique proposed by Yang and Aplin (1997).

Over the past twenty years a small number of articles have been published concerning the grain size characteristics of both contemporary and ancient fine grained sediments have been published. Key studies include Kranck, (1975, 1984); Kranck and Milligan (1985), Jones *et al.*, (1992), Stevens *et al.*, (1996) and Curran *et al.*, (2004). Kranck (1975, 1984), who worked with geologically recent material, made the initial observation that the grain size spectra of fine grained sediments comprised two components: a flocculated, fine grained, clay-rich population and an unflocculated, relatively coarser, silt rich population. Kranck and Milligan (1985) attempted to set out a theoretical basis that could account for the presence of these two components and proposed a numerical model capable of describing both components. Jones *et al.*, (1992) made detailed descriptions of the spatial distribution and grain size characteristics of a number of abyssal plain turbidites and were able to account for their observations with process based interpretations. Stevens *et al.*, 's (1996) study of the contemporary distribution of grain sizes in the Baltic Sea contributed to the realization that the models and theories of Kranck and co-workers were seemingly ubiquitous. Curran *et al.*, (2004) analysed muds deposited as fine grained turbidites on the Laurentian Fan and Sohm Abyssal Plain; this study investigated the relationships between deposited grain size spectra and hydrodynamic conditions using a modified Kranck model. Their findings illustrated that throughout the dispersal system of the Laurentian Fan, changes in the volume of the deposited floc fraction reflect perturbations in energy and suspended sediment concentration downslope. To date the majority of grain size based studies have focused on case studies of contemporary or geological recent material; this work will investigate the relevance of the work sited above to geological samples and aims to take a global view following on from Kranck and Milligan's (1991) concepts, outlined in an their article on grain size in oceanography.

1.2 Integration of sedimentology and physical property data for mudstones

The lack of physical data describing mudstones has been noted on numerous occasions. For example, in his discussion on the relative successes and failure of basin scale fluid flow modeling Waples (1998) notes the dearth of relevant data for non-reservoir sediments, such as source rocks and caprocks (which are typically clastic mudstones). Waples (1998) goes on to note that coupled with the dearth of relevant sample scale data there is also significant ignorance associated with system permeabilities, which are partly dependent upon the geometrical arrangement of the various lithologies that create the basin fill. The 3D distribution of mudstones, and hence their physical properties has been noted by Bohacs (1998) as a key uncertainty: what are the sizes and shapes of mudstone lithosomes as a function of depositional environment and how best to describe them? In addition to these considerations, it is also vital to address the key problem of extracting depositional information from individual mudstone samples, since these commonly form the main data source, particularly for calibration of geophysical measurements. How do we judge depositional environment from common data types such as grain size distribution, geophysical log response, seismic properties and architectures?

A number of previous studies have certainly set a precedent for integrating the sedimentological and physical properties of fine grain sediments. Hamilton (1971, 1980) discussed the prediction of sediment properties based upon empirical relationships identified by assessing various physical properties (including grain size) and their potential variability. In the geological literature, Wetzel (1987) and Wetzel and Balson (1992) applied the inverse of what is attempted in this study by inferring sedimentological properties from the physical properties of fine grained sediments recorded using wireline logs. In the geotechnical literature, studies have used facies as a basis of understanding sediments that exhibit differing physical properties (e.g. Hein and Gorsline, 1981).

In the geological, geophysical and geotechnical disciplines attempts have been made to correlate and understand the relationships between sedimentological characteristics (grain

size distribution) and the physical properties of fine grained marine sediments. However virtually all this work is focused upon specific case studies, making the generic implications of such studies difficult to place into a global context. The work in this thesis will attempt to produce a synopsis of previous work of relevance and establish a framework in which a holistic approach to fully understanding fine grained marine sediments in terms of their sedimentological, geotechnical, physical and geometrical properties. The ultimate goal is to be able to predict the grain size of these sediments and therefore their physical properties spatially, potentially forming the basis of predictive flow and seal capacity models for mudrocks and facilitating accurate population of large scale fluid flow models.

Studies of the relationship between grain size, compaction and the pore-throat properties of fine grained artificial slurries, soils and geological samples (e.g. Fies (1992); Griffiths and Joshi (1989); Dewhurst *et al.*, (1998)) have generally not considered the sedimentological aspects of the samples in question. Where grain size is reported, it is typically reduced to some static description such as % particles $<2\mu\text{m}$ (% clay content). Fies (1992) did investigate the interaction of clay sized particles with silt and sand sized material in influencing the pore-throat properties of artificial slurries; however the relevance of his findings for geological materials awaits confirmation.

1.3 Flow properties of mudstones

The Hagen-Poiseuille equation, upon which many pore-throat size distribution based permeability models are based, shows that permeability rapidly increases with pore-throat radius and illustrates that it is the pore-throat size distribution of a mudstone that controls its flow properties (absolute and relative permeability, capillarity etc) (Dewhurst *et al.*, 1999b). Early studies of the pore-throat size distributions of mudstones showed that with increasing effective stress or burial the mean pore-throat size decreases, reaching values $<10\text{nm}$ at depths of 3 -5km (Borst, 1982; Griffiths and Joshi, 1989, 1990; Katsube and Williamson, 1994, 1995). The compaction of mudstones at shallow depths (thus low effective stresses) has been shown to proceed via the preferential collapse of the largest

pore-throats with little effect apparent upon the smaller pore-throats (Delage and Lefebvre. 1984; Griffiths and Joshi, 1989, 1990; Dewhurst *et al.*, 1998). However much of this work was performed on material simply characterized as mudstone, clay, soil etc and therefore detailed interpretations were problematic (cf. Dewhurst *et al.*, 1999b). In a series of papers, Dewhurst *et al.*, (1998, 1999a) and Yang and Aplin (1998) investigated the hypothesis that lithology (described by the clay content (% particles $<2\mu\text{m}$)) and porosity exert a principal control upon the pore-throat size distributions of both artificially and naturally compacted mudstones. In these papers it was illustrated that the variation in mean pore-throat sizes seen at a single porosity can be attributed to differences in grain size (e.g. Yang and Aplin, 1998). At any one effective stress a coarser grained mudstone has a broader pore-throat size distribution than a finer grained mudstone, although the degree of difference decreases with increasing effective stress (Dewhurst *et al.*, 1999a,b).

In summary the flow properties of mudstones are fundamentally related to the pore-throat networks which in turn are primarily controlled by two variables: grain size distribution and porosity (compaction state). However within this framework uncertainties remain, for example Dewhurst *et al.*, (1999a) noted that their data fell into a silt/sand-rich group and a clay-rich group, which exhibited quite different properties (such as pore-throat size distribution, porosity-hydraulic conductivity relationship etc). From this data it was unclear if these properties varied continuously with grain size or whether there is a clay fraction at which properties change abruptly.

1.4 Significance of mudstones for the oil industry

The importance of the flow properties of mudstones within the oil industry largely falls into four inter-related contexts: overpressure prediction, migration studies, column height analysis and prediction and understanding reservoir barriers and baffles. Within these contexts the first three all involve understanding the fluid flow properties of mudstones; it is the intimately related characteristic properties of low permeability and high capillary entry pressure which makes mudstones of quantitative significance in these contexts.

Mudstones form essential components of petroleum systems, forming both the source rock and caprock in many clastic petroleum systems. Due to their physical properties they form the rate limiting component within a petroleum system. To date two approaches have been implemented in basin scale migration modeling:

- (a) capillary pressure field modeling whereby migration is modeled purely as a function of capillary forces;
- (b) full physics Darcy flow modeling.

A fundamental problem besets both modeling strategies; the high resolution of capillary pressure field models requires a high level of data input, which is currently not matched by our understanding of the sedimentological heterogeneity and architecture of mudstone sequences and how this relates to the corresponding pore-throat network properties of the mudstones. Similarly the full physics approach taken by Darcy flow models requires the permeability structure along with the multiphase properties of mudstones to be understood spatially and accurately quantified. Our current understanding of all aspects of mudstones, particularly the inter-relationships between spatial distribution, depositional mechanism and fluid flow properties, seriously lags behind our ability to model the movement of fluids through them. This fact has implications for any attempt to understand and model how fluids move through and interact with mudstones over geological time scales.

At the human time scales of petroleum reservoir development and exploitation the low permeability of mudstones typically leads to their fluid flow properties becoming irrelevant within reservoir description. However for this very reason they form barriers or baffles within petroleum reservoirs; laterally extensive mudstones will form barriers to flow while mudstones of limited extent form baffles. Thus in this context it is the depositional geometry of mudstones which is of importance (along with any post depositional deformation).

The work carried out in this study will potentially aid many aspects of the quantification of mudstones and their flow properties within basin modeling work flows and in integrating dynamic fluid data with rock property data. In addition, greater understanding

of the depositional characteristics of mudstones may aid correlations between depositional process and dimensions, thus allowing their ability to act as barriers or baffles to be understood.

1.5 Dataset

The samples that make up this dataset have been gathered from the results of analytical work carried out at the University of Newcastle over a number of years. Although the dataset was not explicitly collated for this project, it remains a unique repository of well characterised mudstone data from a broad range of tectonic settings, sedimentary environments and geological ages.

The raw data from the grain size analysis, grain density, high pressure mercury injection capillary pressure (MICP) experiments etc was generated by technicians at the University of Newcastle. The analyses carried out in this work were carried out on this raw data, which in some cases was manipulated in order to derive the frequency distribution, for example.

There was generally an absence of ancillary, data geological contextual data for the samples utilised in this study. Effective stress data, mineralogical data and time-temperature histories are notable data which were not available, reducing the degree of certainty associated with any conclusions drawn on the controls of the evolution of physical properties of these samples. However, the porosity will give a measure of the maximum effective stress experienced – and is thus used here as an estimate of the degree to which the samples have been subjected to compressive stresses. The lack of mineralogical data together with time-temperature histories makes it impossible to get a significant appreciation of the extent to which to which the grain size and pore-throat size distributions of the samples have been affected by diagenetic processes, this work therefore concentrates purely upon the effect of compaction (porosity loss) and grain size in controlling the pore-throat size distribution. The fact that the grain size distributions obtained are superficially very similar to those obtained from contemporary sediments

(e.g. Kranck *et al.*, 1996) provides circumstantial evidence that the effects of diagenesis in altering the grain size distribution are limited.

1.6 Thesis structure

This work is structured as follows: Chapter 2 examines the sedimentological characteristics of the samples utilized in this study, focusing on grain size distribution due to its control upon the pore-throat network (Dewhurst *et al.*, 1998, 1999a,b). Detailed analysis of the grain size distribution is coupled with observations made from petrographic thin sections and Back Scattered Electron Microscope (BSEM) images for the first time. Simplifying strategies or classifications are favoured over detailed interpretation of single samples because the aim of this project is, in part, to integrate sedimentological properties with flow properties. In addition, if successful, establishing a generic, grain size classification, based on relevant criteria will aid communication, and reduce ambiguity between those engaged in mudstone research (cf. Flemming, 2000).

The third chapter builds on the first chapter and integrates the findings based upon the sedimentological analysis of these samples with the results of mercury injection capillary pressure (MICP) experiments, used to characterize the pore-throat size distribution and hence the pore-throat network of these samples. The nature of the samples pore-throat networks as functions of both lithology and porosity are investigated.

In the third chapter a numerical classification procedure for application to grouping quantitative grain size distribution data is investigated. Datasets comprising grain size percentage (e.g. % clay, % silt etc) and moment statistics, frequency distribution data at two scales of resolution and a combined dataset are investigated in terms of which data best segregate differing mudstone lithologies. Each grouping is investigated with regard to how well the established groups or mudstone grain size distribution (GSD) types correlate with pore-throat network properties and the classification proposed in Chapter 2.

The fifth chapter investigates the statistical distribution of parameters used to reduce pore-throat size distribution data when both lithology and compaction state are constrained. By constraining both lithology and porosity (shown to be the primary control upon mudstones pore-throat network (Dewhurst *et al.*, 1999a,b) other factors, such as sample type, temperature, etc are emphasized allowing their influence to be judged. The regression and prediction of the critical capillary entry pressure (CEP) is investigated using differing subsets and predictor variables.

Each of the chapters are written as a standalone piece of work and include full discussions and conclusions relevant to each individual chapter. In the discussion and conclusions each of the chapters are described and their findings and conclusions integrated into a final synopsis of this works major results and findings. A number of future avenues of research are suggested based on the findings made during this study.

Chapter 2 On the nature of natural mudstone grain size distributions – characteristics, processes and typing

2.0 Introduction

Mudstones are the most common sediment type comprising approximately 65% of the global sedimentary inventory (Aplin *et al.*, 1999). Approximately 50-70% of oceanic sediment is comprised of continental siliciclastics (Kranck, 1980), and down-slope re-sedimentation processes are fundamental in the transport and deposition of this material in marine settings (Gorsline 1984); the ~90% turbidite component of abyssal sediments attests to the importance of these processes in delivering sediment to the deep ocean (Kranck, 1980). The grain size distribution is one of the most fundamental properties of a fine-grained sedimentary rock and is utilised routinely in the Earth sciences for classification (e.g. Blatt *et al.*, 1980), sedimentological studies (e.g. Stevens *et al.*, 1996; Kranck and Milligan, 1991) and for understanding the physical properties of such sediments (Hein, 1991; Yang and Aplin, 1998; Dewhurst *et al.*, 1999a; Midttømme and Roaldset, 1999).

This work aims to distil what is currently known about the nature of mudstone grain size distributions in terms of both sedimentological interpretations and in terms of parameterization techniques. Because grain size is fundamental both in linking deposits to sedimentary processes (Kranck and Milligan, 1991) and in terms of understanding the physical properties of muds (Dewhurst *et al.*, 1999b; Midttømme and Roaldset, 1999), a classification methodology based on grain size is pertinent to both sedimentological studies and studies of the physical properties of these sediments. A new mudstone grain size classification or typing framework is therefore proposed in this study, reflecting the integration of a variety of grain size parameters combined with petrographic observations. This work was carried out on a dataset comprising 166 mudstone samples for which grain size data were available; in doing so a framework in which further investigations of how the grain size distribution relates to other properties such as the pore size distribution will be established (see subsequent Chapters). This classification is proposed for siliciclastic

mudstones and is therefore not applicable to fine-grained carbonates, biogenic sediments or true pelagites (which may have significant loess content).

2.1. Background

2.1.1 *Behaviour of fine-grained sedimentary particles (<63µm) in aquatic environments*

In marine settings clay and some silt-sized particles generally act cohesively and are primarily deposited as flocs. Flocculation is a complex process with at least 14 possible mechanisms that can cause clay and silt, along with organic, biogenic and colloidal material etc to aggrade (Eisma, 1993 p.135). The essential processes that drive flocculation are cohesion and collisions (Whitehouse *et al.*, 2000). Cohesion is a complex property that is controlled by many factors such as mineral composition, salinity, concentration of organic matter, etc. Collisions of particles will be a function of the particle concentration of the water column. Fine-grained sediment exhibits two distinct modes of behaviour in the marine environment; particles above $\sim 10\mu\text{m}$ behave non-cohesively, while particles below $\sim 10\mu\text{m}$ behave cohesively (McCave *et al.*, 1995). This dichotomy in mode of behaviour can be accounted for on both compositional and physical grounds; below $10\mu\text{m}$, clay minerals, whose surfaces have charge imbalances, begin to be present in significant proportions (Weaver, 1989; McCave *et al.*, 1995). Van der Waals attraction also begins to become a significant force, for example the ratio of Van der Waals attraction to particle weight increases by two orders of magnitude from $10\mu\text{m}$ to $1\mu\text{m}$ (McCave *et al.*, 1995). Figure 2.1 illustrates that the critical erosion stress (τ_e) required to entrain quartz particles into a moving body of water decreases approximately exponentially with particle size down to $\sim 10\mu\text{m}$, after which it increases signifying the onset of cohesive behaviour between quartz particles below this size.

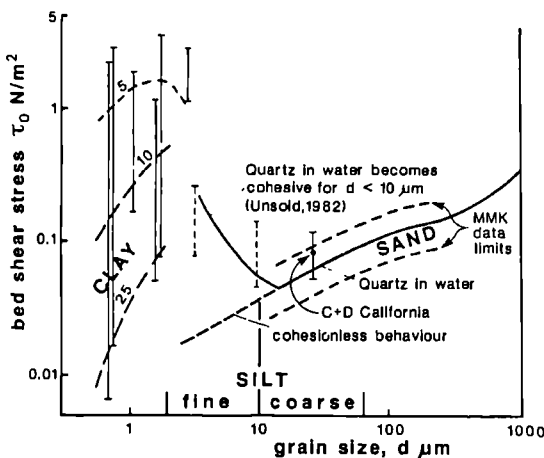


Figure 2.1. Plot of critical bed shear stress τ_0 ($\approx \tau_e$) for the erosion of quartz particles, data from Unsold (1982) and McCave et al., (1995). "C+D" refer to the clayey silt measured by Caccione and Drake (1986) and are the mean and range of the in situ critical erosion stress. "MMK data limits" refer to the limits of the high quality data evaluated by Miller et al., (1977). The data in the clay range are contoured for void ratio (\approx level of consolidation). From McCave et al., (1995), Figure 4.

2.1.2 Mudstone grain size parameters and their relationship to depositional processes

There have been many grain size distribution parameters applied to mudstones; here three of these methods, chosen to reflect both ubiquity and sophistication, are used to investigate and classify the distributions reported in this study.

2.1.2.1 Moment Statistics

The application of moment statistics intrinsically approximate grain size data to a log normal distribution, the first moment reports the arithmetical mean of the distribution, subsequent moment statistics quantify departures from log normality (Appendix A2.1). A number of studies have employed bi-variate plots of various statistical parameters derived from sedimentary grain size distributions to identify different depositional environments (e.g. Okazaki *et al.*, 2000) and/or mechanisms (e.g. Stevens *et al.*, 1996). These studies have been predominantly carried out on samples from known environments and are therefore used to illustrate separation between pre-determined environments/facies or geographical areas.

There has been a large degree of criticism of the use of moment statistical methods in the analysis of sedimentary rocks (e.g. Ehrlich, 1983); much of this criticism has focused on the implicit assumption that grain size distributions are approximately log-normal. More sophisticated methods, such as the log-hyperbolic distribution (LHD), have been proven to enhance the degree of separation between different sedimentological environments (e.g. Sutherland and Lee, 1994). Despite the potential improvement offered by these techniques, they have not been applied to large or diverse datasets; furthermore such techniques are computationally intensive, have only been applied to sands and do not fit all observed distributions (Christiansen and Hartmaann, 1991). The majority of the studies reporting new methods for quantifying grain size distributions have assessed beach environments and the deposition of sand-sized material, which is a physically distinct system from that of the sub-aqueous deposition of clay, silt and fine sand. Previous works appraising the log-normal distribution have had the advantage of knowing from which environments samples have been drawn; thus differing methods of quantifying grain size distributions may be assessed with regard to which technique best discriminates between environments; however, their utility outside the tested depositional settings is entirely unknown. Despite methods such as the LHD being capable of improved environmental discrimination, process based arguments for this improvement are not offered (e.g. Sutherland and Lee, 1994). Furthermore, in this study it will be shown that many fine-grained sediment are composed of bi or tri-modal distributions, each component of which can be adequately described by the Kranck grain size model (cf. Kranck and Milligan, 1985; Kranck *et al.*, 1996a, b).

In a study of grain size distributions taken from fine-grained sediment in the Baltic Sea Stevens *et al.*, (1996) attempted to recognize textural provinces representative of differing sedimentary processes using cross-plots of moment statistics. The data presented by Stevens *et al.*, (1996) demonstrate two main trends: the degree of sorting increases for both the finest and coarsest samples (Fig. 2.6b); the skewness values plot as a diagonal trend and increase with increasing mean grain size (Fig. 2.6b). The sorting – mean grain size trend has been suggested to reflect the mixing of two separate populations, representing different modes of deposition, i.e. a coarse fraction deposited by traction transport and a

fine fraction deposited by suspension. A minima in sorting (i.e. highest standard deviation) is recorded when each population is present in approximately equal proportions (Ashley, 1978; Stevens *et al.*, 1996). Stevens *et al.*, (1996) noted that the increased degree of sorting for the finer grain sizes may not be real as grain size analysis measurements have a threshold size below which the grain sizes cannot be quantified and thus have to be summed into a single bin (e.g. 0-2 μ m). A similar explanation has been suggested for the trend observed for the skewness versus mean grain size trend; when tractional transport dominates, deposition of coarser material will be prevalent, leading to the deposition of a coarser, positively skewed (phi notation) grain size distribution; when suspension deposition is dominant the opposite case will occur (Stevens *et al.*, 1996). When both modes of deposition are approximately equal Stevens *et al.*, (1996) suggest the skewness value will be ~ 0 (see Fig. 2.6b).

2.1.2.2 Sortable Silt

The first attempt to extract information pertinent to palaeocurrent strength from the grain size distributions of fine-grained sediments was carried out by McCave *et al.*, (1995). Sorting occurs via re-suspension and depositional events by processes of selective particle entrainment and aggregate break up (McCave *et al.*, 1995). The controlling parameters are critical depositional stress (τ_d), critical erosion stress (τ_e) and critical suspension stress (τ_s) where typically $\tau_d < \tau_e < \tau_s$ for non-cohesive material; when stress is $>\tau_e$ and $<\tau_s$, particles will move as bedload and some material will be sorted by becoming trapped in the viscous sublayer, while smaller particles continue to be transported (McCave *et al.*, 1995).

As discussed in Section 2.1.1, fine-grained sediment particles exhibit two distinct modes of behaviour in the aquatic environment; sediment above $\sim 10\mu$ m behaves non-cohesively while sediments below $\sim 10\mu$ m behaves cohesively (McCave *et al.*, 1995). The silt component coarser than 10 μ m thus responds to hydrodynamic processes and its properties may be used in some way to infer palaeocurrent speed (McCave, *et al.*, 1995).

2.1.2.3 Kranck model

Research carried out by workers led Kranck and co-workers, during 1980 to 1996, on the grain size frequency spectra of both suspended sediment and bottom sediment led to the development of a grain size distribution model able to differentiate between floc and grain settling processes (Kranck and Milligan, 1985; Kranck *et al.*, 1996a, b). The initial concepts were set out by Kranck (1980, 1984) based upon a series of settling experiments performed with differing concentrations of suspended sediment in both fresh and salt water.

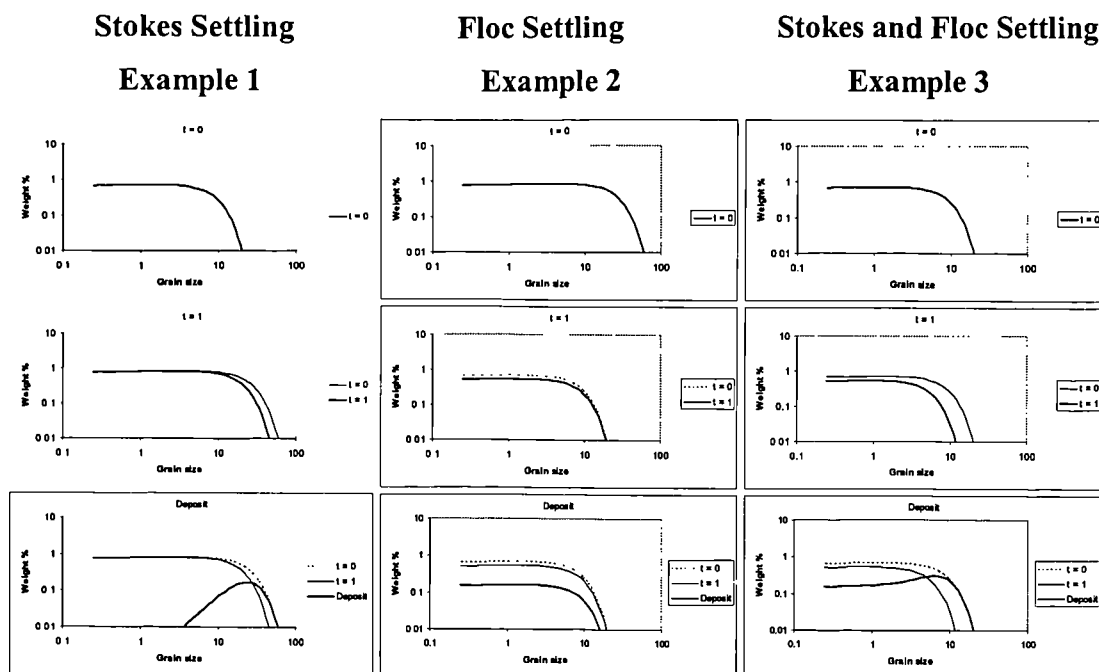


Figure 2.2. Suspended and deposited grain size distributions for: (a) unflocculated, (b) flocculated and (c) mixed suspended grain size distributions; t_0 represents the initial conditions, t_1 represents a point in time where conditions have altered such that material is deposited from suspension. Based on Kranck (1984).

In Figure 2.2 a series of depositional events are represented. At the initial point ($t = 0$) the suspended sediment grain size distribution is shown; after some time step ($t = 1$) the hydrodynamic conditions are altered such that material is deposited from suspension (e.g. due to decreased turbulence, increased sediment concentration). In figure 2.2 example 1

only the coarsest material is deposited, with the finer grained material remaining in suspension. This is the expected case for an unflocculated source suspension which settles out according to the suspended sediment's settling rate (i.e. dependent upon the Stokesian diameter of the particles). This produces a well-sorted deposit, enriched in coarse material relative to the suspension. In example 2 material of all grain sizes present in the suspension are deposited. This case is relevant when the entire suspended grain size spectrum is flocculated, so that material is deposited independent of the distribution of individual grain sizes. Example 3 is a combination of 1 and 2; in this case a proportion of material is deposited in flocculated form and a further component is deposited as single particles at rates dependent upon their Stokesian diameter. In example 1 Stokesian diameter (i.e. grain size) is the controlling factor and thus larger particles are deposited prior to smaller ones. The concentration of suspended sediment is the controlling factor on deposition rate in example 2, and relates to the assumption that flocs are made up of grains which have the same size distribution as the whole suspension (Kranck, 1980). The result of this duplication is that each floc has the same relative settling rate (e.g. Sternberg *et al.*, 1999) and results in deposits which retain the size distribution of the suspension. The absolute settling rate is dependent upon the rate at which flocs form and grow, which is dependent upon particle concentration (Kranck, 1984; Berhane *et al.*, 1997).

The Kranck and Milligan model (1985) can be fitted to the grain size distributions of fine-grained sediments and is based on the assumption that the deposition of fine particles occurs at rates proportional to the exponential of their settling rate from an unsorted turbulent source suspension (Kranck and Milligan, 1991). A simplified form of the equation describing a component of the size distribution is given by (Milligan and Loring, 1997):

$$C = \Delta Q w^{(m+n)} e^{-Kw} \quad (2.1)$$

where C is concentration in a size class, ΔQ is the concentration at a reference settling velocity, and w is the settling velocity calculated using Gibbs *et al.*, (1971). The variable m is hypothesized to be the slope of the source suspension as defined by the straight line

portion for the curve starting at $0.7\mu\text{m}$ and typically has a value between 1 and -1 (Kranck *et al.*, 1996a; Milligan and Loring, 1997). This model differentiates between floc settled, single grain settled and coarser material that has been subjected to higher energy and hence further sorting (Kranck *et al.*, 1996a, b). The exponent n controls the nature of the GSD model fit – i.e. flocculated or single grain. Material that plots as a straight line on a log-log plot has been deposited in a flocculated form from an unsorted source suspension; the exponent n has integer values of 0 for this proportion of the curve (Kranck *et al.*, 1996a; Milligan and Loring, 1997). For the portion of the curve that corresponds to single grain settled material, termed a ‘one round distribution’ by Kranck *et al.*, (1996a, b) the integer n has a value of one, and values of >1 for the coarsest material (Figure 2.3); K describes the maturity of the depositional process, i.e. the extent to which the coarser grains have settled out; K has units of (s cm^{-1}) as it multiplies the settling rate in the exponent of Eq. 2.1 (Kranck *et al.*, 1996a) and increases as the maximum and mean diameter of the suspension decreases due to settling. The relationship between the parameters derived in the fitting routine to the physical processes active during the transport and deposition of fine-grained sedimentary particles is illustrated in Figure 2.4.

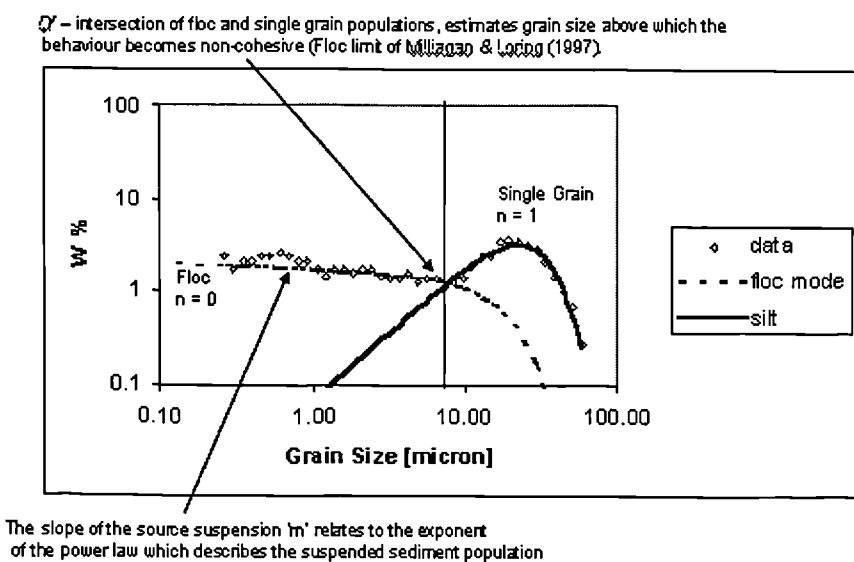


Figure 2.3. A disaggregated inorganic grain size spectra illustrating the floc and single grain ('one round') components of a fine-grained sediment.

The model of Kranck and Milligan (1985) and Kranck *et al.*, (1996a, b) has never been verified by laboratory experiments and thus the dependence of K upon factors such as concentration, shear velocity and depth are unknown. However, Kranck and Milligan (1985) did show a relationship between K and sediment concentration for data taken from the surface layer of the Orinoco River (Kranck and Milligan, 1985); they argued that since a feature of river transport is the relationship between total sediment concentration and discharge and hence depth-dependent currents – then the coefficient K does describe the adjustment of sediment size distribution to flow dynamics (Kranck and Milligan, 1985).

The potential for using the Kranck model to quantify physical processes in a global sense, particularly in energetic environments should not be overstated. The reason for this is that the physical factors with which the model parameters correspond to, such as the sediment source (and thus the source suspension slope m), flocculation state (dependent upon concentration, organic matter (ppm), Ph, mineralogy, salinity), are not constant through time or for any one setting or location. Therefore the model can only be used in a truly quantitative manner for samples collected from a single event (e.g. Curran *et al.*, 2004). In a global sense the model simply provides a useful framework with which to parameterize mudstone grain size distributions, allowing the qualitative comparison of differing mudstone samples.

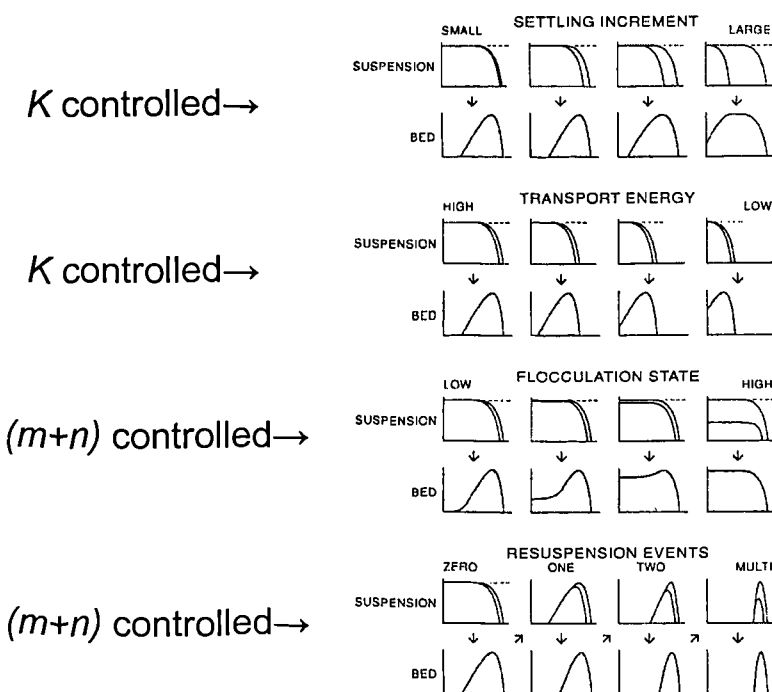


Figure 2.4. Hypothetical sketch illustrating the correspondence between the Kranck model parameters and processes active in the transport and deposition of fine-grained sedimentary particles. From Kranck and Milligan (1991), Fig. 23.8.

2.1.3 Grain size studies

A seemingly ubiquitous observation is that fine-grained sediments have bimodal grain size distributions, irrespective of the grain size analysis technique (e.g. Bulfinch and Ledbetter, 1984; Driscoll *et al.*, 1985; Kranck and Milligan, 1985; McCave *et al.*, 1995; Stevens *et al.*, 1996).

Examples of the results of some of these studies are shown in Figures 2.5 – 8; Figures 2.5 and 2.6 represent analyses of modern superficial fine-grained sediments whereas Figures 2.7 and 2.8 represent analyses undertaken on Pleistocene cores retrieved from the deep ocean. Despite huge variations in sedimentary environments, water depths, sediment sources etc; and the different analytical methods employed, the similarity in the form of the grain size distributions is striking. Essentially all the distributions either represent entirely flocculated material or a combination of flocculated and ‘Stokes’ settled material, providing strong evidence for the universality of the concepts and models proposed by Kranck and her co-workers described in Section 2.1.2.3.

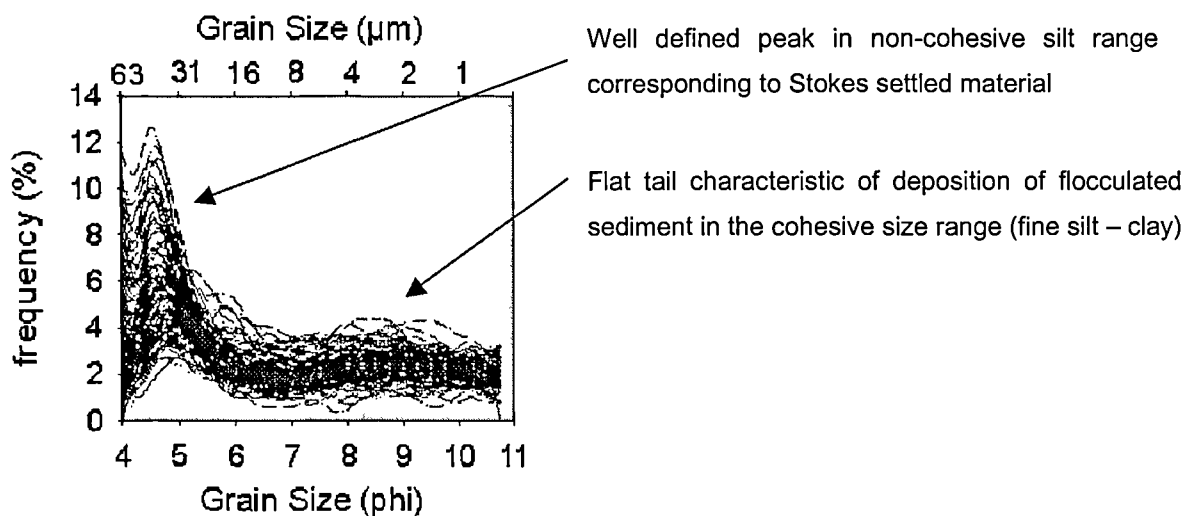


Figure 2.5. Grain size spectra analysed by a Sedigraph 5100 of superficial, nearshore muds from the Southern North Sea. From Chang *et al.*, (2004).

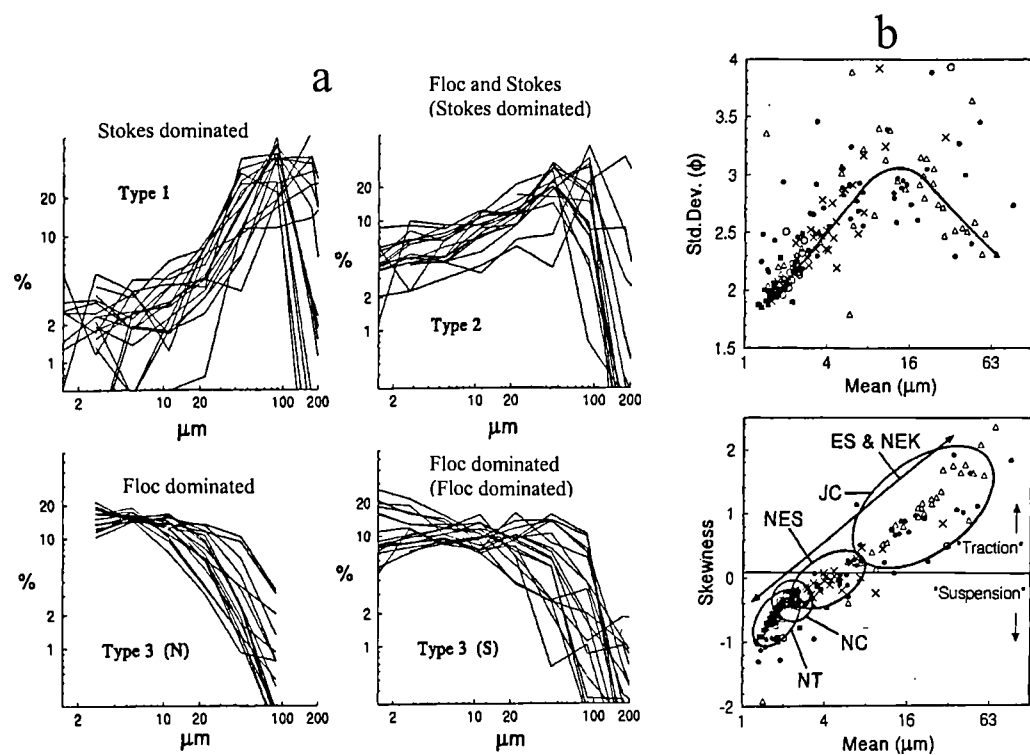


Figure 2.6. (a) Grain size spectra of superficial muds from the southern Baltic Sea (Kattegat and southern Skagerrak) analysed by a Coulter Counter; (b) and their moment statistic bi-variate cross plots. From Stevens *et al.*, (2004).

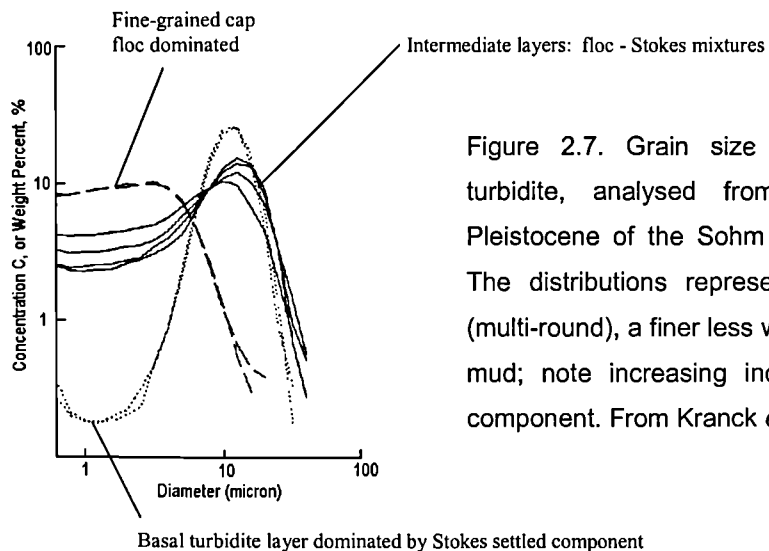


Figure 2.7. Grain size distributions from a graded turbidite, analysed from a core taken from the Pleistocene of the Sohm Abyssal Plain, North Atlantic. The distributions represent a well sorted coarse silt (multi-round), a finer less well sorted silt and a flocculated mud; note increasing incorporation of the flocculated component. From Kranck *et al.*, 1996b.

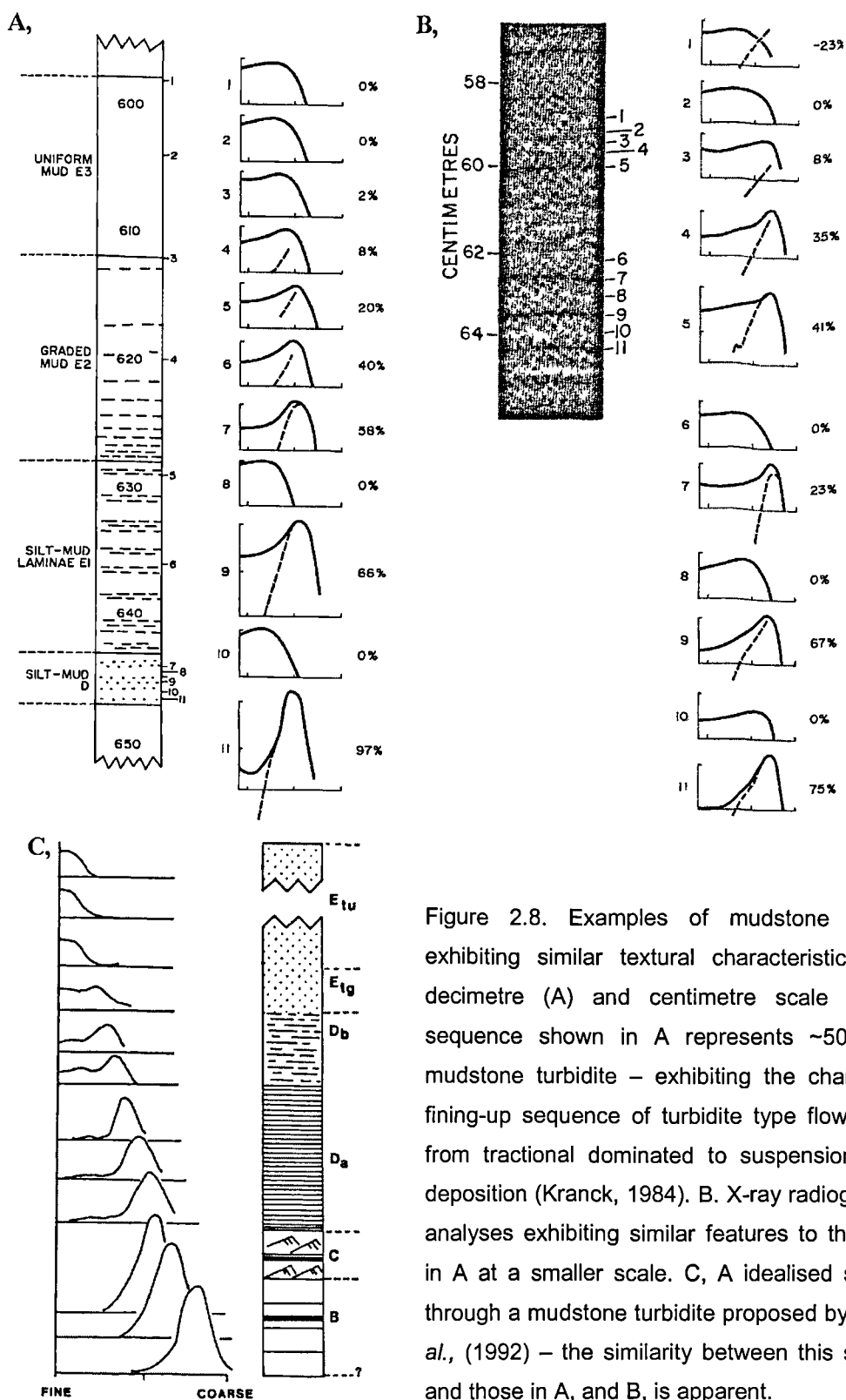


Figure 2.8. Examples of mudstone turbidites exhibiting similar textural characteristics at the decimetre (A) and centimetre scale (B). The sequence shown in A represents ~50cm of a mudstone turbidite – exhibiting the characteristic fining-up sequence of turbidite type flow evolving from tractional dominated to suspension fall out deposition (Kranck, 1984). B. X-ray radiograph and analyses exhibiting similar features to those seen in A at a smaller scale. C. A idealised sequence through a mudstone turbidite proposed by Jones *et al.*, (1992) – the similarity between this sequence and those in A, and B, is apparent.

2.1.4 Integration of parameters and models

The inventory of sedimentary basins is typically dominated by mudstones (e.g. Aplin *et al.*, 1999) which are primarily deposited by density flow processes (*sensu* Mulder and Alexander, 2001). These processes are particularly important in the formation of deltas, channel-levee and deep sea fan lobe systems (Mulder and Alexander, 2001). For example, it has been proposed by Lindsay *et al.*, (1984) that up to 50% of the sediment deposited in Mississippi River mouth bar deposits is ultimately deposited in deep water via a variety of slope failure mechanisms (sub-aqueous density flows *sensu* Mulder and Alexander (2001)). Curran *et al.*, (2004) suggest that much of the mud present in marine sedimentary basins is deposited by turbidity currents (Piper, 1978). Thus the majority of volumetrically significant mudstones in sedimentary basins will have grain size distributions which can be understood in terms of a floc and ‘Stokes’ settled component and may conform to the sequences present in Figure 2.5 – 2.8.

Recently Curran *et al.*, (2004) studied a single red-brown turbidite cored at six locations following an offshore transect across the Laurentian Fan. Stow and Bowen (1980) had previously studied similar sediments from the same area using standard grain size techniques and moment statistics, demonstrating that there is a decrease in modal grain size down-slope (see Fig. 2.9). Stow and Bowen (1980) suggested that as single silt grains and flocculated silt plus clay particles are deposited from a turbidity current the increased turbulence near the sea bed breaks up a high proportion of the flocs resulting in a preferential deposition of coarser silt grains upslope, as once flocs are destroyed the small constituent particles are ejected back into the flow. Turbulence decreases down-slope where lower shear permits an increasing proportion of finer material (and weaker flocs) to be deposited, resulting in a down-slope decrease in the average bottom sediment grain size (Stow and Bowen, 1980; Curran *et al.*, 2004). The work carried out by Stow and Bowen (1980) allowed Curran *et al.*, (2004) to compare grain size parameters and the insights into the depositional process that they can potentially provide.

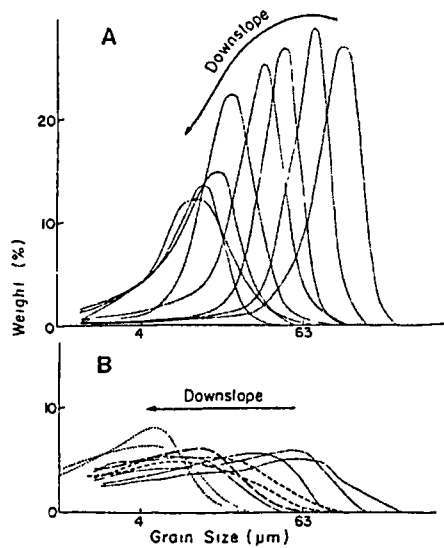


Figure 2.9. Down-slope fining of a series of fine sands / coarse silts (A) and muds (B) from a transect on the Laurentian fan from a proximal to distal location. From Stow and Bowen, (1980).

In Curran *et al.*’s (2004) study, moment statistical values, sortable silt values and the Kranck model were all applied allowing comparison of these techniques on a well constrained set of samples. The results and analysis of Curran *et al.*, (2004) suggested that the sortable silt parameter provided the least information, simply revealing that the mean diameter of the sortable silt decreased down-slope due to preferential deposition of the coarsest grains (Fig. 2.10a). However, they did not consider the percentage of sortable silt. In terms of the moment statistics, it was shown that the mean grain size mirrored the down-slope fining trend picked out by the sortable silt parameter (see Fig. 2.10b). This down-slope trend was accompanied by an increase in sorting quantified by the decrease in standard deviation (Fig. 2.10c). Stevens *et al.*, (1996) suggested that mean grain size – sorting trends reflect the interplay of cohesive and non-cohesive grain size populations; when they are equally mixed the sorting (i.e. standard deviation) is maximized and when one mode dominates it is minimized (Section 2.1.2.1). Thus the trend probably reflects the increasing proportion of flocculated material down-slope. Skewness was also seen to decrease down-slope (Fig. 2.10d), possibly reflecting the increasing influence of suspension deposition (cf. Section 2.1.2.1; Stevens *et al.*, 1996).

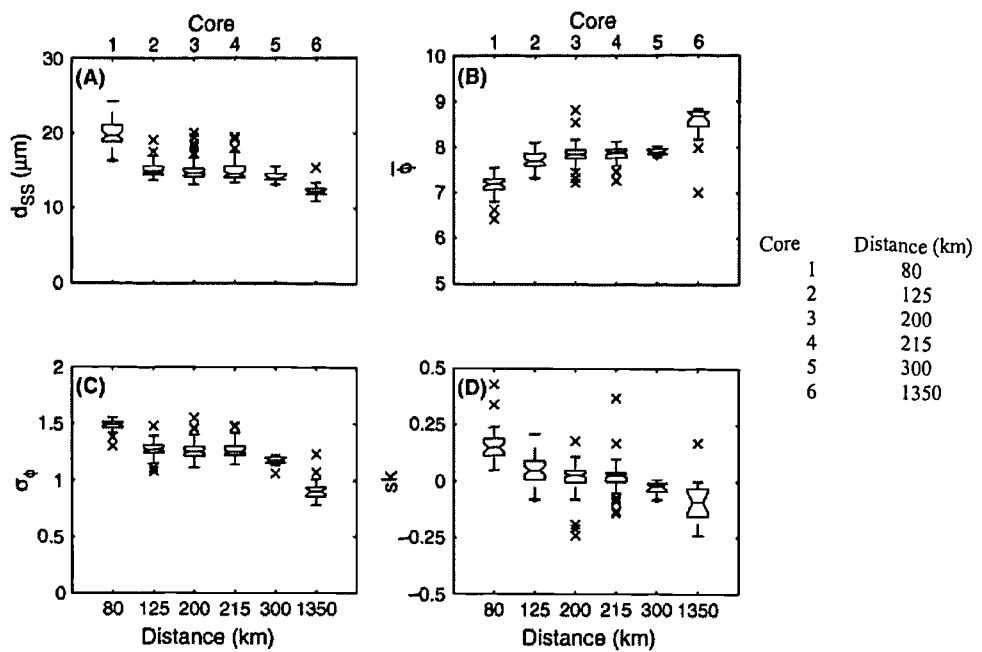


Figure 2.10. Boxplots showing the variability and down-slope evolution of various grain size parameters for each core taken across the Laurentian Fan; the box represents the lower, middle and upper quartiles of the data set. The lines extending from the box show the extent of the data set within 1.5 of the interquartile range, and 'x' represents outlier values. Sortable silt mean diameter (d_{ss} μm) computed according to McCave *et al.*, (1995) decreases down-slope similar to d^\wedge of the 'inverse floc model' of Curran *et al.*, (2004), reflecting the progressive slowing of turbidity currents as they deposit sediment (A). Measures of moments of mean phi diameter (B), standard deviation of mean phi diameter (C) and skewness (D) are also shown. From Curran *et al.*, (2004).

In terms of the Kranck model parameters, Curran *et al.*, (2004) used a second generation model termed the 'inverse floc' model. In this model two new parameters were introduced; D_f corresponds to the intersection of the floc and non-cohesive silt components and d^\wedge corresponds to the maximum floc size and replaces the K parameter. From the analysis of the six Laurentian Fan cores Curran *et al.*, (2004) demonstrate that the m ('source slope') parameter only varies slightly as expected for a turbidite deposit of the same composition or source (Fig. 2.11a). The D_f ('floc limit') is virtually constant except for the most distal core. Curran *et al.*, (2004) suggest that this indicates that the packing of fine grains does not change significantly down-slope for $\sim 300\text{ km}$ (Fig. 2.11b). There is a significant decrease in D_f at the most distal core taken on the Sohm abyssal plain. This observation,

according to Curran *et al.*, (2004), reflects a decrease in suspended sediment concentration such that floc formation is hindered. Combined with decreasing turbulence, the decline in concentration leads much of the sediment to be deposited as single grains rather than flocs (Curran *et al.*, 2004). The d^\wedge parameter (which is approximately inversely proportional to the fitted floc mode K value) exhibits a clear evolution down-slope (Fig. 2.11b); in proximal locations d^\wedge is highest indicating that floc size is maximized, probably reflecting relatively high suspended sediment concentrations. The d^\wedge value is seen to decrease across the fan as the suspended sediment population evolves and the concentration and turbulence decreases (Fig. 2.11d). In the most distal location d^\wedge is low reflecting the depletion of the largest grains from the available sediment population and the decreases in concentration and turbulence.

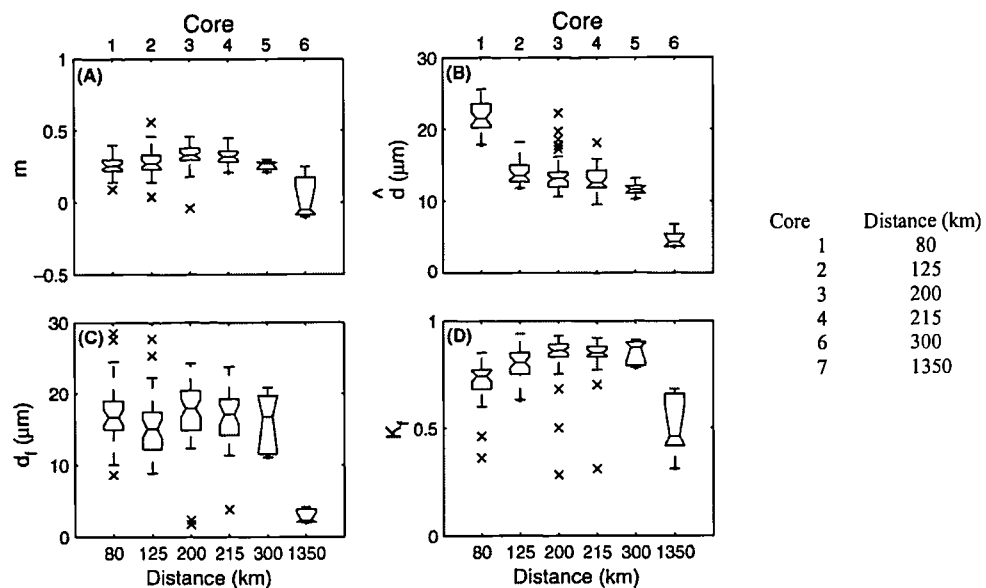


Figure 2.11. Boxplots showing the down-slope evolution of the inverse floc model (\approx Kranck model) parameters across the Laurentian Fan. Boxplots show the variance of each parameter with depth for each core, the box represents the lower, middle and upper quartiles of the data set. The lines extending from the box show the extent of the data set within 1.5 of the interquartile range, and 'x' represents outlier values. The 'source slope' m (A) is uniform down-slope, as expected for turbidites formed from the same source material. The 'falloff diameter', d^\wedge (B), 'floc limit', d_f (C) and estimated mass fraction deposited as flocs, K_f (D) show variation with down-slope position that can be explained by a simple conceptual model of particle packing. From Curran *et al.*, (2004).

Overall application of the second generation Kranck model did not specifically change Curran *et al.*'s (2004) interpretation and conceptual model of deposition on the Laurentian Fan relative to that of Stow and Bowen (1980) who used more basic procedures. Even so the application of the model did improve the understanding of the packing and the nature of deposition of mud on the Laurentian Fan (Curran *et al.*, 2004).

To summarise, three grain size distribution reduction techniques have been discussed; moment statistics, sortable silt and the Kranck model. From the examples of mudstone grain size distributions presented here it is clear that they are commonly bimodal in form and thus their approximation to log-normality will usually be poor. However, despite this, the mean grain size in combination with the standard deviation and skewness parameters can be used to differentiate samples and infer the relative proportions of floc- and Stokes-settled components in a qualitative manner. The mean sortable silt diameter has been shown to typically mirror the moment mean grain size (Curran *et al.*, 2004). As the information it carries may be quite subtle this parameter is likely to be of more use in detailed regional studies where multiple samples from well constrained stratigraphic settings are available for analysis. The Kranck model has been shown to separate and quantify the floc- and Stokes settled components of fine-grained sediment grain size distributions allowing understanding of the nature of deposition and particle packing of the sediment. There is currently no quantitative link to distinct depositional mechanisms or settings, and the parameters are sensitive to many factors such sediment concentration, turbulence, sediment source, sea water chemistry, etc, which may change rapidly on a geological time scale. All three techniques are utilized in this study in order to extract the maximum information from each grain size distribution analysed.

2.2 Samples

The samples selected for analysis in this work represent an extremely broad range of sedimentary settings, including dryland river / ephemeral lake, nearshore deltaic to deep water continental slope environments. Such diversity in environments provides a global aspect to this dataset and any significant difference between the grain size distributions derived from such different settings are likely to be readily apparent. However, the ancillary data associated with the samples utilized in this study was typically extremely sparse, complicating any interpretation of the processes responsible for their deposition. Brief summaries of each of the areas used are given below.

2.2.1 Deep water, Iota Area (IOTA)

The samples from the Iota Area were recovered from 3 deep water wells and are of Plio-Pleistocene to Miocene age. The wells penetrate mud-rich siliciclastic sequences contained within mini-basins formed by salt withdrawal in approximately 2500 – 3000m of water on deep water fan and continental slope environment.

2.2.2 Deep water, Eta Area (ETA)

The samples were recovered from two wells on a continental slope at 1200 – 1500ms water depth. The depositional setting in this area is a continuous depositional system which connects through the slope topography, passing from the upper slope into intra-slope basins. The sediments are predominantly siliciclastic and are associated with channel fed re-sedimentation events (largely in the form of turbidites and debris flows) which are inter-bedded with hemipelagic intervals.

2.2.3 Jurassic sediments, North and Central Viking Graben, North Sea

The samples used in this study are drawn from the Lower, Middle and Late Jurassic sediments of the Central and Viking graben. The formations represented in this study are briefly described below:

2.2.3.1 Lower Jurassic: Dunlin Group

Drake Formation (NOR-1; NOR-4; NOR-6; NOR-9; NOR-10; NOR-22; NOR-23; NOR-24; NOR-25).

The Drake Formation is composed of a unit of sandy and calcareous grey marine mudstones (originally named as the Dunlin Shale Member or Drake sub-unit) lying above the sand-prone Cook Formation, and is overlain erosionally by the Middle Jurassic Brent Group (Underhill, 1998). The Drake Formation commonly contains thin beds of oolitic sideritic ironstones; similar units exposed in the onshore equivalent Cleveland Ironstone Formation have been interpreted by Macquaker and Taylor (1996) as representing the correlative equivalent of sequence boundaries or part / all of the forced regression system tract. The upper parts of the Drake formation show evidence of shallowing thought to be due to progradation above the acme of the early Jurassic transgression (point of maximum retrogradation) (Underhill, 1998). The Drake unit represents deposition in an open shallow marine shelf setting (Partington *et al.*, 1993).

2.2.3.2 Middle Jurassic: The Viking Graben – Brent Group

The Brent Group represents the most important reservoir sequence within the North Sea; it was deposited in a paralic, deltaic and shallow marine environment (Partington *et al.*, 1993) and represents a broadly regressive-transgressive wedge of diachronous sediment recording the outbuilding and subsequent retreat of a large wave-dominated delta (Underhill, 1998).

Rannoch Formation (NOR-12; NOR-26)

The Rannoch Formation is the stratigraphically lowest member of the Brent Group; the formation represents a progradational stage and is dominated by sandstone deposition in a high energy, storm-dominated, middle shoreface environment (Underhill, 1998).

Ness Formation (NOR-2; NOR-3; NOR-7; NOR-8)

The Ness Formation records the last major stage of progradation of the Brent Delta and also includes the onset of its retrogradation (Underhill, 1998); the formation consists of a heterolithic sequence of sandstones, mudstones and coals thought to represent deposition in a delta-top environment (Underhill, 1998).

Brent Formation (NOR-27; NOR-29)

2.2.3.4 Late Jurassic – Humber Group

Heather Formation (NOR-5; NOR-11; NOR-21)

The Heather Formation records deposition in the North Sea during the most significant phase of synrift extensional activity (Underhill, 1998). The Heather Formation is dominated by grey, silty marine mudstones deposited in restricted marine shelf (Partington *et al.*, 1993) and lies between the coarse siliciclastics of the Brent and Fladen groups and the more organic-rich Kimmeridge Clay Formation (Underhill, 1998).

2.2.4 Zeta Area

The sediments of the Zeta Area were deposited in a back-arc basin formed in response to the north-dipping subduction of the Neo-Tethyan Ocean. The sediments record the evolving drainage systems and exhumation patterns during continental deformation; as much as 10km of sediment have been deposited in the last 5.5Ma. Deposition was greatest

in the Lower Pliocene when a sea level lowstand (associated with the Messinian salinity crisis) resulted in several rivers prograding into the basin interior following the palaeo-sea's isolation from the open ocean. Depositional environments in this setting have been shown to include sheetflood, fluvial, playa mudflat and lacustrine settings.

2.2.5 Chi Area

The Chi Area, a sub-basin of a foreland basin system, is formed by the obliquely converging margins of two complex plates. The sedimentary succession is dominantly siliciclastic and approximately 12km deep, deposited throughout the Pliocene and Pleistocene and thus sedimentation has been rapid. This sediment has been primarily supplied by a palaeo-river into a delta system which has prograded over a current- and storm-influenced shelf during this period. The siliciclastic wedge is formed by both marine and terrestrial siliciclastic megasequences as a series of prograding wedges overlying a pre-Pliocene or lower Pliocene mobile shale facies.

2.3 Methods

2.3.1 Standard Techniques

The samples analysed in the study comprise side-wall cores, core plugs, and cuttings. The bulk of the analyses were therefore performed on intact pieces of rock $\sim 1\text{ cm}^3$ in size. The samples were prepared for grain size analysis using the technique of Yang and Aplin (1997) where samples are subjected to a series of freeze-thaw cycles which gently disaggregate the sample. After a variable number of cycles, the disaggregated sample was introduced into a $\sim 100\text{ml}$ solution with a suspended sediment concentration between $\sim 1\text{-}2\%$ by weight (in line with the recommendations made by Coakley and Syvitski (1991) along with 5ml of dispersant (33g L^{-1} sodium hexametaphosphate and 7g L^{-1} sodium carbonate). The sample was then further disaggregated by subjecting the solution to ultrasonic treatment for periods of ~ 1 hour. Once this treatment was complete the solution

was sieved at 63 μm in order to remove the sand fraction (if present) which was then dried, weighed and recorded.

The sub-63 μm grain size distribution was determined using a Sedigraph 5000ET following the technique of Coakley and Syvitski (1991). Just prior to introduction to the Sedigraph's settling cell, a further 5 ml of dispersant was added to the solution and the samples were agitated for 30 minutes using a magnetic stirrer, ensuring no flocculation occurred. The errors resulting from both electrical and mechanical effects in the Sedigraph method have been estimated to be $+/-1\%$ (Coakley and Syvitski, 1991). Previous intra-laboratory tests on the precision of the Sedigraph based on repeat testing of samples obtained results found to be with $+/-2\%$ of each individual size subclass on the previous measurement (e.g. Dewhurst *et al.*, 1999c).

The resulting grain size cumulative curves were corrected for the removal of the >63 μm component using equation 2.2. The clay content (% <2 μm) and the sortable silt content (% >10 μm) was derived from the cumulative curve following correction of the Sedigraph data using an equation derived from intra-laboratory calibration of the Sedigraph to the pipette method (Yang and Aplin, *pers. comm.*) (Equation 2.3).

$$X_{\text{corr}} = X_{\text{sed}}(1-X_{63}) \quad (2.2)$$

$$X_{\text{pip}} = 5.64 + 0.41386X_{\text{corr}} + 0.004518X_{\text{corr}}^2 \quad (2.3)$$

where X_{sed} refers to values recorded directly from the cumulative curve generated from the Sedigraph analysis; X_{63} refers to the weight % of the material removed from sieving at 63 μm ; X_{corr} refers to the values corrected for removal of the >63 μm material and X_{pip} refers to the values calibrated to the pipette method.

The grain size frequency distribution was derived by directly digitizing the grain size cumulative curve producing approximately 2000 data points. The data points forming the digitized cumulative curve were numerically differentiated and summed into 0.2 phi bins,

thus describing the sub-63 μm grain size frequency distribution as 40 data points. These data points are only corrected for removal of the >63 μm material; the pipette calibration was not applied as it was derived for material <20 μm and here the entire grain size distribution is of interest.

In a series of papers published between 1980 and 1996 Kranck and co-workers advocated the plotting of fine-grained sediment grain size spectra on log-log plots, because portions of different samples with similar size distributions plot as similar shapes, irrespective of the nature of the rest the distribution. This approach emphasizes the straight line segments which reflect the unsorted size distribution of flocculated material, which is thought to be inherited directly from primary weathering of the source rocks (Kranck and Milligan, 1985). In this study Kranck's technique is followed and the grain size frequency distributions are plotted as log – log spectra of grain size (μm) versus weight %.

2.3.2 Moment Statistics

The moment statistics generated in this study were calculated using the method of Griffiths (1962, p. 90, table 5.4) for data summed in whole phi bins. (Appendix A2.1).

2.3.3 Kranck model fitting

The equation established in the Kranck model (Equation 2.1) may be put into linear form by taking the log of both sides (Kranck *et al.*, 1996a):

$$\ln C = \ln A Q + (m+n) \ln w - K w \quad (2.4)$$

A least squares regression was carried out in Excel to estimate the parameters ($\ln A Q$, $m+n$, K) from the components of observed grain-size distributions. When appropriate the floc-silt intersection, termed D_f after Curran *et al.*, (2004), was also calculated. This parameter estimates the grain size diameter at which particle behaviour changes from non-cohesive to cohesive and thus estimates the maximum particle size that will be incorporated into flocs.

2.3.5 Petrography

Thin sections were prepared for every sample for which sufficient core plug or side-wall core sample material was available. Sections were thinned to $\sim 20\mu\text{m}$ due to the opacity of mudstones, grinding and polishing was performed within oil in an attempt to minimize sample damage. After initial optical work the samples were carbon-coated and analysed using a Jeol 6400 Scanning Electron Microscope (SEM) equipped with a Link backscattered electron (BSE) detector.

2.4 Results

All the data were initially plotted up and analysed in a heuristic manner. Initial analyses of the 166 samples utilized in this study revealed a spectrum of grain size distributions which were only loosely related to the sample location. This spectrum ranged from very fine-grained, entirely flocculated sediments with high clay contents and very few particles coarser than $10\mu\text{m}$ to relatively coarse, sand-silt-clay mixtures. Inspection of the data suggest that the shape of the grain size distribution and the associated Kranck model parameters are consistent and that a number of ‘types’ could account for the bulk of variability present in the dataset. Combining this data with inspection of the corresponding petrographic and electron microscope images strengthened this contention. Thus analysis of the shape of the grain size distribution, its Kranck parameters and the microscopy images lead to a conceptual grain size typing framework being established. The moment statistics and sortable silt parameters were integrated and assessed once the dataset had been partitioned into types on the basis described above. For this dataset six grain size ‘types’ were identified and are described below.

2.4.1 Type 1 – floc dominated

The first grain size type recognized in this study represents the finest end-member of the spectrum. Examples of two Type 1 grain size distributions together with their moment statistic values and Kranck model parameters is given in Figure 2.12. This grain size distribution type is referred to as low concentration flocculated GSD's as it is dominated by a floc settled component according to the Kranck and Milligan (1985) model, and typically has high K values (averaging 239.5). As the value of the K parameter increases with the 'maturity' of the depositional process (Section 2.1.2.3, Figure 2.4; Kranck and Milligan, 1985; Kranck *et al.*, 1996a, b) these sediments represent deposition at the distal ends of sediment transport paths. Examples of this grain size distribution types are drawn from deep water Iota Area and Zeta Areas only and represent 13% of the total grain size distribution dataset used in this study. Standard sedimentary parameters and statistics are given in Table 2.1 and the parameters derived from fitting the Kranck model are given in Table 2.2. These sediments are typically rich in microfossils (see Figs 2.13, 2.15 and 2.16).

A thin section taken from a deep water Iota Area sample with a Type 1 grain size distribution is shown in Figure 2.13. This example illustrates the ungraded, homogeneous characteristic of these sample types. The examples shown in Figures 2.13 and 2.16 exhibit similarities to the tan, ungraded mudstone facies from the Middle Eocene Cozy Dell Formation (southern California) pictured by O'Brien and Slatt (1990, p. 83). This facies was interpreted to have been deposited in a submarine slope setting by slow sedimentation from hemipelagic settling or from the distal portion of waning turbidity currents in an environment analogous to the modern Mississippi delta front (O'Brien and Slatt, 1990). Two Back Scattered Electron Microscope (BSEM) images of Type 1 samples are shown in Figures 2.14 and 2.15. At this scale there is still a lack of any obvious structure and the sample can be described as homogeneous. The example in Figure 2.15 appears particularly fine-grained with very few particles $>10\mu\text{m}$ visible at all. Some microfossil fragments are embedded within the clay-rich matrix.

In Figures 2.16 and 2.17 cm scale images of the thin section are combined with the corresponding grain size distribution and magnified (x4) image. Figure 2.16 represents a sample taken from a deep water Iota well as a side wall core. It exhibits very similar characteristics to the sample shown in Figure 2.12: a very fine grain size, and a homogeneous, un-laminated appearance at the cm, mm and μm scale (Figs. 2.13 - 16). These characteristics are thought to be representative of slow sedimentation from hemipelagic settling or from the distal portion of waning turbidity currents. The high proportion of microfossils seen in this facies provides possible further evidence for slow sedimentation rates.

The second example does exhibit bedding at the mm scale, being darker at the base and lightening upwards, probably indicating coarsening of the grain size. The magnified image was taken from the base of Figure 2.17a. The magnified image is homogeneous and un-laminated at the μm scale (Fig. 2.17c). This particular sample is a Zeta Area core plug sample; the mud dominated section from which it was retrieved has recently been interpreted as representing a transgression of a regional lake. Thus this sample probably represents slow sedimentation during a low energy phase of the lake's history.

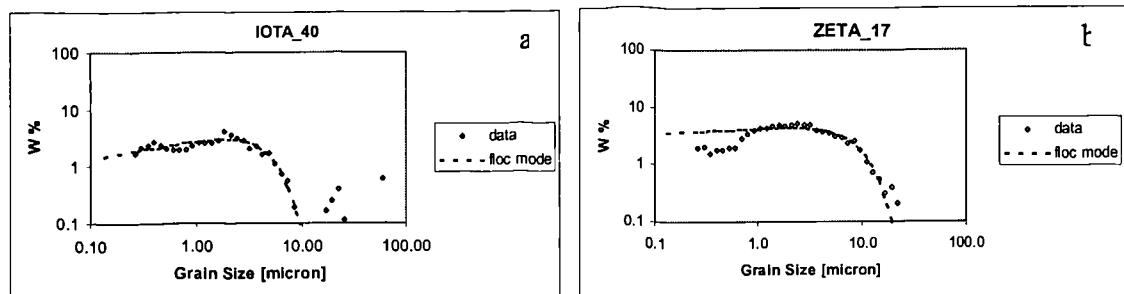


Figure 2.12. Disaggregated grain size spectra of Type 1 GSD Types on log-log weight percent – grain size (μm) plots; (a) Iota Area example – 67% clay, $1.4\mu\text{m}$ mean grain size (mgs), modeled 'floc' parameters: ΔQ 1.14, $(m+n)$ -0.0933, K 97.16. (b) Zeta Area example – 40.2% clay, $2.0\mu\text{m}$ mgs, modeled 'floc' parameters: ΔQ 5.2, $(m+n)$ 0.0089, K 113.6.

Code	Whole distribution stats							SS mean (μm)
	% Clay	% Sand	% Silt	%>10um	Mean Grain Size (μm)	SD	Skewness	
IOTA_3	66	0.5	34	12	1.5	1.5	-0.2	24
IOTA_13	73	0.1	27	12	1.0	1.6	-1.3	24
IOTA_22	73	0.1	27	9	1.0	1.4	-0.7	30
IOTA_30	61	0.1	39	11	1.3	1.6	-0.6	19
IOTA_37	58	0.1	42	13	1.8	1.7	-0.4	21
IOTA_40	67	0.0	33	10	1.4	1.5	-0.6	31
IOTA_43	58	0.6	41	16	1.6	1.8	-0.6	19
IOTA_44	44	0.8	55	21	1.8	1.8	-0.8	25
IOTA_45	71	0.1	29	12	1.0	1.6	-1.0	21
IOTA_63	51	2.6	47	22	1.8	1.8	-0.8	21
IOTA_66	60	0.3	40	14	1.5	1.7	-0.8	26
IOTA_68	52	0.2	48	19	1.9	1.8	-0.9	27
IOTA_69	49	1.7	50	21	2.0	1.7	-0.8	26
IOTA_70	52	4.2	44	12	1.6	1.5	-0.5	21
IOTA_71	55	0.0	45	14	1.5	1.6	-0.7	21
IOTA_73	42	1.1	56	17	2.0	1.7	-0.6	30
IOTA_74	46	0.5	53	25	2.1	1.9	-0.7	21
ZETA_5	53	0.0	47	10	1.4	1.4	-0.2	14
ZETA_7	43	0.5	57	10	1.8	1.3	-0.1	16
ZETA_8	29	2.3	69	23	2.9	1.6	-0.1	18
ZETA_17	40	0.0	60	13	2.0	1.4	-0.1	14
ZETA_23	36	6.4	57	25	2.2	1.6	-0.2	18

Table 2.1. Sedimentary parameters and moment statistics derived from samples with a Type 1 GSD..

Code	Kranck Model Parameters				r^2
	ΔQ	$\log \Delta Q$	$n + m$	K	
IOTA_3	1.1	0.1	-0.1	111.0	0.92
IOTA_13	0.1	-2.0	-0.3	56.2	0.91
IOTA_22	31.1	3.4	0.3	1143.7	0.81
IOTA_30	4.4	1.5	0.0	284.4	0.94
IOTA_37	9.9	2.3	0.2	246.0	0.85
IOTA_40	17.4	2.9	0.2	517.1	0.91
IOTA_43	1.5	0.4	-0.1	72.3	0.96
IOTA_44	20.4	3.0	0.2	383.5	0.93
IOTA_45	0.9	-0.2	-0.1	215.4	0.94
IOTA_63	1.8	0.6	-0.1	114.3	0.94
IOTA_66	2.8	1.0	0.0	210.0	0.94
IOTA_68	7.7	2.0	0.1	336.0	0.97
IOTA_69	7.9	2.1	0.1	230.5	0.91
IOTA_70	24.1	3.2	0.2	450.0	0.93
IOTA_71	7.5	2.0	0.1	382.7	0.98
IOTA_73	45.8	3.8	0.3	456.4	0.80
IOTA_74	14.0	2.6	0.2	382.9	0.81
ZETA_5	2.4	0.9	-0.1	210.2	0.95
ZETA_7	24.5	3.2	0.2	260.0	0.95
ZETA_8	41.9	3.7	0.3	170.4	0.96
ZETA_17	6.0	1.8	0.0	102.0	0.96
ZETA_23	15.2	2.7	0.2	156.2	0.95

Table 2.2. Kranck model parameters derived from the fitted floc-component of Type 1 sample grain size distributions.

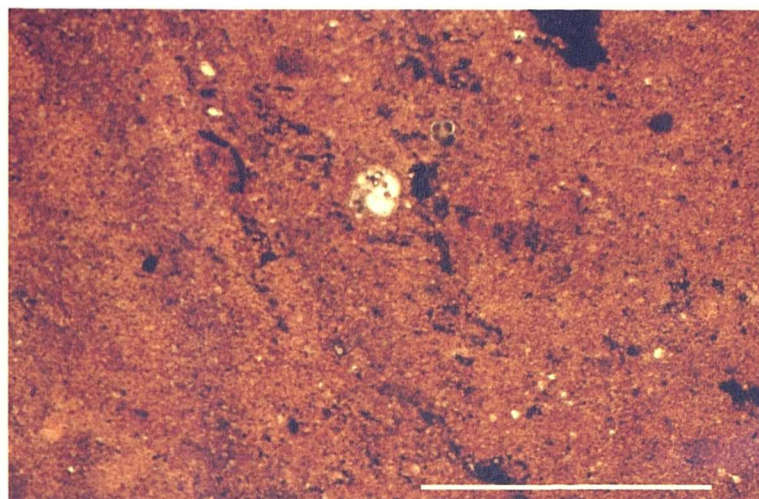


Figure 2.13. Transmitted-light photomicrograph (plane light, x4) taken from a thin section of a sample with a Type 1 grain size distribution (IOTA_69). The thin section illustrates homogeneous, ungraded sediment consistent with deposition from suspension fall-out of flocculated material primarily $<10\mu\text{m}$. A number of foraminifera tests are visible in the picture. The scale bar (bottom right) is $1000\mu\text{m}$.

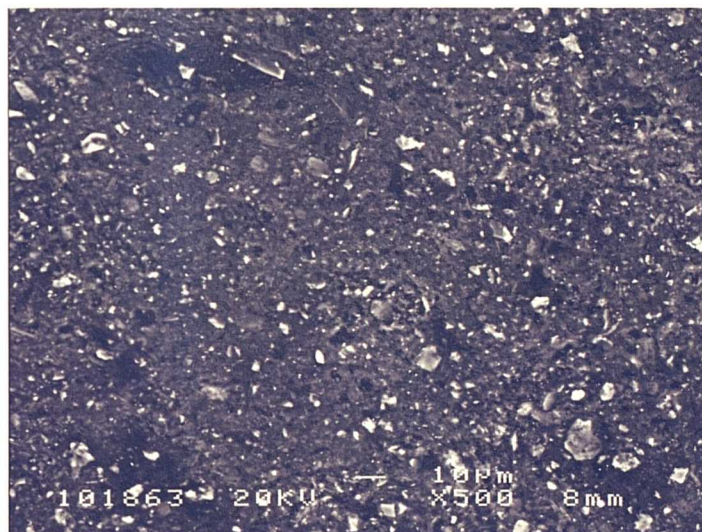


Figure 2.14. Back scattered electron-optical micrograph (BSEM) of a sample with a Type 1 grain size distribution (IOTA_3). The field of view is $\sim 100\mu\text{m}$. Silt grains, typically $<15\mu\text{m}$ in size 'float' in a matrix of finer silt and clay indicating co-deposition of material at this scale.

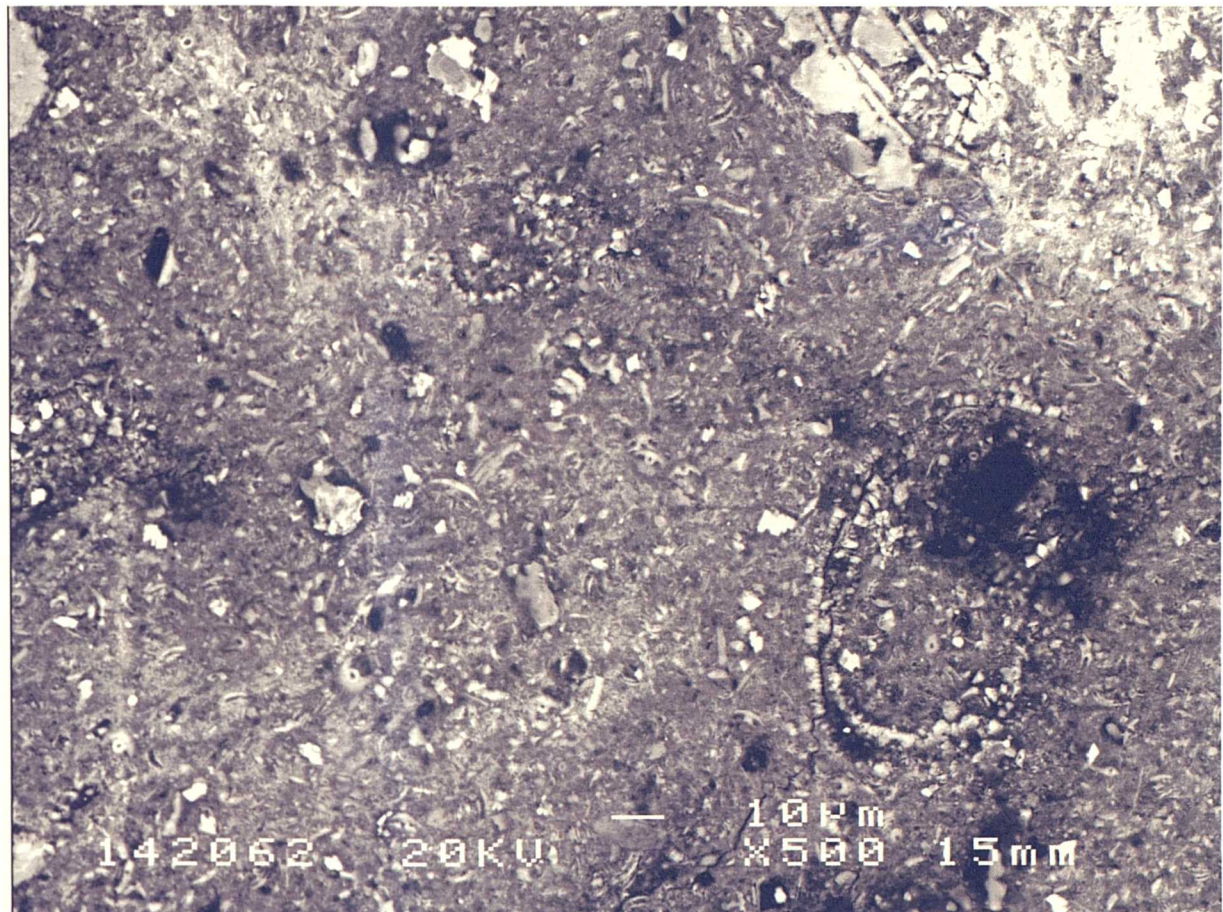


Figure 2.15. Back scattered electron micrograph (BSEM) of a sample with a Type 1 grain size distribution (IOTA_30). The field of view is $\sim 100\mu\text{m}$. There are very few silt grains, and those that are present are typically $<10\mu\text{m}$ in size. These grains along with a number of microfossil types 'float' in a matrix of finer silt and clay indicating co-deposition of material at this scale.

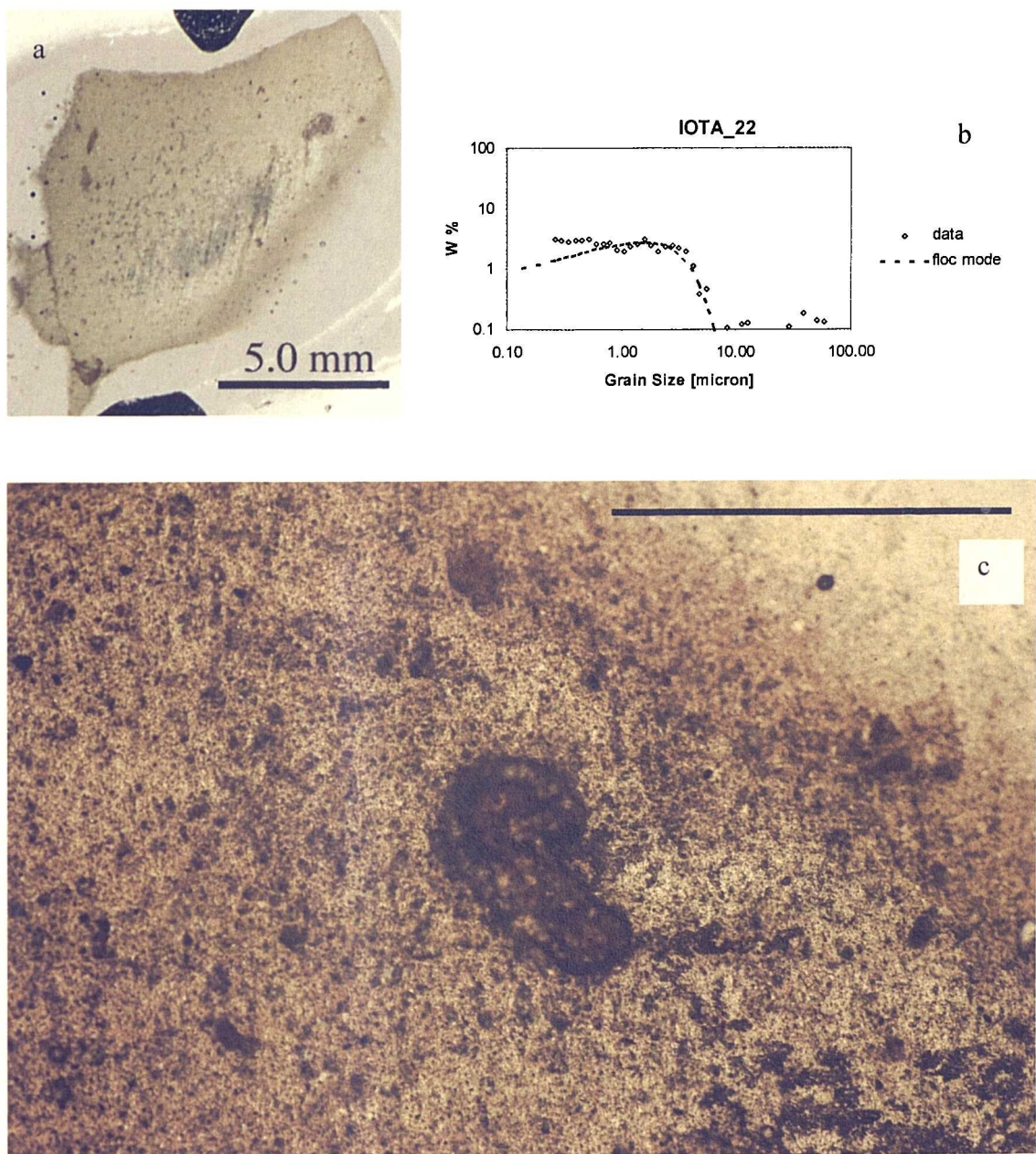


Figure 2.16. Example of a Type 1 sample (IOTA_22) recovered from a deep water Iota Area well illustrating: (a) an image of the thin section itself, (b) the corresponding grain size distribution, and (c) a transmitted-light photomicrograph (plane light, x4). The thin section illustrates homogeneous, ungraded sediment consistent with deposition from suspension fall-out of flocculated material primarily $<10\mu\text{m}$. A foraminifera test is clearly visible in the centre of the picture. The scale bar (top right) is $1000\mu\text{m}$.

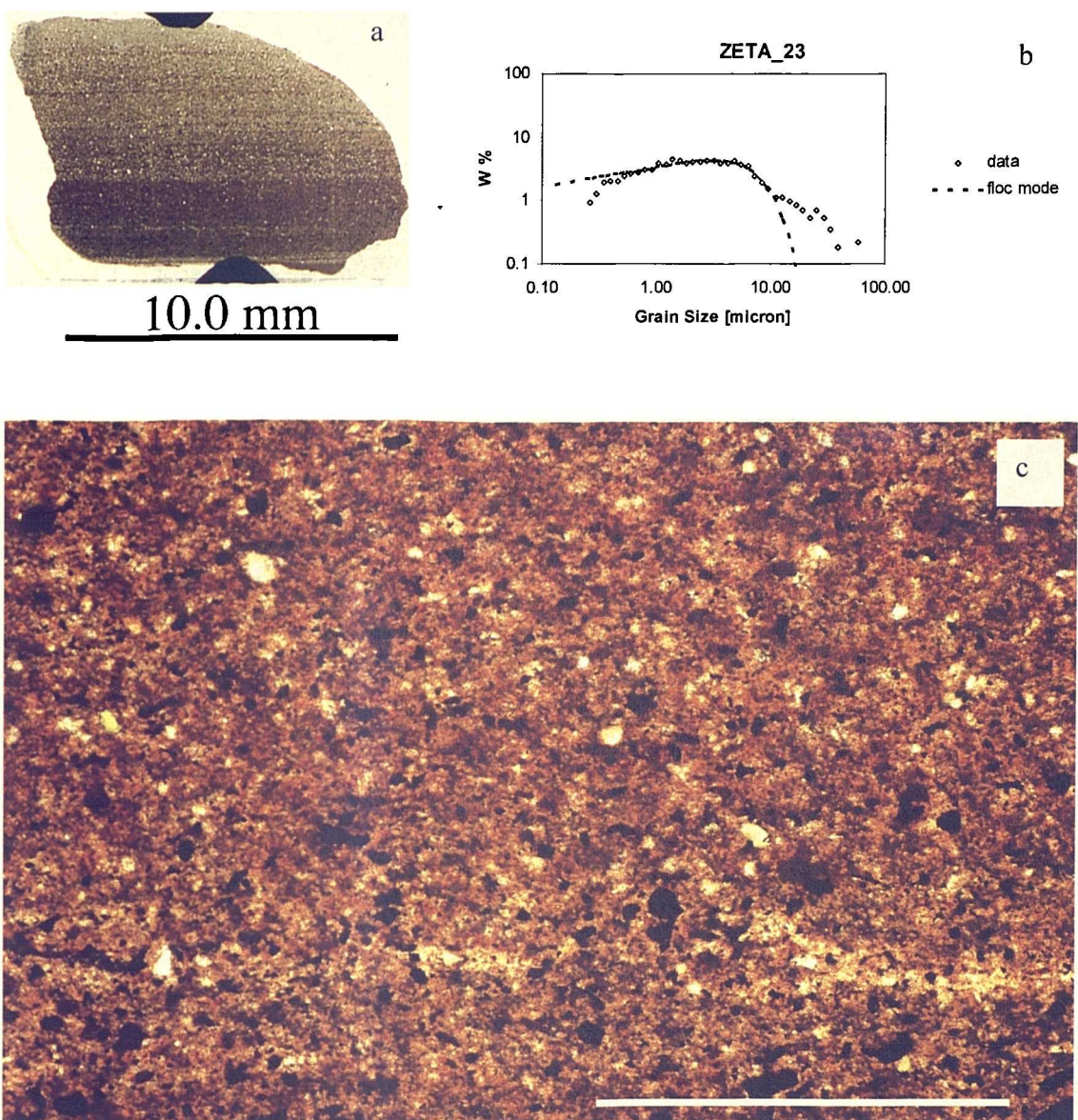


Figure 2.17. Example of a Type 1 sample (ZETA_23) recovered from a Zeta Area well illustrating: (a) an image of the thin section itself, (b) the corresponding grain size distribution, and (c) a transmitted-light photomicrograph (plane light, x4). The thin section illustrates homogeneous, ungraded sediment consistent with deposition from suspension fall-out of flocculated material primarily $<10\mu\text{m}$. The scale bar (bottom right) is $1000\mu\text{m}$.

2.4.2 Type 2 – high concentration flocculated spectra

Further analysis of the sediments dominated by a floc deposited component led to the recognition of the Type 2 grain size spectra termed ‘high concentration’ flocculated spectra. This grain size distribution (GSD) type is similar to that of Type 1; however, it also incorporates a significant silt component as floc deposited material. Examples are given in Figure 2.18. A low K parameter derived from the Kranck model fit is characteristic of these sample types (averaging 27) (Table 2.4). Examples of these grain size distribution types are drawn from all the locations included in this study (deep water Iota Area, Jurassic North Sea, deep water Eta, Chi and Zeta Areas) and represent 19% of the total grain size distribution dataset used in this study. Sedimentary statistics are given in Table 2.3 and the parameters derived from fitting the Kranck model are given in Table 2.4.

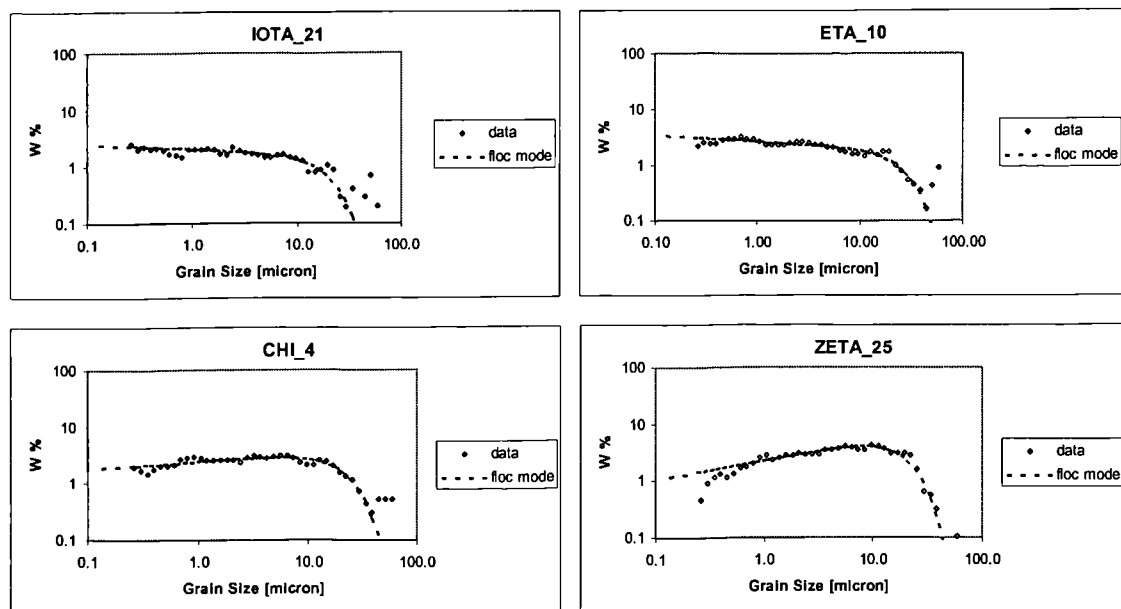


Figure 2.18. Disaggregated grain size spectra of Type 2 GSD examples on log-log weight percent – grain size (μm) plots; (a) Iota example – 59% clay, $2\mu\text{m}$ mean grain size (mgs), modeled ‘floc’ parameters: ΔQ 3.82, $(m+n)$ -0.0464, K 20.84. (b) Deep water Eta example – 48% clay, $2.2\mu\text{m}$ mgs, modeled ‘floc’ parameters: ΔQ 1.57, $(m+n)$ -0.0577, K 11.495. (c) Chi example – 37% clay, $2.8\mu\text{m}$ mgs, modeled ‘floc’ parameters: ΔQ 4.23, $(m+n)$ 0.06, K 17.57. (d) Zeta example – 25% clay, $3.9\mu\text{m}$ mgs, modeled ‘floc’ parameters: ΔQ 11.05, $(m+n)$ 0.1694, K 23.3.

The observation that the spectra characteristic of Type 2 GSDs incorporate material $>10\mu\text{m}$ deposited as flocs is somewhat contradictory to the evidence given for the boundary between non-cohesive and cohesive behaviour at $\sim 10\mu\text{m}$ for fine-grained sediment particles in section 2.1.1. It is proposed here that these sediments have been deposited from a flow or water column with a high suspended sediment concentration. Implicit in the fitting of the Kranck grain size model is the use of a settling velocity (W_s) as calculated for settling under 'clear water' Newtonian conditions; however, as sediment concentration increases grain / floc settling becomes hindered. A simplified model for calculating the hindered settling velocity (W_h) is:

$$W_h = W_s (1 - Cf)^n \quad (2.5)$$

where Cf is the volume concentration and n is an exponent, here taken as 2.32 (Richardson and Zaki, 1958; Talling, 2001). Holding the model parameters in Equation 2.5 constant but altering the settling rate shows that as sediment concentration increases, the grain size incorporated into the floc settled component also increases (Figure 2.19).

When fitting the model the effect of sediment concentration is accounted for by the K parameter (Section 2.1.2.3; Kranck and Milligan, 1985); thus the low K values recorded for Type 2 GSD spectra are thought to reflect their deposition from high concentrations. A relationship between K and sediment concentration was presented by Kranck and Milligan (1985) for samples taken from the Orinoco River (Section 2.1.2.3). Further evidence for deposition from high sediment concentrations comes from petrographic analysis of samples in this classification. In Figure 2.20 a thin section taken from a Zeta Area sample shows an example of a Type 2 grain size distribution in which mudstone clasts are clearly visible; the presence of such clasts in a matrix of primary deposited material indicates that the flow must have been of high concentration in order to generate the competence required to transport and deposit mudstone clasts.

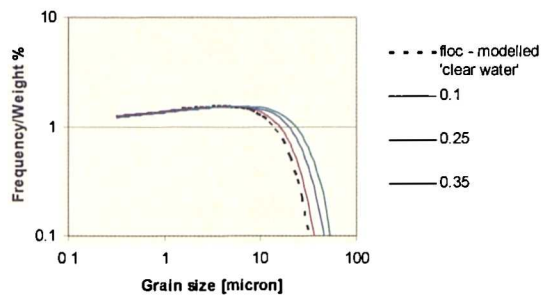


Figure 2.19. Result of applying the Kranck grain size model holding the ΔQ , $(m+n)$, and K parameters constant but altering the settling velocity using Equation 1.5 for increasing sediment volume concentrations (C_f).



Figure 2.20. Thin section (plane light) taken from a Zeta Area sample with a Type 2 grain size distribution. Intraclasts of mudstone are clearly visible in a matrix of silt and clay providing evidence for deposition from a high concentration (non-Newtonian) flow. The field of view is ~ 2.7 mm.

Code	Whole distribution stats							SS mean (µm)
	% Clay	% Sand	% Silt	%>10µm	Mean Grain Size (µm)	SD	Skewness	
IOTA_9	64	0.3	36	14	2.0	1.8	-0.3	16.9
IOTA_14	61	0.0	39	14	1.9	1.8	-0.4	18.1
IOTA_17	61	0.1	39	17	2.2	1.9	-0.4	19.1
IOTA_21	59	0.2	41	19	2.0	2.0	-0.5	19.2
IOTA_28	60	0.1	40	19	1.7	1.9	-0.5	15.8
IOTA_46	48	0.0	52	21	2.1	1.8	-0.3	17.2
IOTA_48	59	1.3	40	18	1.6	1.8	-0.7	17.5
IOTA_59	39	1.9	60	30	2.6	1.9	-0.6	22.8
ETA_4	60	0.4	40	19	1.7	1.9	-0.7	19.4
ETA_8	55	0.1	45	17	1.6	1.8	-0.6	17.3
ETA_10	48	1.0	51	25	2.2	2.0	-0.5	19.7
ETA_12	63	0.1	37	14	1.4	1.8	-0.8	17.5
ETA_1	64	0.3	35	18	2.0	2.1	-0.6	21.0
ETA_11	49	3.0	48	23	1.9	1.9	-0.5	17.3
ETA_14	57	0.3	43	20	2.1	2.1	-0.3	17.8
ETA_16	57	5.4	38	22	1.5	1.8	-0.8	19.2
ETA_17	54	3.2	42	18	1.6	1.7	-0.4	14.2
ETA_18	56	2.5	42	29	2.5	2.1	-0.6	22.2
ETA_19	57	2.4	41	26	2.3	2.1	-0.5	20.5
ETA_20	59	4.2	37	23	1.8	1.9	-0.6	18.9
NOR_10	36	0.2	64	38	3.6	1.9	0.2	17.4
CHI_2	53	0.1	47	18	1.8	1.8	-0.5	17.3
CHI_3	45	0.6	55	30	2.7	2.1	-0.3	20.3
CHI_4	38	0.7	62	29	2.8	1.9	-0.1	18.6
CHI_11	47	0.4	53	23	2.3	2.0	-0.2	18.8
ZETA_1	47	2.3	50	25	2.4	1.9	-0.3	18.1
ZETA_3	48	0.9	51	24	2.4	2.0	-0.4	19.6
ZETA_25	25	0.3	75	38	3.9	1.8	0.3	16.5
ZETA_27	32	2.4	66	25	2.5	1.6	-0.1	15.4
ZETA_14	38	0.1	62	29	2.9	1.9	0.0	17.8

Table 2.3. Sedimentary parameters and moment statistics derived from samples with a Type 2 grain size distribution.

Code	Kranck Model Parameters				r^2
	ΔQ	$\log \Delta Q$	$n + m$	K	
IOTA_9	1.0	0.0	-0.1	30.0	0.93
IOTA_14	2.7	1.0	0.0	64.2	0.94
IOTA_17	1.9	0.6	0.0	32.2	0.84
IOTA_21	1.3	0.3	0.0	23.8	0.89
IOTA_28	5.1	1.6	0.1	52.4	0.81
IOTA_46	3.4	1.2	0.0	31.9	0.95
IOTA_48	0.7	-0.4	-0.1	16.7	0.87
IOTA_59	0.1	-0.3	-0.2	1.2	0.97
ETA_4	1.6	0.4	-0.1	47.5	0.95
ETA_8	1.4	0.3	-0.1	37.5	0.96
ETA_10	1.5	0.4	-0.1	12.8	0.97
ETA_12	1.1	0.1	-0.1	56.2	0.95
ETA_1	0.5	-0.6	-0.1	2.8	0.66
ETA_11	1.5	0.4	-0.1	16.4	0.96
ETA_14	1.8	0.6	0.0	13.9	0.73
ETA_16	1.1	0.1	-0.1	50.4	0.94
ETA_17	2.9	1.1	0.0	65.1	0.96
ETA_18	1.1	0.1	-0.1	3.5	0.94
ETA_19	1.2	0.2	-0.1	5.8	0.94
ETA_20	1.5	0.4	0.0	32.2	0.95
NOR_10	5.3	1.7	0.1	12.6	0.97
CHI_2	2.5	0.9	0.0	44.0	0.96
CHI_3	2.0	0.7	0.0	6.1	0.94
CHI_4	4.2	1.4	0.1	17.6	0.94
CHI_11	2.1	0.8	0.0	17.4	0.93
ZETA_1	1.4	0.4	-0.1	12.4	0.94
ZETA_3	1.2	0.2	-0.1	7.3	0.94
ZETA_25	11.1	2.4	0.2	23.3	0.93
ZETA_27	8.3	2.1	0.1	64.5	0.87
ZETA_14	5.8	1.8	0.1	22.3	0.97

Table 2.4. Kranck model parameters derived from the fitted floc-component of samples with a Type 2 grain size distribution.

It is interesting to note the similarity between the characteristic Type 2 grain size spectra and the composite grain size spectra derived for a complete turbidite sequence shown in Figure 2.21; this observation is consistent with the interpretation of flow ‘freezing’ and en-masse deposition of suspended material characteristic of high concentration mud-rich density flows for the formation of Type 2 grain size spectra. A representative BSEM image of a Type 2 sample is illustrated in Figure 2.22. At this scale the structure is similar to that seen in Type 1 mudstones; there is a lack of any obvious structure and the sample would be described as homogeneous and matrix-supported.

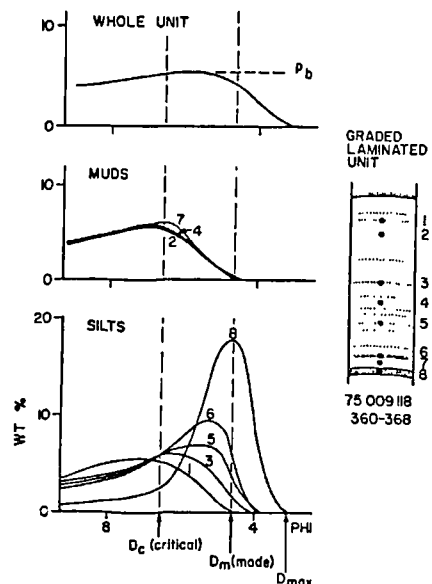


Figure 2.21. Typical smoothed weight % grain size frequency curves recorded by Stow and Bowen (1980) from mud-rich turbidites. Individual lamina (1-8) were analysed in this study, and silt, mud and a predicted whole unit grain size curve (top) are presented. This section is 8 cm in length. D_c (critical) refers to the smallest grain size settled by Stokesian settling and indicates a crude estimate of actual stress (τ) at the time of deposition within Stow and Bowen’s (1980) model.

Images of thin sections, their corresponding grain size distribution and magnified images are given in Figures 2.23 and 2.24. At the millimetre scale both samples lack any obvious structure and no lamination is apparent. The Chi Area sample (Fig. 2.23) is somewhat coarser than the Iota sample (Fig. 2.24) with clay contents of 60% and 52% respectively; the Chi sample also has a mean grain size $\sim 1\mu\text{m}$ larger than the Iota sample (Table 2.3). The coarser nature is not readily apparent from visual inspection of the grain size distributions, although the Chi sample does have a lower K value derived from fitting the Kranck model (Table 2.4), perhaps signifying a higher transport energy (Figure 2.4).

However, the coarser nature of the Chi sample is apparent from inspection of the magnified thin section images (Figs. 2.23c and 2.24c).

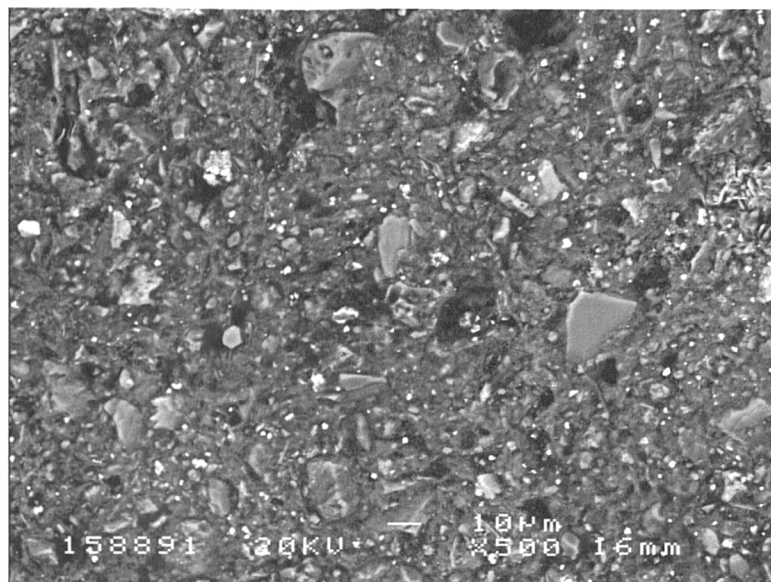


Figure 2.22. Back scattered electron-optical micrograph (BSEM) representative of a sample with a Type 2 grain size distribution (IOTA_46). The field of view is $\sim 120\mu\text{m}$. Silt grains, typically 5 – $30\mu\text{m}$ in size 'float' in a matrix of finer silt and clay indicating co-deposition of material at this scale.

There is a high degree of similarity between the structure of the two samples shown in Figures 2.23 and 2.24. There is a lack of structure at this scale and both samples would be described as matrix-supported (i.e. larger silt grains, when present, float within a matrix of finer silt and clay particles), giving a homogeneous appearance to the texture. Comparison of the BSEM image shown in Fig. 2.22 with Figures 2.23 and 2.24 indicates that the structure of these sediments is similar at both scales.

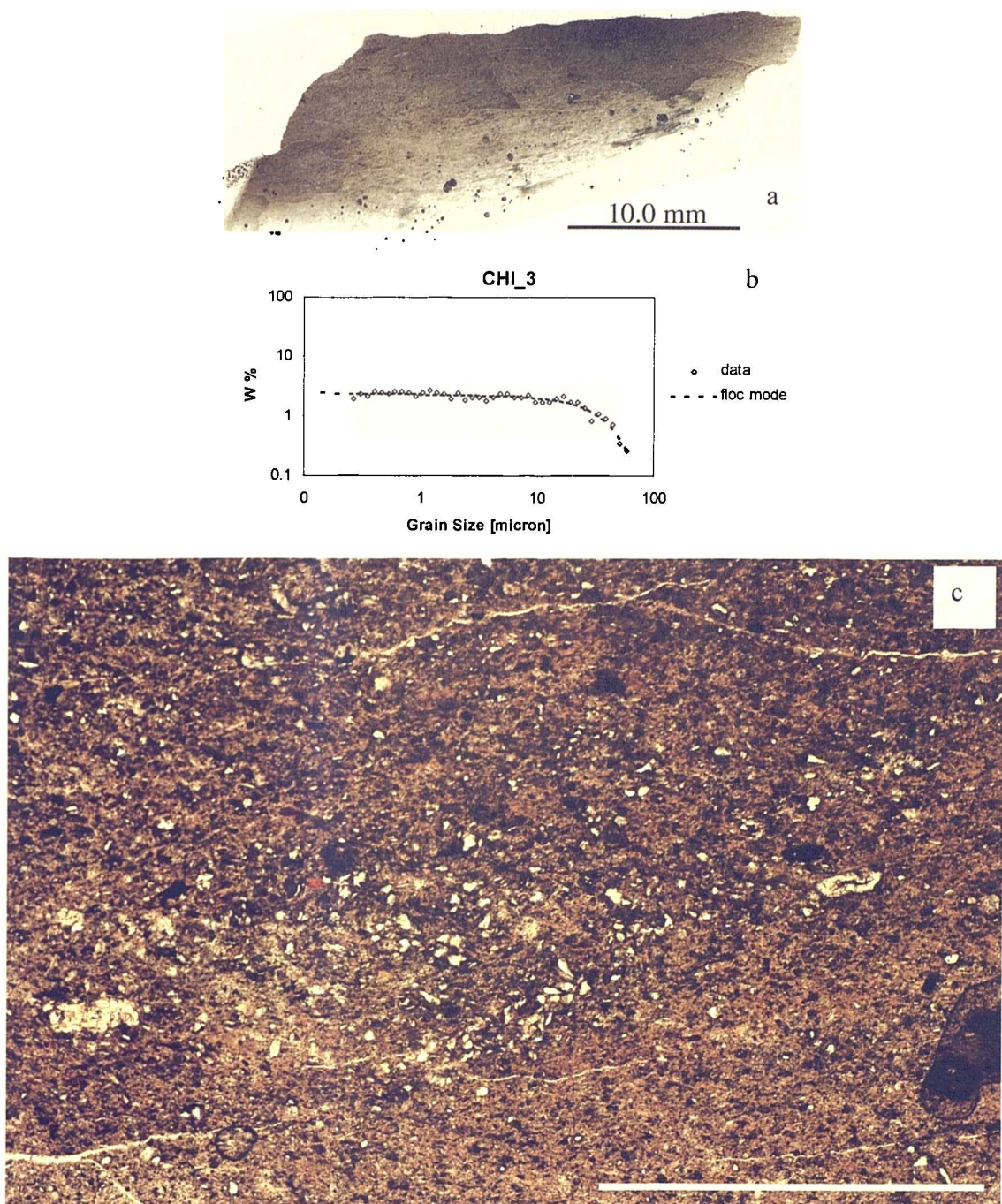


Figure 2.23. Example of a Type 2 sample (CHI_3) recovered from a Chi Area well illustrating: (a) an image of the thin section itself, (b) the corresponding grain size distribution, and (c) a transmitted-light photomicrograph (plane light, x4). The thin section illustrates a homogeneous, ungraded sediment with silt and some sand grains float in a clay and fine silt matrix. The scale bar (bottom right) is 1000 μ m.

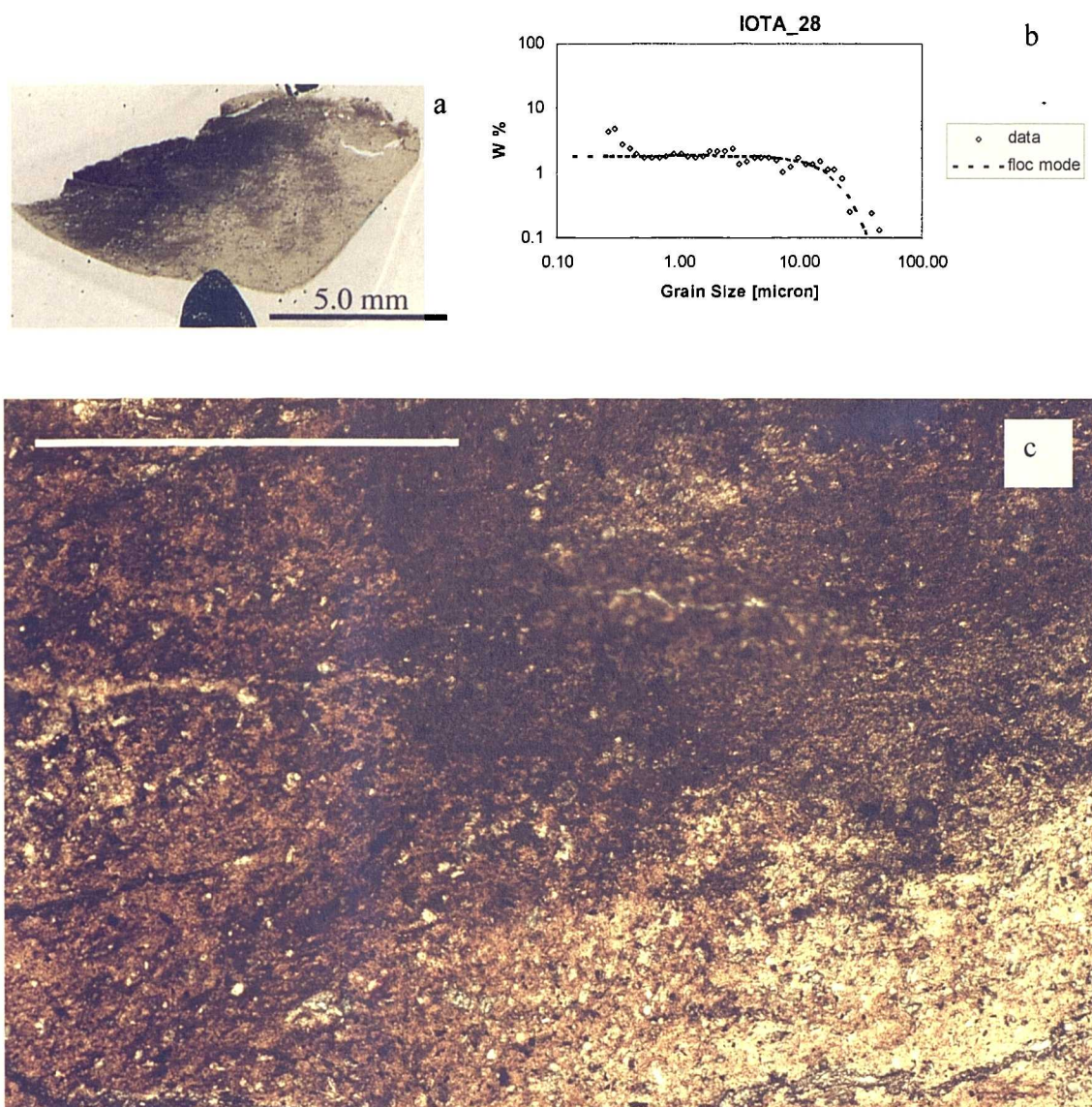


Figure 2.24. Example of a Type 2 sample (IOTA_28) recovered from an Iota Area well illustrating: (a) an image of the thin section itself, (b) the corresponding grain size distribution, and (c) a transmitted-light photomicrograph (plane light, x4). The thin section illustrates homogeneous, ungraded sediment with coarse silt particles floating in a clay and fine silt matrix. Note that the alteration in colour is thought to simply reflect variations in section thickness. The scale bar (top left) is 1000 μ m.

2.4.3 Type 3 – floc dominated, floc silt mixtures

The Type 3 grain size distribution represents the finest member of a 3-part classification of spectra comprising both a floc and ‘Stokes’ settled mode. These spectra are composed of a dominant floc-settled component and a minor silt component deposited as single grains either from a static water column or from a dilute flow. Characteristic of these distributions is either a silt modeled ($m+n$) value of <0.7 or of >1 (Figure 2.25). When the ($m+n$) value is <0.7 the minor silt component is relatively broad (Figure 2.25b); when this value is >1 the silt component is much tighter (Figure 2.25a), possibly reflecting either distinct depositional processes and / or distinct grain size populations. Type 3 sediments have an average floc-non-cohesive silt intersection (D_f) value of $10\mu\text{m}$, with this value ranging between 5 and $18\mu\text{m}$. The Type 3 group was split into two further sub-groups where $m+n <0.7$ or $m+n >0.7$. The $m+n <0.7$ group had an average D_f of $7.6\mu\text{m}$ and a range of $5 - 9\mu\text{m}$; whereas the $m+n >0.7$ group had an average D_f of $12\mu\text{m}$ and a range of $9 - 18\mu\text{m}$. This result suggests that when the $m+n$ parameter is large (i.e >0.7), coarser material is incorporated into flocs and vice versa, potentially providing insight to the hydrodynamics and processes responsible for the formation of these sedimentary deposits. Examples of this grain size distribution type are drawn from deep water Iota Area, deep water Eta, Chi and Zeta Areas and represent $\sim 8\%$ of the total grain size distribution dataset used in this study. Sedimentary statistics are given in Table 2.5 and the parameters derived from fitting the Kranck model are given in Table 2.6.

A series of images depicting samples with a Type 3 grain size distribution at a range of scales are given in Figures 2.26 – 2.28. In Figure 2.26 a BSEM image of a Type 3 sample is shown, illustrating the matrix-supported, homogeneous character of these sediment types.

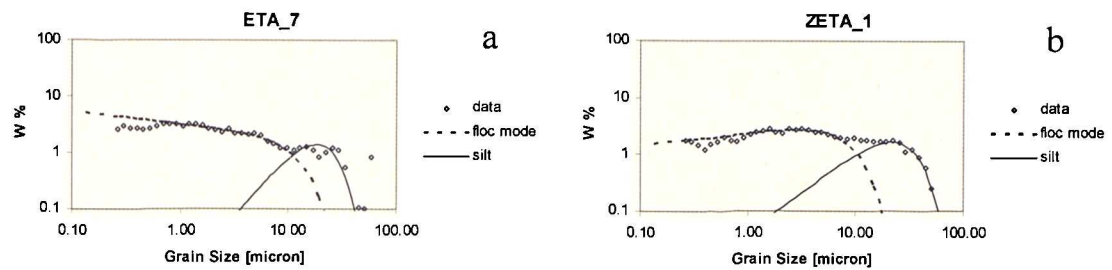


Figure 2.25. Disaggregated grain size spectra of Type 3 GSD Types on log-log weight percent – grain size (μm) plots; (a) deep water Eta example – 50% clay, $1.9\mu\text{m}$ mgs, Q 214.8, $(m+n)$ 1.1, K 33.5. (b) Zeta example – 44% clay, $3\mu\text{m}$ mgs, modeled 'silt' parameters: ΔQ 1.2, $(m+n)$ 0.72, K 14.6.

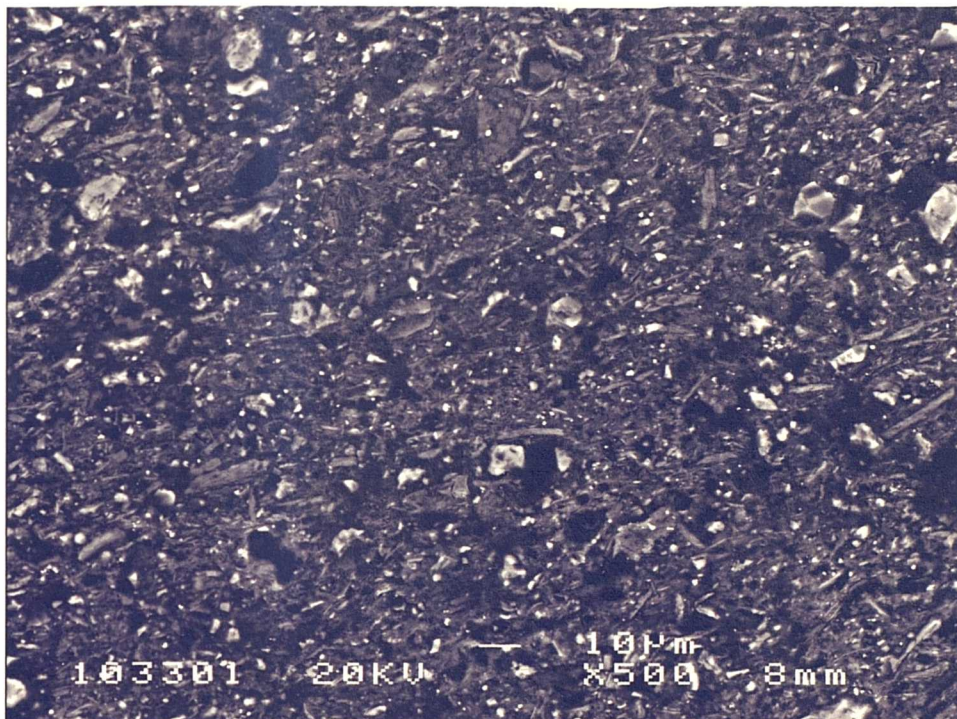


Figure 2.26. Back scattered electron-optical micrograph (BSEM) of a deep water Iota sample (IOTA_4) with a Type 3 grain size distribution (field of view $\sim 120\mu\text{m}$). In this example minor sortable silt particles 'float' in a matrix of finer silt and clay indicating co- deposition of material at this scale.

Code	Whole distribution stats							
	% Clay	% Sand	% Silt	% >10μm	Mean Grain Size (μm)	SD	Skewness	SS mean (μm)
IOTA_4	60	0.1	40	18	2.0	1.8	-0.6	19.3
IOTA_6	48	0.1	52	22	2.6	1.9	-0.2	18.8
IOTA_7	63	0.2	37	19	1.8	2.0	-0.7	19.7
IOTA_12	57	0.1	43	21	2.5	1.9	-0.4	19.1
IOTA_23	56	0.0	44	21	2.0	2.0	-0.5	19.7
IOTA_26	55	0.1	45	19	1.9	1.8	-0.6	19.3
IOTA_29	56	0.1	44	17	2.2	1.7	0.0	19.0
IOTA_35	54	0.0	46	21	2.5	1.9	-0.2	17.9
IOTA_36	54	0.0	46	20	2.4	1.9	-0.3	18.2
IOTA_58	52	0.8	47	17	1.8	1.7	-0.6	17.1
IOTA_62	50	2.2	48	25	2.2	1.8	-0.5	18.9
IOTA_67	45	1.6	53	14	1.7	1.6	-0.5	21.4
ETA_7	51	0.2	49	22	1.9	1.9	-0.7	20.6
ZETA_1	44	0.3	56	29	3.1	2.0	-0.2	20.1
ZETA_4	56	0.4	44	17	1.8	1.7	-0.7	21.0
CHI_14	56	0.2	44	14	1.9	1.7	-0.4	20.5

Table 2.5. Sedimentary parameters and moment statistics derived from samples with a Type 3 grain size distribution.

Figures 2.26 – 2.28 show images and grain size data for Type 3 samples from the deep water Iota Area and Chi Area. The two examples in Figs 2.27 and 2.28 are typical of Type 3 samples with Iota_4 having a clay content of 60% and Chi_14 having a clay content of 56%. The samples are similar in terms of the textures they exhibit at a range of scales. Each of the samples is homogeneous and unstructured and would be described as having a matrix-supported texture (i.e. the larger silt grains, when present, float within a matrix of finer silt and clay particles). The homogeneous character and lack of any sign of lamination both at the μm (Figure 2.25) and mm scale (Figs 2.27 - 28) indicates that the floc-silt components found in Type 3 grain size distributions are deposited simultaneously, and do not form discrete layers.

Code	Floc mode					Silt mode					$Df(\mu\text{m})$
	ΔQ	$\log \Delta Q$	$n + m$	K	r^2	ΔQ	$\log \Delta Q$	$n + m$	K	r^2	
IOTA_4	8.5	2.1	0.1	346.0	0.94	4.3	1.5	0.3	16.6	0.65	7.9
IOTA_6	5.7	1.7	0.1	54.4	0.86	75414.9	11.2	3.0	47.4	0.82	18.2
IOTA_7	0.9	-0.1	-0.1	46.5	0.88	589.0	6.4	1.3	61.9	0.96	9.4
IOTA_12	2.6	0.9	0.0	104.1	0.64	5.4	1.7	0.3	23.9	0.86	7.5
IOTA_23	3.1	1.1	0.1	46.1	0.67	1064542927	20.8	4.4	167.0	1.00	12.6
IOTA_26	1.2	0.2	-0.1	122.9	0.89	1.9	0.6	0.1	11.5	0.95	7.6
IOTA_29	6.3	1.8	0.1	149.5	0.74	9627.3	9.2	2.1	70.8	0.97	11.9
IOTA_35	7.0	1.9	0.1	273.0	0.84	8.7	2.2	0.3	31.1	0.95	5.1
IOTA_36	7.9	2.1	0.2	211.4	0.68	45561.7	10.7	2.3	75.6	0.99	11.8
IOTA_58	1.1	0.0	-0.1	73.1		57.3	4.0	0.6	86.1		6.8
IOTA_62	3.7	1.3	0.0	97.1	0.88	1808.0	7.5	1.6	46.0	0.95	11.8
IOTA_67	11.4	2.4	0.1	276.5	0.96	4.6	1.5	0.5	13.3	0.84	9.9
ETA_7	1.2	0.2	-0.1	60.1		214.8	5.4	1.2	33.5		11.0
ZETA_1	6.0	1.8	0.1	115.6	0.74	30.0	3.4	0.7	14.6	0.99	10.4
ZETA_4	4.4	1.5	0.0	233.8	0.96	11.8	2.5	0.6	28.4	0.81	8.4
CHI_14	8.4	2.1	0.1	152.9	0.95	46.3	3.8	1.2	21.7	0.85	13.8

Table 2.6. Kranck model parameters derived from the fitted floc component and non-cohesive silt components of Type 3 sample grain size distributions.

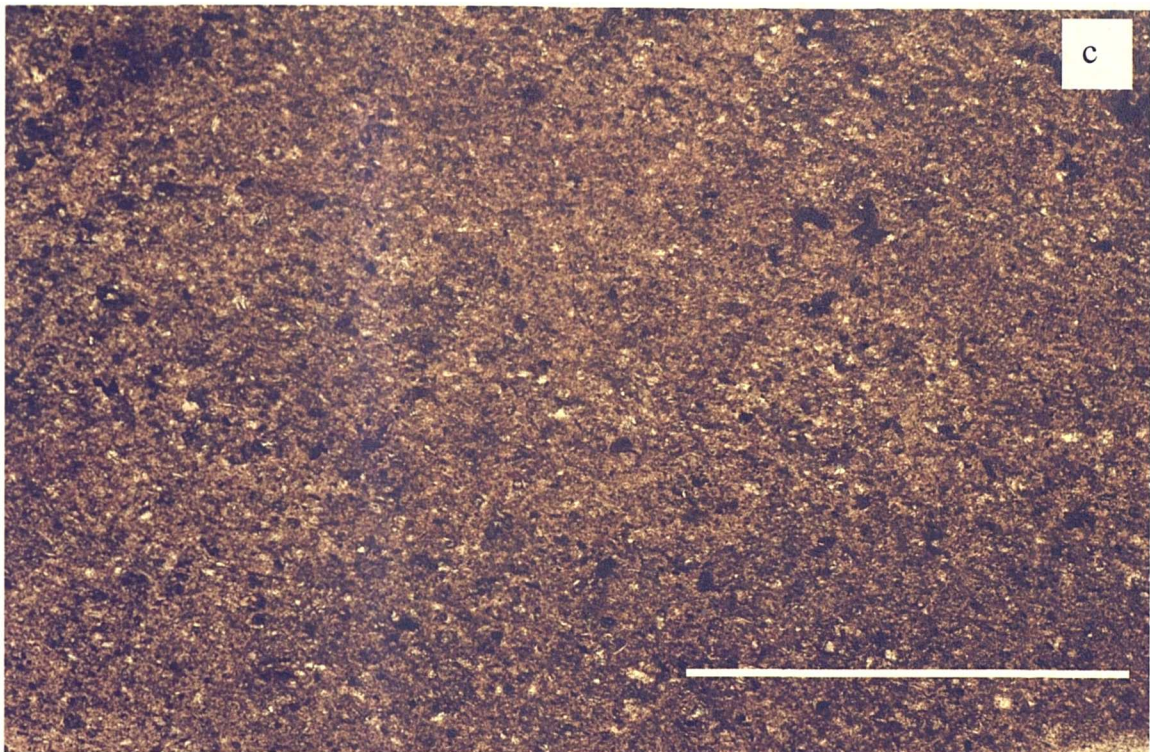
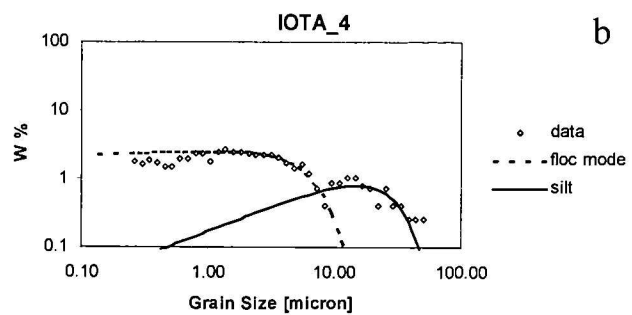
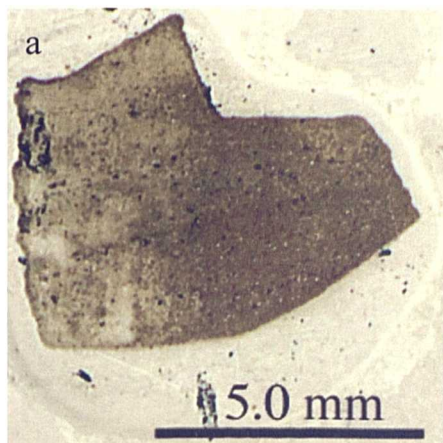


Figure 2.27. Example of a Type 3 sample (IOTA_4) recovered from a deep water Iota Area well illustrating: (a) an image of the thin section itself, (b) the corresponding grain size distribution, and (c) a transmitted-light photomicrograph (plane light, x4). The thin section illustrates homogeneous, ungraded clay and fine silt matrix. The scale bar (bottom right) is 1000 μ m.

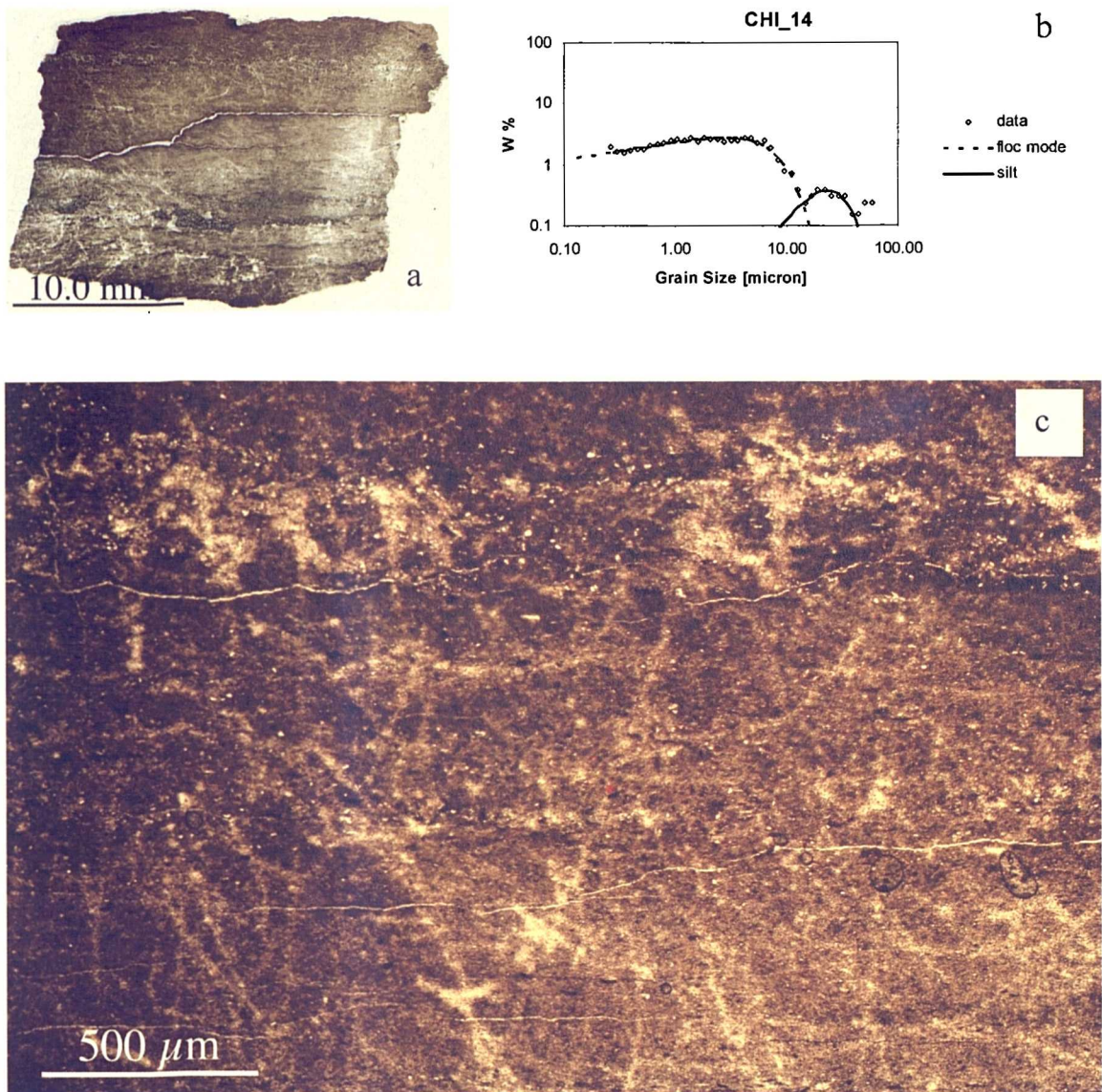


Figure 2.28. Example of a Type 3 sample (CHI_14) recovered from a Chi Area well illustrating: (a) an image of the thin section itself, (b) the corresponding grain size distribution, and (c) a transmitted-light photomicrograph (plane light, x2). The thin section illustrates homogeneous, ungraded clay and fine silt matrix. The scale bar (bottom right) is 500 μ m.

2.4.4 Type 4 – floc silt mixtures

The Type 4 grain size distribution represents sediments composed of approximately equal proportions of floc settled and Stokes settled silt material (Figure 2.29). Examples of Type 4 grain size spectra are drawn from deep water Iota Area, Jurassic North Sea, deep water Eta, and Zeta Areas and represent 23% of the total grain size distribution dataset used in this study. Sedimentary statistics are given in Table 2.7 and the parameters derived from fitting the Kranck model are given in Table 2.8. The silt – Stokesian settled component typically has $m+n$ values >0.5 and are generally consistent with the framework established by Kranck. Type 4 sediments have an average floc-non-cohesive silt intersection (D_f) value of $9.6\mu\text{m}$, ranging between 3 and $19\mu\text{m}$. Characteristic Type 4 grain size distributions are presented in Figure 2.29. These samples are thought to form from the co-deposition of flocculated and single grain material, largely from dilute flows.

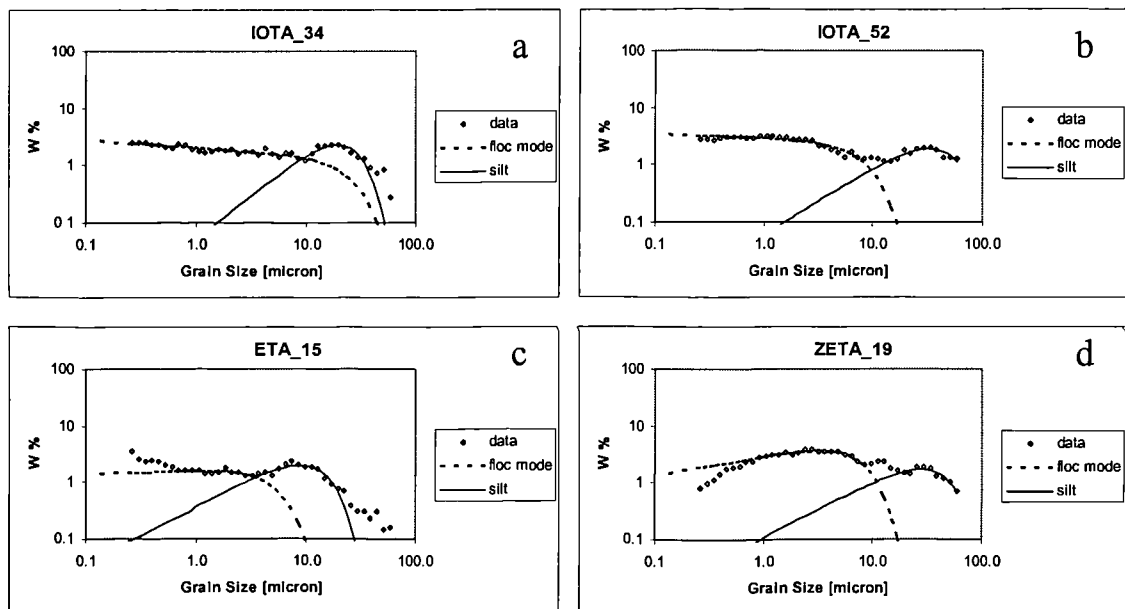


Figure 2.29. Disaggregated grain size spectra of Type 4 GSD Types on log-log weight percent – grain size (μm) plots; (a) Iota example – 48% clay, $2.9\mu\text{m}$ mean grain size (mgs), modeled ‘silt’ parameters: ΔQ 61.9, $(m+n)$ 0.78, K 20.3. (b) Iota example – 43% clay, $2.5\mu\text{m}$ mgs, modeled ‘silt’ parameters: ΔQ 12.2, $(m+n)$ 0.57, K 5.3. (c) deep water Eta example – 54% clay, $2\mu\text{m}$ mgs, modeled ‘silt’ parameters: ΔQ 33.8, $(m+n)$ 0.49, K 59.7. (d) Zeta example – 30% clay, $3.4\mu\text{m}$ mgs, Q 9.1, $(m+n)$ 0.48, K 6.8 (Figure 2.6 for BSEI of this example).

Back scattered electron microscope images of examples with Type 4 grain size distributions are shown in Figures 2.30 and 31; both samples are from a deep water, Iota Area well. Although the fields of view are different ($\sim 120\mu\text{m}$ and $\sim 500\mu\text{m}$) the images have a very similar appearance. In both cases sortable silt grains ($>10\mu\text{m}$) are floating in a matrix of fine silt and clay. The slightly coarser nature of Type 4 samples can be seen by comparing the BSEM images of a Type 3 example (Fig. 2.26) with a Type 4 example (Fig. 2.30). Each individual sortable silt grain is typically isolated and is rarely in contact with more than one other sortable silt grain, this sediment would therefore be described as matrix-supported.

Figures 2.32 and 2.33 combine images of thin sections (cm scale) with the corresponding grain size distribution and magnified (x4) images for Type 4 samples. Figure 32 shows data for a deep water Iota Area sample. The thin section image illustrates that the sample is an unstructured, homogeneous brown mudstone at the mm scale. The magnified image shows a featureless sediment with a fine-grained, homogenous texture. Figure 2.33 shows data for a North Sea sample; the thin section image illustrates the bioturbated nature of this sample, with numerous flattened burrows. This sample is coarser than the Iota Area example, with respective clay contents of 36% and 51% and mean grain sizes (μm) are 3.5 and 2.6. However, despite the coarser nature of the North Sea sample, the texture would still be described as matrix-supported. Inspection of Fig. 2.33c indicates that the majority of sortable silt and sand grains are isolated by the fine silt and clay matrix. As for Type 3 distributions, the homogeneous character and lack of any sign of lamination both at the μm (Figs. 2.30 and 2.31) and mm (Figs. 2.32 - 33) scales indicates that the floc-silt components found in Type 4 grain size distributions are deposited simultaneously and do not form discrete layers. The average D_f value for Type 4 samples equals $9.6\mu\text{m}$ in agreement with the approximate $10\mu\text{m}$ boundary suggested by McCave *et al.*, (1995) (Section 2.1.1); the only exception is two Eta Area examples (Table 2.8) in which the floc-silt limit lies at $\sim 3\text{-}4\mu\text{m}$, suggesting that the hydrodynamic and chemical conditions resulted in material $>5\mu\text{m}$ largely behaving as single grains.

Code	% Clay	% Sand	% Silt	% >10um	Whole distribution stats			SS mean (µm)
					Mean Grain Size (µm)	SD	Skewness	
IOTA_1	51	0.1	49	21	2.6	1.8	-0.3	19.2
IOTA_5	48	0.1	52	23	2.4	1.9	-0.3	18.7
IOTA_8	51	0.2	49	21	2.3	1.9	-0.5	20.4
IOTA_10	52	0.1	48	18	2.3	1.8	-0.2	16.6
IOTA_16	56	0.2	44	10	2.6	1.9	-0.1	18.0
IOTA_18	56	0.1	44	18	2.2	1.8	-0.3	16.9
IOTA_19	60	0.0	40	19	2.7	1.9	-0.2	18.5
IOTA_20	47	2.8	50	34	2.6	2.3	-0.6	24.9
IOTA_24	47	4.3	49	38	3.6	2.3	-0.2	25.7
IOTA_25	52	0.2	48	13	2.1	2.0	-0.5	19.6
IOTA_27	50	2.7	47	30	2.9	2.2	-0.5	26.5
IOTA_31	46	2.1	52	33	3.2	2.2	0.0	20.1
IOTA_32	50	0.1	50	31	3.1	2.2	-0.1	21.8
IOTA_34	48	0.1	52	33	2.9	2.2	-0.3	21.5
IOTA_39	51	0.3	49	27	2.2	2.2	-0.5	20.3
IOTA_41	53	0.9	46	28	3.1	2.2	-0.3	22.6
IOTA_42	50	2.1	48	30	2.8	2.2	-0.4	23.6
IOTA_47	51	0.1	49	24	2.1	2.0	-0.5	18.6
IOTA_49	47	0.8	52	26	1.8	2.1	-0.8	21.7
IOTA_50	50	0.0	50	28	2.5	2.1	-0.6	23.7
IOTA_51	42	0.8	57	34	2.7	2.2	-0.6	25.9
IOTA_52	44	3.3	52	34	2.5	2.2	-0.7	26.4
IOTA_53	55	0.2	45	34	3.1	2.2	-0.4	26.4
IOTA_54	58	1.9	40	30	2.6	1.9	-0.5	20.7
IOTA_61	50	0.5	49	31	3.0	1.9	-0.3	20.9
IOTA_64	45	1.6	53	29	2.6	2.0	-0.5	22.0
NOR_4	36	4.5	59	41	3.5	2.1	-0.1	22.4
NOR_1	41	0.7	59	34	3.0	1.9	-0.1	19.0
ETA_5	47	3.4	50	31	2.3	2.1	-0.7	22.9
ETA_9	60	0.5	39	24	1.7	2.0	-0.9	15.9
ETA_15	54	0.4	45	20	2.1	2.0	-0.3	16.8
ZETA_9	27	3.4	70	38	3.8	2.1	-0.1	23.5
ZETA_10	22	1.8	76	44	4.7	2.0	0.2	22.7
ZETA_11	23	0.0	77	43	4.5	2.0	0.0	23.7
ZETA_20	33	2.5	64	33	3.4	1.9	0.0	18.7
ZETA_19	30	2.7	67	34	3.4	1.9	-0.3	22.2

Table 2.7. Sedimentary parameters and moment statistics derived from samples with a Type 4 grain size distribution.

Code	Floc mode					Silt mode					$Df(\mu\text{m})$
	ΔQ	$\log \Delta Q$	$n + m$	K	r^2	ΔQ	$\log \Delta Q$	$n + m$	K	r^2	
IOTA_1	2.8	1.0	0.02	76.3	0.87	13.9	2.6	0.52	19.9	0.96	11.5
IOTA_5	7.1	2.0	0.12	133.8	0.90	7.4	2.0	0.31	20.5	0.89	8.6
IOTA_8	10.2	2.3	0.15	226.4	0.93	118.5	4.8	1.28	19.9	0.98	10.7
IOTA_10	5.7	1.7	0.11	126.6	0.79	344.7	5.8	0.99	84.0	0.95	8.1
IOTA_16	9.2	2.2	0.19	211.0	0.82	262.6	5.6	0.93	89.5	0.90	6.7
IOTA_18	7.6	2.0	0.14	187.4	0.78	62.3	4.1	0.70	58.9	0.98	7.6
IOTA_19	5.5	1.7	0.15	98.3	0.62	219.9	5.4	0.98	66.8	0.95	8.8
IOTA_20	4.1	1.4	0.08	162.7	0.64	175.2	5.2	1.26	15.7	0.97	10.1
IOTA_24	2.9	1.1	0.06	103.2	0.62	13.1	2.6	0.51	7.4	0.74	8.6
IOTA_25	1.5	0.4	-0.07	55.2	0.75	81.7	4.4	0.88	28.1	0.93	9.9
IOTA_27	4.3	1.5	0.09	183.6	0.52	113.2	4.7	1.34	12.5	0.99	11.1
IOTA_31	8.2	2.1	0.19	275.4	0.59	10.2	2.3	0.35	11.9	0.98	5.2
IOTA_32	2.1	0.8	0.03	70.9	0.39	89.8	4.5	0.89	22.1	0.92	8.8
IOTA_34	1.1	0.1	-0.07	12.3	0.78	61.9	4.1	0.78	20.3	0.79	9.2
IOTA_39	7.0	1.9	0.16	147.6	0.81	213.1	5.4	1.14	25.9	0.98	9.5
IOTA_41	2.1	0.7	0.02	89.4	0.63	17.1	2.8	0.57	12.8	0.88	8.5
IOTA_42	4.0	1.4	0.08	138.8	0.80	22.7	3.1	0.67	13.2	0.87	9.0
IOTA_47	4.3	1.5	0.08	96.9	0.77	19.1	2.9	0.51	23.8	0.95	8.7
IOTA_49	5.6	1.7	0.09	142.2	0.91	11.7	2.5	0.51	11.4	0.95	9.4
IOTA_50	1.1	0.1	-0.10	41.4	0.94	14.6	2.7	0.58	9.9	0.93	10.4
IOTA_51	6.3	1.8	0.08	242.4	0.91	133.8	4.9	1.15	14.4	0.93	9.1
IOTA_52	2.0	0.7	-0.04	109.2	0.87	12.2	2.5	0.58	5.3	0.74	9.7
IOTA_53	5.8	1.8	0.08	134.0	0.91	18.5	2.9	0.67	6.9	0.46	10.5
IOTA_54	2.7	1.0	-0.04	105.1	0.98	347.2	5.8	1.22	29.6	0.96	10.3
IOTA_61	6.3	1.8	0.08	101.7	0.81	19.2	3.0	0.58	13.2	0.93	10.8
IOTA_64	5.4	1.7	0.06	152.5	0.74	21.9	3.1	0.81	9.2	0.76	11.2
NOR_4	4.0	1.4	0.06	113.3	0.73	140.3	4.9	0.99	17.7	0.94	9.2
NOR_1	9.6	2.3	0.13	100.5	0.89	12.7	2.5	0.31	20.7	0.906	8.2
ETA_5	2.1	0.7	-0.04	107.1	0.93	82.5	4.4	1.44	10.0	0.85	14.1
ETA_9	1.6	0.5	-0.07	652.6	0.92	536.6	6.3	1.11	57.5	0.78	4.7
ETA_15	2.2	0.8	0.04	311.3	0.33	33.8	3.5	0.49	59.7	0.88	3.5
ZETA_9	6.2	1.8	0.10	27.4	0.77	6.8	1.9	0.45	3.0	0.73	20.0
ZETA_10	17.8	2.9	0.23	86.1	0.94	10.6	2.4	0.34	6.3	0.97	10.9
ZETA_11	14.1	2.6	0.19	92.9	0.89	16.0	2.8	0.46	7.7	0.90	10.9
ZETA_20	7.6	2.0	0.12	66.3	0.73	30.6	3.4	0.51	23.5	0.99	9.7
ZETA_19	12.4	2.5	0.16	142.6	0.94	9.1	2.2	0.48	6.1	0.91	11.0

Table 2.8. Kranck model parameters derived from the fitted floc-component and non-cohesive silt components of sample with Type 4 grain size distributions.

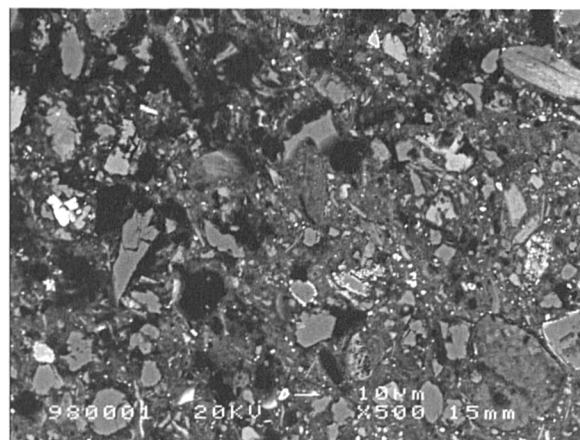


Figure 2.30. Back scattered electron-optical (BSEM) micrograph of a deep water loita (IOTA_1) sample with a Type 4 grain size distribution (field of view ~120 μm). In this example sortable silt (21%) sits in a matrix of finer silt and clay indicating co-deposition. The black areas visible in the image are thought to be sample damage (plucking) caused by the preparation process.

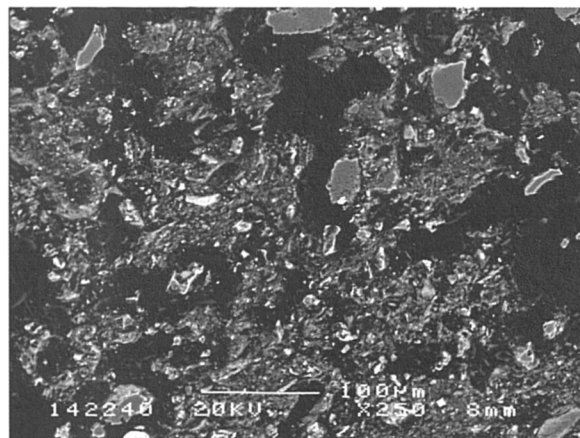


Figure 2.31. Back scattered electron-optical (BSEM) micrograph of a deep water loita (IOTA_31) sample with a Type 4 grain size distribution (field of view ~500 μm). In this example sortable silt (33%) and some minor sand (2%) sit in a matrix of finer silt and clay indicating co-deposition. The black areas visible in the image are thought to be sample damage (plucking) caused by the preparation process.

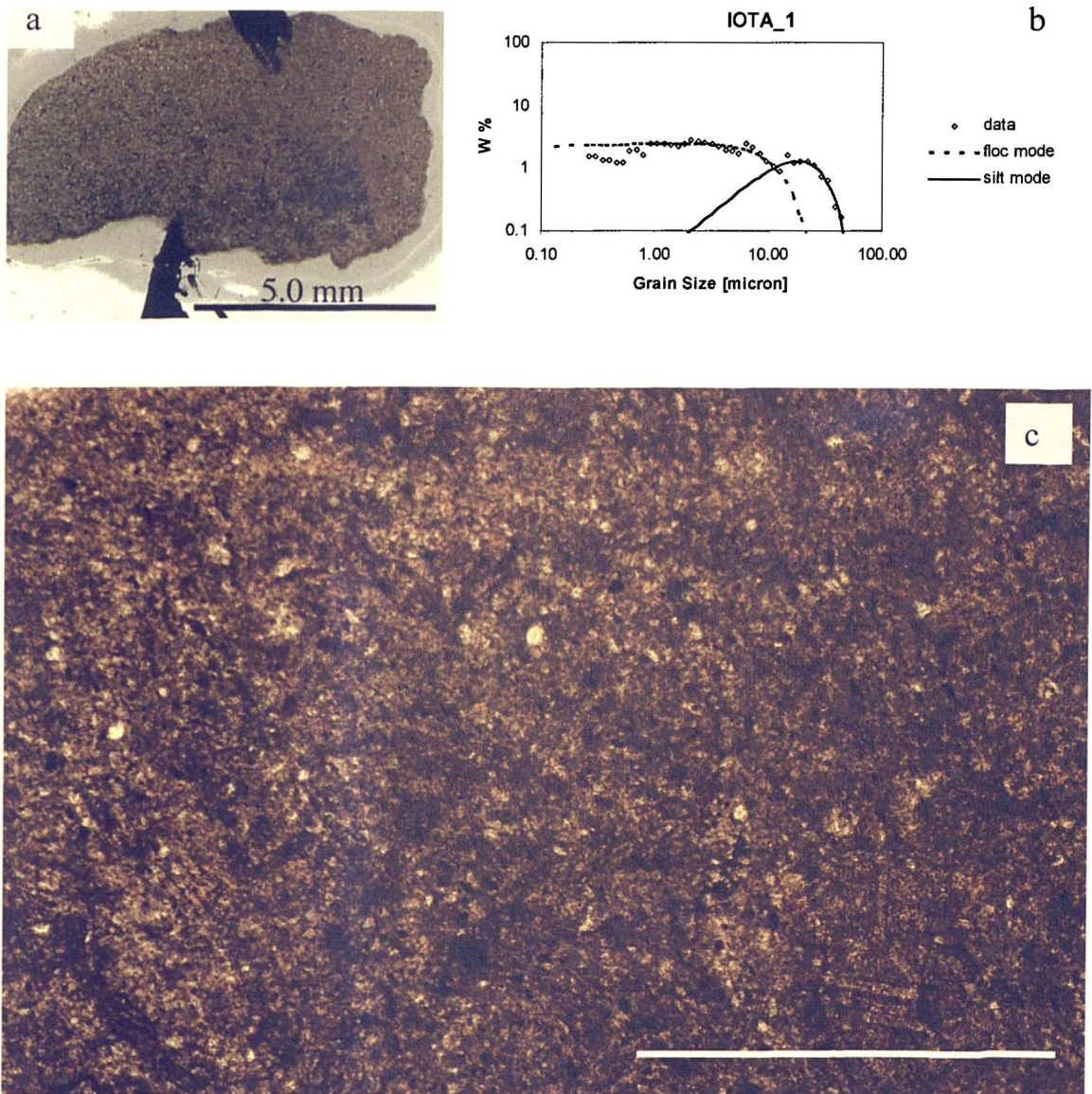


Figure 2.32. Example of a Type 4 sample (IOTA_1) recovered from a deep water IOTA well illustrating: (a) an image of the thin section itself, (b) the corresponding grain size distribution, and (c) a transmitted-light photomicrograph (plane light, x4). The thin section illustrates the homogeneous, ungraded texture of this sediment which comprises sortable silt (21%) and some microfossils which float in a clay and fine silt matrix. The scale bar (bottom right) is 1000 μ m.

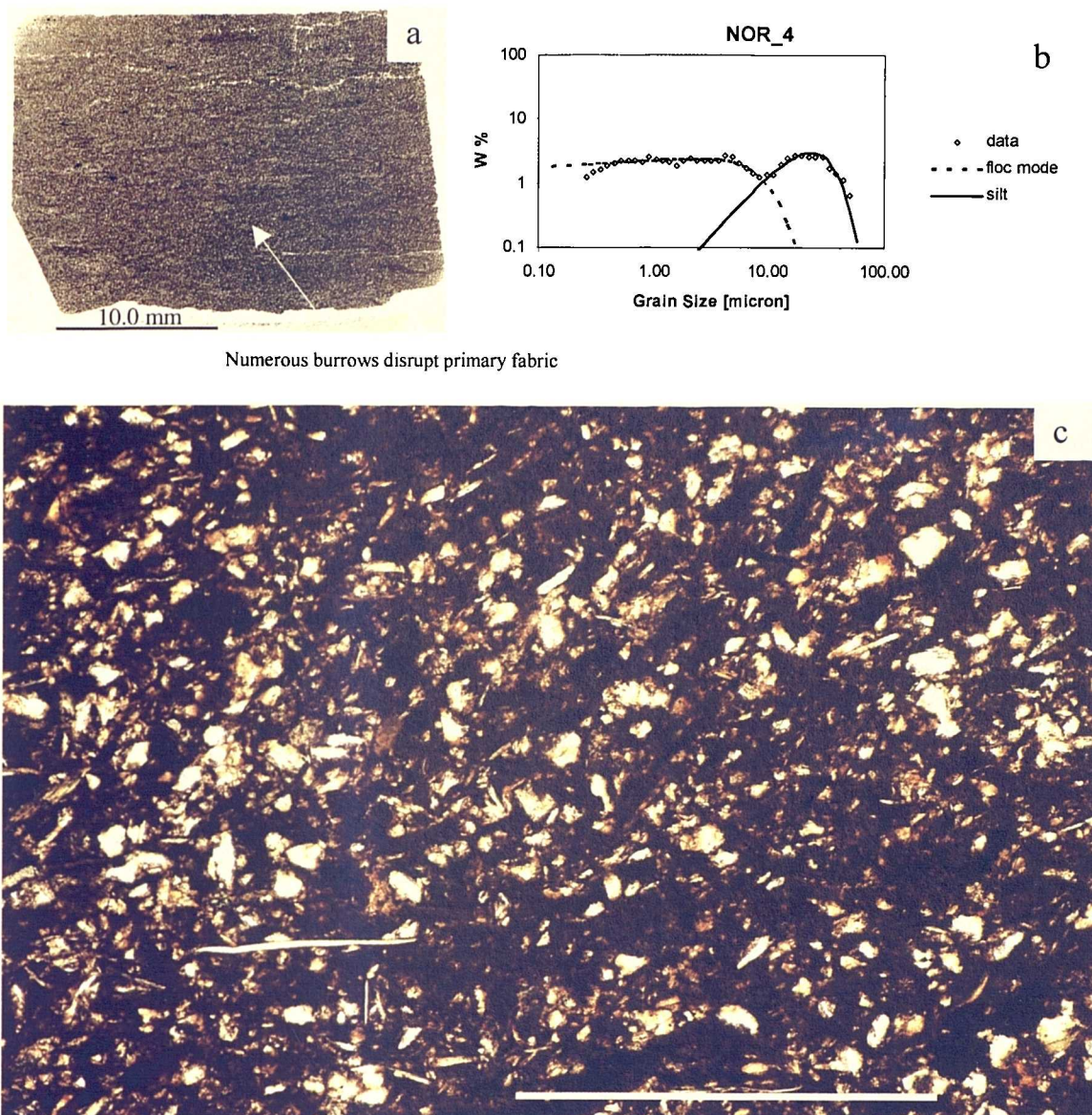


Figure 2.33. Example of a Type 4 sample recovered from a North Sea well illustrating: (a) an image of the thin section itself, (b) the corresponding grain size distribution, and (c) a transmitted-light photomicrograph (plane light, x4). The thin section illustrates the homogeneous, ungraded texture of the sediment with sortable silt (40%) and some minor sand (4.5%) floating in a clay and fine silt matrix. The presence of burrows prohibits the interpretation of the process responsible for deposition since the primary fabric is disrupted. The scale bar (bottom right) is 1000 μ m.

2.4.5 Type 5 – silt dominated, floc silt mixtures

The Type 5 grain size distribution is characterized by a coarse, silt-rich component and a minor floc component. Examples of Type 5 grain size distributions are predominantly drawn from the Jurassic North Sea and Zeta Sea locations; the Chi and the deep water, Iota Area are also represented. Type 5 grain size distributions represent 11% of the total dataset used in this study. This sediment type has an average floc-non-cohesive silt intersection (D_f) value of $7.9\mu\text{m}$, ranging between 2 and $13\mu\text{m}$. Sedimentary statistics are given in Table 2.9 and the parameters derived from fitting the Kranck model are given in Table 2.10. Grain size distributions of typical Type 5 examples are presented in Figure 2.34.

Combined thin section images, grain size distributions and magnified images (x4) for three Type 5 examples are given in Figures 2.35 – 37. In Figure 2.35a a $\sim 2\text{mm}$ feint bedding (*sensu* Macquaker and Adams, 2003) can be seen from the slight variations in colour. However the thin section image (Fig. 2.35c) illustrates a homogeneous unstructured texture. In this example the floc-limit (i.e. the intercept between the floc and single grain settled populations) is at $3\mu\text{m}$, suggesting that the hydrodynamic and chemical conditions resulted in material $>3\mu\text{m}$ largely behaving as single grains and thus non-cohesively possibly relating to the low salinity conditions of the proto-lacustrine system. In Figure 1.36a the thin section image illustrates the homogeneous character of the silt-rich component; clay-rich material is present as a central feature which apparently intrudes into the siltier material. This clay-rich feature may be a flame structure indicative of soft sediment deformation, probably relating to water escape (J. Macquaker, *pers. comm.* 2004). It is unknown whether or not the grain size distribution was derived from a sample volume that was composed of only the homogeneous silt-component or both this and the clay-rich material visible in the thin section image (Fig. 2.36c). The magnified image is of the silt-rich component and illustrates its homogeneous, unstructured texture. This sample contains 62% sortable silt (Table 2.9) which can be seen to form a framework, with the darker, clay-rich areas having a patchy distribution (Fig. 2.36). On the scale of this magnified image this sample would be described as framework supported. The thin section

image (Fig. 2.37a) from the third example has a mottled character, with the darker, finer grained lenses corresponding to infilled burrows. The magnified image (Fig. 2.37c) illustrates the patchy nature the coarse-silt rich and clay-rich components which comprise this sediment (Fig. 2.37b). In Figure 2.38 images from a single sample at three scales of observation are combined; the thin section image clearly shows the well-bedded character of this sample. The detail of individual lamina is revealed in the magnified image, each individual lamina having a sharp base and a graded top. The BSEM image was taken from a silt-rich portion of a single lamina. Lamination formed by the presence of thin beds was commonly recorded for Type 5 samples; an example is shown in Figure 2.39, the lamination corresponds to alteration of coarse silt – and clay – dominated deposition; a discontinuity surface also presents evidence of erosion by bottom currents. Figure 2.40 exhibits a whole range of textures recorded in Type 5 examples, including lamination, bioturbation and homogeneous textures.

To summarise, the observation's made on Type 5 samples of this dataset has revealed that these sediments are dominated by 'sortable silt' size material and exhibit four textures:

- 1) Homogenous, unstructured, coarse silt-rich sediment with minor clay size material (Figure's 2.35c, 2.36c).
- 2) Bedding, described as lamination, at various scales (Fig. 2.35a ~2mm; Fig. 2.38b ~0.5mm) indicative of alternating conditions of clay-suppressed and enhanced clay deposition.
- 3) Possible flame structures. Clay-rich intrusive material penetrating into a coarse silt dominated matrix (Fig 2.36a).
- 4) Bioturbation. Clay-filled burrows formed within a coarse silt dominated matrix (Fig. 1.37).

Each of these textures constrain the interpretation of the depositional processes responsible for the formation of these deposits; such as the co-deposition of coarse silt and clay sized material (1), alternating conditions and / or depositional events (2), and post depositional processes such as soft sediment deformation (3) and bioturbation (4).

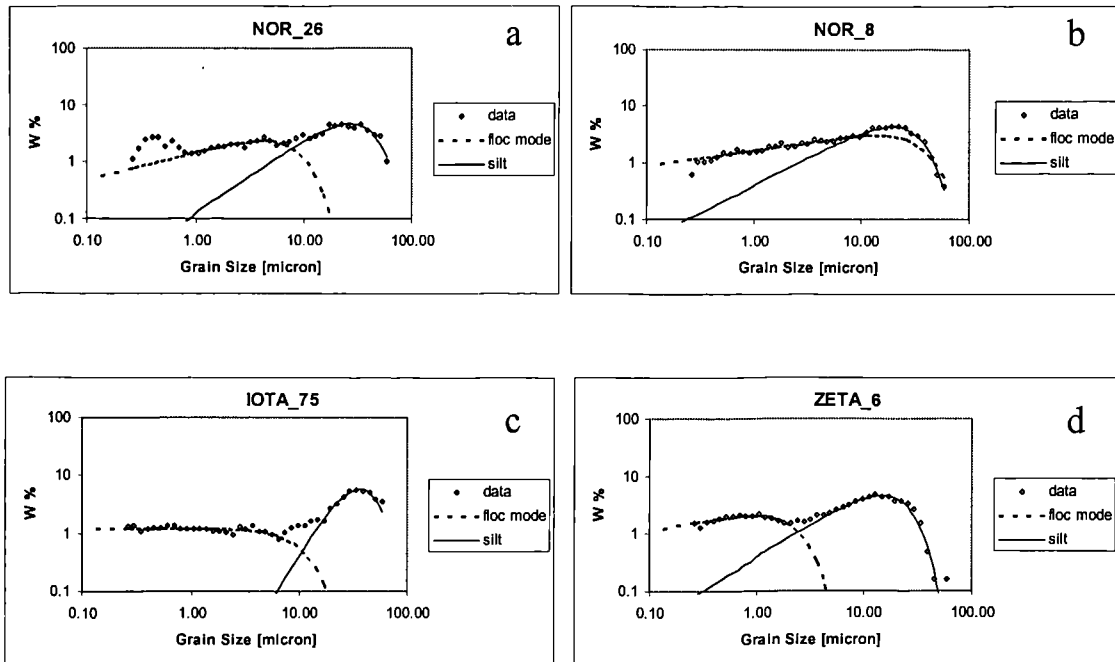


Figure 2.34. Disaggregated grain size spectra of Type 5 GSD Types on log-log weight percent – grain size (μm) plots; (a) Jurassic North Sea example – 13% clay, 5.7 μm mean grain size (mgs), modeled ‘silt’ parameters: ΔQ 3.5, $(m+n)$ 0.55, K 8.0 (Figure 2.38 for thin-section of this example). (b) Jurassic North Sea example – 22% clay, 5.9 μm mgs, modeled ‘silt’ parameters: ΔQ 3.5, $(m+n)$ 0.48, K 12.0. (c) Iota Area example – 27% clay, 8.9 μm mgs, modeled ‘silt’ parameters: ΔQ 708.7, $(m+n)$ 1.59, K 11.8. (d) Zeta Area example – 28% clay, 4.5 μm mgs, Q 65.8, $(m+n)$ 0.558, K 24.1.

Code	Whole distribution stats							
	% Clay	% Sand	% Silt	%>10µm	Mean Grain Size (µm)	SD	Skewness	SS mean (µm)
NOR_2	36	1.3	63	49	5.3	1.9	0.7	19.0
NOR_3	16	4.3	80	72	9.6	2.0	1.3	25.0
NOR_5	18	4.7	77	71	10.1	2.0	1.4	25.9
NOR_6	38	4.5	57	48	3.9	2.1	0.2	20.4
NOR_7	27	0.9	72	44	4.1	2.0	0.4	18.7
NOR_8	22	1.7	76	55	5.9	2.0	0.6	21.2
NOR_12	28	3.2	69	42	4.1	1.9	0.2	19.0
NOR_26	13	3.0	84	60	5.7	2.3	0.7	24.6
NOR_28	19	0.4	80	57	6.7	1.6	1.0	18.9
ZETA_12	22	0.1	78	65	6.9	2.0	1.2	19.7
ZETA_13	19	0.0	81	65	7.8	2.0	1.3	21.1
ZETA_15	22	0.2	78	61	6.9	2.0	1.3	19.7
ZETA_6	29	0.0	71	48	4.6	2.0	0.6	18.1
ZETA_16	26	1.9	72	54	5.5	2.0	0.8	19.0
CHI_8	34	0.8	65	36	3.5	2.1	0.0	21.9
CHI_9	22	4.6	74	62	7.8	2.2	0.9	27.6
ETA_21	25	0.0	75	56	5.9	2.6	0.7	32.7
IOTA_75	27	9.8	64	64	8.8	2.4	1.3	31.4

Table 2.9. Sedimentary parameters and moment statistics derived from samples with a Type 5 grain size distribution.

Code	Floc mode					Silt mode					Df(µm)
	ΔQ	$\log \Delta Q$	$n + m$	K	r^2	ΔQ	$\log \Delta Q$	$n + m$	K	r^2	
NOR_2	8.5	2.1	0.19	6.9	0.92	472.4	6.2	1.05	30.8	0.98	11.6
NOR_3	10.3	2.3	0.24	144.9	0.74	19477.2	9.9	2.06	32.0	0.98	10.3
NOR_5	3.2	1.2	0.11	40.9	0.74	2613.0	7.9	1.61	22.3	0.99	9.9
NOR_6	7.3	2.0	0.12	96.9	0.79	35.7	3.6	0.53	15.5	0.86	7.6
NOR_7	6.0	1.8	0.12	26.7	0.67	66.5	4.2	0.62	21.7	0.98	8.8
NOR_8	5.8	1.8	0.14	6.6	0.86	32.6	3.5	0.48	12.1	0.99	8.3
NOR_12	16.1	2.8	0.22	68.7	0.95	28.8	3.4	0.44	22.4	0.99	9.4
NOR_26	12.9	2.6	0.24	128.4	0.82	47.0	3.9	0.64	8.7	0.89	7.8
NOR_28	50.4	3.9	0.44	92.8	0.92	213.5	5.4	0.82	24.8	0.98	8.0
ZETA_12	3.1	1.1	0.12	614.6	0.33	55.9	4.0	0.55	13.4	0.96	2.4
ZETA_13	5.2	1.7	0.16	763.5	0.77	90.6	4.5	0.65	16.7	0.94	2.9
ZETA_15	3.9	1.4	0.15	79.1	0.59	961.8	6.9	1.13	33.7	1.00	6.2
ZETA_6	10.1	2.3	0.16	1721.5	0.79	65.8	4.2	0.56	24.1	0.98	2.5
ZETA_16	3.1	1.1	0.07	132.7	0.52	353.0	5.9	0.92	32.7	0.69	5.1
CHI_8	6.0	1.8	0.11	38.4	0.85	25.3	3.2	0.63	11.0	0.91	14.0
CHI_9	5.6	1.7	0.15	62.9	0.80	143.8	5.0	0.97	10.5	0.94	9.9
ETA_21	-	-	-	-	-	4630.8	8.4	2.40	14.3	0.98	
IOTA_75	1.3	0.2	0.00	88.0	0.40	342.9	5.8	1.35	10.2	0.95	10.6

Table 2.10. Kranck model parameters derived from the fitted floc-component and non-cohesive silt components of Type 5 sample grain size distributions. [Note low Df values for the Zeta Area Samples].

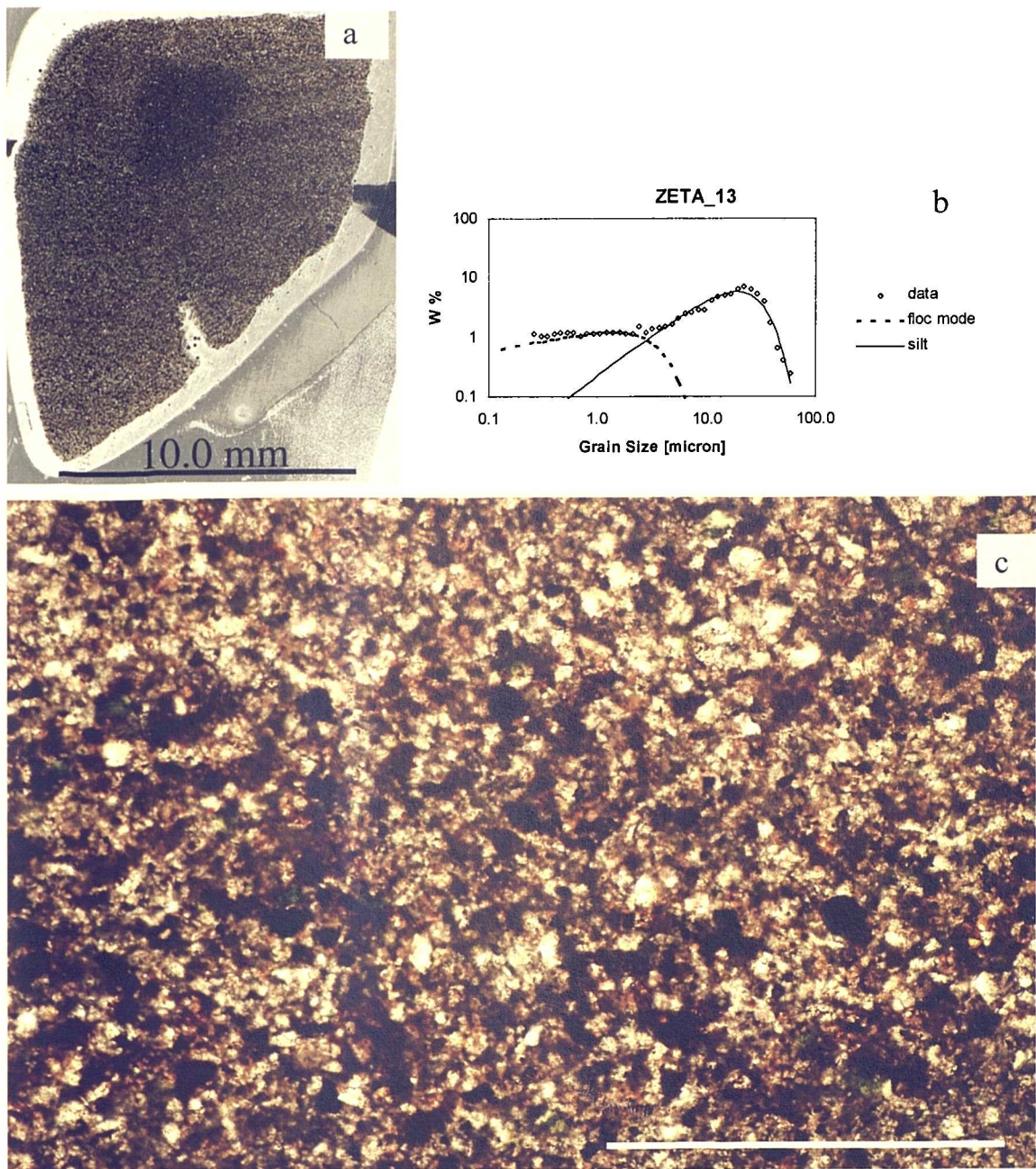
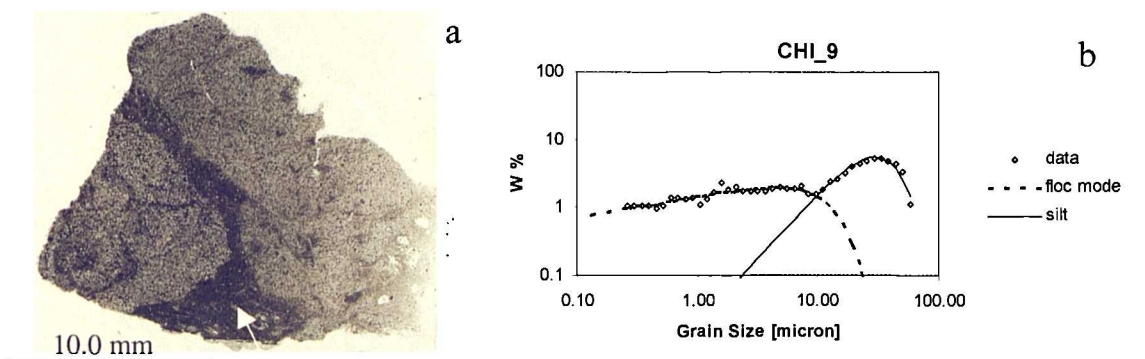


Figure 2.35. Example of a Type 5 sample recovered from a Zeta Area well illustrating: (a) an image of the thin section itself, (b) the corresponding grain size distribution, and (c) a transmitted-light photomicrograph (plane light, x4) taken from a thin section of a sample (ZETA_13) with a Type 5 grain size distribution; the patchy appearance relates to silt-rich and silt-poor areas. The scale bar (bottom right) is 1000 μ m.



Possible clay-rich flame structure, slurried appearance of the fine sandstone suggests soft sediment deformation

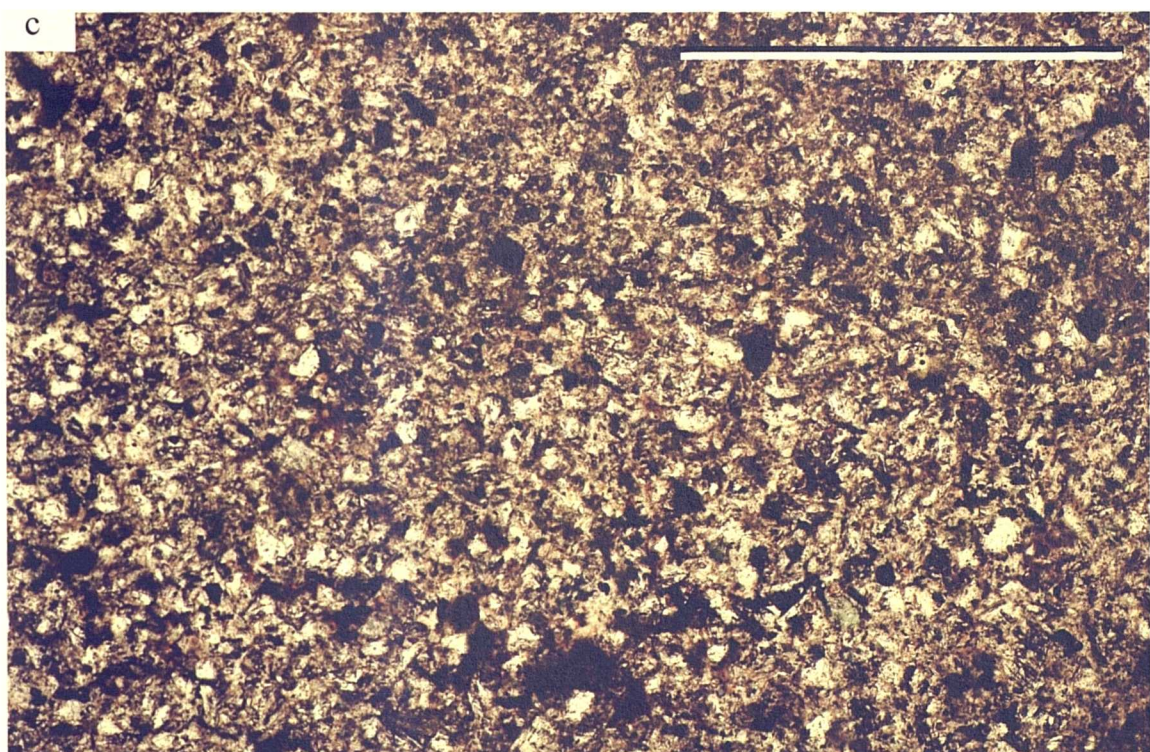
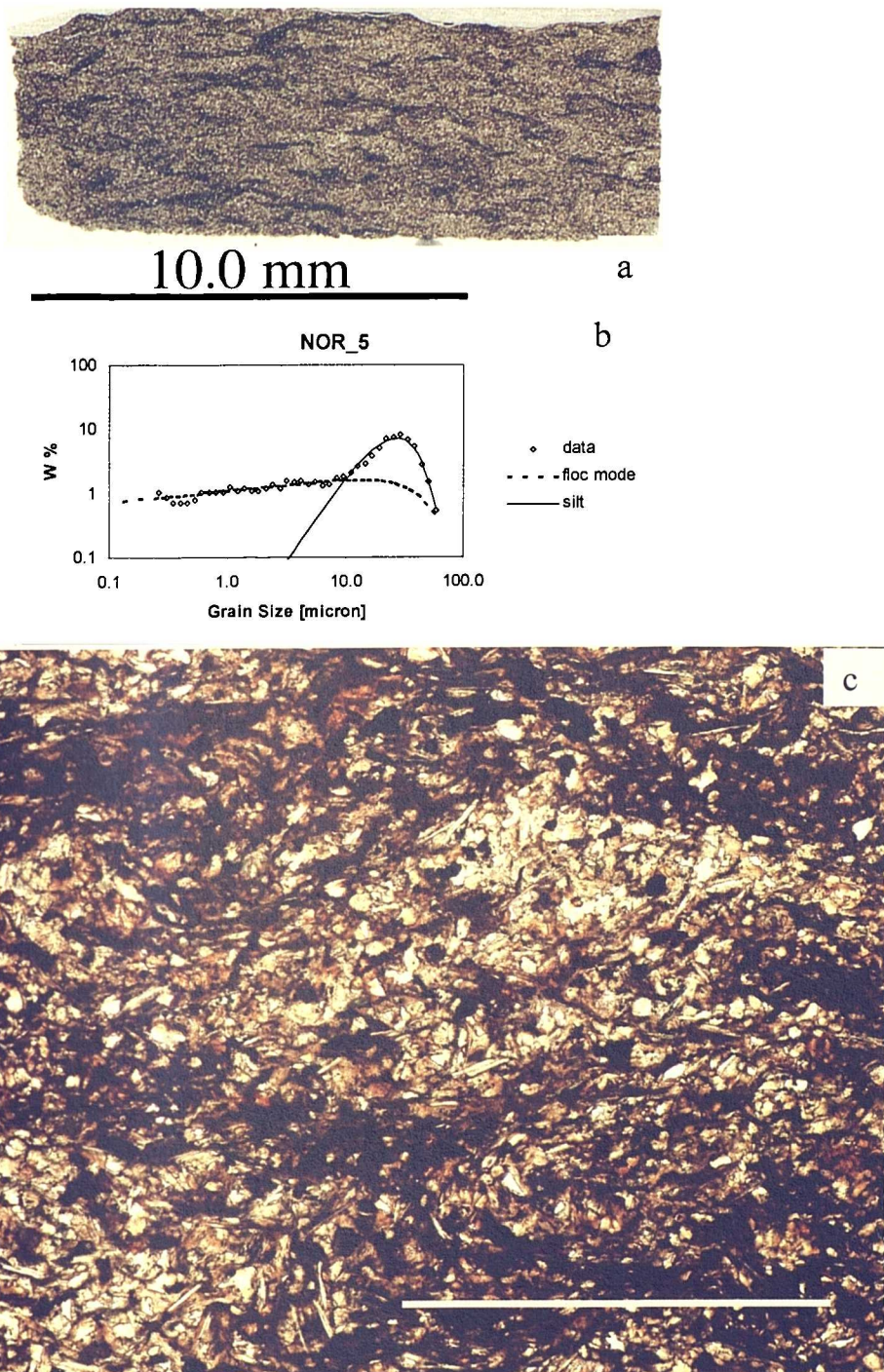


Figure 2.36. Example of a Type 5 sample recovered from a Chi Area well illustrating (a) an image of the thin section itself (b) the corresponding grain size distribution and (c) a transmitted-light photomicrograph (plane light, x4) taken from a thin section of a sample (CHI_9) with a Type 5 grain size distribution; the light appearance of the thin section reflects the silt-rich nature of this sample (21% clay). The scale bar (top right) is 1000 μ m.



[Figure 2.37. Example of a Type 5 sample recovered from a North Sea well illustrating: (a) an image of the thin section itself, (b) the corresponding grain size distribution, and (c) a transmitted-light photomicrograph (plane light, x4) taken from a thin section of a sample (NOR_5) with a Type 5 grain size distribution; the mottled appearance of the thin section relates to the bioturbated nature of this sample. The scale bar (top right) is 1000μm.

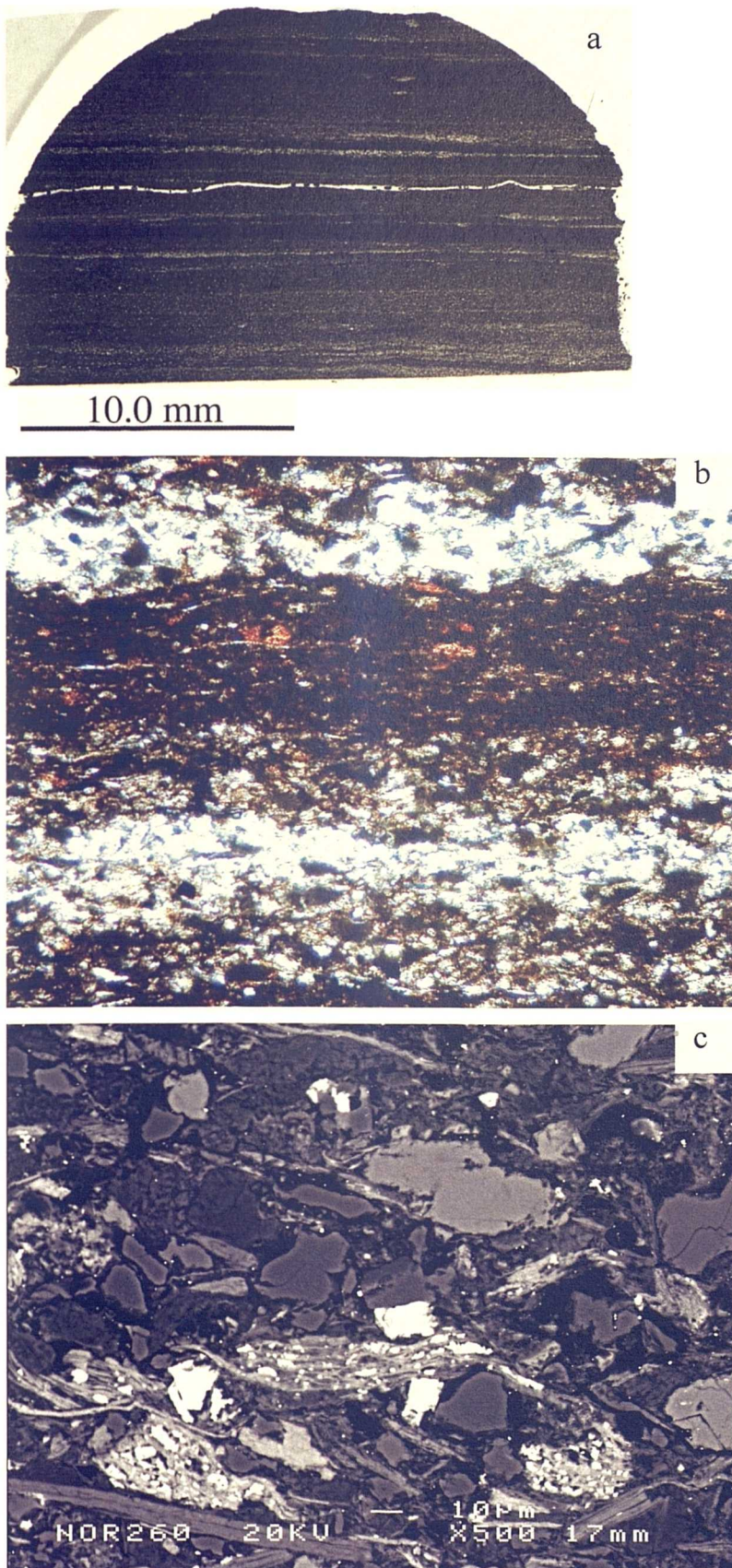


Figure 2.38. Illustrating 3 scales of observation for NOR-26 (Rannoch Formation, Jurassic) with a Type 5 grain size distribution. (a) Thin section image: lighter, silt rich-lamina are clearly visible. (b) Transmitted-light photomicrograph (plane light, x10) showing alternation of quartz-rich layers with darker clay and organic-rich layers (TOC 2.83). The layers have sharp bases and graded tops. (c) BSEM micrograph of NOR-26 (Rannoch Formation, Jurassic North Sea) illustrating arrangement of grains. (grain size spectra for this sample in Figure 2.34a).

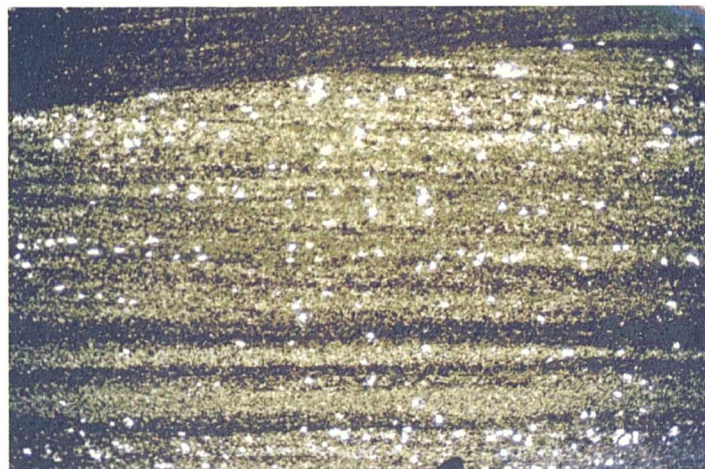


Figure 2.39. Transmitted-light photomicrograph (plane light) of Zeta_12 exhibiting low-Etale lamination; the lamina have sharp bottom and top contacts indicating the actions of bottom currents (cf. Schieber, 1999). The field of view is ~2.7mm.



Figure 2.40. Transmitted-light photomicrograph (plane light, x10) of Zeta_20. This sample represents a fine-grained example of a Type 5 grain size distribution with a clay content of 33% and a mean grain size of $3.35\mu\text{m}$. In the lower half of the photomicrograph this sample largely lacks lamina, towards the top indistinct laminae and an erosion surface picked out by a silt-rich layer are present. A number of flattened burrows are also present. The field of view is ~2.7mm.

2.4.6 Type 6 – sandy mudstones and siltstones

Those samples with a sand content >10% were classified as sand-rich mudstones and siltstones; although these samples were assigned into a single GSD type, three sub-types were recognized, each of which are described below.

2.4.6.1 Type 6a floc dominated sandy mudstones.

The first sand-rich sample type is only represented by two samples; these samples have a grain size distribution characteristic of deposition by flocculated material. One of the examples is from the Zeta Area and the other is from the Jurassic North Sea (Figure 2.41). Sediment characterized by a mixture of flocculated clay with a significant sand component is non-intuitive and requires explanation. The Zeta Area example has a flocculated grain size spectra similar to a Type 1 distribution in what is essentially a sandstone— it has a mean grain size of $2.4\mu\text{m}$ (for the $0 - 63\mu\text{m}$ component) and a clay content of only 15% (62% of the distribution was sand). From the thin section image it can be seen that there are small, discrete darker, clay-rich patches in amongst what is a homogeneous fine sand matrix; this structure indicates that clay flocs were deposited simultaneously with the sand particles.

The second example is from the Jurassic North Sea is different to the previous example; its grain size spectra is similar to that of a Type 2 sediment, characteristic of deposition of flocculated material from high suspended sediment concentration. The thin section is darker than Zeta_26 (Fig. 2.41a, b) reflecting the higher clay content relative to the previous example; this sample has a mottled texture indicative of bioturbation. In this case the sand component may have been transported within a clay-rich laminar flow (cf. Baas and Best, 2002) and thus both components would have been deposited simultaneously initially (see figure 2.41). This sample is presented in Figure 2.42 at three scales of observation.

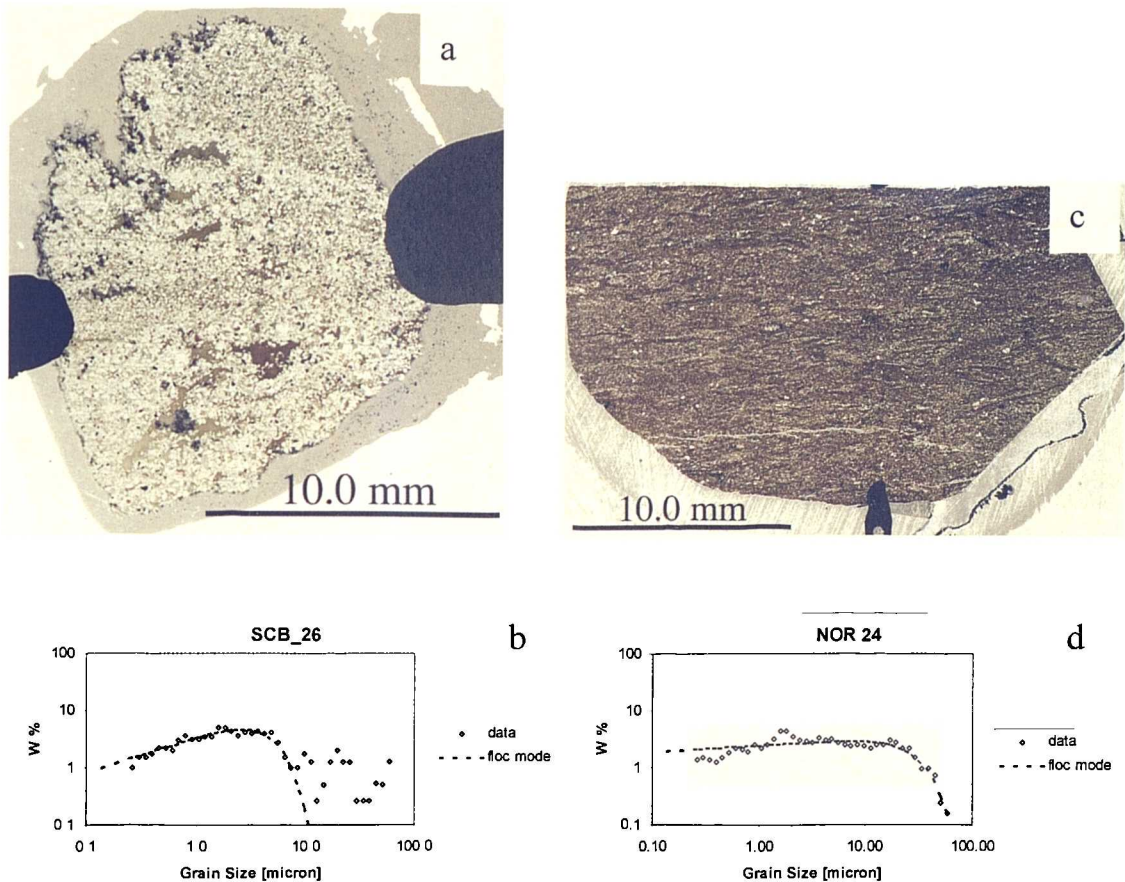


Figure 2.41. Paired thin section images and grain size distributions for Type 6 samples with a mixed floc-sand grain size distribution (a) Thin section image of ZETA_26 (which is essentially a sandstone) and (b) disaggregated grain size spectra of ZETA_26 on log-log weight percent – grain size (μm) plots – 15% clay, 62% sand, $2.4\mu\text{m}$ mean grain size (mgs), modeled 'floc' parameters: ΔQ 4.42, $(m+n)$ 0.3528, K 289.88 (c) Thin section image of NOR_24; (d) disaggregated grain size spectra of NOR_24 on log-log Weight percent – grain size (μm) plots – 28% clay, 13% sand, $3.4\mu\text{m}$ mgs, modeled 'floc' parameters: ΔQ 3.97, $(m+n)$ 0.053, K 9.49 (cf. Figure 2.42 for further images).

Code	GSD type	Whole distribution stats					SS mean (μm)		
		% Clay	% Sand	% Silt	% >10μm	Mean Grain Size (μm)	SD	Skewness	
ZETA_26	6	15	63.0	22	76	2.4	1.8	-0.6	22.2
NOR_24	6	29	13.5	58	46	3.4	1.9	-0.1	19.5
NOR_9	6b	21	16.6	62	61	5.4	2.0	0.5	21.5
NOR_11	6b	13	33.8	54	73	6.6	2.1	0.5	27.7
NOR_21	6b	31	16.6	53	56	3.9	2.4	0.0	25.0
NOR_22	6b	22	23.8	54	52	3.7	1.9	-0.2	22.8
NOR_23	6b	35	11.3	53	50	3.9	2.3	-0.1	24.8
NOR_25	6b	31	22.1	47	54	3.1	2.2	-0.4	25.8
NOR_27	6b	18	25.9	56	70	7.6	2.0	1.0	22.9
NOR_29	6b	20	22.3	58	70	8.4	2.3	1.1	29.6
IOTA_55	6b	34	15.2	51	54	3.7	2.3	0.1	22.3
IOTA_57	6b	31	10.8	59	30	2.8	1.9	-0.3	19.5
IOTA_65	6b	44	13.7	42	20	1.9	1.8	-0.9	25.3
IOTA_72	6b	32	15.6	52	55	3.5	2.3	-0.4	26.4
ZETA_22	6b	24	11.9	64	58	5.2	2.3	0.3	28.1
CHI_11	? - 6b	47	?	53	23	2.3	2.0	-0.2	18.8
IOTA_11	6c	32	18.8	49	59	5.5	2.5	0.4	30.7
CHI_5	6c	16	19.2	65	78	13.2	2.1	1.6	32.8
CHI_7	6c	25	12.2	63	64	6.8	2.4	1.0	27.8
CHI_12	6c	31	10.1	59	52	4.8	2.5	0.4	28.5
CHI_13	6c	26	10.1	64	58	6.6	2.3	0.6	28.7
ETA_22	6c	28	10.0	62	57	5.4	2.4	0.6	26.4
ETA_23	6c	29	26.3	45	62	3.4	2.7	-0.2	30.0
ZETA_24	6c	12	33.2	55	72	6.4	2.0	0.5	23.9

Table 2.11. Sedimentary parameters and moment statistics derived from samples with a Type 6 grain size distribution.

Code	GSD type	Floc mode					Silt mode					$Df(\mu\text{m})$
		ΔQ	$\log \Delta Q$	$n + m$	K	r^2	ΔQ	$\log \Delta Q$	$n + m$	K	r^2	
ZETA_26	6	58.1	4.1	0.31	436.0	0.88	-	-	-	-	-	-
NOR_24	6	3.7	1.3	0.03	10.6	0.93	-	-	-	-	-	-
NOR_9	6b	6.3	1.8	0.11	52.6	0.59	92.9	4.5	0.77	15.4	0.95	9.5
NOR_11	6b	16.4	2.8	0.23	107.2	0.80	43.3	3.8	0.69	7.1	0.89	10.9
NOR_21	6b	2.7	1.0	0.01	391.6	0.77	39.8	3.7	0.67	9.7	0.90	5.3
NOR_22	6b	38.6	3.7	0.30	204.3	0.74	108.7	4.7	0.97	12.6	0.86	10.0
NOR_23	6b	3.1	1.1	0.03	109.8	0.25	222.6	5.4	1.14	16.1	0.85	9.5
NOR_25	6b	2.0	0.7	-0.04	90.2	0.76	115.3	4.7	1.14	11.9	0.79	11.2
NOR_27	6b	9.4	2.2	0.24	24.0	0.81	52.9	4.0	0.63	11.1	0.95	9.2
NOR_29	6b	5.3	1.7	0.14	175.2	0.75	239.7	5.5	1.23	9.6	0.92	8.9
IOTA_55	6b	0.7	-0.3	-0.11	26.7	0.78	66.2	4.2	0.74	15.8	0.97	7.7
IOTA_57	6b	8.7	2.2	0.11	131.9	0.79	8.0	2.1	0.25	16.5	0.97	8.0
IOTA_65	6b	4.6	1.5	0.03	219.2	0.95	33.0	3.5	1.02	12.8	0.68	10.6
IOTA_72	6b	2.5	0.9	0.03	293.0	0.95	70.5	4.3	0.99	11.5	0.95	7.4
ZETA_22	6b	4.0	1.4	0.06	81.5	0.61	322.7	5.8	1.33	12.1	0.95	11.7
CHI_11	? - 6b	2.1	0.8	-0.03	17.4	0.93	-	-	-	-	-	-
IOTA_11	6c	2.5	0.9	0.04	331.4	0.79	185.6	5.2	1.26	9.7	0.93	6.7
CHI_5	6c	27.3	3.3	0.42	282.2	0.74	69.0	4.2	0.86	4.9	0.97	6.9
CHI_7	6c	27.2	3.3	0.43	107.0	0.86	27.8	3.3	0.58	5.9	0.62	8.3
CHI_12	6c	2.5	0.9	0.06	517.9	0.75	15.5	2.7	0.55	3.8	0.96	4.7
CHI_13	6c	6.7	1.9	0.16	111.2	0.55	59.9	4.1	0.86	7.1	0.96	9.8
ETA_22	6c	2.0	0.7	0.04	18.8	0.85	60.7	4.1	0.89	7.8	0.98	11.9
ETA_23	6c	-	-	-	-	-	51.5	3.9	0.99	6.1	0.94	-
ZETA_24	6c	7.5	2.0	0.15	10.6	0.75	36.0	3.6	0.74	6.4	0.83	21.7

Table 2.12. Kranck model parameters derived from the fitted floc-component and non-cohesive silt components of samples with Type 6 grain size distributions.

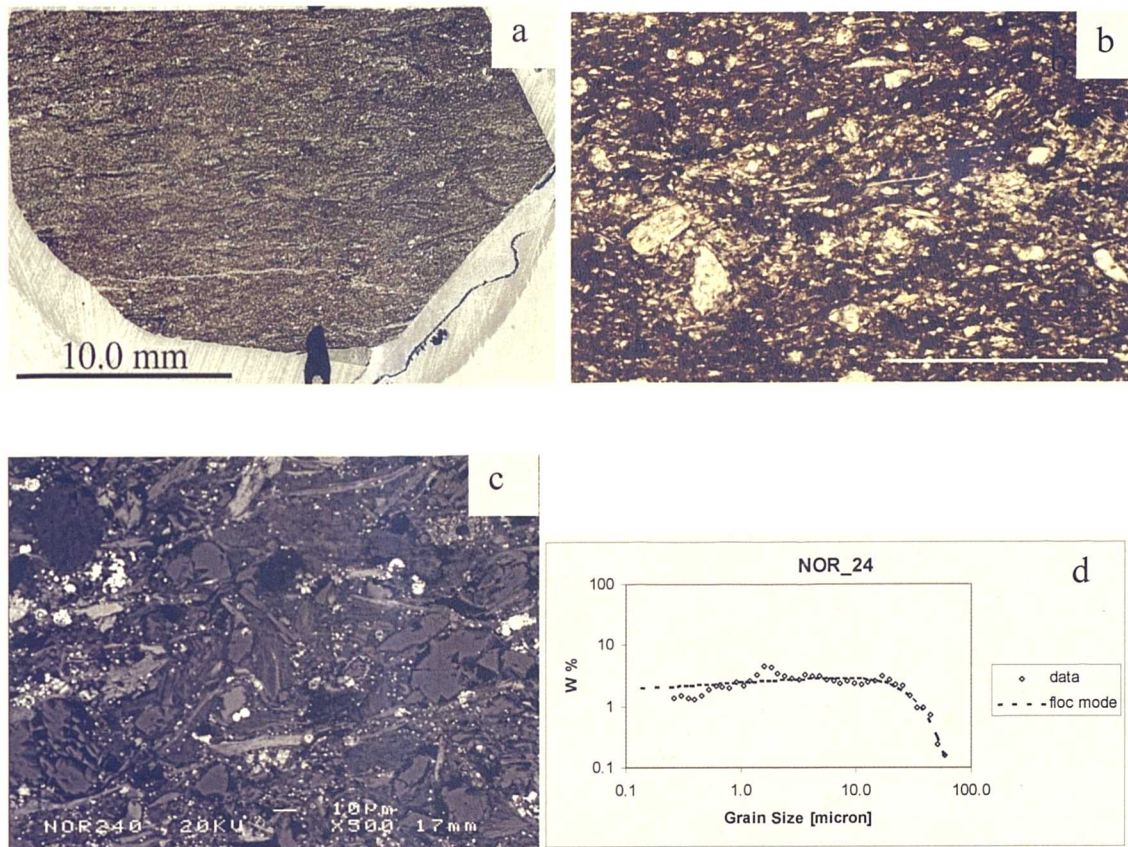


Figure 2.42. Illustration of NOR-24 (Drake Formation, Jurassic North Sea) a Type 6a sample with a mixed floc-sand grain size distribution: (a) the thin section scale exhibiting a mottled texture characteristic of bioturbation, (b) a magnified (x4) image, and (c) a BSEM micrograph illustrating a chaotic arrangement of grains with a broad range of sizes consistent with deposition from high concentration, as evidenced by the grain size distribution (d).

2.4.6.2 Type 6b floc – silt – sand mixtures

The second sand-rich, fine-grained sediment type identified in this study has sub-63 μm grain size distributions similar in form to those of Types 3, 4 and 5 (cf. sections 2.4.3 – 2.4.5). Examples of this type are predominantly drawn from the North Sea Jurassic and deep water Iota Area, with a single example from the Zeta Area. Representative grain size distributions for Type 6b sediments are presented in Figure 2.43. These grain size types represent ~8% of the total grain size distribution dataset used in this study. Sedimentary statistics are given in Table 2.11 and the parameters derived from fitting the Kranck model are given in Table 2.12. The clay, silt and sand components of each of these grain size distribution types may have been either deposited simultaneously or separately, as discrete depositional events. For Type 6b samples the D_f value averages 10.1 μm , ranging between 5 and 21 μm .

Figure 2.44 shows images and grain size data from a Type 6b sample where the sand component has been deposited simultaneously with the sub-63 μm component. The evidence indicative of co-deposition comes from the thin section where sand grains can be seen to be ‘floating’ in a clay and fine silt matrix. In contrast, Figure 2.45 shows distinctive sand and coarse silt rich layers; the contact shown in Figure 2.45c between a silt and clay layer sharply overlain by a coarse silt – fine sand layer is actually the base of an erosive feature visible in the thin section. In this example it is likely that the clay and coarse silt components were deposited by an event distinct from that which deposited the coarse silt – fine sand material which comprises the erosive feature.

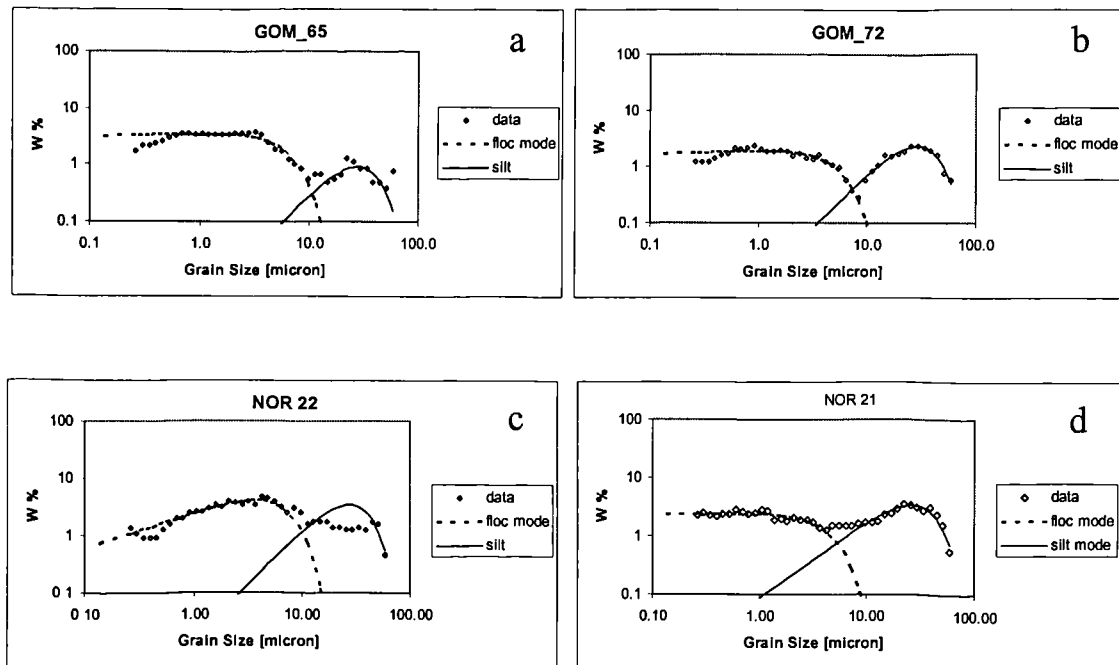


Figure 2.43. Disaggregated grain size spectra of Type 6 samples composed of floc-silt-sand components on log-log weight percent – grain size (μm) plots; (a) Iota Area example – 44% clay, 13% sand, $1.91\mu\text{m}$ mean grain size (mgs), modeled 'silt' parameters: ΔQ 3.5, $(m+n)$ 1.01, K 12.8. (b) Iota Area example – 32% clay, 15% sand, $3.5\mu\text{m}$ mgs, modeled 'silt' parameters: ΔQ 4.3, $(m+n)$ 0.99, K 11.5. (c) Jurassic North Sea example – 23% clay, 23% sand $3.7\mu\text{m}$ mgs, modeled 'silt' parameters: ΔQ 108.7, $(m+n)$ 0.96, K 12.6 [note poor fit]. (d) Jurassic North Sea example – 30% clay, 16% sand $3.9\mu\text{m}$ mgs, ΔQ 39.8, $(m+n)$ 0.67, K 9.7.

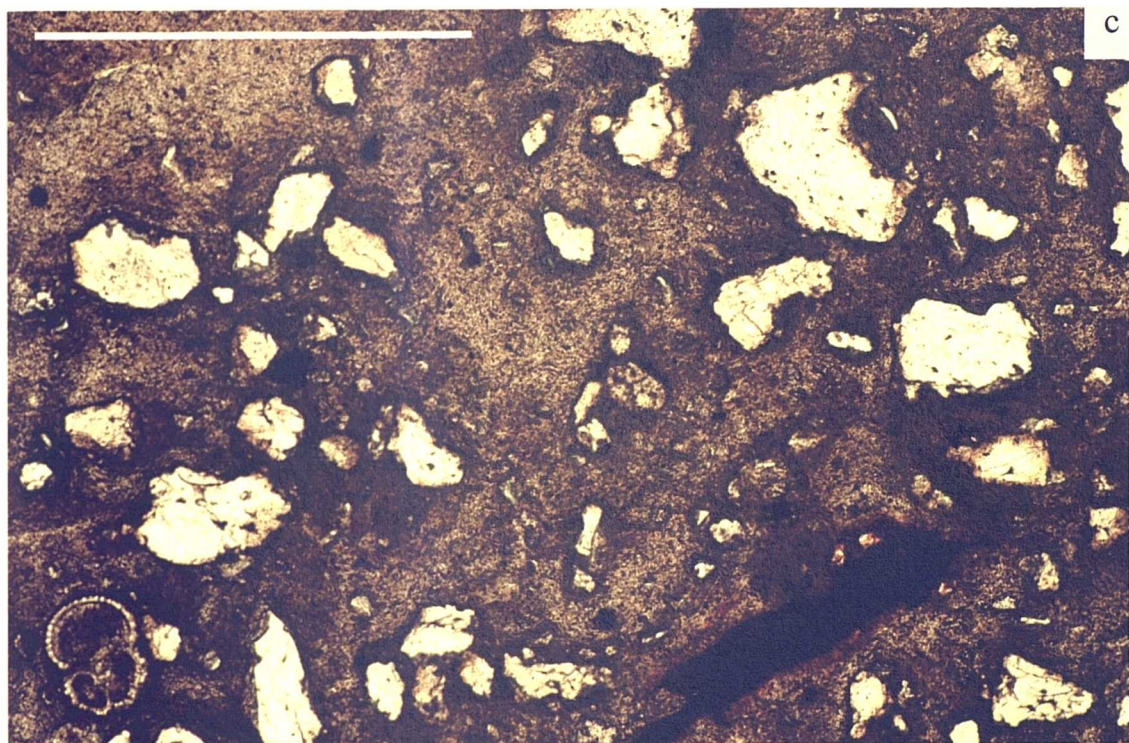
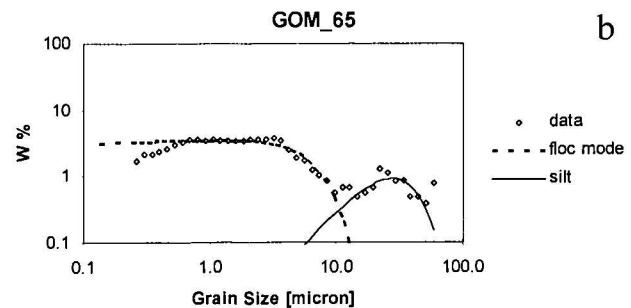
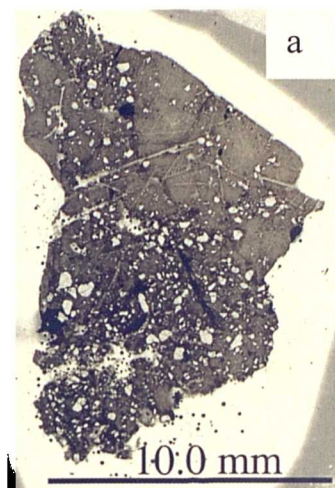


Figure 2.44. Example of a Type 6b sample recovered from a deep water IOTA well illustrating: (a) an image of the thin section itself, (b) the corresponding grain size distribution, and (c) a transmitted-light photomicrograph (plane light, x4) taken from a thin section of a sample (IOTA_65) with a Type 6 grain size distribution composed of floc-silt-sand components; isolated, poorly-sorted sand grains float in a matrix of clay and fine silt. The scale bar (top left) is 1000 μ m.

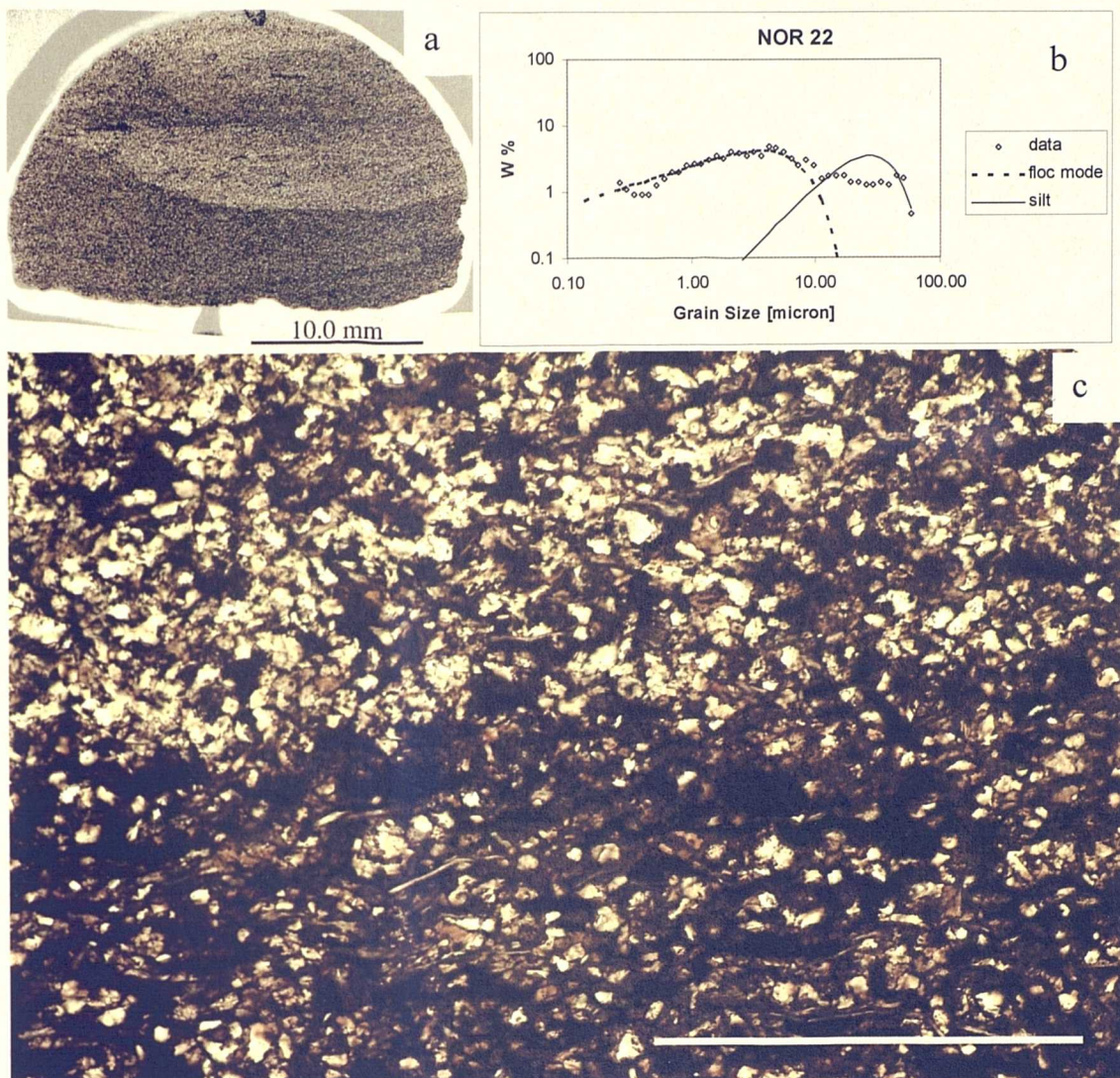


Figure 2.45. Example of a Type 6b sample recovered from a North Sea well illustrating: (a) an image of the thin section itself illustrating the presence of at least one coarser grained erosive feature, (b) the corresponding grain size distribution [note poor fit for the silt component], and (c) a transmitted-light photomicrograph (plane light, x4) taken from a thin section of a sample (NOR_22) with a Type 6 grain size distribution composed of floc-silt-sand components; the erosive feature visible in (a) can be seen in the base of the section. The scale bar (bottom right) is 1000 μ m.

2.4.6.3 Type 6c – clay-silt-sand mixture: continuous distribution truncated by sieving

The third sand-rich fine-grained sediment type recognized here is characterized by seemingly continuous grain size distributions that have been truncated by the sieving procedure (at 63 μm) carried out prior to Sedigraph analysis; examples of these grain size distributions are shown in Figure 2.46. Samples with Type 6c grain size distributions are drawn predominantly from the Chi Area, with some samples from the Iota, Eta and the Zeta Areas. Type 6c grain size distributions represent ~5% of the total dataset used in this study. Sedimentary statistics are given in Table 2.11 and the parameters derived from fitting the Kranck model are given in Table 2.12. For these Type 6 samples the D_f value averages 8 μm , ranging between 4 and 11 μm .

Analysis of the thin sections corresponding to Type 6c grain size distribution samples showed that a range of textures were associated with this Type 6 sub-type. Two fabrics characterise the group: homogeneous unstructured textures; and heterogeneous, combinations of various sedimentary structures. An example of a homogenous Type 6c sample is given in Figure 2.47, images at three scales of observation (mm to μm) along with the truncated grain size distribution (Fig. 2.47d) are illustrated. In the thin section image some faint lamination may be present, corresponding to the slight variation in colour. It is clear from the magnified petrographic (x4) and the BSEM image that at these scales this sample lacks any clear structure and the sand grains have clearly been deposited at the same time as the silt and clay flocs; analysis of these images indicates that this sample is likely to have been deposited rapidly (cf. O'Brien and Slatt, 1990). Type 6c samples with homogeneous textures are believed to represent high concentration density flows where the sand component is 'carried' in a matrix of silt and clay. The prominent silt peak associated with the apparently continuous distribution seen in Figure 2.47d suggests that the sortable silt and sand components were hydrodynamically sorted, implying that turbulence within in the depositing flow was sufficient to allow a degree of sorting.

The second texture associated with Type 6c sediments is illustrated in Figure 2.48 along with the corresponding grain size. In this case, because of the highly heterogeneous nature

of the thin section image, analysis of the grain size distribution is complicated; the distribution may relate to a single bed and thus a single event or may represent a mixture of a variety of the beds, which could possibly account for the high scatter seen in the clay size range (Fig. 2.46a, 2.48b). A number of sedimentary structures are visible in the thin section image including lamination, cross-lamination, coarsening- and fining-up sequences. The thin section bears similarities to the Sandy Mudstone facies association of Schieber (1999), interpreted to represent deposition in a nearshore deltaic environment. There are also similarities with the Moenkopi Formation (Lower Triassic) investigated by O'Brien and Slatt (1990) which was also interpreted to represent deposition in fluvially and tidally influenced shallow marine setting.

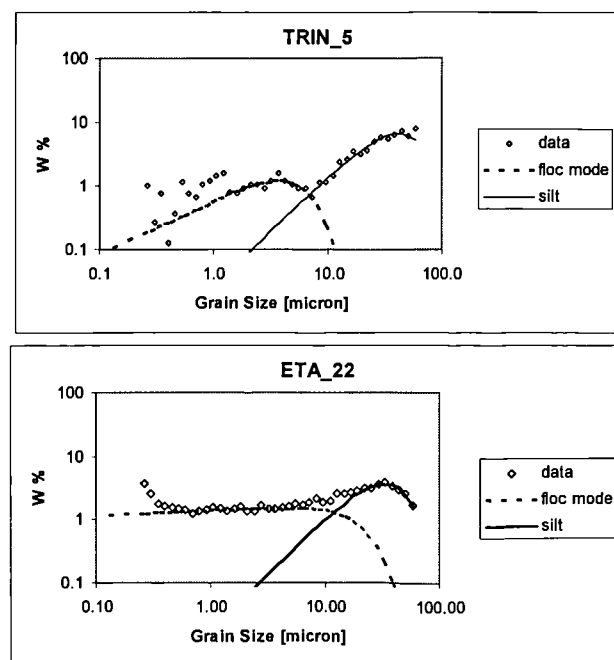


Figure 2.46. Disaggregated grain size spectra of Type 6c GSD Types on log-log weight percent – grain size (μm) plots; (a) Chi Area example – 15% clay, 19% sand, 13.2 μm mean grain size (mgs), modeled 'silt' parameters: ΔQ 69.0, $(m+n)$ 0.86, K 4.9 [note poor fit for the floc component]. (b) Eta Area example – 28% clay, 10% sand 5.4 μm mgs, modeled 'silt' parameters: ΔQ 60.7, $(m+n)$ 0.89, K 7.7.

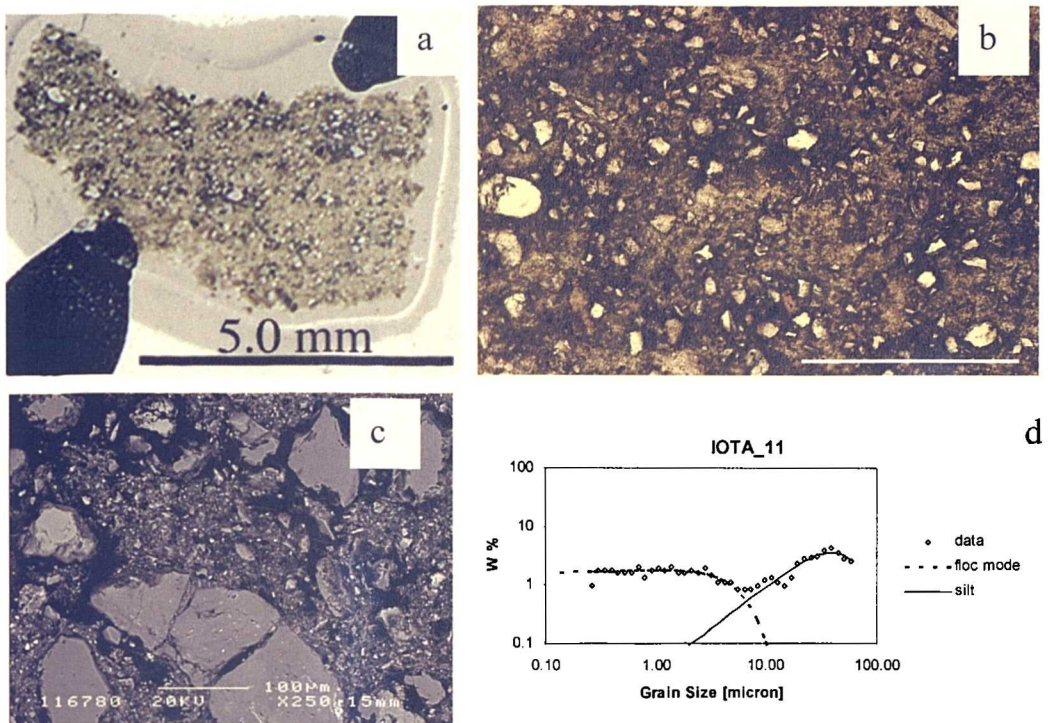


Figure 2.47. Example of a Type 6 sample recovered from a deep water Iota well illustrating: (a) an image of the thin section itself, (b) a transmitted-light photomicrograph (plane light, x4) taken from the thin section illustrating the unstructured mix of floc, silt and sand components, the scale bar (top left) is 1000 μ m, (c) a BSEM image exhibiting a similar texture to that seen in the magnified image, and (d) the corresponding grain size distribution.

Overall, in contrast to Types 1 – 4 the examples illustrated for Type 6 grain size distributions represent a highly heterogeneous grouping despite the further sub-division into the three sub-groupings. Analysis of the grain size distributions and petrographic thin sections has revealed samples relating to a whole spectrum of sedimentary processes emphasizing the non-uniqueness of these grain size types in terms of sedimentary environments highlighting the limitation of using grain size analysis alone in making process-based sedimentological interpretations.

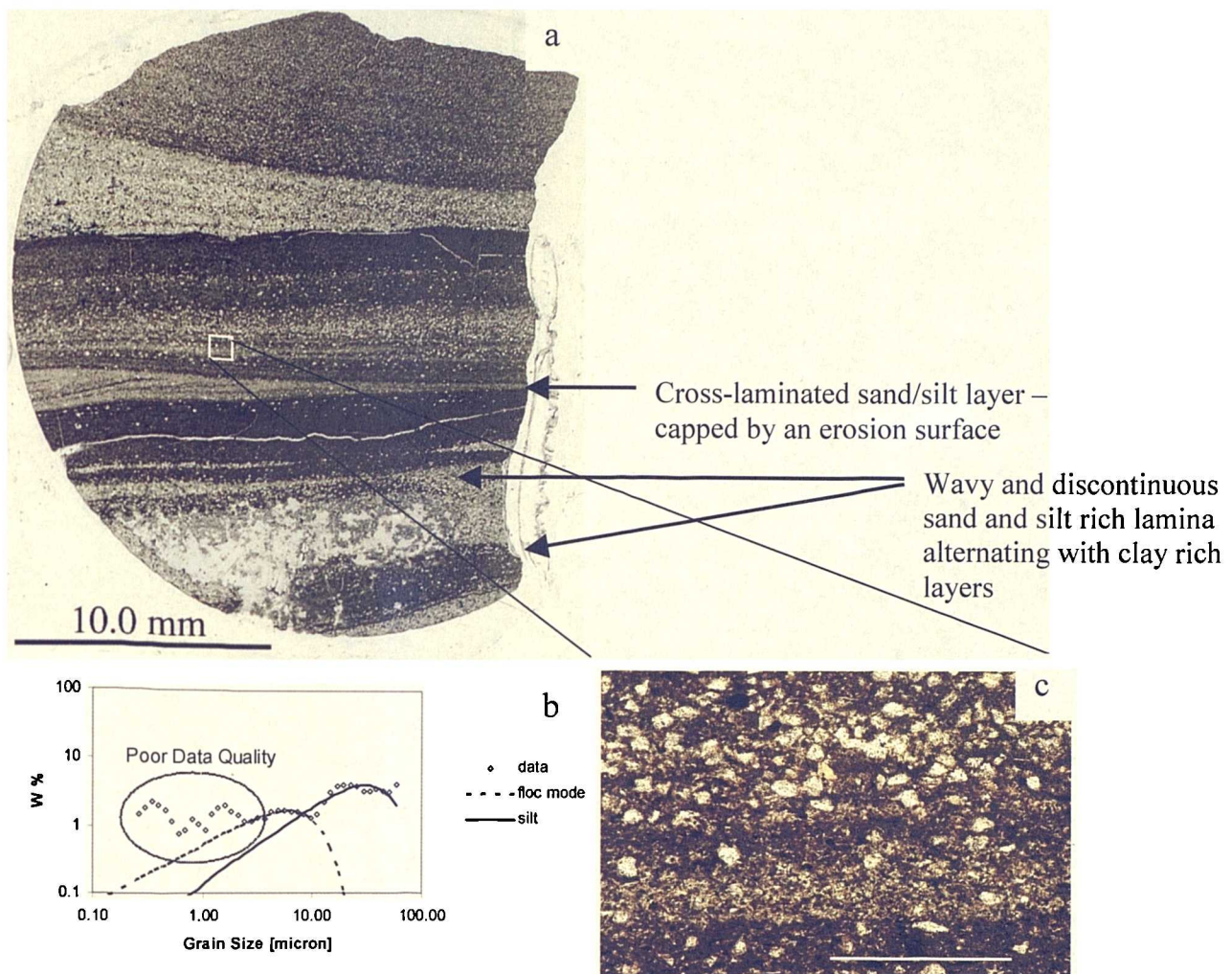


Figure 2.48. Integrated image of: (a) a thin section of a Chi Area Type 6c sample illustrating a variety of sedimentary structures interpreted as representing deposition in marine nearshore environment (see text), (b) the corresponding grain size distribution [note poor data quality], and (c) a magnified (x4) image of a coarsening-up sequence. The scale bar (bottom right) is 1000µm.

2.4.7 Comparison of GSD Types

In this section a series of figures are used to illustrate key distinctions between the grain size distribution types established in Sections 2.4.1 – 2.4.6 in terms of percentage clay–silt–sortable silt–sand, moment statistics and Kranck model parameters. The form of the grain size spectra was the main characteristic upon which the ‘Types’ were based. Representative grain size distributions are shown in Figure 2.49. There is clearly a continuum between these distributions and the progression from very fine-grained, entirely flocculated sedimentary deposits to coarse grained floc – non-cohesive silt – sand mixtures.

Figure 2.50 shows magnified thin section and BSEM images characteristic of grain size Types 1 to 5. Type 6 was omitted because of its heterogeneous nature. Figure 2.50 simply reflects floc – non-cohesive silt mixtures. Differences in the magnified thin section images of Types 1 – 4 are subtle and would possibly not be emphasized during a routine petrographic study. Despite the difference in form of the grain size distribution characteristic for these sediments (Figure 2.49) they appear largely homogenous at this scale. There is an obvious difference between the Type 4 and Type 5 thin section images.

In contrast to the thin section images, the BSEM images do clearly illustrate a progressive coarsening from Type 1 to Type 5. This indicates that grain size analysis more closely corresponds to BSEM images; possibly due to the greater proximity in terms of scale between these two methods. The range of the percentage clay–silt–sortable silt–sand for each of the grain size types is described by box-plots in Figure 2.51. Types 1 – 4 are essentially indistinguishable based solely on these parameters. Types 5 and 6 clearly differentiate both from each other, and from Types 1 – 4 based on the percentage silt and sand parameters (Fig. 2.51b, d).

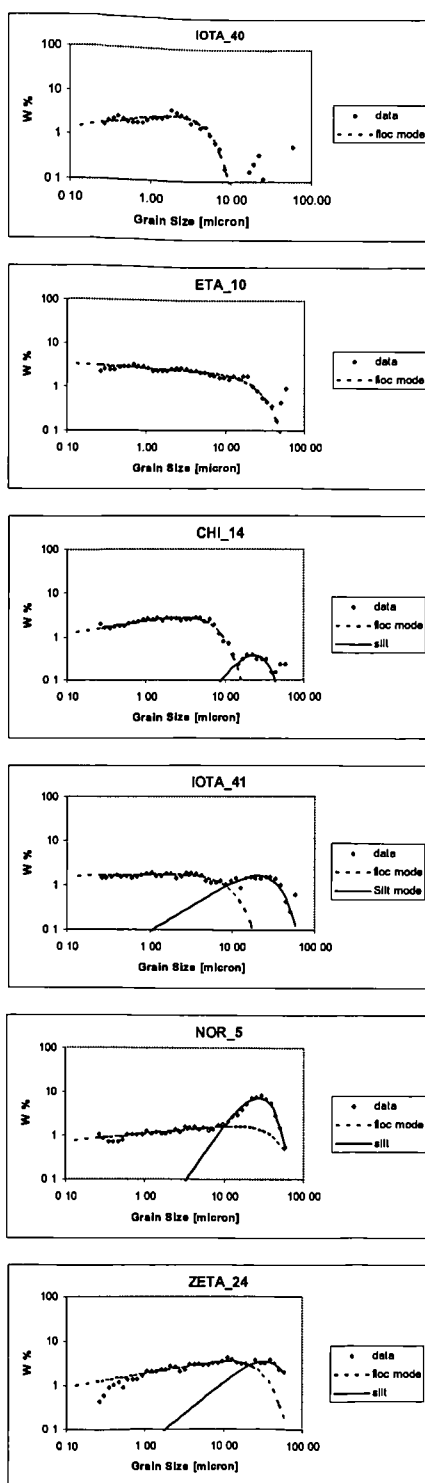


Figure 2.49. Exemplar grain size distributions for each of the six grain size types proposed in this study along with pie-charts describing the distribution of the grain size types as a function of location.

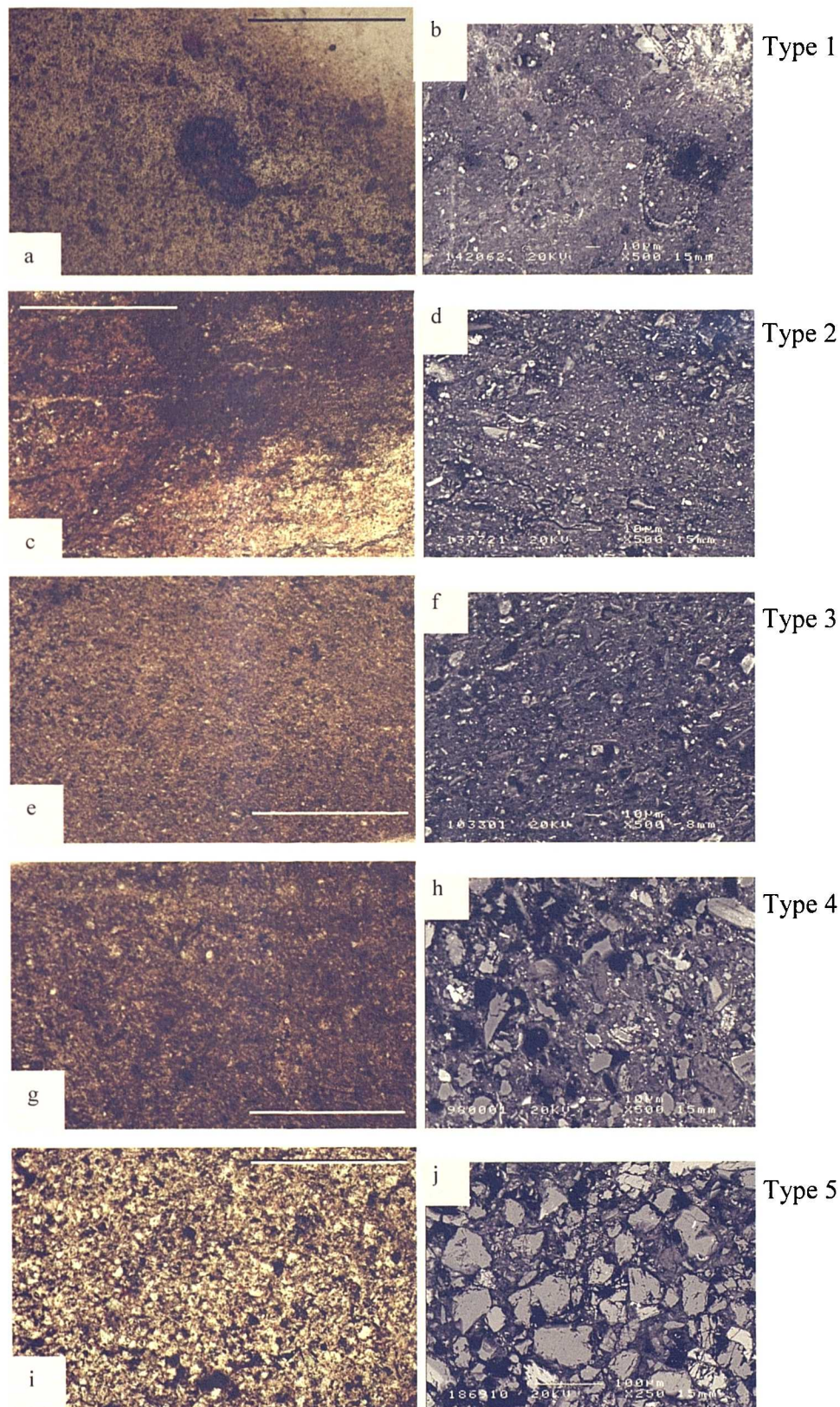


Figure 2.50 (previous page). Paired magnified thin section (x4, PPL) and BSEM images for Type 1 (a, b), Type 2 (c, d), Type 3 (e, f), Type 4 (g, h) and Type 5 (i, j) Note. scale change for the Type 5 BSEM image.

The % sortable silt ($\% > 10\mu\text{m}$) shows the greatest correspondence with the grain size types proposed (Fig. 2.51c). This observation is useful as the sortable silt parameter has been successful in inferring palaeocurrent strength of depositing flows in deep sea sediments (e.g. McCave *et al.*, 1995). However, caution is required if sediment concentrations were high as the $\sim 10\mu\text{m}$ non-cohesive – cohesive boundary is not rigid but dependent upon hydrodynamic and chemical conditions. For example, if material up to $15\mu\text{m}$ is incorporated into flocs, then this component will not be hydrodynamically sorted and will therefore not relate to the current strength but would be included with the ‘sortable silt’ component. A potential way round this would be to use the D_f value, derived from fitting the floc and non-cohesive silt components, rather than $10\mu\text{m}$, as the boundary from which to calculate the ‘sortable silt’ percentage and mean size, although further studies would be required to test this hypothesis.

The range of the moment statistic parameters for each of the grain size types is described by box-plots in Figure 2.52, whilst moment statistic cross-plots for each of the grain size types are given in Figs 2.53 and 2.54. From the box plots it can be seen that the mean grain size, standard deviation and skewness value generally increase from Type 1 to Type 6. The standard deviation corresponds most closely with the grain size types proposed and relates to the increasing non-cohesive silt component which decreases the degree of sorting (cf. Section 2.2.2 - 4; Stevens, *et al.*, 1996). Again, it is clear from the box plots that in terms of the moment statistics there is a significant jump between Type 4 and Type 5 particularly in terms of the mean grain size and skewness value. The moment statistic cross plots illustrate that if these parameters were used alone then it would be very difficult to differentiate Types 1 through 4. If used in isolation, the end members (i.e. Types 1 and 5/6) would be differentiated but further resolution of the dataset would not be possible.

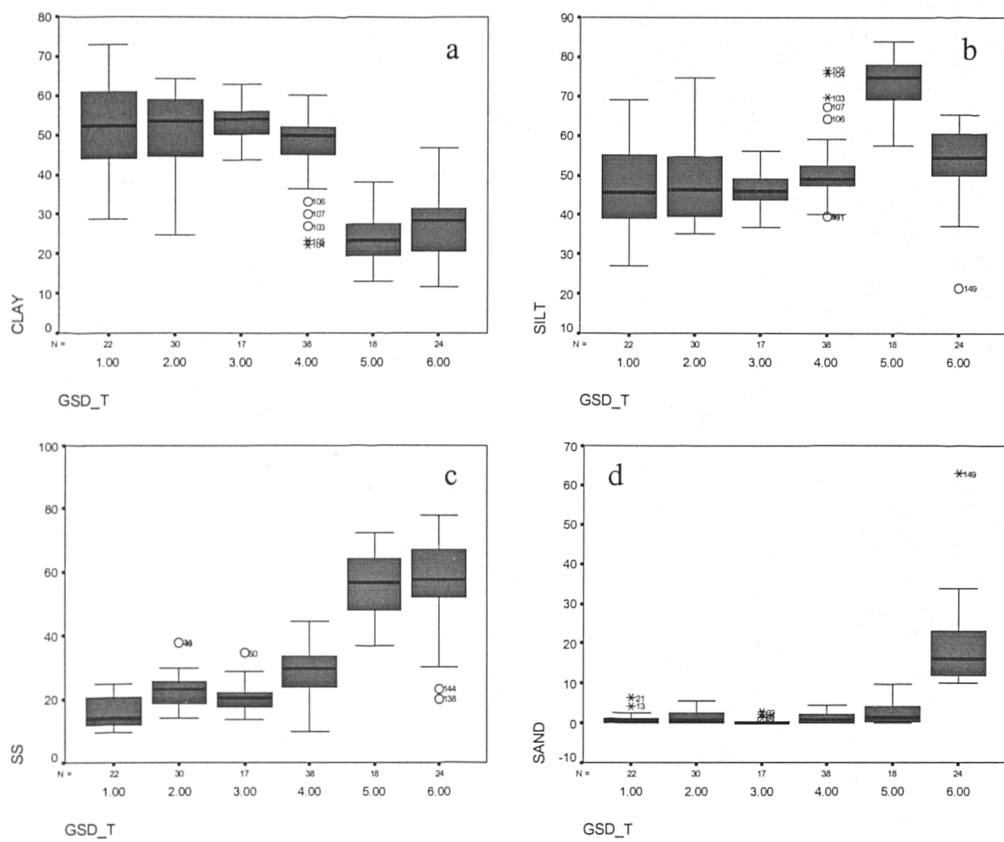


Figure 2.51. Boxplots for the grain size measures for the six mudstone grain size distribution Types proposed in this study showing: (a) clay content (weight %.), (b) silt content (weight %.), (c) sortable silt content (weight %.), and (d) sand content (weight %.).

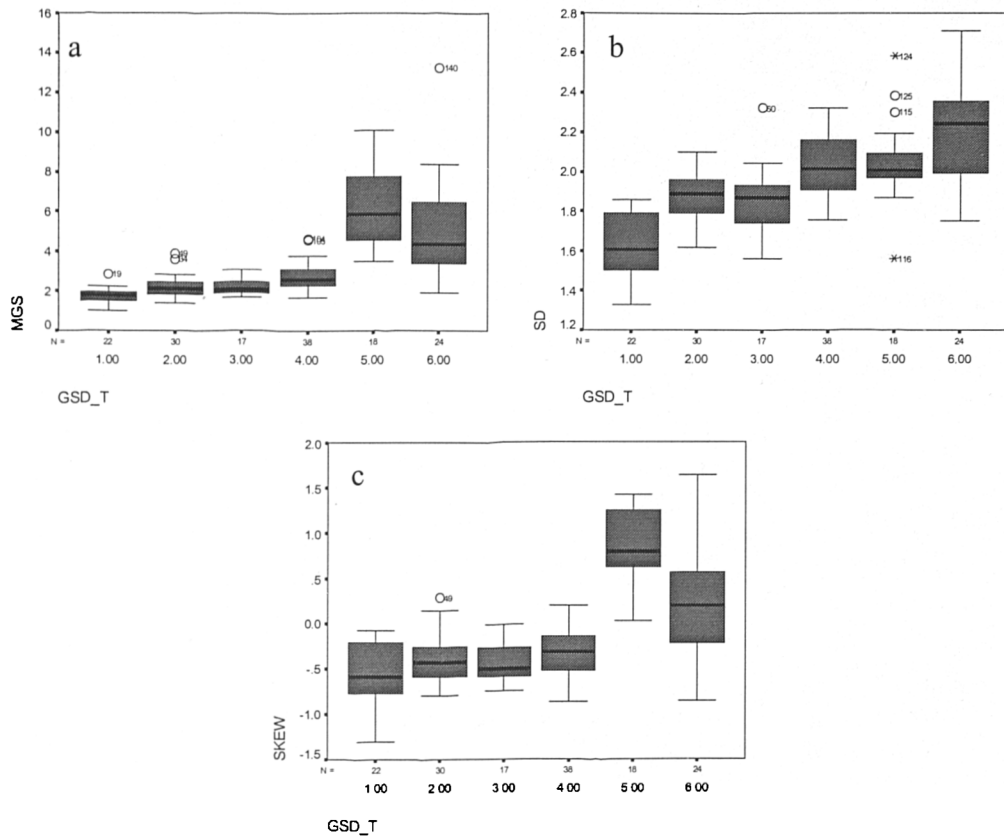


Figure 2.52. Boxplots for the moment statistics for the six mudstone GSD types proposed in this study showing: (a) mean grain size, (b) standard deviation, and (c) skewness.

The range of the derived Kranck model parameters for the floc components for each of the GSD types are shown in Figure 2.55. There is a high degree of overlap between the grain size types, with the exception of the Type 2 K value which has a much tighter distribution relative to the other grain size types (discussed in Section 2.4.2). Type six GSD's have a particularly wide range of Kranck parameter values for the floc component, reflecting the heterogeneous nature of this grouping (Section 2.4.6).

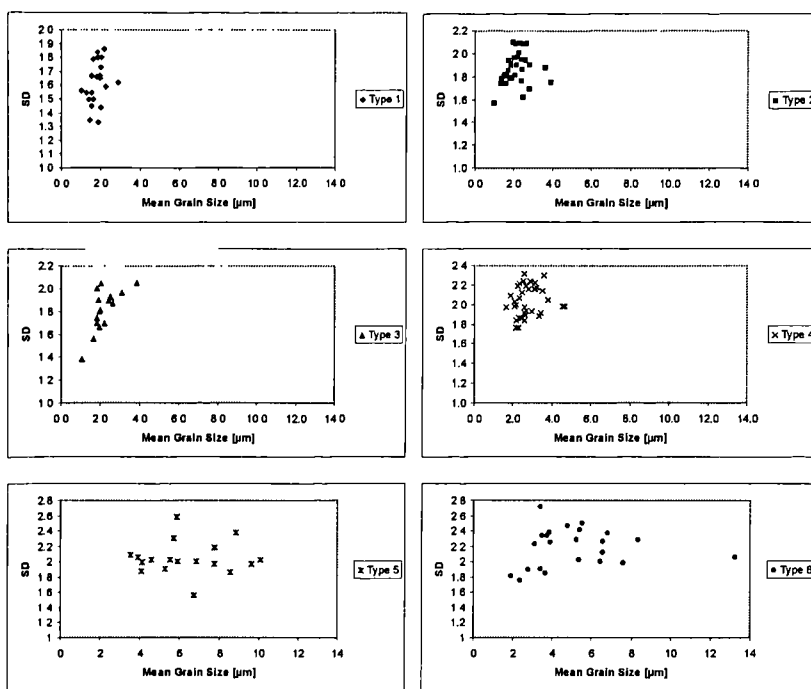


Figure 2.53. Mean grain size (μm) versus standard deviation for the 6 GSD types identified in this study.

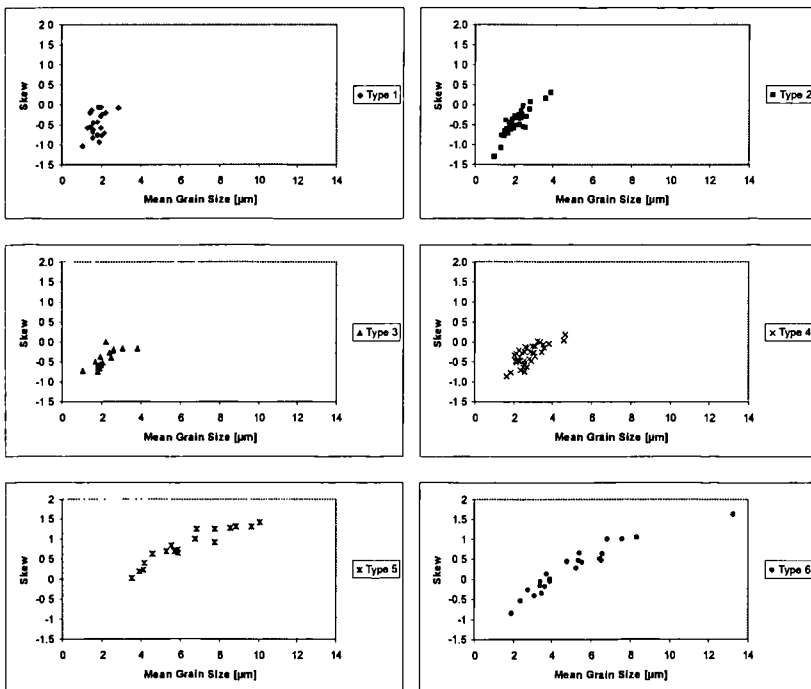


Figure 2.54. Mean grain size (μm) versus skewness for the 6 GSD types identified in this study.

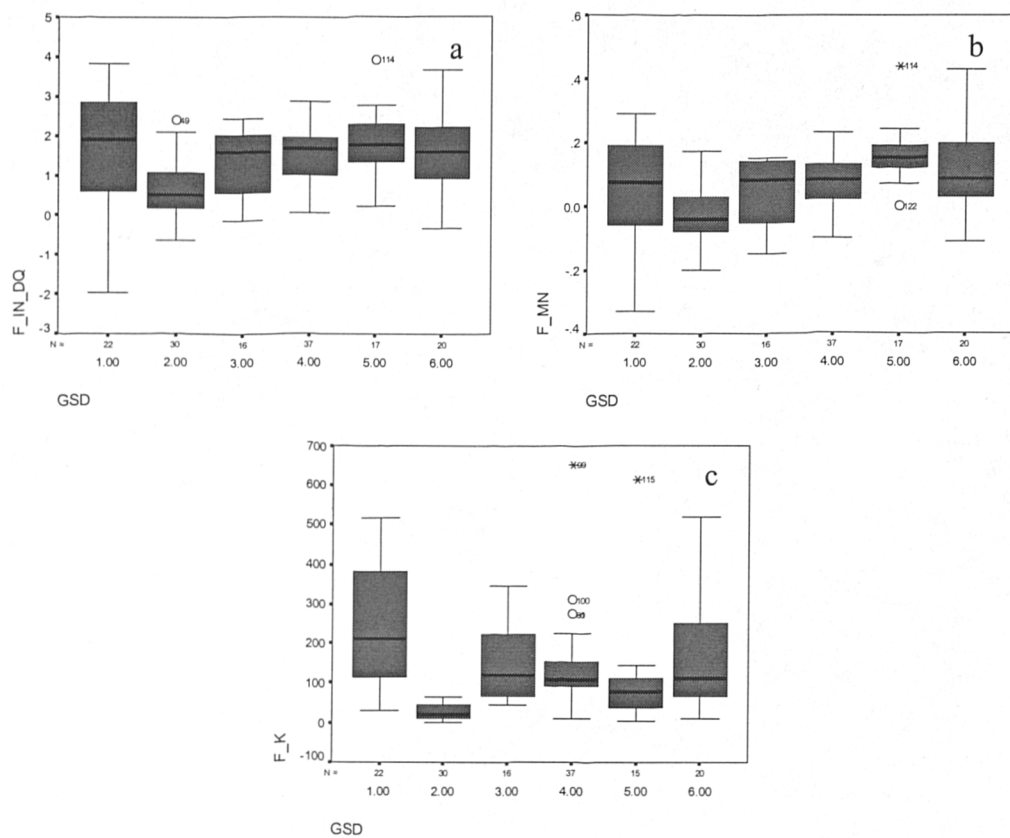


Figure 2.55. Boxplots for the Kranck model parameters obtained from fitting the model to the flocculated components of the grain size distribution for each respective ype: (a) In Delta Q, (b) $m+n$, and (c) K .

An explanation of the Kranck model terms is given briefly below: ΔQ is the concentration at a reference settling velocity. The variable m is hypothesized to be the slope of the source suspension. Material which plots as a straight line has been deposited in flocculated form from an unsorted source suspension; the exponent n has integer values of 0 for this proportion of the curve (Kranck *et al.*, 1996a; Milligan and Loring, 1997). For the portion of the curve that corresponds to 'Stokes' settled material, the integer n has a value of one, and values of >1 for the coarsest material (these terms are combined in the regression as m is effectively constant for a particular setting). The K parameter increases as the maximum and mean diameter of the suspension decreases (i.e. fines) due to settling, describing the maturity of the depositional process.

In terms of the K parameter there is a decrease both in terms of the mean and range of the K value from Type 1 to Type 5, if Type 2 and Type 6 are excluded. This is thought to represent the increasing turbulence and concentration from Type 1 to Type 5/6 involved in the formation of these deposits. A relationship between K and sediment concentration was inferred by Kranck and Milligan (1985). Sediment concentration and depositional energy (i.e. velocity gradient and turbulence) are interrelated and would vary as a function of depositional process and distance from point source. These factors are interrelated as turbulence may be damped by sediment concentration, particularly clay (cf. Baas and Best, 2002); essentially higher concentrations encourage floc growth while higher turbulence hinders and reduces floc growth producing a subtle interplay between these factors. The decrease of the K parameter from Type 3 to Type 6 is also seen for the non-cohesive silt component (Fig. 2.56), and again is thought to relate to the increasing ‘energy’ involved in the deposition of Type 3 to Type 6 GSD’s, albeit with a degree of overlap between the GSD types.

In conclusion, based purely upon the quantitative values of the derived Kranck model parameters for both the floc and non-cohesive silt components the grain size types, would be difficult to distinguish. In a similar fashion to the percentage parameters and the moment statistics the end members would be segregated on the basis of the Kranck model parameters, but some of the subtleties of the classification are likely to be missed. Implicit in fitting the model is the visualization of the grain size distribution which provides a clearer basis upon which to differentiate the grain size characteristics of mudstone samples.

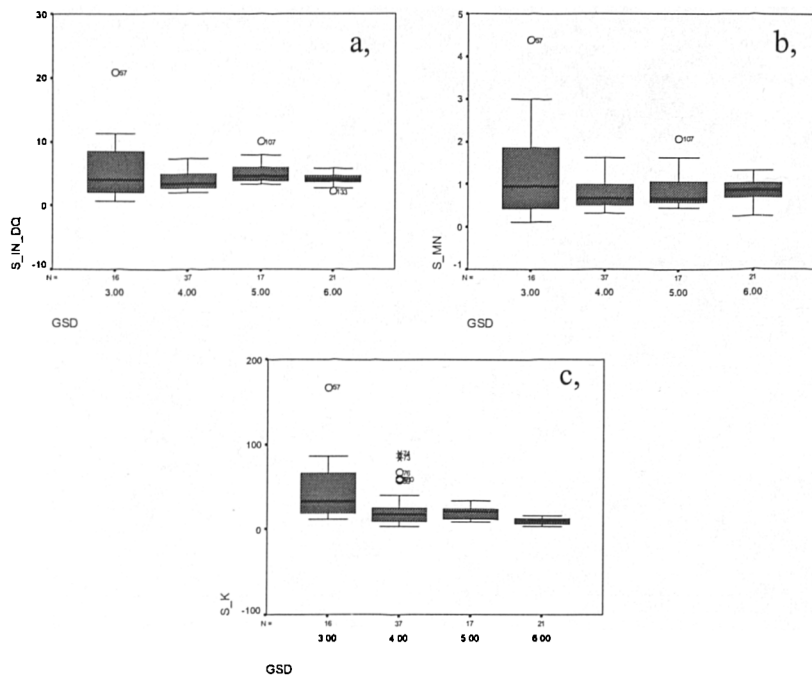


Figure 2.56. Boxplots for the Kranck model parameters obtained from fitting the model to the single grain settled components of the grain size distribution for each respective Type: (a) Delta Q, (b) $m+n$, and (c) K .

The mean and variation of the floc – non-cohesive silt intersection (D_f) for GSD types 3 – 6 is illustrated by the box plots in Figure 2.57. There is a high degree of overlap between the samples although there is subtle decrease in terms of the mean D_f from Type 3 to Type 5. The D_f value was not found to correlate well with any of the parameterization described above. The D_f value was also plotted as a function of location, no trends were apparent, but the mean values were all close to $10\mu\text{m}$ (cf. Section 2.1.1, Fig. 2.58). The largest number of samples were retrieved from the Iota Area, in order to isolate any potential regional effects, D_f was plotted as a function of grain size type for a Iota subset (Fig 2.59), illustrating that Type 3 samples have a very large spread and that there is a decrease in D_f from Type 3 to Type 6 (Fig. 2.59). The D_f parameter relates to the boundary at which particle behaviour switches between cohesive and non-cohesive and will therefore be a complex function of many parameters, possibly accounting for the wide range of values observed for grain size types 3 – 6.

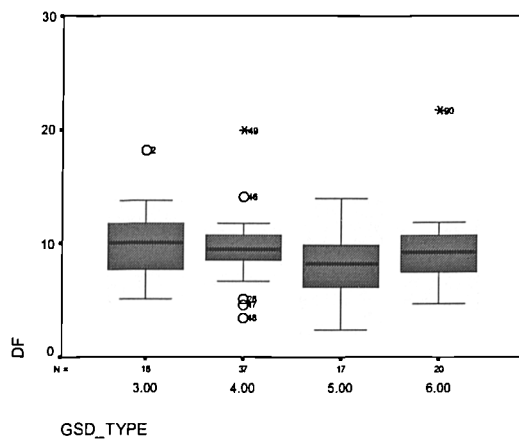


Figure 2.57. Floc – silt intersection [D_f] values (μm) for GSD types 3 – 6. Note the mean value is close to $10\mu\text{m}$ in agreement with McCave *et al.*’s (1995) suggestion that this value represents an approximate boundary between cohesive and non-cohesive behaviour.

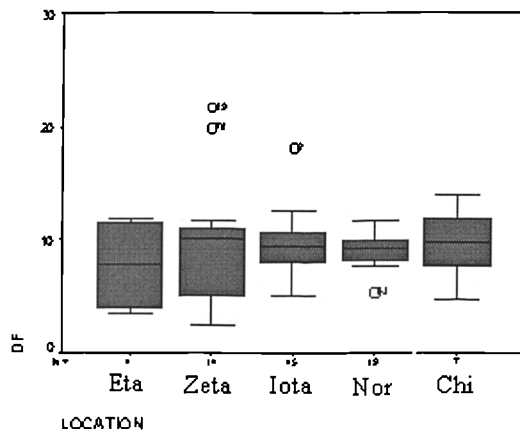


Figure 2.58. Floc – silt intersection [D_f] values (μm) for 5 locations represented in this study. Note the mean value is close to $10\mu\text{m}$, in agreement with McCave *et al.*’s (1995) suggestion that this value represents an approximate boundary between cohesive and non-cohesive behaviour.

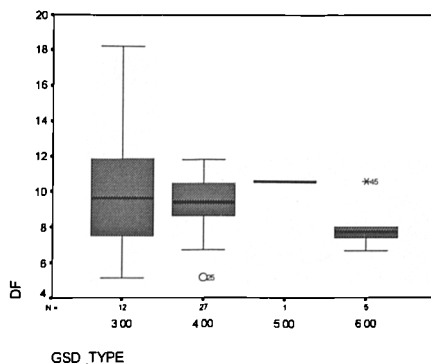


Figure 2.59. Floc – silt intersection $[D_n]$ values (μm) for Iota Area samples. For Types 3 and 4 the mean value is close to $10\mu\text{m}$, but there is a high variation. For Type 6 the mean floc-silt size is lower suggesting flocs were of smaller size. Refer to text for discussion.

2.5. Discussion

The consistency in the form of the grain size distribution reported for both the samples used in this study and those reported from the literature (Section 2.1.3) is remarkable and suggests that simplifying schemes for grouping ‘global’ grain size ‘types’ for mudstones is appropriate. The classification presented in the preceding sections provides a framework within which to place grain size analyses of mudstones. As for many geological classification systems (e.g. the Wentworth grain size scale) it places a somewhat artificial structure upon what is likely to be a natural continuum. The continuum is essentially a mixing of the cohesive and non-cohesive components of a sediment population which reflects depositional, chemical and sedimentary source factors. It is felt that this classification aids the process-based interpretation of mudstones and would enhance the understanding of depositional systems within a case study context. Furthermore, classifying mudstones into groupings based on grain size will aid the analysis of their corresponding physical properties, as grain size along with porosity (compaction state) is the principle control of important physical properties such as permeability (e.g. Yang and Aplin, 1998).

Previous studies which rely upon some quantitative measure of the grain size distribution such as Steven *et al.*’s (1996) moments statistic based study of the fine-grained sediments

of the Baltic Basin did reveal large general trends and identified some of the processes active in the various regions studied. However, that work was largely qualitative in nature and detailed interpretation of individual samples were not possible with the technique used. Flemming (2000) proposed a classification for gravel-free mudstones on the basis of ternary plots of sand-silt (<62.5 - 2 μ m)-clay(<2 μ m) (Figure 2.60).

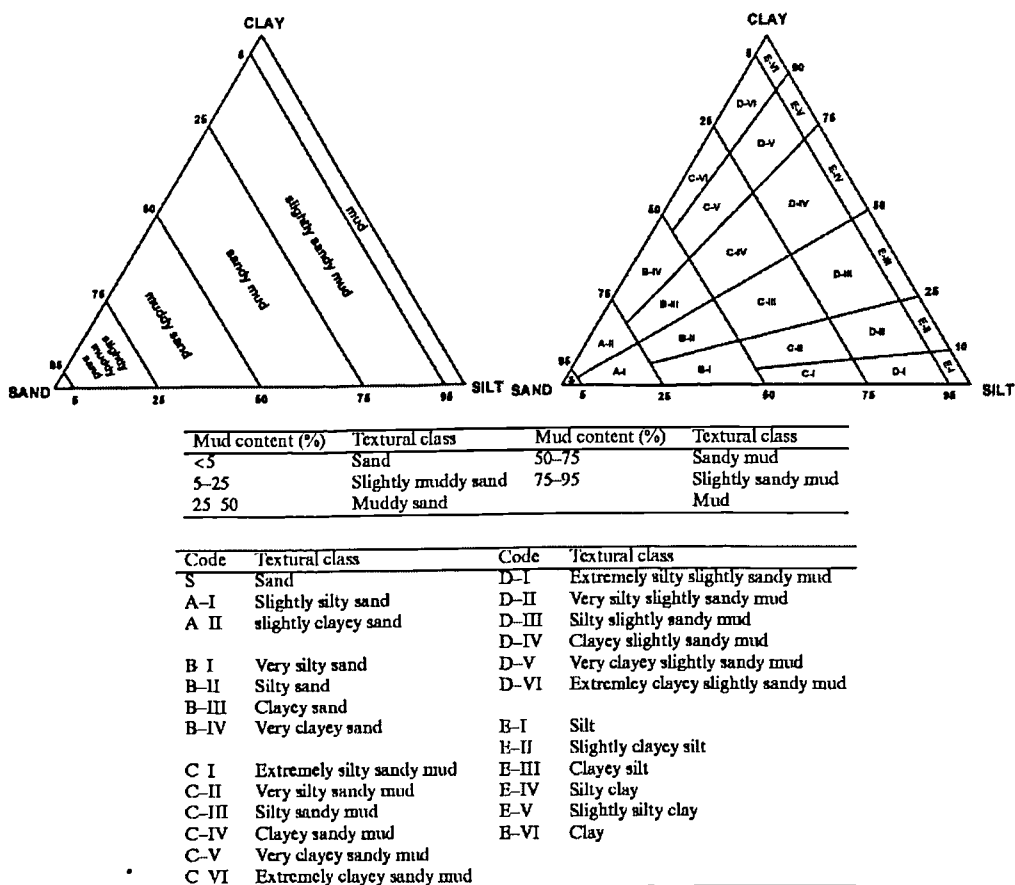


Figure 2.60. Ternary diagrams, percentage boundary table and letter-number code table of the 'hydrodynamic', sand/silt/ratio based classification scheme of Flemming (2000).

Ternary plot based classification have been proposed for various sediment types since the 1950's (Flemming 2000 and refs. therein). Essentially there are an almost infinite number of ways of dividing up a ternary plot and one method is unlikely to have any more value in a process sense than any other. Despite the antiquity of the method Flemming's (2000) aim of harmonizing the various classification schemes proposed is valid. Flemming (2000)

presents a series of examples from inter-tidal and shelf environments which illustrate a progressive fining corresponding to a decrease in depositional energy; two shelf examples are given in Figure 2.61. The two different locations are clearly differentiated although with a high degree of scatter. By plotting the sand-silt-clay components on ternary graphs the implicit assumption is made that these three components have unique hydrodynamic behaviours; however, as proposed by McCave *et al.*, (1995), the boundary between cohesive and non-cohesive behaviours falls at approximately $10\mu\text{m}$; thus, if to be useful in a process sense such plots should honour this boundary. It is likely that the trends identified on conventional ternary plots illustrating the progressive hydrodynamic sorting would not differ greatly if they were plotted as sand – sortable silt – clay but this would be an improvement and may reveal subtle trends potentially masked by the conventional method. It is felt that the separating sand and ‘sortable silt’ components is valid as sand predominantly travels as bed-load while silt is transported largely in suspension.

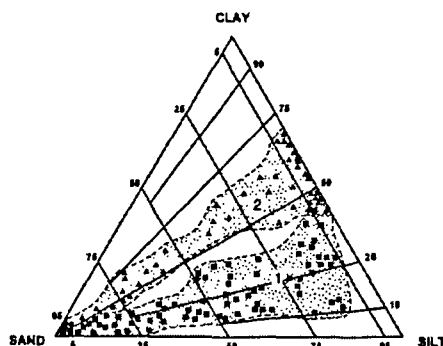


Figure 2.61. Ternary diagram illustrating textural trends identified in open shelf environments. Band 1. Bering Shelf. Band 2. Central Gulf of Alaska Shelf. From Flemming (2000).

When classifications of mudstones are adhoc and performed within the confines of isolated datasets (e.g. Schieber, 1999) the generic implications, if any, of any individual study are difficult to elucidate. A generic classification scheme was proposed by Macquaker and Adams (2003). However, this work was entirely focused on investigations of mudstones using microscopy (optical and SEM) with no reference made to grain size data. This omission is significant as grain size is a fundamental control upon control on flow dynamics, particle behaviour and hence sedimentation. Because considerable information

can be extracted from both optical/SEM studies and grain size studies an integrated approach offers the way forward in the sedimentological analysis of mudstones. An example would be a Type 1 calcareous, nannoplankton-bearing, clay-rich mudstone; this description conveys that the sediment is clay rich (in the size sense) and was deposited in an entirely flocculated form in a low energy, low sediment concentration setting along-side calcium carbonate formation in waters that were rich in plankton. The addition of terms relating to the fabric of the sediment, such as ‘bioturbated’ increases the detail of the description.

From the analysis described in Sections 2.4.1 – 2.4.7 it is clear that the majority of thin sections analysed, particularly for GSD Types 1 – 4, exhibited structureless textures. A number of examples of structureless mudstones from a range of marine environments are presented by O’Brien and Slatt (1990), including:

- (a) The argillaceous units of the Ferron Sandstone Member, Mancos Formation (Cretaceous) representing a marine shelf proximal to a delta complex (O’Brien and Slatt, 1990, pp.78 – 80, Fig. A2).
- (b) The mudstones of the Cozy Dell Formation (Mid. Eocene) representing a submarine slope facies (O’Brien and Slatt, 1990, pp.82 – 83, Fig. A).
- (c) The Pico Formation (Pliocene) representing a deep marine turbidite facies (O’Brien and Slatt, 1990, pp.86 – 87, Fig. C).

The absence of sedimentary structures is generally thought to indicate rapid deposition (e.g. O’Brien and Slatt, 1990) and is the preferred explanation for the samples presented in Sections 2.4.2 – 2.4.4. In the case of Type 1 the lack of structure coupled with the high occurrence of microfossils may indicate slow sedimentation rates and/or thorough bioturbation.

The observation that many of the samples analysed here, and particularly those for Types 1 – 4 lack any distinctive sedimentary structures contrasts with some previous studies of mudstone thin sections (e.g. Schieber, 1999). However slide orientation could potentially play a role; all the thin sections were made from plug or side-wall core samples – and thus should have been made approximately perpendicular to bedding. If thin sections were in

fact made approximately parallel to bedding then the sample may appear much more homogeneous than it actually appears. Types 5 and 6, when not recovered from deep water settings, had a much higher occurrence of sedimentary structures. A number of possibilities may account for this. The slides, particularly the magnified (x4 PPL) thin section image's were typically 2 – 3mm wide whereas Schieber's (1999) sections were typically between 6 – 40mm wide, therefore sedimentary structures may simply not be easily discernable at this scale. It may also simply reflect the nature of the tectonic setting from which the respective sample sets were retrieved. For example, the Iota Area samples commonly used as the exemplar for Types 1 – 4 probably have been deposited rapidly via gravity driven re-sedimentation processes. In contrast, the epicontinental shelf samples from the North Sea and Chi Area used here, along with those of Schieber (1999) would have been deposited in significantly shallower water, with potentially much slower sedimentation rates (thus allowing a greater influence of current, wave and storm associated processes).

The choice of grain size parameterization applied will depend upon the goal of the study being carried out (cf. Curran *et al.*, 2004). This study has illustrated that no one parameterization technique was able to fully account for the GSD types proposed here; visualisation of the grain size frequency distribution along with observation made from thin section and BSEM images were found to be most useful in partitioning the grain size types. But neither of these techniques are quantitative. Combining these techniques with quantitative descriptions has provided the basis for establishing these GSD types; however, further work is required before quantitative grain size parameterization techniques can be linked to specific depositional processes and their hydrodynamic characteristics.

As floc size increases the size spectrum of incorporated grains increases (Kranck, 1991), therefore as floc size increases there is concomitant increase in the size of the particles incorporated into the flocs. Both the floc size and disaggregated grain size vary with total concentration, suggesting that flocs are relatively stable entities which do not change during alternating settling and re-suspension (Kranck and Milligan, 1992). The wide variation in the floc – non-cohesive silt intersection or 'floc limit' (D_f) seen for Types 3 – 6

may relate to the differing hydrodynamic conditions under which the sediment was deposited; floc size [and hence the size of the material incorporated into the floc] increases initially with G , the root mean square velocity gradient and then decreases (Fig. 2.62; Berhane *et al.*, 1997; van Leussen, 1988). Whereas floc size continuously increases with suspended sediment concentration that acts to dampen turbulence and hence velocity gradient (cf. Baas and Best, 2002), floc size is not uniquely related to G , but the % of material $> D_f$ is and thus may be used to infer palaeo-hydrodynamic conditions. However more detailed work is required to investigate further the potential for extracting palaeo-hydrodynamic information from the grain size distributions of mudstones. Fully constrained and quantified laboratory flume based studies are likely to yield the best results in terms of elucidating the potential relationships suggested here.

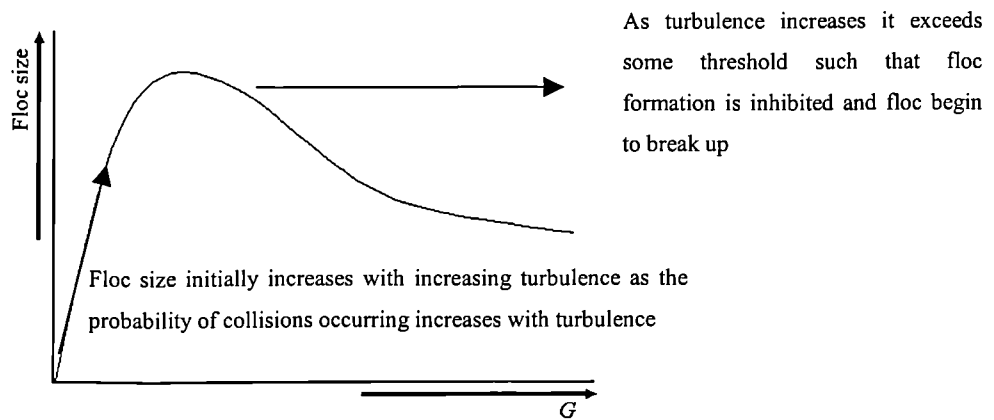


Figure 2.62. Effect of turbulence on floc size; G is the root mean square velocity gradient. (Berhane *et al.*, 1997; van Leussen, 1988).

The value of the insights provided by combining grain size analysis with petrographic and BSEM based observations lie in interpreting whether or not the floc, silt and possibly sand modes recognised from analysis of the grain size distribution relate to a specific depositional event or a series of events. Furthermore, understanding of the fabric of a rock and knowledge of the nature of its grain size distribution greatly enhances the interpretation of omni-directional MICP experiments carried out on the same samples. For example, how you would account for the presence of a bi-modal pore size distribution would be dependent upon the texture of the sample – it may relate to two domains of

effective porosity (i.e. in the case of a homogenous rock with a bi-modal grain size distribution) or may simply relate to a laminated sediment.

On a larger scale previous classifications for sediments have compiled data on modern and ancient rocks and have integrated this data into facies types representing differing processes which fit into a series of hypothetical sedimentary models, a good example of such a classification system is that proposed by Pickering *et al.*, (1986) for deep water sediments (Figure 2.63). The classification scheme presented in this study integrates with the scheme of Pickering *et al.*, (1986) with the individual grain size types proposed, potentially supplemented by Macquaker and Adam's (2003) descriptive scheme, building into facies which make up Pickering *et al.*, 's (1986) class C, D, E and F (cf. Figure 2.63).

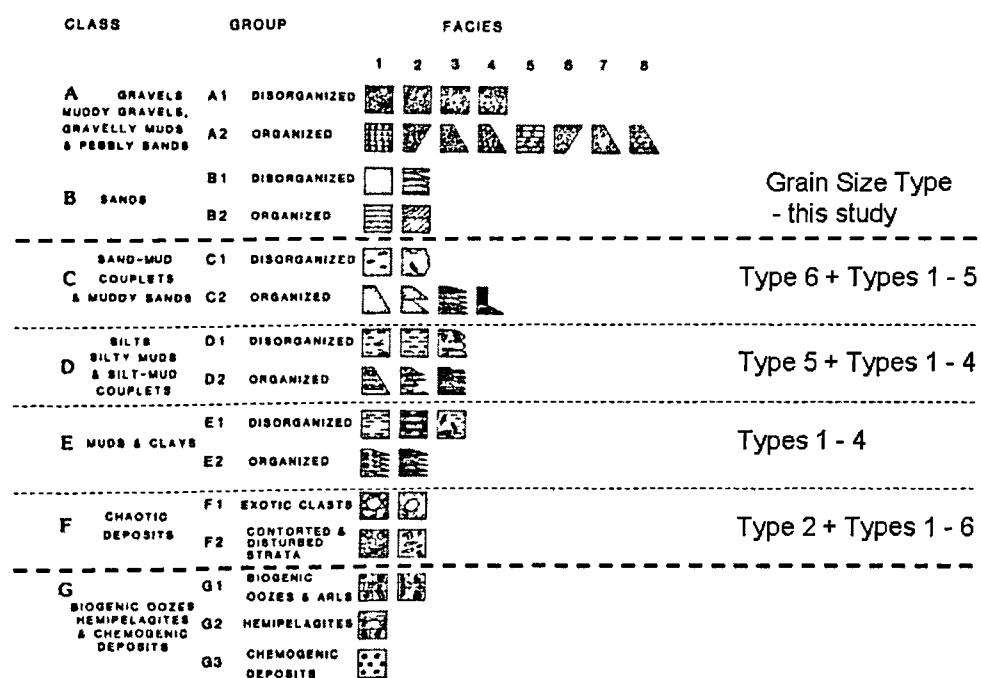


Figure 2.63. Integration of the deep-water facies classification scheme of Pickering *et al.*, (1986) with the mudstone GSD types proposed in this study. The hierarchical nature of the scheme is related to facies class (of Grain size Classes A – G only C to F are relevant here), internal organisation, and composition. Individual facies are based on internal structures, bed thicknesses, composition and potentially GSD type, as proposed in this study.

2.6. Chapter 2 Conclusions

The work presented here proposes a new grain size based siliciclastic mudstone classification system. Six separate mudstone grain size types have been proposed, based on work which for the first time integrates: (a) the process based grain size based model of Kranck (e.g. Kranck and Milligan, 1985), (b) observations made from both petrographic and BSEM images, and (c) numerical grain size based descriptions. The process based model of Kranck has been used to infer both the mode of settling (flocs or Stokes settled single grains) and thus the nature of the particle packing. The classification system proposed is probably non-exhaustive; however, it is felt that most of the potential variation which siliciclastic mudstones may exhibit has been captured. The boundaries between the types are not rigid and the typing scheme and framework could be adapted to suit the goals of a particular study.

The numerical descriptions utilised had limited success in differentiating and providing information on the nature and depositional character the sediment. The % sortable silt did show the best correspondence to the GSD types proposed; but this parameter provided no information on the process of deposition or the particle packing (i.e. floc or single grain deposited). The approximate boundary at $10\mu\text{m}$ between cohesive and non-cohesive behaviours proposed by McCave *et al.*, (1995) was found to be an appropriate rule of thumb, but not as an absolute value as D_f was seen to vary between $3\mu\text{m}$ and $21\mu\text{m}$. This variation could potentially be exploited in order to infer the conditions present in the water column at the time of deposition; this hypothesis awaits verification. Material $>10\mu\text{m}$ was incorporated into flocs based on the analysis of Type 2 samples; this material will clearly not relate to hydrodynamic conditions as it will not have been hydrodynamically sorted, thus care should be taken when attempting to apply ‘sortable silt’ as a palaeocurrent measure, particularly in locations where high suspended sediment concentrations are likely.

The moment statistics had a high degree of overlap, particularly for Types 1 – 4. The combination of the mean grain size, standard deviation and skewness did give a relative

idea of the potential degree of mixing between flocculated and single grain settled populations but only to the degree that the end member samples could be separated. The moment statistic provided no information upon the potential particle packing. The Kranck model parameters also showed a high degree of overlap; however, the fitting processes and plotting the log-log grain size spectra allows the recognition of the floc and non-cohesive silt components which ultimately forms the basis of the grain size typing framework proposed here. Furthermore, there is the potential of correlating the Kranck model parameters, particularly K and D_f , with the hydrodynamic, chemical and concentration conditions present at time of deposition.

Analysis using a hindered settling rate suggests that Type 2 grain size distributions are deposited from high sediment concentration thus potentially allowing the sediment concentration in at least part of the water column at time of deposition to be estimated for the first time. This work would potentially allow turbidites and debris flows to be differentiated. Further work concerning the interplay between hydrodynamic conditions and concentration and the resulting grain size spectra could substantially increase the information extracted from the analysis of mudstone grain size distributions.

This classification scheme should not be seen as a rival to other sediment classification schemes, such as the descriptive scheme of Macquaker and Adams (2003) and that proposed for deep water sediments by Pickering *et al.*, (1986). Integration of these three schemes could potentially significantly improve the process-based sedimentological interpretation of continuous records of sedimentary deposits by providing both a process-based and temporal record of sedimentation. Indeed it is felt that such a generic, process-based, descriptive analysis of mudstones will provide the level of detail that will allow mudstones to be elevated to a level of understanding comparable to that currently enjoyed by sandstones and carbonates.

Chapter 3 Integrating detailed grain size distributions with the characteristics of natural mudstone pore-throat size distributions at varying compaction states

3.0 Introduction

The lithological inventory of sedimentary basins is dominated by mudstones which commonly comprise at least 60% of basin fill. Due to their volumetric significance muds and mudstones are the primary control upon fluid flow in sedimentary basins (cf. Aplin, Fleet and Macquaker, 1999). The flow properties mudstones have been shown to be principally controlled by two variables: porosity (which ranges between ~80 – 5%) and grain size (with particle diameters potentially ranging over 5 orders of magnitude) (Dewhurst *et al.*, 1998; Yang and Aplin, 1998; Dewhurst *et al.*, 1999a,b). Despite the importance of constraining the flow properties of mudstones there have been relatively few integrated studies of the porosity, grain size distribution and pore-throat size distributions of mudstones. In the previous Chapter six clastic mudstone lithologies or grain size types were proposed, this classification is thought to capture the bulk of potential variation in terms of grain size for clastic mudstones.

This work describes a detailed study of the influence of grain size ‘type’ reflecting the nature of the entire grain size distribution upon the dynamic evolution of the pore-throat size distribution of mudstone samples taken from five different sedimentary basins. Detailed grain size analysis of numerous marine mudstones (e.g. Kranck, 1984; Kranck and Milligan, 1985; Stevens *et al.*, 1996; Jones and McCave, 1998; and this work, see Chapter 1) have demonstrated that the grain size distributions of such sediments are composed of (a) flocs and (b) a ‘stokes settled’ silt and sand component (see Chapter 1). The aim of this study is to investigate the influence of these components upon the nature and distribution of the lacunar and clay-fabric pore space with decreasing porosity from a variety of mudstones from five sedimentary basins, analysed using the mercury injection capillary pressure (MICP) technique.

Previous work pertinent to this study has largely been carried out by soil scientists, for example, Fiés (1992) investigated the influence of sand and silt phases (termed skeleton) in the division of textural porosity which he divided into lacunar pore space and clay-fabric pore space. This and further work by Fiés and Bruand (1998) showed that in clay/silt/sand mixtures with increasing clay content, the inter-connected lacunar pores were decreasing in volume and modal size, but continued to exist as 'hidden' pores (not connected or at least connected by smaller clay fabric pores). In their paper Fiés and Bruand (1998) stated that it is the packing of the elementary particles (i.e. clay-silt or clay-silt-sand) in soil that largely determines the textural pore space and its dependent properties such as permeability. Griffiths and Joshi (1989) investigated the microlevel scale compaction of clays using mercury intrusion porosimetry (MIP).

In studies of geological data Dewhurst *et al.*, (1998, 1999a) investigated the London Clay and performed a detailed study of the influence of lithology, simplistically described by clay content (% of particles $<2\mu\text{m}$) on the loss of porosity and permeability during artificial mechanical compaction.

3.1 Previous studies of the integration of grain size and pore size data

3.1.2 Artificial slurries

Fiés and Bruand (1990) and Fiés (1992) investigated the relationship between the grain size distribution and the distribution of porosity as a function of pore-throat size in soils. In soil science the porosity formed due to the packing of the particles which make up the sediment is termed *textural porosity* (Childs, 1969 p.94). In these studies the bulk textural porosity is divided between *clay-fabric pore space* and *lacunar pore space* (Fiés, 1992 and refs. therein); clay fabric pore space relates to that formed by clay-particle packing, lacunar (simply meaning gap) pore space relates to that formed by silt and/or sand grains (termed skeleton by Fiés, 1992). Earlier work had established that this distinction between lacunar and clay-pore space was valid for soils (e.g. Fiés, 1984); Fiés (1992) noted that as the size and / or proportion of the silt/sand framework decreases, the peak

corresponding to the lacunar porosity approaches the clay-fabric peak, suggesting that as the modal size of the silt/sand framework decreases the lacunar and clay-fabric porosity distributions may merge. To test this hypothesis Fiés (1992) mixed sediments composed of between 5-90% clay (particles $<2\mu\text{m}$) with silt components with modal sizes of $4\mu\text{m}$ (2-10 μm range), $6\mu\text{m}$ (2-20 μm range), $13\mu\text{m}$ (2-20 μm range), $20\mu\text{m}$ (20-50 μm range), and glass beads of $400\mu\text{m}$ (400-430 μm range); once dried these mixtures were analyzed using Hg porosimetry. Although Fiés (1992) provides no information on bulk porosity, the synthetic samples formed by initially wet slurries are likely to be of high porosity.

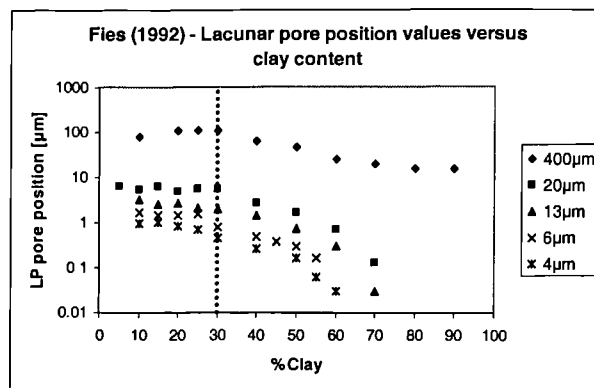


Figure 3.1. Lacunar pore (LP) mode obtained from a volume pore density distribution (VPD) curve as a function of clay content for different sized silt components; for the sand size material LP mode virtually remains constant irrespective of clay content; however for the silt clay mixtures, once clay contents exceed 30%, the LP begins to be influenced by the clay sized particles, resulting in the LP reducing as a function of clay content.

Fiés (1992) results showed that for the glass bead – clay mixtures the volumetric pore density curves (VPD) were always bi-modal irrespective of clay content, where the modes represent the clay fabric related pores (SP) and the lacunar pores (LP) related to the bead framework. For the silt – clay mixtures the VPD curves became unimodal when clay content exceeded 60%. The size of the LP is dependent upon the size of the silt component at a single clay content. At clay contents $<30\%$ the diameter of the modal size of the LP peak remains constant for each respective silt component size (see

Fig. 3.1); however when the clay content exceeds 30% the LP peak decreases as a function of increasing clay content (see Fig. 3.1 and Fig. 3.2).

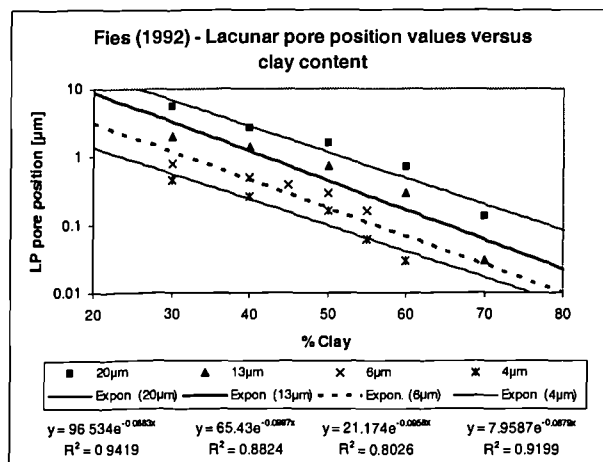


Figure 3.2. Lacunar pore (LP) mode obtained from a VPD curve as a function of clay content for different sized silt components; LP modal values are constant for clay contents <30% and decrease exponentially with increasing clay content at clay contents >30%.

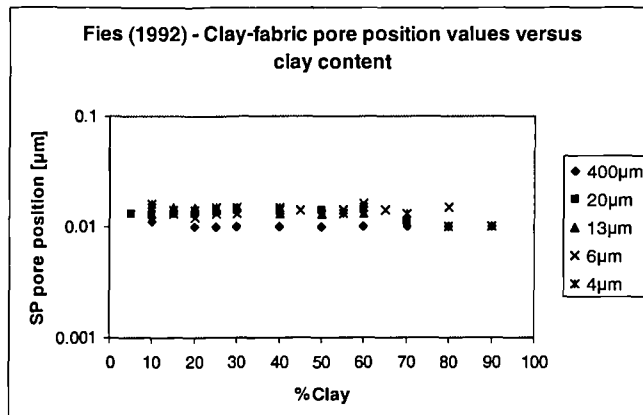


Figure 3.3. Clay fabric (SP) pore mode obtained from a VPD curve as a function of clay content for different sized silt components; SP virtually remains constant irrespective of silt component distribution or clay content.

From Figure 3.4 it can be seen that as the clay content increases the distance between the lacunar pore peak and clay-fabric peaks reduces, and at high clay contents the distribution

becomes unimodal (Fiés, 1992). From his experimental results, Fiés made the following observations:

- 1) The modal pore diameter corresponding to the clay fabric pores remains constant for both the clay-sand and clay-silt mixtures – irrespective of clay content (see fig. 3.3).
- 2) There is a highly significant linear correlation between the volume of the small pores and clay content for the clay-sand mixture; whereas such a relationship only exists for the clay-silt mixtures when clay contents are <40%. The volume of small pores (V_{SP}) was calculated by $V_{SP} = V_T - V_{0.05}$ where V_T equals total pore volume and $V_{0.05}$ equals pore volume down to $0.05\mu\text{m}$, thus V_{SP} is equal to volume intruded between $0.05\mu\text{m}$ and $0\mu\text{m}$ theoretically; the value of $0.05\mu\text{m}$ was taken from earlier work by Fiés(1984)on the MICP analysis of clays.

These observations led Fiés (1992) to claim that for the clay-sand mixture, V_{SP} solely represents intrusion into the clay-fabric, with the sand framework being wholly distinct. For the clay-silt mixtures the V_{SP} values increase as the modal size of the silt component decreases; V_{SP} remains parallel to the clay-fabric V_{SP} line (determined from the clay-sand mixture for clay contents <40% (Fiés, 1992) indicating that for these clay contents the lacunar and clay-fabric components are distinct. When clay contents exceed 40% V_{SP} values move away (i.e. increase in value) from the V_{SP} determined entirely from clay-fabric pores (see Figure 3.5), indicating that the V_{SP} cannot be solely attributed to the pores formed by the clay-fabric. This suggests that the lacunar pore and clay-fabric pore populations begin to merge and interact at clay contents >40% in these high porosity mixtures. Despite this merger of the two textural porosity domains, the diameter of clay fabric modal pore-throat size seemingly remains constant, implying that the amalgamation of the two domains does not act in any to increase the size distribution of the clay fabric pore space.

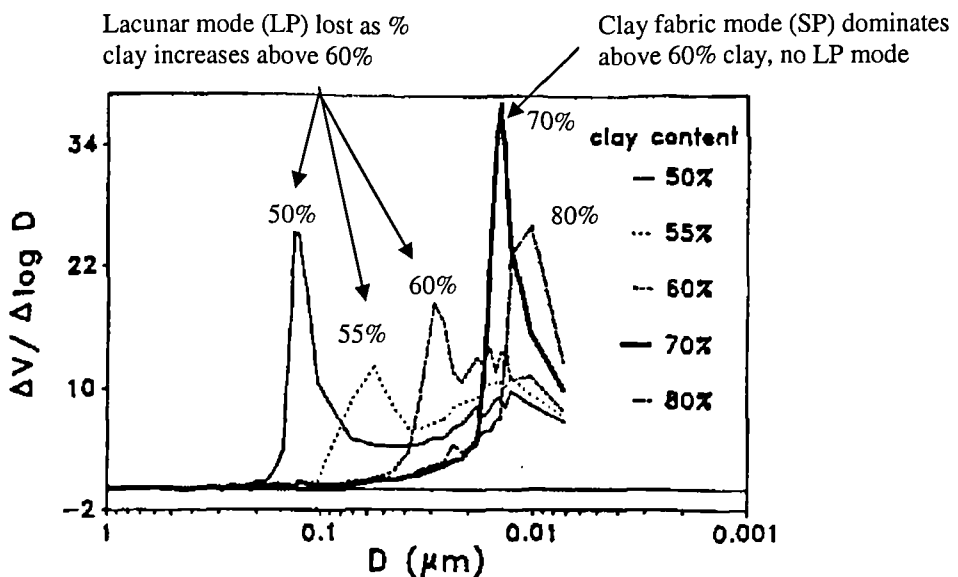


Figure 3.4. Evolution from a bimodal to unimodal pore density distribution curve (VPD) obtained with clay-silt mixtures (4 μm) when clay contents exceed 50% (From Fiés, 1992. Fig. 3).

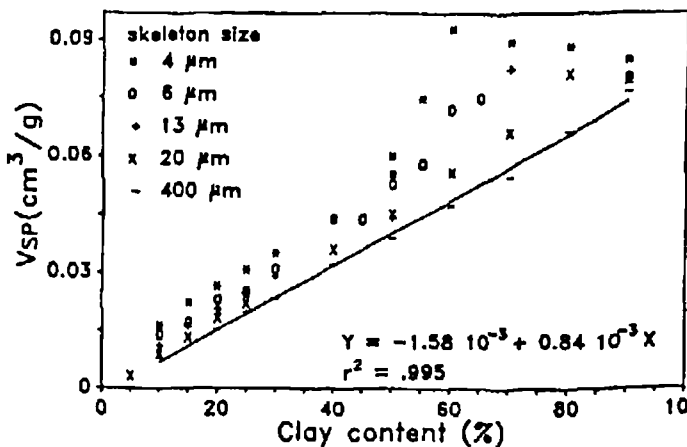


Figure 3.5. Effect of the sand / silt framework upon the relationship between V_{SP} (volume intruded into pores of diameter $\leq 0.05\mu\text{m}$) and clay content of the clay-sand / silt mixtures. The regression line represents the correlation between V_{SP} and clay content obtained for the glass bead (400 μm) – clay mixtures, the highly significant regression coupled with the observation that the position of the V_{SP} modal diameter was constant led Fiés(1992) to the conclusion that the V_{SP} measured on the clay-bead mixtures represents intrusion purely into clay fabric pore space – thus departures from this line indicates interaction of the V_{SP} and V_{LP} domains.

3.1.2 Soils and soil compaction

Griffiths and Joshi (1989) investigated the microlevel scale compression of clays using mercury intrusion porosimetry (MIP). Four differing soils were investigated using this technique; two intrusions were performed on each sample tested. It was proposed by Griffiths and Joshi (1989) that two types of porosity can be determined from two successive intrusion cycles; the first intrusion fills all of the connected pore space, thus giving total ('effective') porosity. The sample is then depressurized which leaves a proportion of mercury trapped within the pore space. A second pressure cycle re-intrudes mercury and is thought to define the pore-throat size distribution of the free porosity and the difference between the two cycles is the 'entrapped porosity' (Griffiths and Joshi, 1989). It has been suggested that the free porosity corresponds to intra-aggregate pores and that the entrapped porosity relates to inter-aggregate pores (Delage and Lefebvre, 1984).

Four standard consolidation tests were performed to a maximum stress of 0.03, 0.12, 0.45 and 1.5MPa. The inter-aggregate or 'free porosity' was estimated by the normalised first minus second intrusion data (see Griffiths and Joshi, 1989). The results suggested that consolidation processes affects only the inter-aggregate pores. The intra-aggregate pores remained near 100% of the liquid limit porosity (i.e. the initial porosity measured prior to compaction), while the inter-aggregate porosity (as measured by the difference between the first and second intrusion runs) was related directly to the consolidation stress (Griffiths and Joshi, 1989). From their results Griffiths and Joshi (1989) concluded that the volume decrease of pore space during consolidation was due to changes in the volumes of the largest existing pores, where this change is represented by a shift towards smaller pore-throat sizes and a reduction in total porosity. Intra-aggregate pore space was not seen to change with increasing consolidation (although note low stresses), no evidence for aggregate formation due to consolidation was found. Volume change was found to be due to deformation and collapse of the inter-aggregate pore space (Griffiths and Joshi 1989).

In a reply to the work by Griffiths and Joshi (1989), Nagaraj *et al.*, (1990) proposed a hypothesis in which the pore space of fine grained sediments could be partitioned into three levels or types:

- 1) Intra-floc (\approx aggregate) pores between individual platelets in a floc with pore radii $<1\text{nm}$ (10\AA).
- 2) Inter-floc pores between two interacting aggregates with radii $<10\text{nm}$ and $>1\text{nm}$ ($<100\text{\AA} - 10\text{\AA}$) depending upon compaction state.
- 3) Large enclosed pores between multiple aggregates and/silt grains, with radii $>>10\text{nm}$ ($>>100\text{\AA}$).

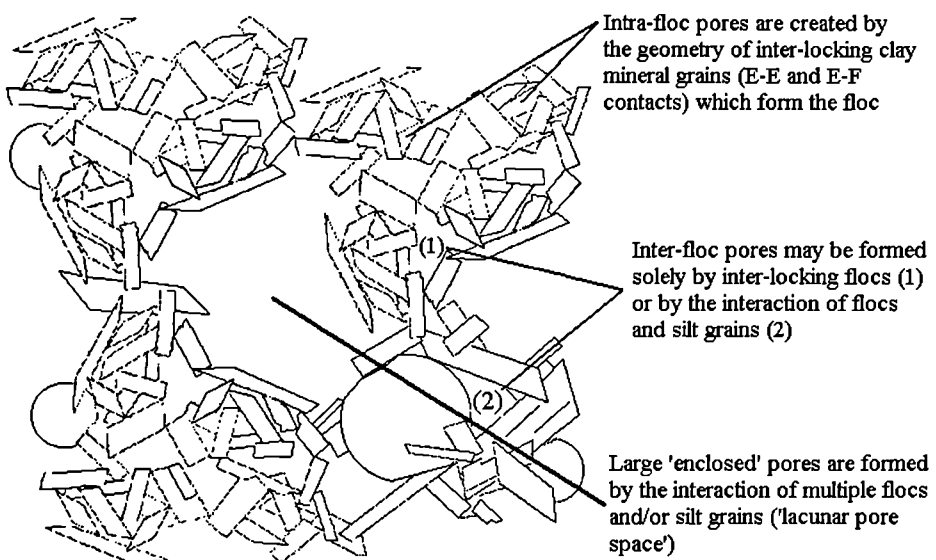


Figure 3.6. Schematic representation of a flocculated fine grained sediment illustrating the nature of the different pore types or levels formed (Adapted from Nagaraj, *et al.*, (1990) Fig. 10) (E-E: edge – edge clay mineral contacts; E-F: edge – face clay mineral contacts).

Nagaraj *et al.*, (1990) argue that the reason behind Griffiths and Joshi's (1989) observation that compaction driven deformation and loss of the pore volume is concentrated in the large pores (2 and 3 above) because that their size is dictated by the surrounding force system (i.e. the applied load), while the intra-floc pores are better able to resist the load because they are formed by fewer particles (cf. Dewhurst *et al.*, 1998, 1999a) and are directly influenced by clay-surface interactions (cf. Nagaraj *et al.*, 1990).

Furthermore at the initial state any load will be focused upon the point contacts which form the largest pores (3) as compaction proceeds the load will be supported by more and more point contacts thus even though applied load is increasing over all the surface area upon which it is applied is also increasing. In conclusion Nagaraj *et al.*, (1990) state that in a more compressible soil, and thus a finer grained soil (cf. Skempton, 1970; Burland, 1990; Aplin *et al.*, 1995) the preferential collapse of the largest pores will be enhanced relative to a less compressible (coarser grained) sediments resulting in a smaller, tighter, better sorted pore throat size distribution with increasing compaction.

3.1.3 Geological materials

In a series of investigations Dewhurst *et al.*, (1998, 1999a) explored the inter-relationship between grain size distribution, porosity and the nature of the pore-throat size distribution. Their data, along with data drawn from both the geotechnical and geological literature illustrate how the pore-throat size distributions of mudstones evolve with increasing compaction. The mean pore throat radius of muds declines with increasing effective stress, with this decrease being primarily driven by the collapse of the largest pores, with the smaller pores remaining relatively unchanged (e.g. Dewhurst *et al.*, 1998). These effects were clearly illustrated by the experimental results of Dewhurst *et al.*,’s investigation of two London Clay samples with distinct grain size distributions (see Figure 3.7). From Figure 3.7 it can be seen how pores with larger pore throats collapse preferentially; this effect is enhanced in the coarser sample which incorporates larger pore throat sizes and a larger overall range of pore throat sizes. The investigation carried out by Dewhurst *et al.*, (1998) showed that at a given porosity (or effective stress), coarser grained mudstones will have greater mean and modal pore throat sizes than finer grained mudstones. Samples classified as clay rich (i.e. clay fraction >50%) have very few pore throats >100nm even at stresses as low as 1.5 MPa, implying that larger pores in these sample types are very unstable and readily collapse under very small loads. In the coarser mudstones the larger pores also preferentially collapse, but do so under much greater loads (cf. Fig. 3.7b) relative to the finer mudstones, implying that they are more stable (Dewhurst *et al.*, 1998, 1999a). The relevance of the observations made by

Dewhurst *et al.*, (1998) for naturally compacted mudstones was confirmed by Yang and Aplin (1998) who studied mudstones which had been naturally compacted to effective stresses between 7.2 and 27.5MPa.

The work carried out by Dewhurst *et al.*, (1999a) utilizing artificially compacted samples of the London Clay illustrated the fundamental influence of clay fraction on the pore throat size distribution, compressibility, surface area and porosity-hydraulic conductivity relationship for these sediments. The data presented by Dewhurst *et al.*, (1999a) was placed into two broad groups of rather distinct properties: a clay-rich group (49% to 66% clay fraction) and a silt/sand-rich group (27% to 33% clay fraction) (both of which contained ~50% sand sized material!).

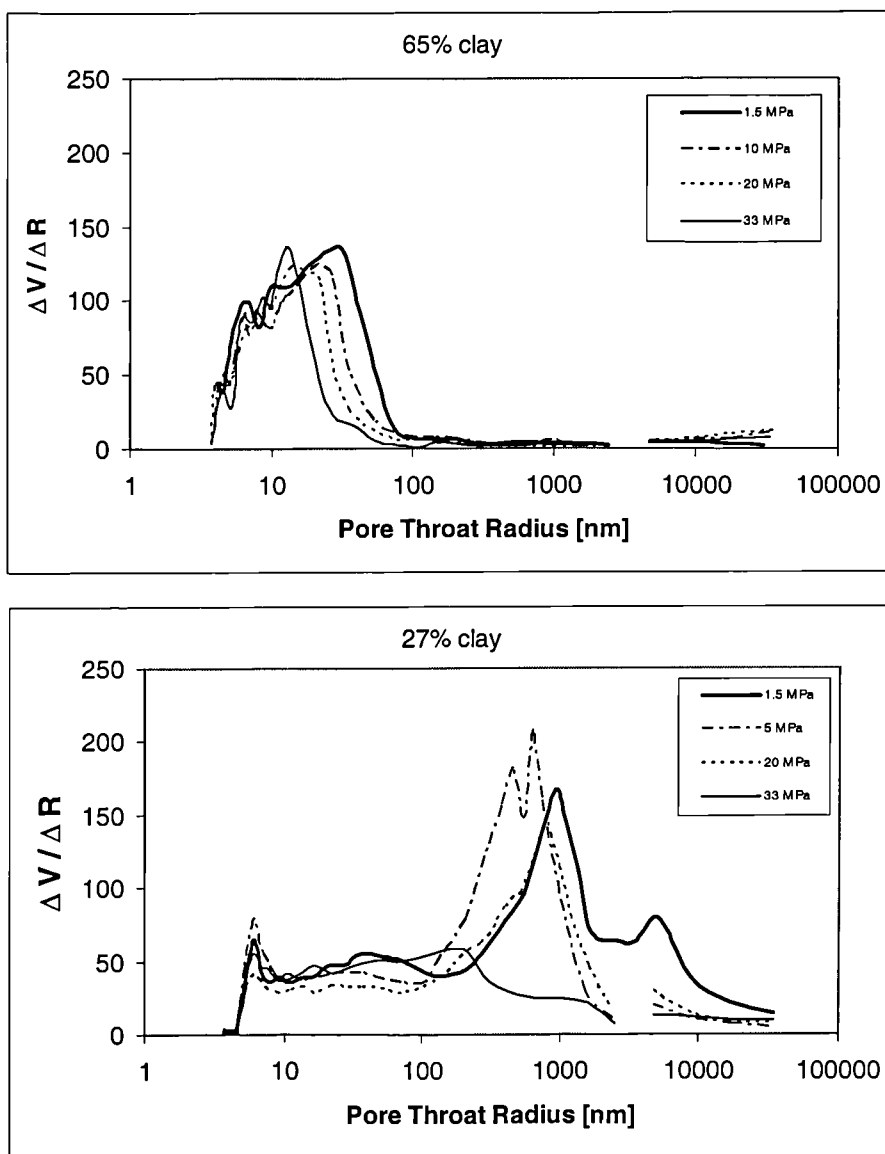


Figure 3.7. Differential pore-throat size distribution curves of two mudstones from the London Clay experimentally compacted to differing levels of effective stress. The sample in (a) has a unimodal distribution where the decreases in porosity with progressive compaction occurs through decreases both in peak height and average peak pore throat radius. Very little porosity exists in pores with throats $>80\text{nm}$. The sample in (b) exhibits a complex, tri-modal distribution; peak heights collapse at $\sim 5\mu\text{m}$ and 800 nm with the third peak virtually unchanging with progressive compaction. The 800nm peak only collapses at the maximum effective stress (33MPa) From Fig 9 and 11 in Dewhurst *et al.*, (1998).

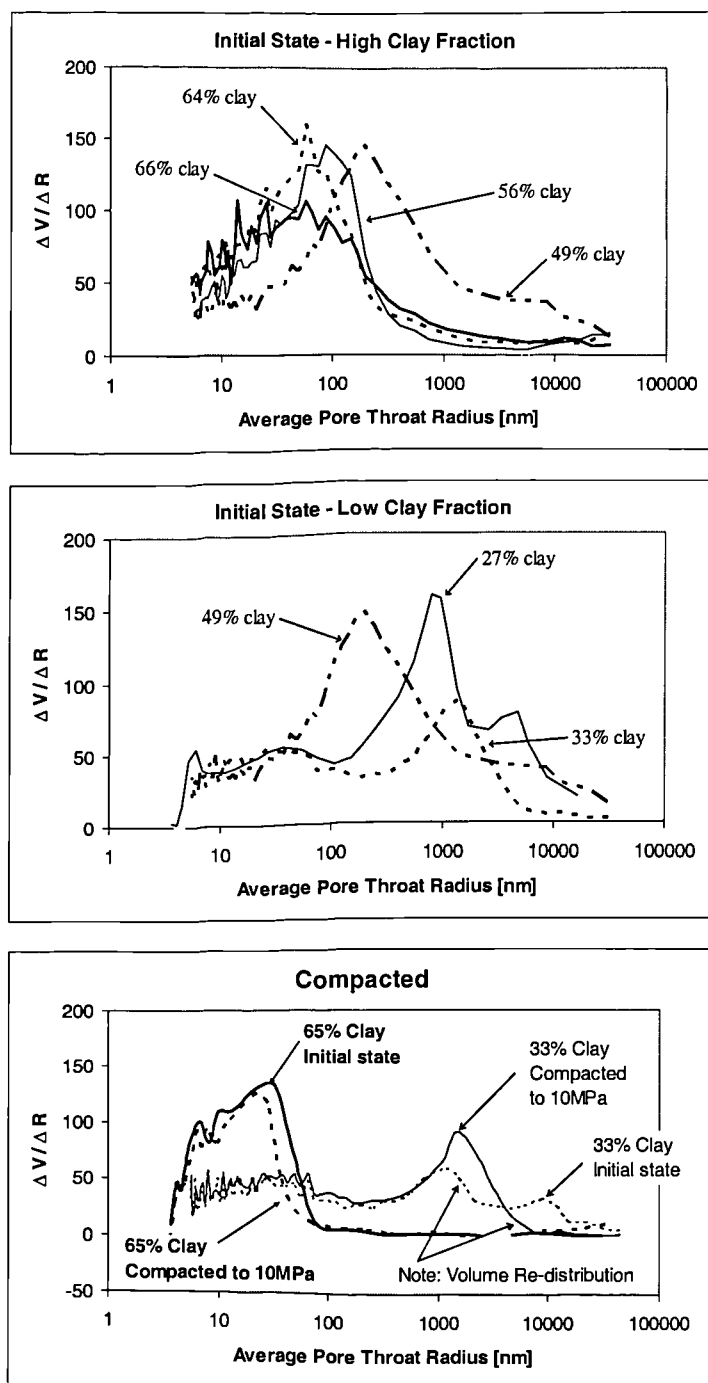


Figure 3.8. Differential pore-throat size distribution curves for initial (naturally overconsolidated to ~1.5 – 2MPa) and compacted samples: (a) silt-rich samples initial distribution; (b) clay-rich samples initial distribution; (c) comparison of initial and compacted (~10MPa) distributions. From Dewhurst *et al.*, (1999a).

The pore-throat size distributions of the initial, uncompacted (preconsolidation stress of around 1.5 – 2 MPa) silt rich muds (27% and 33% clay fraction) are shown in Figure 3.8a. These distributions are bi-modal (tri-?) in form with modal sizes of ~6000nm and 3000nm respectively. In contrast the clay rich samples (56-66% clay fraction) have unimodal pore-throat size distributions which are very similar in form, with modes between 60 and 120 nm respectively (Dewhurst *et al.*, 1999a).

Except for the 49% clay sample, the data shown in Figures 3.7 and 3.8 readily divide into two groups, divided on the basis of clay content, which exhibit significantly different pore throat size distribution properties. Compared to the coarse grained (low clay) group the clay-rich group has a much smaller range of pore throat sizes at all levels of effective stress. Dewhurst *et al.*, (1999a) noted that without more samples with clay fractions between 33 and 49% it is not clear whether there is a clay fraction at which the properties change abruptly or that the physical properties of the London Clay vary continuously. Dewhurst *et al.*, (1999a) argue that the potential for an abrupt change in behaviour is real due to the decreases in clay content is accompanied by an increase in the amount of silt and/or sand grains. When this component is comprised of relatively coarse rounded grains of quartz and feldspar (with distinct properties to platy clay minerals), if its proportion reaches some critical value the probability of developing a framework or skeleton is increased creating a sediment which would differ in its geomechanical properties.

From the London Clay data Dewhurst *et al.*, (1999a) proposed that for the silt/sand rich samples the silt and sand grains interact strongly, potentially forming a framework or skeleton which acts to reduce compressibility and thus preserving the larger pores to greater levels of effective stress. The bimodal forms of the pore throat size distributions (Figs 3.7b, 3.8a,c) for the silt/sand rich samples imply two levels of particle interaction, involving the interaction of sand and silt grains, and a second from the packing of the clay matrix, which dominates in finer grained muds (Dewhurst *et al.*, 1999a). In clay-rich muds (clay fraction >50%) the clay fabric governs the compaction and any silt or sand grains are sufficiently isolated that they exert a minor influence on compaction (Dewhurst

et al., 1999a). The clay-rich pore-throat size distributions are unimodal, reflecting the dominance of the clay matrix in controlling the compaction behaviour.

3.1.4 Synopsis – slurries to soils to ‘geological’ mudstones

A synopsis of the observations made by a variety of workers on the relationships between clay content and the distribution of porosity in soils and fine grained sediments is given in Table 3.1. Nagaraj *et al.*, (1990) hypothesized that the ideal distribution of porosity in a sediment with both aggregates (\approx flocs) and single grains can be visualized in terms of intra-floc pore space; inter-floc pore space and large enclosed pore space which is here implied as corresponding to the lacunar pore space of Fiés (1992). Common between soil scientists and geologists is the recognition of two modes or ‘domains’ of porosity which occur in fine grained sediments relating to pores formed by the silt/sand grains (*lacunar* pore space) and the clay matrix (clay fabric pore space relating to intra- and inter-floc pore space). Fiés (1992) showed that when clay fraction is <30% then the lacunar pore space is constant (at approximately constant porosity). This observation has led to the suggestion that below 30% clay content the formation of a silt / sand framework (‘skeleton’) and thus pore space is inevitable, and exists independently of the clay fabric pore space. Above 30% clay the two pore space ‘domains’ begin to interact – the 49% clay sample of Dewhurst *et al.*, (1999a) provides an example of this interaction (see Figure 3.8a,b), where the pore throat size is seemingly intermediate between the two end members (although note the high porosity ~47%). Below clay contents of 40% it is argued by Fiés (1992) that the lacunar and clay fabric ‘domains’ are distinct; similarly Dewhurst *et al.*, (1999a) hypothesized that between 33% and 49% clay there may be either a smooth continuation of variation in properties or a clay content at which an abrupt transition in behaviour occurs. It was illustrated by Fiés (1992) that, in highly porous artificial slurries, as clay content increased between 30% and 60% clay fraction the *lacunar* pore mode decreases in both modal size and volume (cf. Figures 3.1, 3.2, and 3.4).

It was noted by both Fiés (1992) and Dewhurst *et al.*, (1998) that the modal pore-throat size relating to the clay fabric pore space remains relatively constant irrespective of variation in the grain size distribution (cf. Fiés, 1992) or the compaction state (porosity) (cf. Dewhurst, *et al.*, 1998). The latter point illustrates that the bulk of the volume loss caused by compaction is contributed to by the preferential collapse of the largest pores, which decrease in stability as the grain size distribution fines (cf. Griffiths and Joshi 1989, Dewhurst, *et al.*, 1999a).

% Clay	Behaviour	Comment
<30	Load-bearing framework ('skeleton') formed by silt / sand; clay sits largely within silt/sand pores	
<40	Distinct <i>lacunar</i> or silt/sand and clay fabric pore modes	Complex interaction between the <i>lacunar</i> and clay fabric domains?
40-60	The two domains begin to strongly interact; <i>lacunar</i> pore mode approaches the clay fabric pore mode with increasing clay content	
>60	Clay fabric dominated - the clay matrix forms the load bearing phase; silt and sand grains sufficiently isolated by clays to have no influence	

Table 3.1. Synopsis of the compactional behaviour and relationship between the *lacunar* (or silt / sand) and clay fabric pore space in soils and fine grained sediments. Based upon the observations and results of Fiés (1992); Fiés and Bruand (1998); Yang and Aplin, (1998) and Dewhurst *et al.*, (1998, 1999a).

From Table 3.1 it can be seen that the distribution of effective porosity (i.e. the connected porosity as measured by an MICP experiment) in fine grained clastic sediments can be thought of as potentially occurring in three states, partly dependent upon clay content:

- 1) Effective porosity is mainly present in the form of lacunar pore space; some minor clay fabric related porosity can also be present (clay contents <40; particularly when <30%).
- 2) Effective porosity occurs in both lacunar and clay fabric pore space; which dominates and how they interact will be dependent upon the overall grain size

distribution, texture (sedimentary structure) and compaction state (clay contents 30 – 60%).

- 3) Effective porosity is concentrated in the clay fabric pore space; no lacunar pore space is present (clay contents >60%).

Obviously the most complex case is in 2, rather than an abrupt change in behaviour at a particular clay content as hypothesized by Dewhurst *et al.*, (1999a), the transition between the ‘framework’ and ‘matrix’ mode of behaviours is likely to be a consequence of the complex interaction of detailed grain size distribution, texture and compaction state. How prevalent this intermediate stage is in geological samples, along with testing the predictions and observations made by previous workers, is a key aim of this study.

3.2 Methods

All the methods used in the grain size analysis of the samples analysed in this work have been described in detail in the previous Chapter. Sample selection strived to avoid cuttings samples whenever possible due to the problems associated with integrating grain size distribution and pore-throat size distribution data over ambiguous volumes of investigation.

3.2.1 *Mercury Injection Capillary Pressure method – converting to Pore-throat size distribution*

The pore throat size distributions (PSD) were measured by the mercury injection capillary pressure (MICP) technique using a Micrometrics porosimeter. The pore throat radius, assuming the surface tension of mercury to be 0.48 N/m and the contact angle between the mercury and particle surface to be 141°, is given by (Yang and Aplin, 1998).

$$r = \left(\frac{746,000}{p} \right) \quad (3.1)$$

where r is pore throat radius in nanometers and p is pressure in kPa. Careful analysis of the resulting pore throat distributions was carried out. Artifacts in the form of large cracks (potentially generated by the sample preparation procedure) were assumed to be represented by secondary peaks on the pore frequency distributions; the true distribution is assumed to end where the numerical differential of the cumulative pore-throat distribution reaches the baseline (Yang and Aplin, 1998). Figure 3.9 shows the genuine pore-throats in blue and the pore-throats generated in the sampling process in red. All calculations were performed using the pore-throat-throat size distribution defined by genuine pore-throats as a function of cumulative porosity.

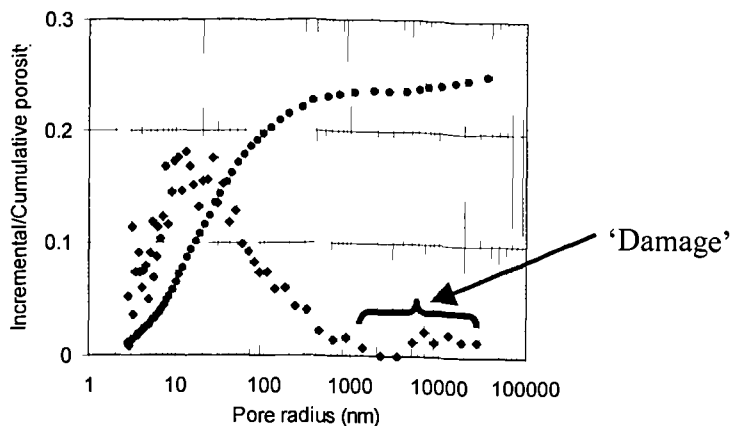


Figure 3.9. Pore-throat-throat size distribution. Genuine pore-throats are in blue and the pore-throats generated in the sampling process in red.

3.2.2 Discussion of the Mercury Injection Capillary Pressure method

The MICP technique is a standard technique and has been utilised to quantify the pore properties of rock for over 40 years. The application of this technique to mudstones has been criticized; the major contentions were summarized by Hildenbrand and Urai (2003) as:

- sample drying (typically performed using an oven set to $\sim 105^\circ\text{C}$) performed prior to analysis can lead to significant shrinkage of clay minerals distorting the pore morphology. Freeze drying techniques can be used to circumvent this effect (e.g. Matenaar, 2002).

- The high pressure required to inject mercury into the pores of mudstones may act to deform the sample.
- The omnidirectional nature of standard MICP analysis does not recover any information about the anisotropy of the sample being analysed.
- Conversion of the mercury-air system to other phases is contentious.

Since the samples analysed in this study were prepared for MICP using the freeze drying method, effects associated with clay shrinkage should be minimised. The omnidirectional nature of MICP experiments should minimize sample damage since the pressure in the mercury phase should be approximately equal in all directions and thus will in effect support the sample during the experiment. It is conceded that MICP experiments yield no information upon any anisotropic features and thus will only yield a gross characterization of a samples pore properties. Hildenbrand and Urai (2003) investigated the morphology of the pore space of mudstones using both MICP and Wood's metal injection. From the results they obtained it was suggested that for the finest grained samples with clay contents above 80%, MICP compresses the sample rather than penetrating mercury into the sample pore network. This effect is quite feasible since the compressibility of a mudstone is directly related to its grain size (Aplin *et al.*, 1995). Hildenbrand and Urai (2003) report that this compression effect is not seen in a sample with 60% and 10% sand and suggest that this sand content provides a framework which resists this compression. Only 3 samples for this dataset have clay contents above 70% and thus for the majority of samples this effect is considered to be negligible.

Hildenbrand and Urai (2003) pointed out that pores with small radii are commonly overestimated by MICP due to the bottle like nature of a proportion of the pores. This point is valid and should be considered when analysing MICP data. But the impact of this observation upon the quantification of fluid flow properties is slight since it is the pore throat radius which determines both the rate of flow of a single phase through a single pore and the ability of a non-wetting phase fluid to enter that pore.

Newsham *et al.*, (2004) applied high-speed centrifuge, MICP and high-pressure porous plate and vapour desorption techniques to the description of the pore network properties of tight gas sands to examine the both pore-throat size distributions and capillary pressure curves. They note issues with the MICP in addition to those recorded by Hildenbrand and Urai (2003) including:

- lack of standards for calibration
- use of contact angle scaling parameters that may not be appropriate for rocks with ultra-low water saturations and high capillary pressures

The results of Newsham *et al.*, (2004) illustrate that saturation distributions are consistently lower when derived from MICP capillary pressure curves when compared to those derived from composite techniques (constructed from vapour desorption, high speed centrifuge and high pressure porous plate methods). This difference may significantly underestimate the irreducible water saturation and thus will have an impact on any mutiphase flow properties derived. The magnitude of this difference was seen to decrease as the porosity and permeability decreased (for tight gas sands). The source of the error which ascribe to this difference were suggested by Newsham *et al.*, (2004) to be the nature of fluids used in the MICP technique and their non-wetting characteristics; however, Newsham *et al.*, (2004) note that MICP is an excellent tool for quantifying a rocks pore-throat size distribution.

3.3. Mudstone grain size distribution (GSD) type characteristics

The nature and characteristics of the grain size distributions representative of the six mudstone GSD types proposed in this study have been described in detail in Chapter 2 and therefore are only briefly summarized here. The key contrasts between the grain size characteristics of each grain size type are illustrated in Figure 3.10 by box and whisker plots. These are summary plots based on the median, quartiles, and extreme values. A line across the box indicates the median. The box represents the interquartile range which contains 50% of values. The whiskers are lines that extend from the box to the highest and lowest values, excluding outliers. The data tables describing the grain size characteristics of each GSD type are given in Chapter 2.

In terms of the clay and silt fractions (Fig. 3.10a,c) there is a high degree of overlap between each mudstone GSD type. The grain size typing spectrum essentially encompasses a spectrum from very fine grained (Type 1) to coarse grained (Type 6) (see Chapter 2). Inspection of the Fig. 3.10a and 3.10c reveals that grain size Types 1 and 2 have extremely broad clay and silt contents – and thus specifically appear to be potentially coarser grained than Types 3 and 4. The low clay – high silt samples for Types 1 and 2 are particularly rich in the 2 - 10 μm silt fraction. Compared in terms of the sortable silt fraction there is a continuous coarsening from Type 1 to Type 6 (Fig. 3.10d). The low clay – high silt samples for Types 1 and 2 have all been drawn from the Zeta Area and the high proportion of fine silt material is thought to indicate the significant input of wind blown material in the Zeta samples as sediments of similar age from this area have been interpreted as deposits of a dryland river/terminal fan setting. Grain size Types 1 – 5 have sand contents below 10%. Grain size Type 6 is differentiated from Types 1 – 5 by its sand content, which is between 10 – 33% for this dataset.

The differences and trends between the grain size GSD types are most clearly shown by the % $>10\mu\text{m}$, mean grain size (μm) and standard deviation of the $<63\mu\text{m}$ component. Although there is still a high degree of overlap, there is a clear increase in % $>10\mu\text{m}$ and mean grain size (μm) from Types 1 to 6; in terms of the mean grain size it is typically $<4\mu\text{m}$ for Types 1 – 4 and shows a high degree of variation for Types 5 and 6. Furthermore the sorting, quantified by the standard deviation, also increases from Type 1 to Type 6.

Overall it can be seen that there is gradual, if subtle coarsening between Types 1 to 4 (although their grain size spectra exhibit clear differences (cf. Chapter 2 Fig. 2.49)). Types 5 and 6 are coarser than the previous types, as is clearly illustrated by the significant increase in material $>10\mu\text{m}$ (see Fig. 3.10d).

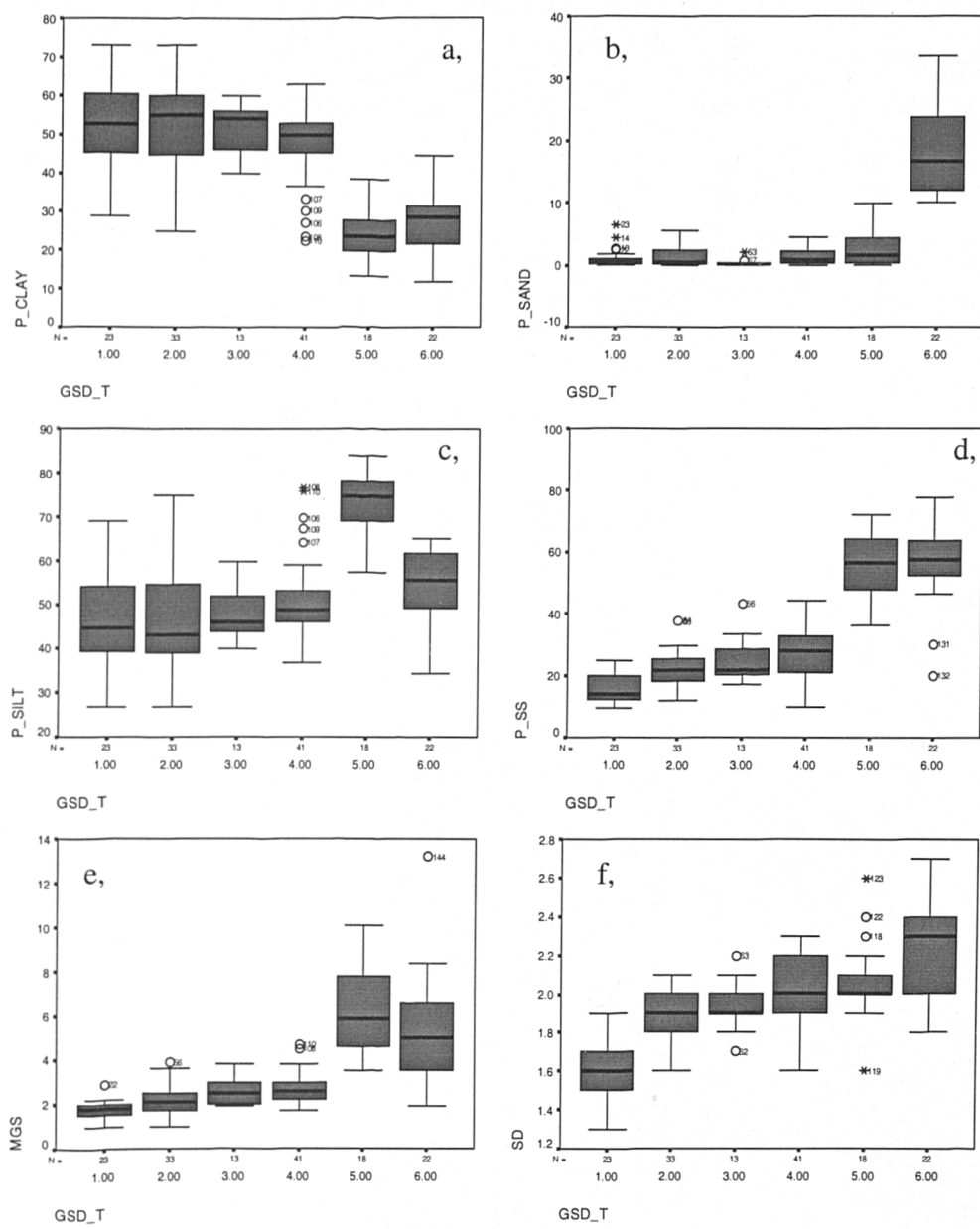


Figure 3.10. Box and whisker plots describing the grain size distribution characteristics of mudstone GSD types 1 to 6 for (a) clay fraction (b) sand fraction (c) silt fraction (d) sortable silt fraction (% $>10\mu\text{m}$) (e) mean grain size (μm) (of the $<63\mu\text{m}$ component) and (f) standard deviation (of the $<63\mu\text{m}$ component).

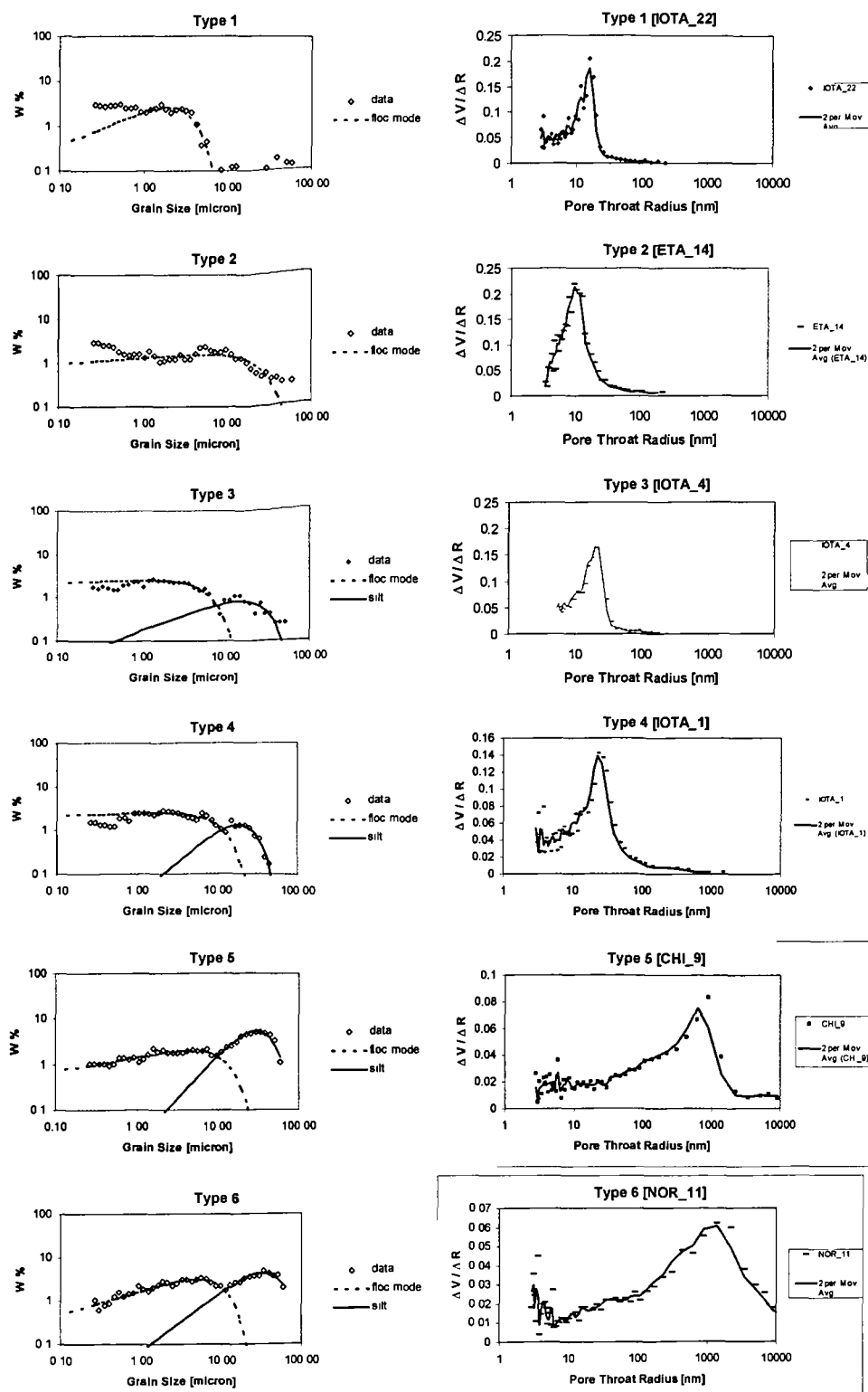
3.4. Results

3.4.1 Relationship between grain size and pore-throat size distribution: Constant porosity.

To investigate the influence of grain size distribution on the pore throat size distributions of mudstones, grain size distribution spectra presented on log-log plots were compared to the corresponding differential pore-throat size distribution (PSD) for examples of each of the grain size types identified in Chapter 2 at a constant porosity value. To assess how this influence may change with differing levels of compaction (porosity levels) 3 sets of each grain size type were analysed at 26%, 17% and 7-9% porosity.

In Figures 3.11 - 3.13 the grain size spectra and PSD's of examples of grain size types 1 – 6 are presented at three compaction states. Although grain size types 1 – 4 exhibit quite different grain size spectra, however their PSD's have very similar characteristics; each is unimodal in form with modal values of ~30nm which decrease with increasing compaction, and there are very few pores with radii >80nm. At each porosity level there is a slight trend to increasing values of r_{mean} and $r_{10\%}$ from Type 1 to 4, reflecting the coarsening of the grain size spectra (see Tables 3.2 - 3.4). These slight differences are illustrated in Figure 3.14. This figure also illustrates that Types 1 – 4 are distinct from Types 5 – 6 in terms of the pore-throat size distribution and that as porosity decreases this difference also decreases (i.e. the difference in pore network parameter values decreases). For the lowest porosity group the distinction in behaviours occurs between Types 3 – 4 however in this case the Type 4 sample is a cutting (see Table 3.4).

Figure 3.11. (Overleaf) Grain size distribution spectra fitted with the Kranck model (Kranck *et al.*, 1996a,b) and differential pore throat size distributions for grain size types 1 – 6 at ~26% porosity.



(a)

Sample	Depth (ft)	Depth (m)	Grain Size Type	Sample type	Corrected Porosity	r mean (nm)	r 10% (nm)	Temperature (C)	Total C (%)	TOC (%)	Measured Gs (g/cm^3)
IOTA_22	12906.0	3933.7	1	SWC	0.263	9.3	18.9	53.9	0.9	0.2	2.809
ETA_14	8284.1	2525.0	2	Cuttings	0.259	13.1	22.5	53.3	4.0	3.2	2.518
IOTA_4	10330.0	3148.6	3	SWC	0.25	13.5	26.4	38.4	1.5	0.7	2.741
IOTA_1	9800.0	2987.0	4	SWC	0.261	28.8	48.9	35.2	1.3	0.5	2.75
CHI_9	12707.9	3873.4	5	Core	0.259	571.0	1231.9				
NOR_11	6718.7	2047.9	6	Plug	0.265	1403.4	3990.3	59.9	1.0	1.0	2.752

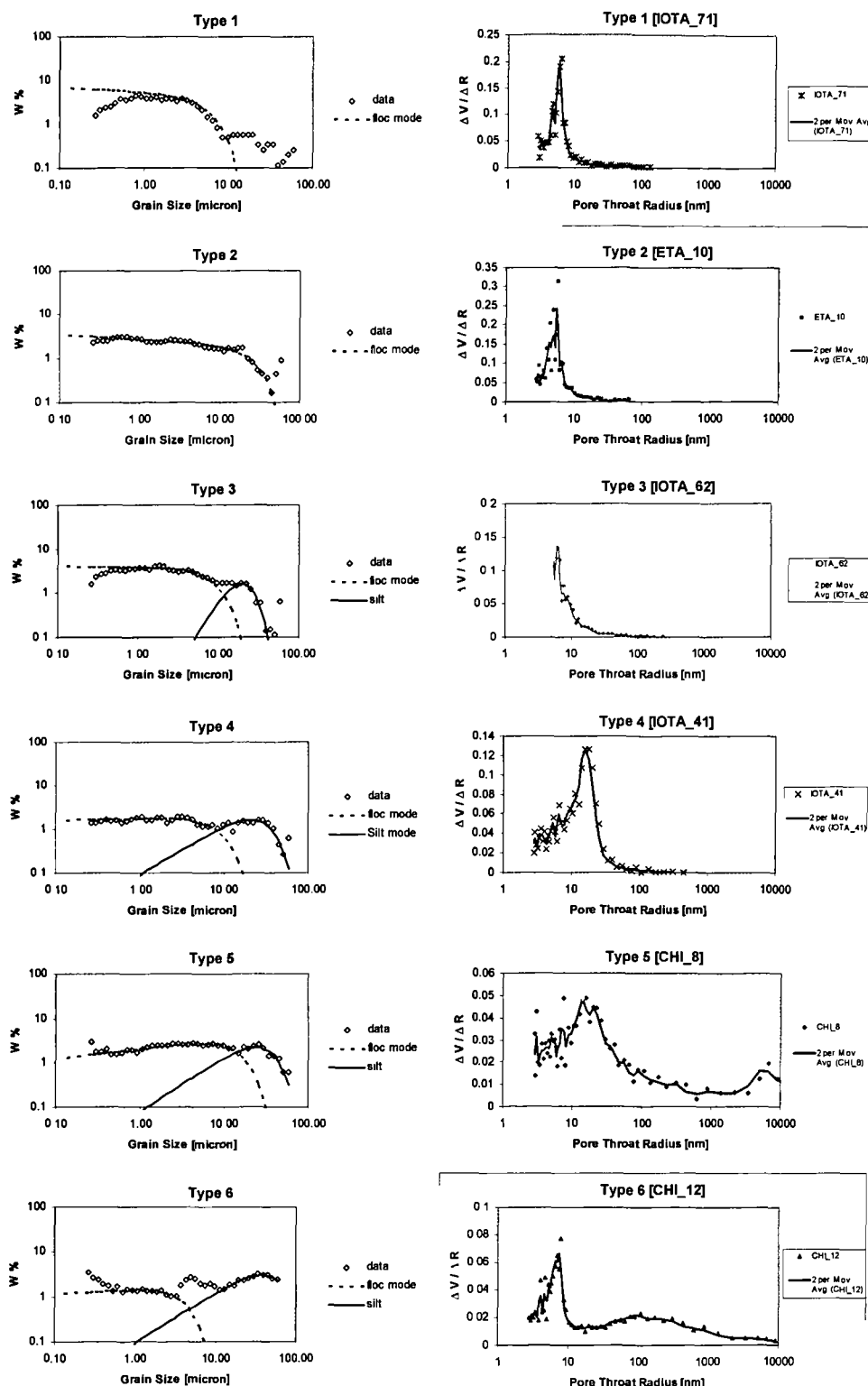
(b)

Sample	mmbstf			Whole distribution stats						Sortable Silt			
	Depth (ft)	Depth (m)	Grain Size Type	% Clay	% Sand	% Silt	% >10µm	Mean Grain Size (µm)	SD	Skewness	SS mean (µm)	SD	Skewness
IOTA_22	12906.0	3933.7	1	73.0	0.1	26.9	9.3	1.0	1.4	-0.7	29.8	0.9	0.2
ETA_14	8284.1	2525.0	2	56.5	0.3	43.2	20.0	2.1	2.1	-0.3	17.8	0.7	-0.3
IOTA_4	10330.0	3148.6	3	60.0	0.1	40.0	17.6	2.0	1.8	-0.6	19.3	0.7	-0.2
IOTA_1	9800.0	2987.0	4	51.0	0.1	48.9	21.4	2.6	1.8	-0.3	19.2	0.6	-0.1
CHI_9	12707.9	3873.4	5	21.5	4.6	73.9	62.5	7.8	2.2	0.9	27.6	0.7	0.1
NOR_11	6718.7	2047.9	6	12.7	33.8	53.5	72.6	6.6	2.1	0.5	27.7	0.7	0.1

Table 3.2 (a) Physical property data and (b) grain size distribution data for samples with a porosity of ~26%. Grain size and pore-throat size distributions shown in Figure 3.10.

Relative to the grain size Types 1 – 4, Types 5 and 6 have quite different PSD's and contrasting grain size spectra. At 26% porosity the PSD's of Type 5 and 6 samples are both clearly bi-modal, with the mode corresponding to the larger pore-throat size being dominant. From inspection of Figures 3.11 – 3.13 it can be seen that with increasing compaction this mode is reduced, reflecting the preferential collapse of the largest pores with increasing effective stress (cf. Dewhurst *et al.*, 1999, 1999a). The small diameter mode, thought to correspond to pores associated with the clay fabric (cf. Fies, 1992; Griffiths and Joshi, 1989; Nagaraj *et al.*, 1990) gradually shifts from ~30nm to ~5nm but increases in height relative to the large pore mode, potentially reflecting the contribution to volume of pores in this size range by compacted lacunar pores (cf. Section 3.1).

Figure 3.12. (Overleaf) Grain size distribution spectra fitted with the Kranck model (Kranck *et al.*, 1996a.b) and differential pore throat size distributions for grain size types 1 – 6 at ~17% porosity.



(a)

Sample	Depth (ft)	Depth (m)	Grain Size Type	Sample type	Corrected Porosity	r_{mean} (nm)	$r_{10\%}$ (nm)	Temperature (C)	Total C (%)	TOC (%)	Measured G_s (g/cm ³)
IOTA_71	22584.8	6775.4	1	SWC	0.17	4.4	8.0	108.6	1.7	0.7	2.812
ETA_10	10600.4	3231.0	2	SWC	0.179	4.8	8.6	91.5	1.3	1.2	2.737
IOTA_42	22044.0	6607.0	3	SWC	0.179	6.1	11.6	105.1	2.3	1.8	2.802
IOTA_41	50656.2	4706.1	4	SWC	0.18	13.6	24.5	69.1	1.4	1.3	2.682
CHI_8	12706.4	3872.9	5	Core	0.177	496.7	1209.5				
CHI_12	13103.5	3993.9	6	Core	0.181	1497.0	5960.5				

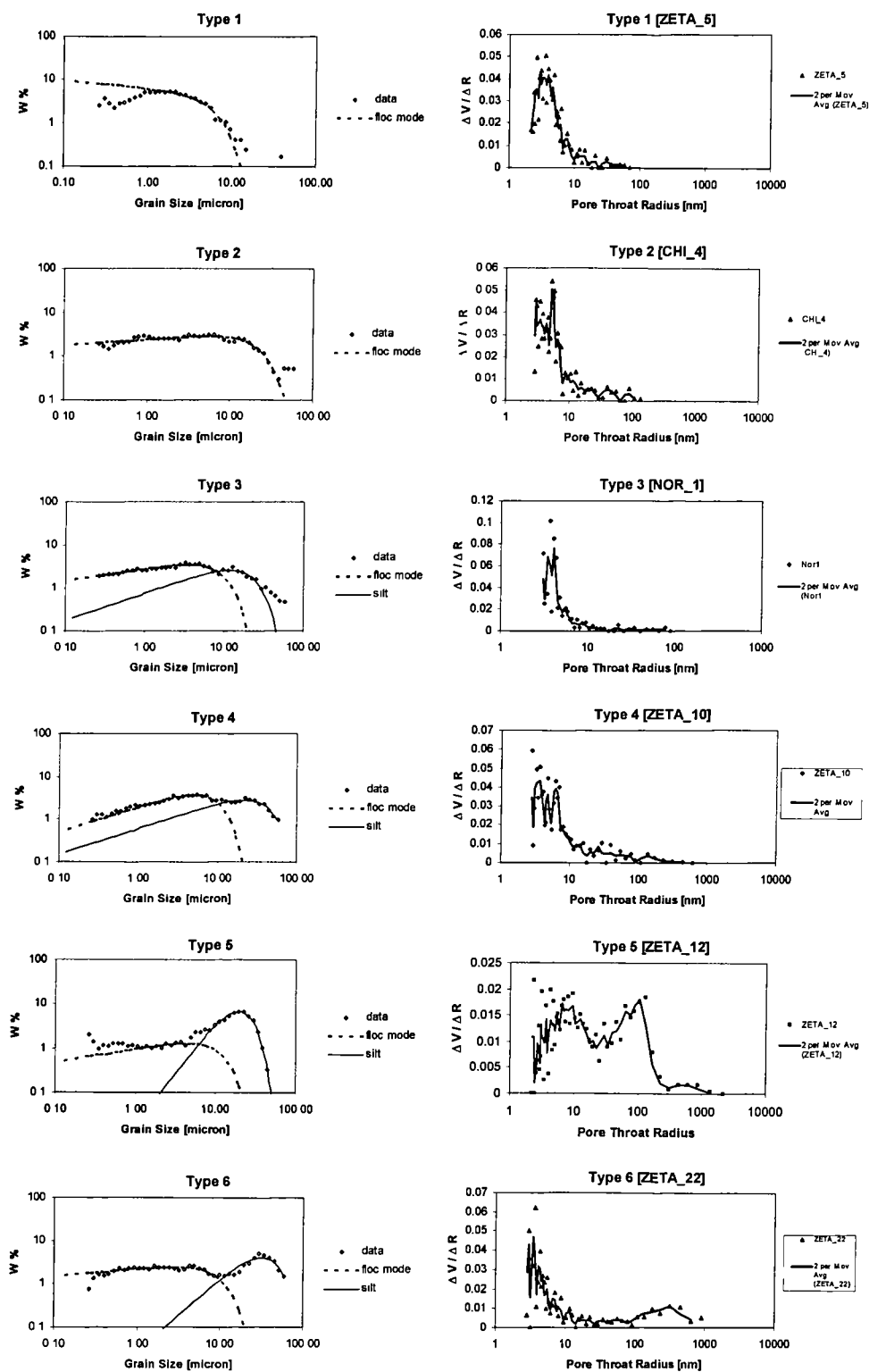
(b)

Sample	mmbstl			% Clay	% Sand	% Silt	% >10μm	Whole distribution stats			Sortable Silt		
	Depth (ft)	Depth (m)	Grain Size Type					Mean Grain Size (μm)	SD	Skewness	SS mean (μm)	SD	Skewness
IOTA_71	22584.8	6775.4	1	55.3	0.0	44.7	14.1	1.5	1.6	-0.7	20.6	0.7	-0.2
ETA_10	10600.4	3231.0	2	48.5	1.0	50.5	25.5	2.2	2.0	-0.5	19.7	0.7	-0.3
IOTA_61	22024.0	6607.0	3	40.0	0.3	59.7	43.3	3.8	2.1	-0.2	24.3	0.8	0.0
IOTA_41	15440.0	4706.1	4	53.0	0.9	46.1	27.9	3.1	2.2	-0.3	22.6	0.7	0.0
CHI_8	12706.4	3872.9	5	34.4	0.8	64.8	36.4	3.5	2.1	0.0	21.9	0.7	-0.1
CHI_12	13103.5	3993.9	6	31.0	10.1	58.9	52.3	4.8	2.5	0.4	28.5	0.8	0.1

Table 3.3 (a) Physical property data and (b) grain size distribution data for samples with a porosity of 18 - 19%. Grain size and pore-throat size distributions shown in Figure 3.11.

The progression between grain size types and with increasing compaction is illustrated by Figure 3.14. At 26% and 17% grain size types 1 – 4 are seen to have very similar values of r_{mean} and $r_{10\%}$, whereas Types 5 and 6 clearly have much broader, bi-modal PSD's and have pore-throat size distributions that incorporate throats with radii approximately two orders of magnitude larger than those in Types 1 – 4. With decreasing porosity the magnitude of the difference between grain size types 1 – 4 and 5 – 6 decreases, so that when porosity has declined to 7-9% the difference has dropped to approximately one order of magnitude (cf. Figure 3.14).

Figure 3.13. (Overleaf) Grain size distribution spectra fitted with the Kranck model (Kranck *et al.*, 1996a,b) and differential pore throat size distributions for grain size types 1 – 6 at 9 – 7% porosity.



(a)

Sample	Depth (ft)	Depth (m)	Grain Size Type	Sample type	Corrected Porosity	r mean (nm)	r 10% (nm)	Temperature (C)	Total C (%)	TOC (%)	Measured Gs (g/cm^3)
ZETA_5	17097.0	5211.1	1	RSW core	0.093	3.5	7.4	123.0	1.2	0.4	2.786
CHI_4	13959.4	4254.8	2	Core	0.074	7.3	8.4				
NOR_1	14552.7	4435.7	3	Plug	0.098	2.8	5.8	142.0	1.5	1.5	2.833
ZETA_10	18241.0	5560.0	4	Cuttings	0.07	29.9	66.9	131.8	2.6	1.5	2.677
ZETA_12	18439.0	5620.3	5	RSW core	0.091	52.1	127.5	133.3	1.3	0.1	2.758
ZETA_22	21349.1	6507.2	6	Core	0.091	76.4	310.8	165.3	0.9	0.3	2.766

(b)

Sample	mmbstl							Whole distribution stats			Sortable Silt		
	Depth (ft)	Depth (m)	Grain Size Type	% Clay	% Sand	% Silt	% >10µm	Mean Grain Size (µm)	SD	Skewness	SS mean (µm)	SD	Skewness
ZETA_5	17097.0	5211.1	1	52.6	0.0	47.4	9.8	1.4	1.4	-0.2	14.5	0.6	-0.4
CHI_4	13959.4	4254.8	2	37.8	0.7	61.5	29.4	2.8	1.9	-0.1	18.6	0.7	-0.2
NOR_1	14552.7	4435.7	3	40.5	0.7	58.7	33.6	3.0	1.9	-0.1	19.0	0.7	-0.2
ZETA_10	18241.0	5560.0	4	22.4	1.8	75.8	44.3	4.7	2.0	0.2	22.7	0.7	0.0
ZETA_12	18439.0	5620.3	5	22.1	0.2	77.6	61.1	6.9	2.0	1.3	19.7	0.5	0.0
ZETA_22	21349.1	6507.2	6	23.7	11.9	64.4	58.1	5.2	2.3	0.3	28.1	0.7	0.1

Table 3.4 (a) Physical property data and (b) grain size distribution data for samples with a porosity of 9 - 7%. Grain size and pore-throat size distributions shown in Figure 3.12.

The observations made from Figures 3.11 – 3.13 indicate that the pore networks of mudstones exhibit two modes of behaviour dependent upon grain size distribution; Types 1 – 4 have tight, unimodal pore throat size distributions corresponding to the load bearing clay ‘matrix’. Types 5 and 6 incorporate a framework created by the interaction and geometry of silt and sand grains which initially acts as the load bearing phase. These samples have bimodal PSD’s reflecting the presence of the larger silt/sand framework associated pores and clay matrix associated pores. With increasing effective stress the clay ‘matrix’ becomes increasingly load bearing via re-arrangement of the grains as the lacunar pore space is reduced due to preferential compaction. This progression is illustrated in Figure 3.14 and indicates that with increasing compaction the influence of grain size distribution is gradually reduced.

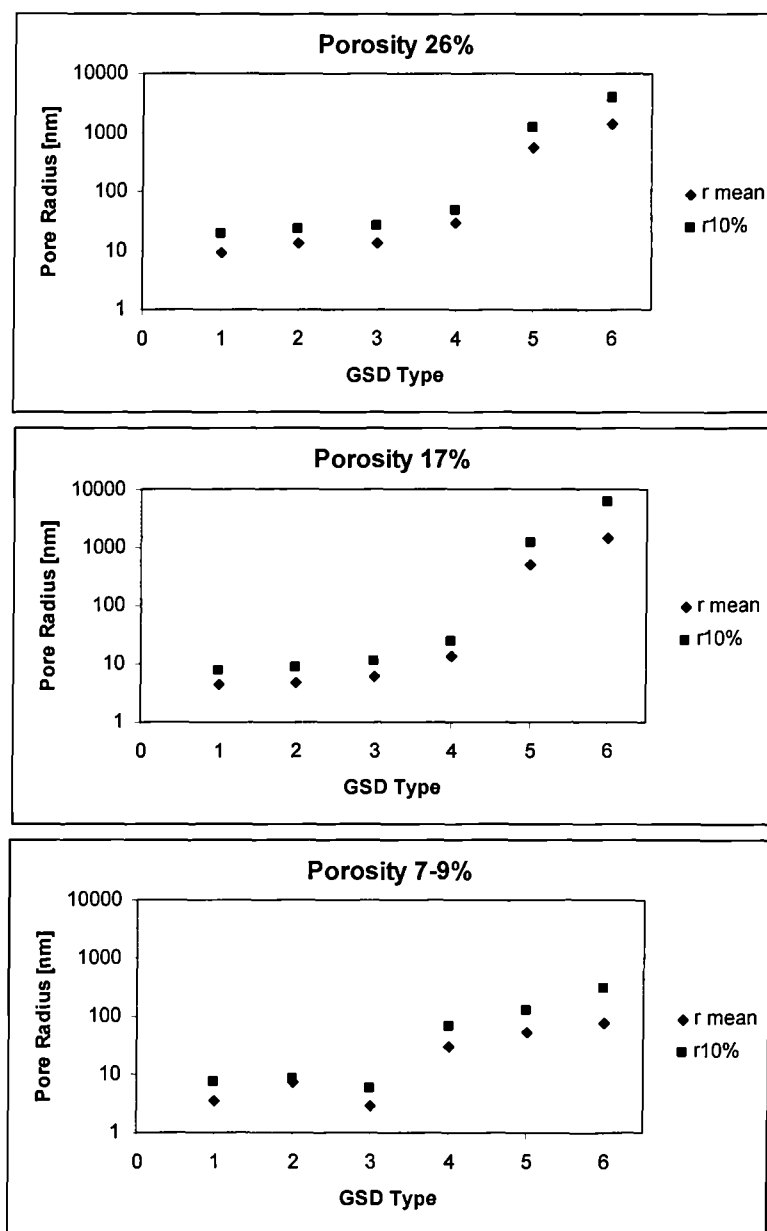


Figure 3.14. r_{mean} and $r_{10\%}$ as a function of grain size distribution type at (a) 26% porosity, (b) 17% porosity and (c) 7 – 9% porosity.

3.4.2 Relationship between pore-throat size distributions and porosity: Constant lithology (grain size distribution type)

To investigate the influence of compaction on the pore-throat size distributions of mudstones of similar lithology, the pore-throat size distributions of samples of the same grain size type at a range of porosities were compared. The samples presented here exhibit similar characteristics to those presented in Section 3.4.1. Initial inspection of the results again revealed two characteristic forms of the differential pore-throat size distributions derived from the samples analysed; grain size types 1 – 4 typically had unimodal distributions with peaks in pore throat radii $<80\text{nm}$ with the bulk of the pore radii being $<100\text{nm}$. Conversely grain size GSD types 5 and 6 typically had bimodal distributions incorporating significant volumes of pores with radii $100 - 10000\text{nm}$ in size. Due to this apparent partition in behaviour types 1 – 4 and types 5 – 6 will be described separately.

Grain size types 1 – 4 exhibit very similar characteristics in terms of their differential pore throat size distributions and how they evolve with decreasing porosity. All the PSD's are unimodal in form and are dominated by pore radii $<100\text{nm}$ (Figs 3.15, 3.17, 3.19 and 3.21). With decreasing porosity there is a progressive shift in the PSD's with both modal values and the intruded volume decreasing. Modal values typically reduce from $\sim 50\text{nm}$ to $<10\text{nm}$ as porosity decreases from $\sim 26\%$ to $<10\%$. As with the pore-throat size characteristics observed in more porous clay-rich materials the bulk of the pore-throat size distribution is thought to be associated with the clay matrix (e.g. Fies, 1992; Griffiths and Joshi, 1989; Nagaraj *et al.*, 1990).

To illustrate the evolution of the breadth of the pore-throat size distribution with decreasing porosities, the 5%, 10%, 20%, 30%, 40% and 50% percentile calculated from the cumulative pore-throat size distribution were cross plotted against porosity. Figures 3.16, 3.18, 3.20 and 3.22 illustrate that r5% - representing the pore throats at the larger end of the PSD decline most rapidly (exponentially) with decreasing porosity. This observation indicates that volume loss ('compaction') is dominantly contributed to by the

collapse of the largest pores, which is in agreement with the observations of Dewhurst *et al.*, (1998, 1999a).

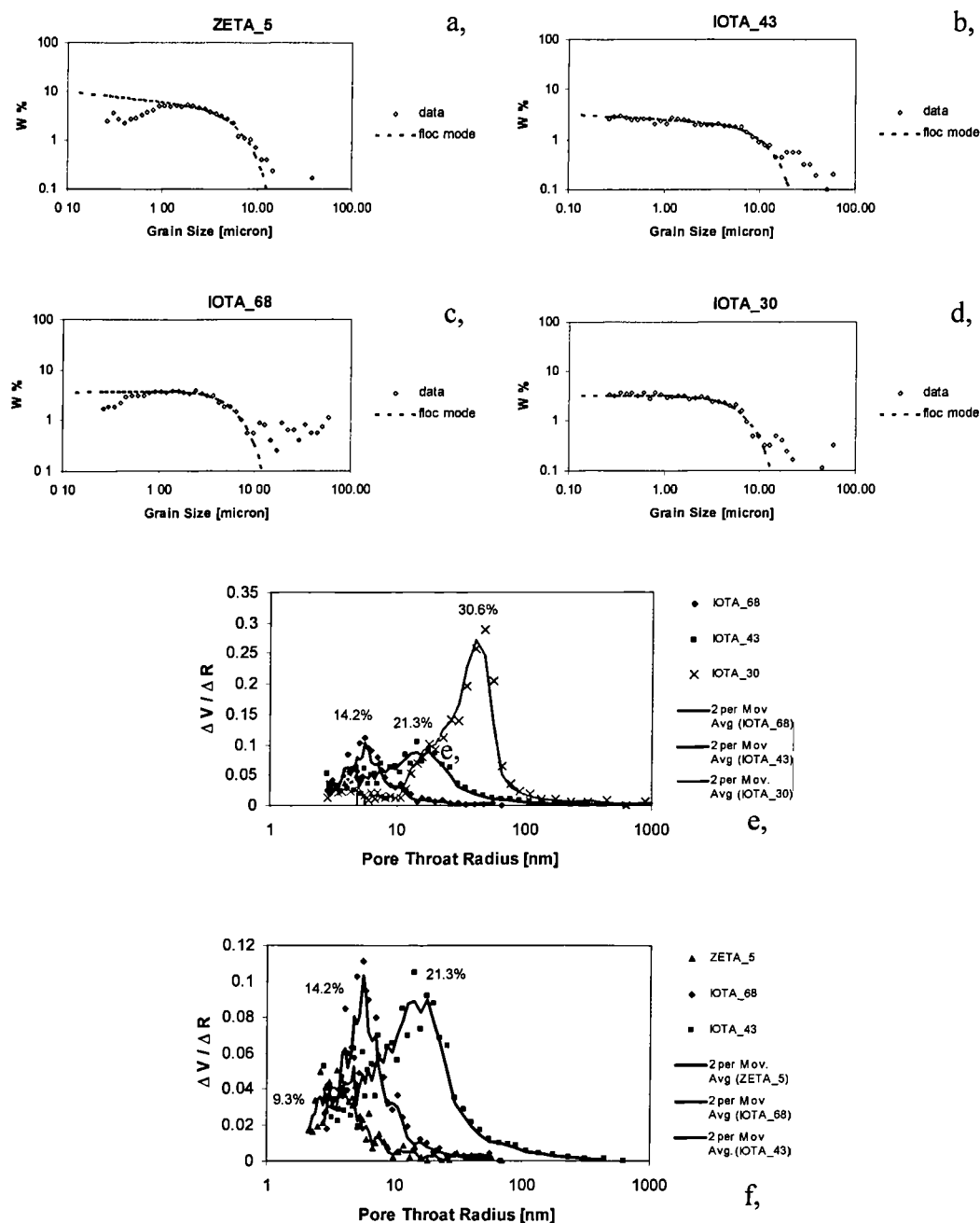


Figure 3.15. Grain size spectra (a – d) and differential pore-throat size distributions (e – f) of Type 1 grain size examples (porosities are given on plots e and f).

(a)

Sample	mmbsfl							Whole distribution stats			Sortable Silt		
	Depth (m)	Depth (ft)	Grain Size Type	% Clay	% Sand	% Silt	% >10µm	Mean Grain Size (µm)	SD	Skewness	SS mean (µm)	SD	Skewness
IOTA_30	5211.1	17096.8	1	61.0	0.1	38.9	11.4	1.3	1.6	-0.6	19.1	0.8	-0.4
IOTA_43	6882.6	22580.6	1	58.0	0.6	41.4	15.7	1.6	1.8	-0.6	18.9	0.7	-0.2
IOTA_68	4767.1	15640.0	1	52.0	0.2	47.8	19.1	1.9	1.8	-0.9	26.5	0.9	0.0
ZETA_5	4330.0	14206.0	1	52.6	0.0	47.4	9.8	1.4	1.4	-0.2	14.5	0.6	-0.4

(b)

Sample	Depth (m)	Depth (ft)	Grain Size Type	Sample type	Corrected Porosity	r mean (nm)	r 10% (nm)	Temperature (C)	Total C (%)	TOC (%)	Measured Gs (g/cm^3)
ZETA_5	5211.1	17096.8	1	RSW core	0.093	3.5	7.4	123.0	1.2	0.4	2.786
IOTA_68	6882.6	22580.6	1	SWC	0.142	4.7	10.7	108.6	1.5	0.7	2.770
IOTA_43	4767.1	15640.0	1	SWC	0.213	17.0	31.9	70.3	0.7	0.6	2.770
IOTA_30	4330.0	14206.0	1	SWC	0.306	51.3	62.0	61.7	10.0	2.0	2.441

Table 3.5 (a) Grain size data and (b) physical property data for Type 1 samples with a porosity of 9 - 30%. Grain size and pore-throat size distributions shown in Figure 3.15.

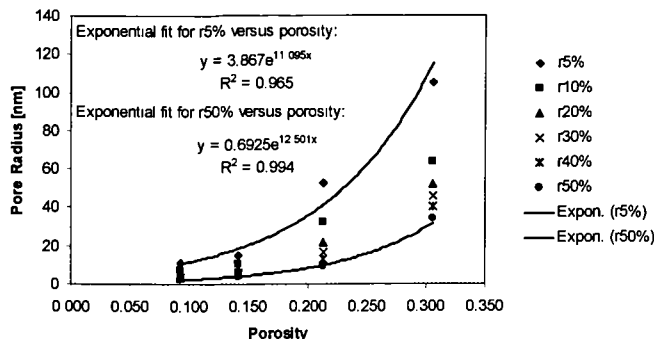


Figure 3.16. Percentile – porosity plot derived from the four Type 1 samples presented in Fig. 3.15; both r5% and r50% decrease exponentially, however the decrease in r5% is much more rapid illustrating that the bulk of compaction occurs through collapse of the largest pores. The observed decrease in r50% simply represents the shift in the PSD as the largest pores are lost by preferential collapse.

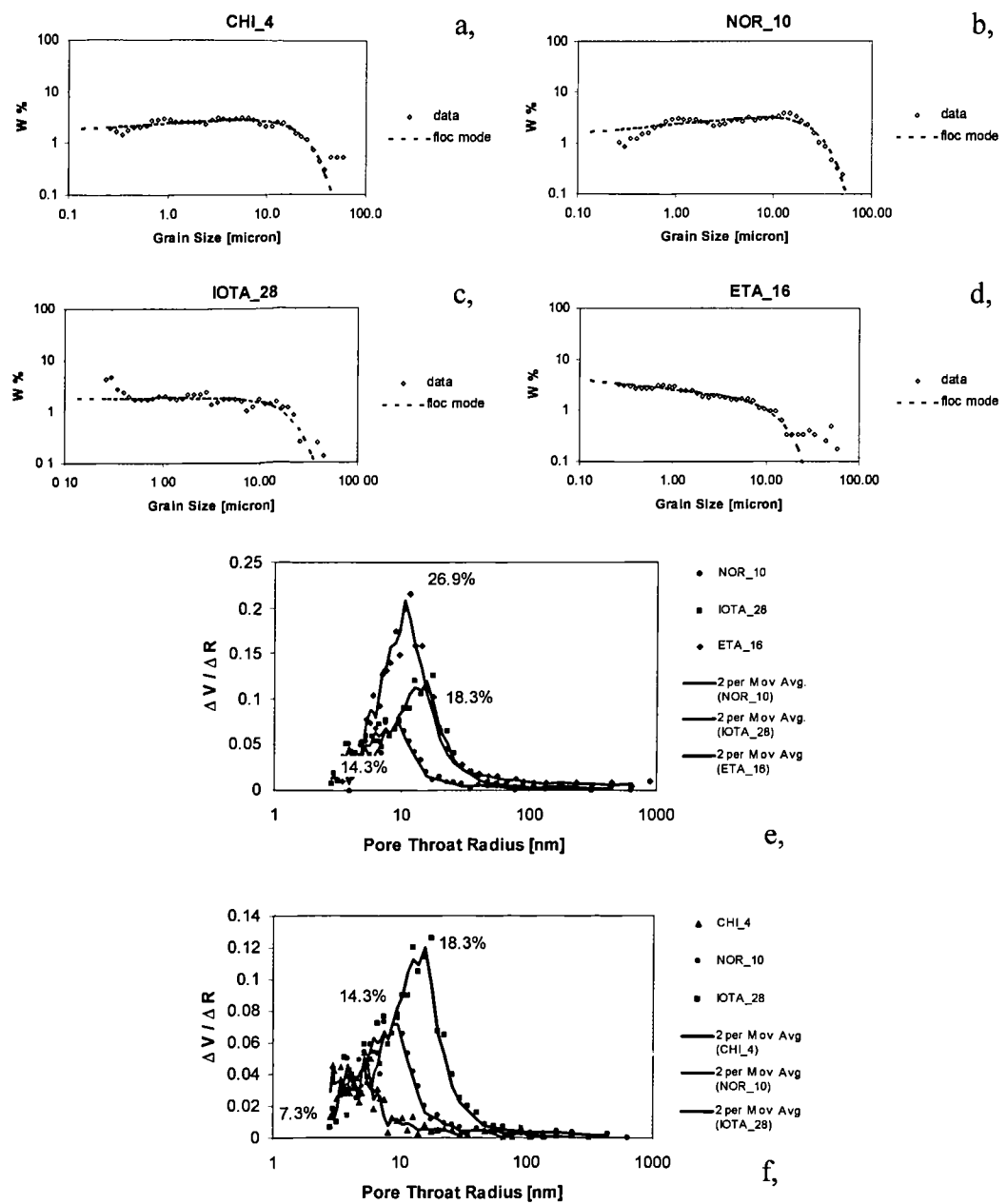


Figure 3.17. Grain size spectra (a – d) and differential pore-throat size distributions (e – f) of Type 2 grain size examples (porosities are given on plots e and f).

(a)

Sample	mmbsft							Whole distribution stats			Sortable Silt		
	Depth (ft)	Depth (m)	Grain Size Type	% Clay	% Sand	% Silt	% >10µm	Mean Grain Size (µm)	SD	Skewness	SS mean (µm)	SD	Skewness
CHI_4	13959.4	4254.8	2	37.8	0.7	61.5	29.4	2.8	1.9	-0.1	18.6	0.7	-0.2
NOR_10	7509.0	2288.8	2	35.9	0.2	63.9	37.7	3.6	1.9	0.2	17.4	0.6	-0.2
IOTA_28	13772.0	4197.7	2	60.0	0.1	39.9	18.9	1.7	1.9	-0.5	15.8	0.5	-0.2
ETA_16	9694.9	2955.0	2	56.8	5.4	37.9	21.7	1.5	1.8	-0.8	19.2	0.8	-0.2

(b)

Sample	Depth (ft)	Depth (m)	Grain Size Type	Sample type	Corrected Porosity	r mean (nm)	r 10% (nm)	Temperature (C)	Total C (%)	TOC (%)	Measured Gs (g/cm^3)
CHI_4	13959.4	4254.8	2	Core	0.074	7.3	8.4				
NOR_10	2288.8	2288.8	2	Plug	0.143	9.6	15.8	84.2	2.7	2.3	2.763
IOTA_28	13772.0	4197.7	2	SWC	0.183	13.6	25.0	59.1	2.4	2.0	2.643
ETA_16	9694.9	2955.0	2	Cuttings	0.269	24.6	32.2	72.7	4.4	3.2	2.512

Table 3.6 (a) Grain size data and (b) physical property data for Type 2 samples with a porosity of 7 - 24%. Grain size and pore-throat size distributions shown in Figure 3.17.

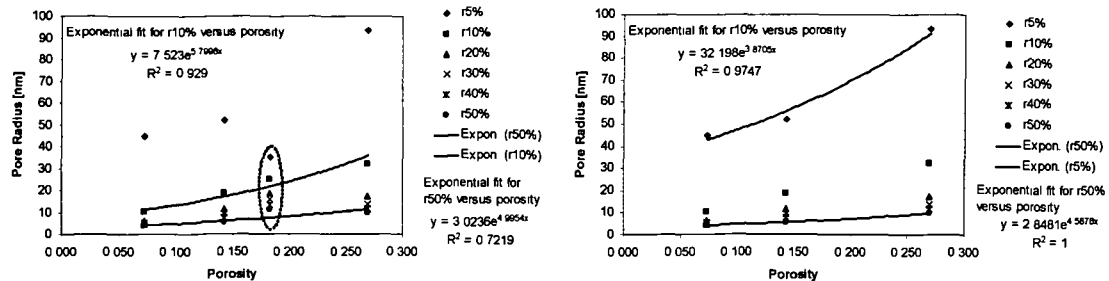


Figure 3.18. Percentile – porosity plot derived from the four type 2 samples presented in Fig. 3.17; (a) the 18% porosity example [IOTA_28] has a very tight pore throat size distribution relative to the other samples; removal of these data results in the data plotting in a similar manner to the other grain size types; r5% decreases exponentially and r50% decreases linearly at much reduced rate illustrating how the bulk of compaction is contributed by the collapse of the largest pores.

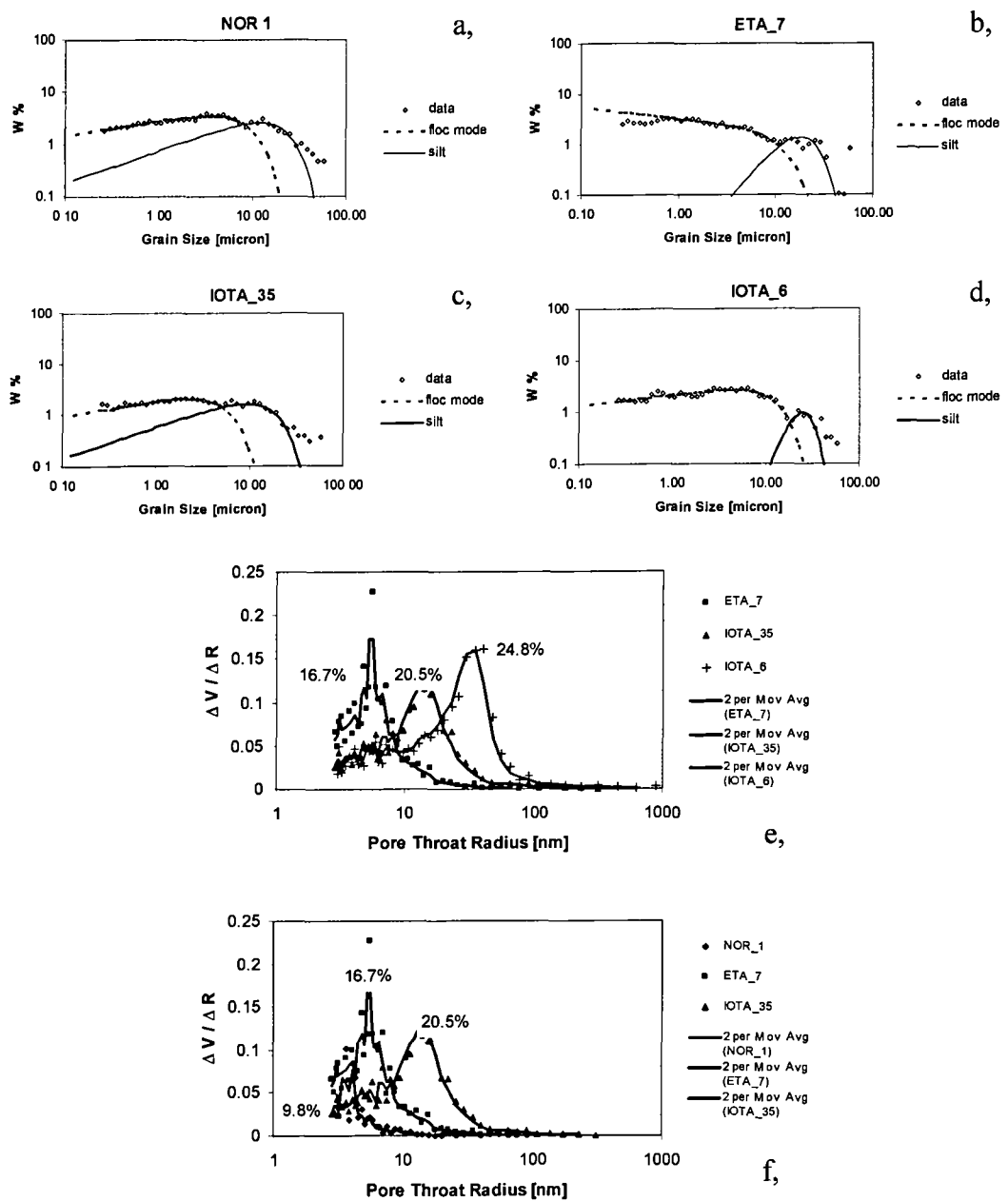


Figure 3.19. Grain size spectra (a – d) and differential pore-throat size distributions (e – f) of Type 3 grain size examples (porosities are given on plots e and f).

(a)

Sample	mmbst							Whole distribution stats			Sortable Silt		
	Depth (ft)	Depth (m)	Grain Size Type	% Clay	% Sand	% Silt	% >10µm	Mean Grain Size (µm)	SD	Skewness	SS mean (µm)	SD	Skewness
NOR_1	14552.7	4435.7	3	40.5	0.7	58.7	33.6	3.0	1.9	-0.1	19.0	0.7	-0.2
ETA_7	9904.9	3019.0	3	50.9	0.2	48.9	21.9	1.9	1.9	-0.7	20.6	0.7	-0.2
IOTA_35	14879.0	4535.1	3	54.0	0.0	46.0	21.5	2.5	1.9	-0.2	17.9	0.7	-0.3
IOTA_6	10690.0	3258.3	3	48.0	0.1	51.9	22.2	2.6	1.9	-0.2	18.8	0.7	-0.2

(b)

Sample	Depth (ft)	Depth (m)	Grain Size Type	Sample type	Corrected Porosity	r mean (nm)	r 10% (nm)	Temperature (C)	Total C (%)	TOC (%)	Measured Gs (g/cm^3)
NOR_1	14552.7	4435.7	3	Plug	0.098	2.8	5.8	142.0	1.5	1.5	2.833
ETA_7	9904.9	3019.0	3	cuttings	0.167	5.6	10.8	82.0	1.1	0.7	2.717
IOTA_35	14879.0	4535.1	3	SWC	0.205	13.0	24.4	65.7	1.3	0.7	2.735
IOTA_6	10690.0	3258.3	3	SWC	0.248	26.7	46.6	40.6	1.7	0.8	2.702

Table 3.7 (a) Grain size data and (b) physical property data for Type 3 samples with a porosity of 9 - 26%. Grain size and pore-throat size distributions shown in Figure 3.19.

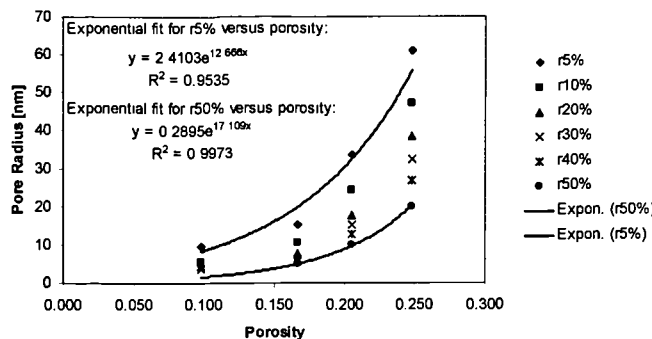


Figure 3.20. Percentile – porosity plot derived from the four type 3 samples presented in Fig. 3.19; both r5% and r50% decreases exponentially, however the decrease in r5% is more rapid illustrating that the bulk of compaction occurs through collapse of the largest pores. The observed decrease in r50% simply represents the shift in the PSD as the largest pores are lost by preferential collapse. (Note r40% and r50% could not be determined for the lowest porosity sample [NOR_1]).

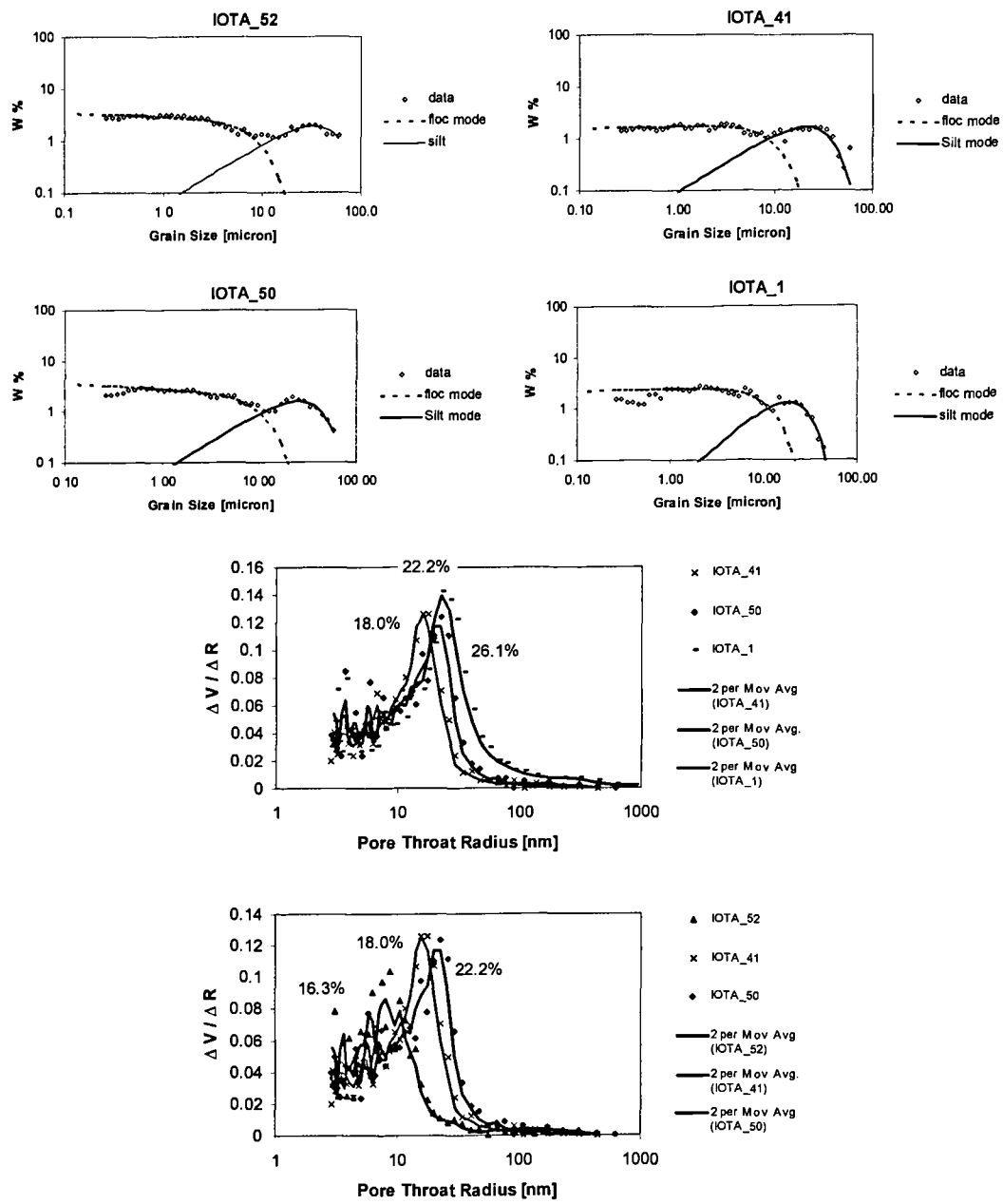


Figure 3.21. Grain size spectra (a – d) and differential pore-throat size distributions (e – f) of Type 4 grain size examples (porosities are given on plots e and f).

(a)

Sample	mmsf							Whole distribution stats			Sortable Silt		
	Depth (ft)	Depth (m)	Grain Size Type	% Clay	% Sand	% Silt	% >10µm	Mean Grain Size (µm)	SD	Skewness	SS mean (µm)	SD	Skewness
IOTA_52	19660.0	5898.0	4	43.0	3.3	53.7	34.0	2.5	2.2	-0.7	26.4	0.8	0.1
IOTA_41	15440.0	4706.1	4	53.0	0.9	46.1	27.9	3.1	2.2	-0.3	22.6	0.7	0.0
IOTA_50	16381.0	4992.9	4	50.0	0.0	50.0	27.8	2.5	2.1	-0.6	23.7	0.7	0.0
IOTA_1	9800.0	2987.0	4	51.0	0.1	48.9	21.4	2.6	1.8	-0.3	19.2	0.6	-0.1

(b)

Sample	Depth (ft)	Depth (m)	Grain Size Type	Sample type	Corrected Porosity	r mean (nm)	r 10% (nm)	Temperature (C)	Total C (%)	TOC (%)	Measured Gs (g/cm^3)
IOTA_52	19660.0	5898.0	4	SWC	0.163	8.0	15.1	89.7	1.2	0.9	2.759
IOTA_41	15440.0	4706.1	4	SWC	0.18	13.6	24.5	69.1	1.4	1.3	2.682
IOTA_50	16381.0	4992.9	4	SWC	0.222	16.3	29.4	74.8	1.0	0.5	2.805
IOTA_1	9800.0	2987.0	4	SWC	0.261	28.8	48.9	35.2	1.3	0.5	2.75

Table 3.8 (a) Grain size data and (b) physical property data for Type 4 samples with a porosity of 16 - 26%. Grain size and pore-throat size distributions shown in Figure 3.21.

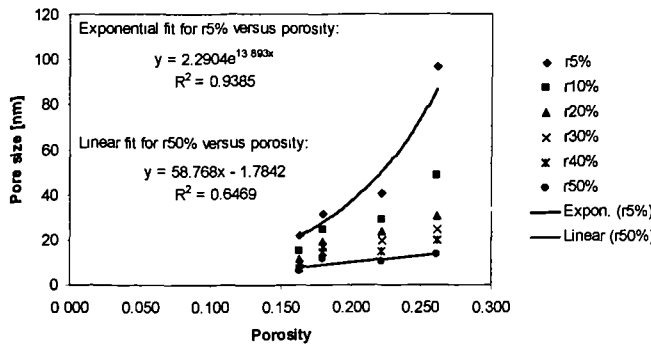


Figure 3.22. Percentile – porosity plot derived from the four Type 4 samples presented in Fig. 3.21; r5% decreases exponentially and r50% decreases linearly, illustrating how the decrease in r5% is more rapid as the bulk of compaction occurs via collapse of the largest pores.

At porosities between 25.9 – 22.3%, the differential pore throat size distributions of grain size Type 5 samples are bimodal, with the first mode occurring between 500 – 800nm

and a second mode between 10 – 40nm (Fig. 3.23e,f). The progressive collapse and loss of the larger mode is illustrated in Figure 3.23e,f; once porosity has decreased to 11% the larger mode has almost disappeared, and the PSD has become unimodal in form and is dominated by pore radii $<100\text{nm}$. The two modes observed in the pore-throat size distributions of Type 5 samples most likely correspond to the lacunar and clay fabric pore space suggested to occur in clay – silt slurries by Fiés(1992). Grain size Type 5 examples characteristically have a significant coarse silt ($>10\mu\text{m}$) component that acts to increase the probability of forming a framework or skeleton that forms the lacunar pore space (cf. Section 3.1). As with Types 1 – 4, the bulk of the volume loss is contributed by the loss of the largest pores as illustrated by Figure 3.24.

The differential pore throat size distributions of the grain size GSD type 6 examples are similar to those of Type 5. They are bimodal in form with the first mode occurring at $\sim 1000\text{nm}$ and a second mode occurring $\sim 10\text{nm}$. Again the decrease in porosity leads to a progressive collapse and loss of the larger mode; the shift in the modal size is not as apparent as in the Type 5 examples (Figure 3.25e,f). The interpretation of this observation is complicated by a lack of knowledge of the size distribution of the sand component itself. Remnants of the larger mode are still present at a porosity of 11% however by this point the pore space is predominantly represented by the clay fabric pore space which apparently remains constant irrespective of porosity. Once porosity has decreased to 7.7% all the pore space resides in pores with radii $<20\text{nm}$ (Figure 3.25f).

In comparison to the other grain size types presented in this study the percentile – porosity plot (Figure 3.26) shows the most extreme reduction in r5% values relative to that of the r50% values with decreasing porosity.

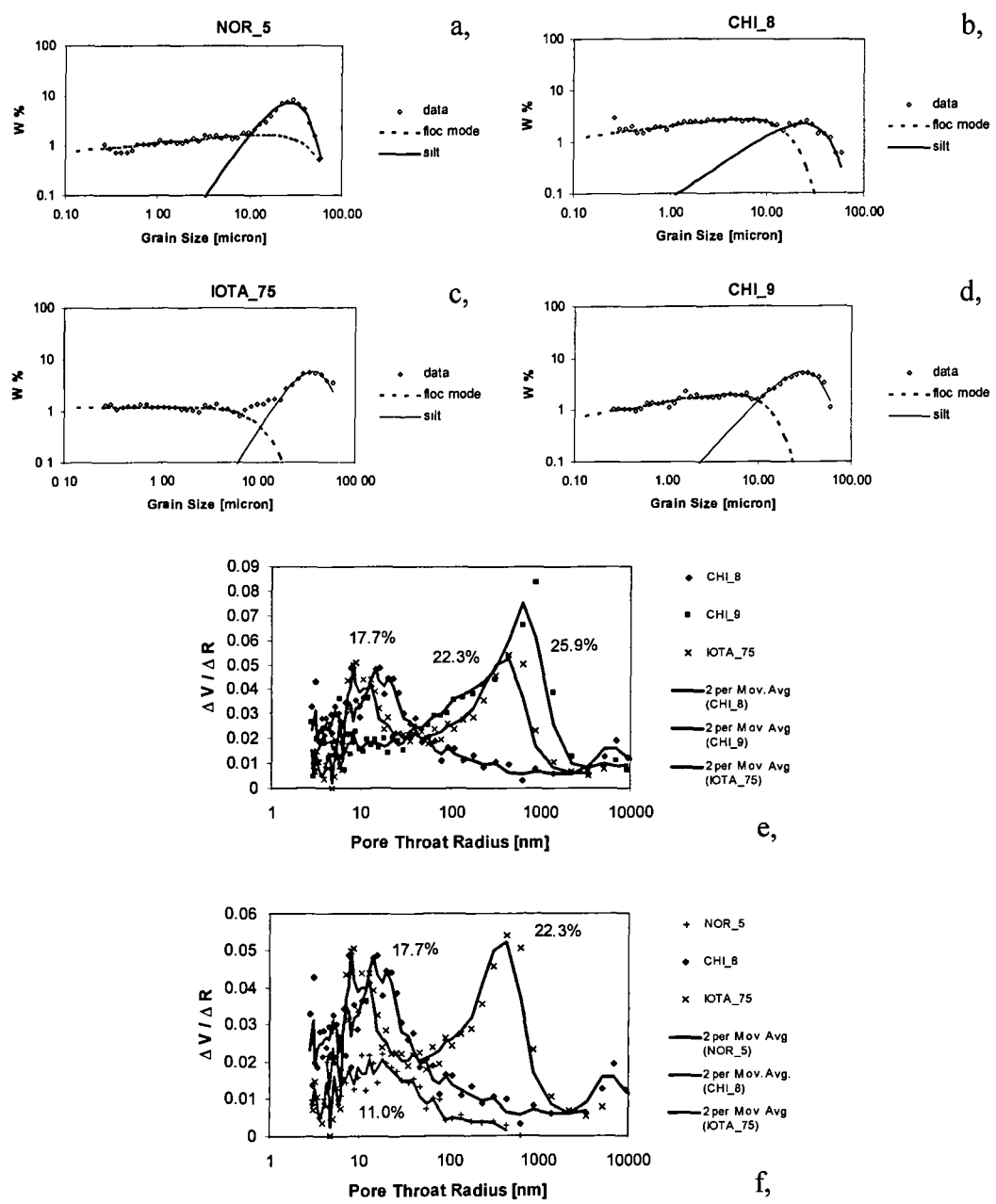


Figure 3.23. Grain size spectra (a – d) and differential pore-throat size distributions (e – f) of Type 5 grain size examples (porosities are given on plots e and f).

(a)

Sample	mmbfsfl		Grain Size Type					Whole distribution stats			Sortable Silt		
	Depth (ft)	Depth (m)		% Clay	% Sand	% Silt	% >10 μ m	Mean Grain Size (μ m)	SD	Skewness	SS mean (μ m)	SD	Skewness
NOR_5	9386.2	2860.9	5	18.1	4.7	77.3	70.6	10.1	2.0	1.4	25.9	0.6	0.1
CHI_8	12706.4	3872.9	5	34.4	0.8	64.8	36.4	3.5	2.1	0.0	21.9	0.7	-0.1
IOTA_75	18691.0	5697.0	5	26.7	9.8	63.5	64.0	8.8	2.4	1.3	31.4	0.7	0.2
CHI_9	12707.9	3873.4	5	21.5	4.6	73.9	62.5	7.8	2.2	0.9	27.6	0.7	0.1

(b)

Sample	Depth (ft)	Depth (m)	Grain Size Type	Sample type	Corrected Porosity	r mean (nm)	r 10% (nm)	Temperature (C)	Total C (%)	TOC (%)	Measured Gs (g/cm^3)
NOR_5	9386.2	2860.9	5	Plug	0.11	24.2	62.0	123.6	0.9	0.8	2.789
CHI_8	12706.4	3872.9	5	Core	0.177	496.7	1209.5				
IOTA_75	18691.0	5697.0	5	SWC	0.223	242.7	652.2				
CHI_9	12707.9	3873.4	5	Core	0.259	571.0	1231.9				

Table 3.9 (a) Grain size data and (b) physical property data for Type 5 samples with a porosity of 11 - 26%. Grain size and pore-throat size distributions shown in Figure 3.23.

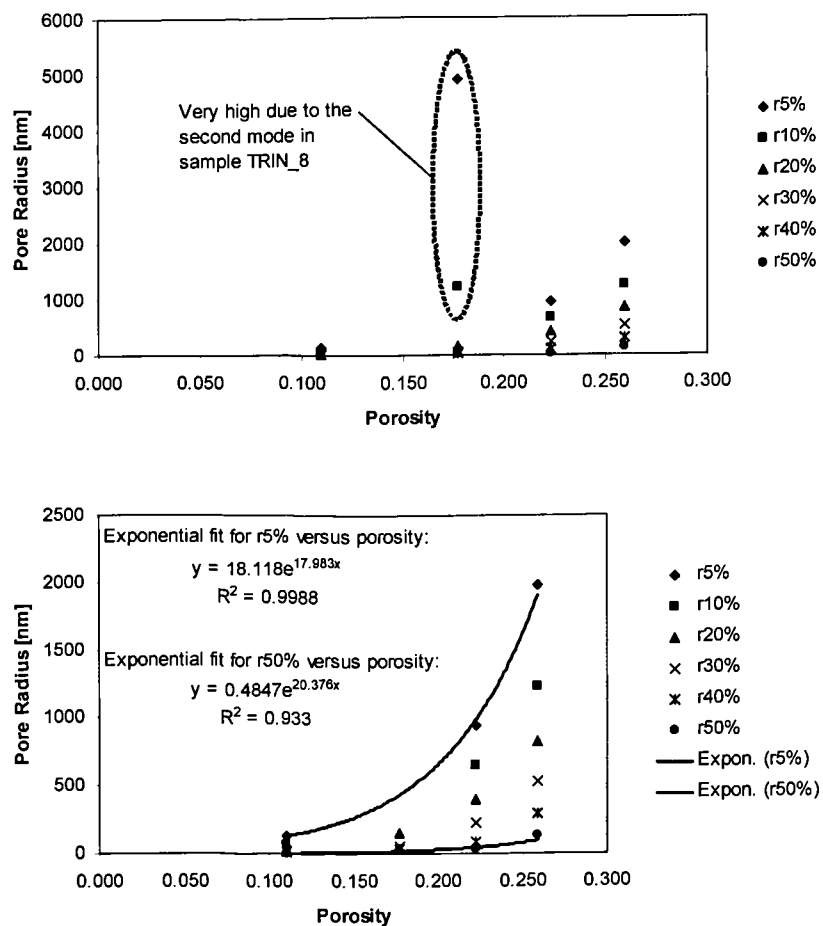


Figure 3.24. Percentile – porosity plot derived from the four Type 5 samples presented in Fig. 3.23; (a) 17.7% example (CHI_8) has a bi-modal form, this second mode occurs at much larger pore radii relative to the first mode (cf. Fig. 3.21e,f) resulting in the lower percentiles (r5%, r10%) having very large values. In (b) these percentiles were removed resulting in the data plotting in a similar manner to the other grain size types; r5% and r50% both decrease exponentially. The rate of decrease for r5% is much greater signifying that compaction occurs through collapse of the largest pores.

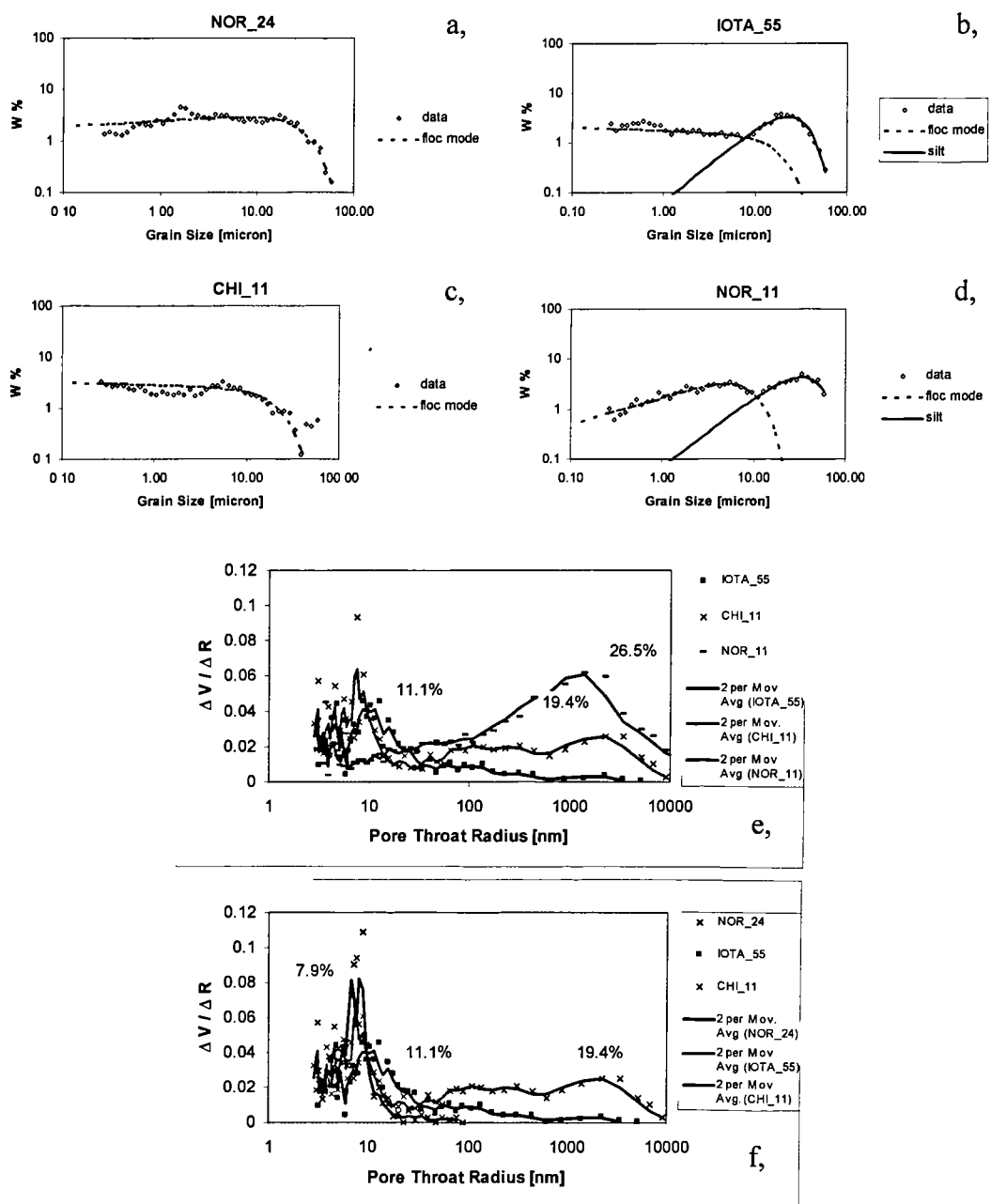


Figure 3.25. Grain size spectra (a – d) and differential pore-throat size distributions (e – f) of Type 6 grain size GSD type examples (porosities are given on plots e and f).

(a)

Sample	mmbst			Whole distribution stats				Sortable Silt					
	Depth (ft)	Depth (m)	Grain Size Type	% Clay	% Sand	% Silt	% >10µm	Mean Grain Size (µm)	SD	Skewness	SS mean (µm)	SD	Skewness
NOR_24	9181.4	2798.5	6	28.6	13.5	57.9	46.2	3.4	1.9	-0.1	19.5	0.6	-0.1
IOTA_55	21587.0	6476.0	6	36.2	15.2	48.6	54.0	3.7	2.3	0.1	22.3	0.6	0.0
CHI_11	13092.5	3990.6	6	30.9	16.4	52.7	39.2	2.3	2.0	-0.2	18.8	0.8	-0.3
NOR_11	6718.7	2047.9	6	12.7	33.8	53.5	72.6	6.6	2.1	0.5	27.7	0.7	0.1

(b)

Sample	Depth (ft)	Depth (m)	Grain Size Type	Sample type	Corrected Porosity	r _{mean} (nm)	r _{10%} (nm)	Temperature (C)	Total C (%)	TOC (%)	Measured Gs (g/cm ³)
NOR_24	9181.4	2798.5	6	Plug	0.079	8.8	11.0	104.6	3.4	2.4	2.696
IOTA_55	21587.0	6476.0	6	SWC	0.111	106.9	146.3	102.2	1.1	1.1	2.662
CHI_11	13092.5	3990.6	6	Core	0.194	731.6	3198.0				
NOR_11	6718.7	2047.9	6	Plug	0.265	1403.4	3990.3	59.9	1.0	1.0	2.752

Table 3.10 (a) Grain size data and (b) physical property data for Type 6 samples with a porosity of 8 - 26%. Grain size and pore-throat size distributions shown in Figure 3.25.

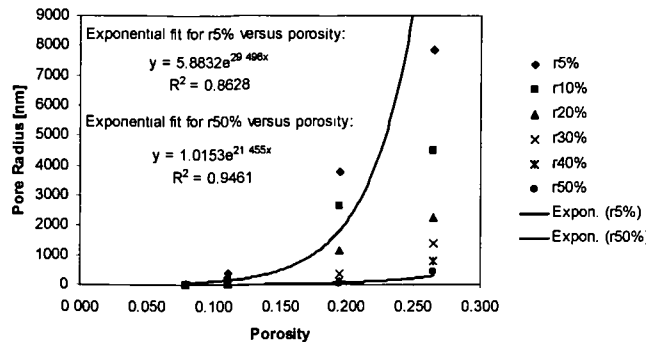


Figure 3.26. Percentile – porosity plot derived from the four Type 6 samples presented in Fig. 3.25; both r5% and r50% decreases exponentially, the decrease in r5% is more rapid illustrating that the bulk of compaction occurs through collapse of the largest pores.

3.4.3 Behaviour of samples with intermediate grain size characteristics

A subset of Type 1 – 4 samples drawn exclusively from the Iota Area was investigated to assess the consistency of the observations made in Sections 3.4.1 and 3.4.2. Figure 3.27 illustrates the decrease in the mean pore-throat size with decreasing porosity from grain size types 1 – 4. In general these cross plots illustrate a consistent behaviour whereby the mean pore throat size decreases exponentially with increasing compaction. There was a high degree of scatter on the Type 4 r mean – porosity cross plot (Fig. 3.27d). The assumption was made that the variability observed on this cross plot was not due to sample quality (all samples were side wall cores).

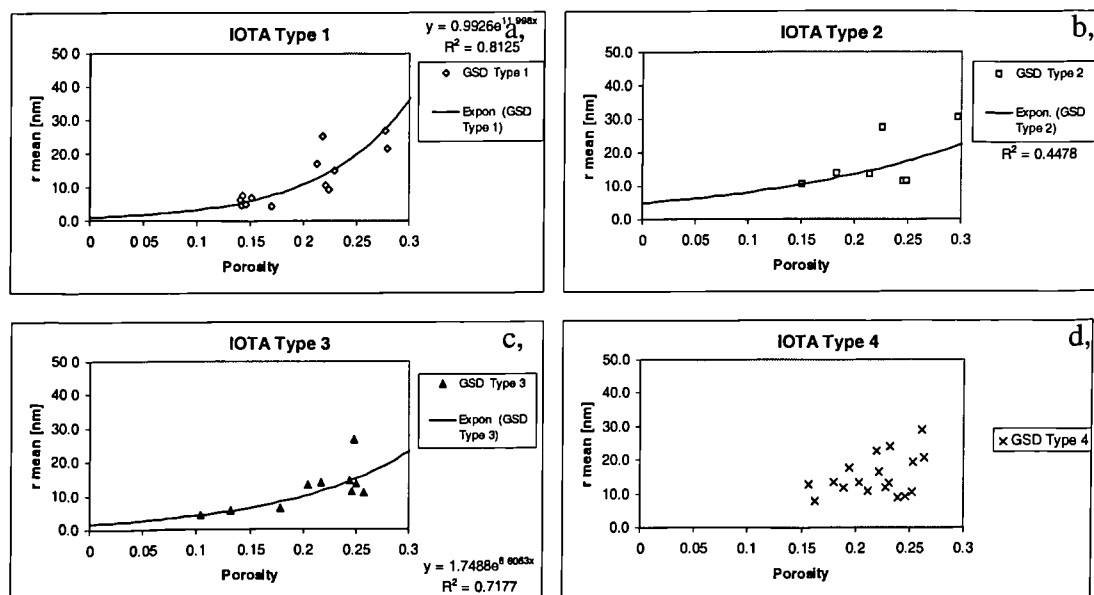


Figure 3.27. Porosity – r mean cross plots for (a) Iota Type 1 samples, (b) Iota Type 2 samples, (c) Iota Type 3 samples and (d) Iota Type 4 samples.

A further subset of the Iota Type 4 group of samples with porosities between 21 – 24% were isolated to assess the degree to which variations in terms of the grain size distribution could account for the variation observed on the r mean – porosity cross plot (Fig. 3.28a).

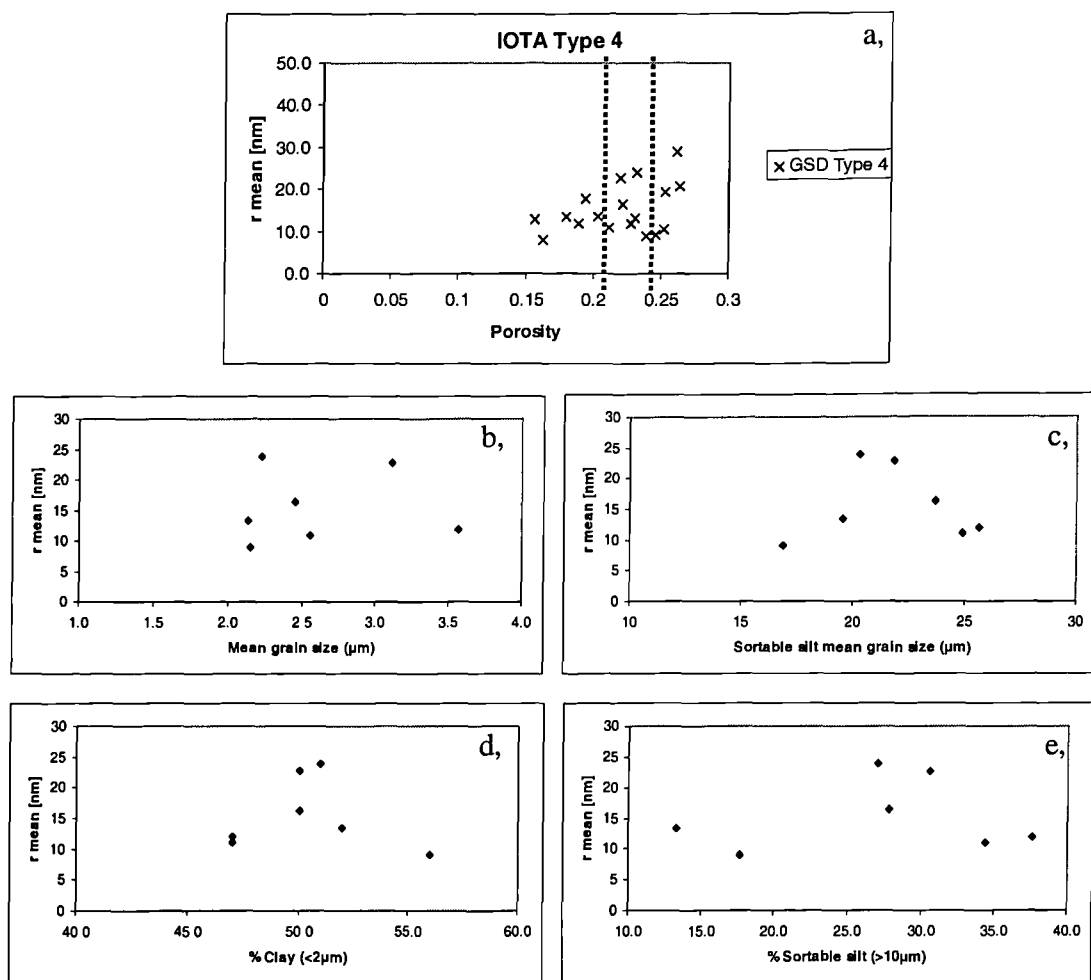


Figure 3.28. Data for the Iota Type 4 subset depicting (a) the porosity – r mean cross plot, the lines demarcate the porosity range (21 – 24%) over which the degree to which variations in grain size distribution could account for the variability seen in the pore-throat size distributions. (b) mean grain size (μm) – r mean cross plot, (c) mean sortable silt grain size (μm) – r mean cross plot, (d) clay content – r mean cross plot and (e) sortable silt – r mean cross plot.

Analysis of the mean grain size (μm), mean sortable silt grain size (μm), clay content (% $<2\mu\text{m}$) and sortable silt content (% $>10\mu\text{m}$) revealed no relationship between the magnitude of these parameters and the r mean value (Fig. 3.28b – e). This result suggests that when porosity is constrained factors over than grain size distribution play a role in controlling the nature of the pore-throat size distributions of mudstones. A similar

investigation for Type 5 – 6 samples could not be carried out as no adequate samples were available in the dataset used in this study.

3.5 Discussion

Comparison of the each of the grain size types PSD's at similar compaction states clearly illustrates the two characteristic forms of PSD's observed in this study of naturally compacted geological samples.

At porosities below ~30% the pore-throat size distributions of Type 1 – 4 mudstones are unimodal. Essentially all pore diameters are smaller than 80nm, with modal values decreasing from ~50nm to <10nm as porosities decrease from 30% to <10%. Type 1 – 4 mudstones have mean grain sizes <4 μ m, are typically comprised of >40% clay particles (% <2 μ m) and have sortable silt fractions (% >10 μ m) below 40% (see Figure 3.5). It is inferred that the load bearing phase in these mudstones is dominated by the clay matrix and that the PSD represents the clay fabric associated porosity suggested by Fiés(1992) to exist in dried clay – silt slurries.

In contrast the PSD's of types 5 – 6 are typically bimodal implying the presence of pore space relating to both, the clay fabric, and silt and/or sand framework. At high porosities pores with diameters up to ~10,000nm are incorporated into the PSD's of Type 5 – 6 samples; modal values decrease by up to two orders of magnitude as porosities decrease from 30% to <10%. At low porosities the larger mode is lost due to the preferential collapse of the largest pores and the PSD's evolve to be similar to those of Type 1 – 4 samples with the pore diameters <100nm. Type 5 – 6 mudstones have mean grain sizes >4 μ m, are composed of <40% clay particles (% <2 μ m) and have sortable silt fractions (% >10 μ m) above 40% (see Figure 3.5). It is inferred that the load bearing phase in these mudstones is initially dominated by a sortable silt (>10 μ m) and / or sand framework and that the PSD represents the lacunar porosity suggested by Fiés(1992) to exist in dried clay – silt slurries.

Previous work has illustrated that a finer grained sediment will compact at a faster rate than a coarser sediment given an identical loading history (e.g. Skempton, 1970; Burland, 1990, Aplin *et al.*, 1995; Dewhurst *et al.*, 1998, 1999). Therefore the grain size Types 1 – 4 would be more compressible than Types 5 – 6. This difference may be accounted for by the differing modes of load bearing regime hypothesised to exist and account for the differing behaviour seen for Type 1 – 4 and Type 5 – 6 with regard to their pore-throat size distributions

The progressive shift and modal decrease in the unimodal PSD's of types 1 – 4 coupled with the percentile – porosity plots illustrates how the bulk of porosity loss predominantly occurs via the collapse of the largest pore (throats), this results in a progressive shift of the PSD to smaller pore throat radii with decreasing compaction quantified by the exponential decrease in $r50\%$. This is thought to reflect both the paucity of large pores in types 1 – 4 and the re-arrangement processes termed densification and volume distortion by Dewhurst *et al.*, (1998). Densification refers to the collapse of clay aggregates, because marine mudstones are partly formed by the deposition of clay flocs or aggregates (cf. Kranck and Milligan, 1985) they can be thought of as one of the elementary building blocks of these sediment types. Volume distortion occurs through the grain boundary shearing / sliding within the aggregates and between the aggregates and the silt and/or sand grains present (cf. Dewhurst *et al.*, (1998) and refs. therein).

The observation that these sample types lack lacunar pores space, which is consistent with their grain size distribution characteristics, coupled with the observation that compaction seemingly occurs through the collapse of all pores is thought to reflect the fact that a framework or skeleton comprising silt and/or sand grains is not present. Thus the load is applied to the large surface area corresponding to the clay-silt 'matrix' formed predominantly by clay aggregates and individual silt grains.

The results of Sections 3.4.1 and 3.4.2 indicate that Type 5 and 6 grain size GSD types exhibit bimodal PSD's which evolve into unimodal PSD's with increasing compaction. The clay fabric pore space present in types 5 and 6 is comparable in terms of its range of

pore-throat radii to the PSD's encountered in types 1 – 4. The lacunar pore space corresponding to the silt and / or sand framework comprises pores with radii up to 3 orders of magnitude larger than those in the clay fabric pore space. Such a difference in size would clearly have a significant influence upon physical properties that are partly dependent upon the pore network such as permeability (e.g. Dewhurst *et al.*, 1999). The percentile – porosity plots for types 5 and 6 were similar to those derived for types 1 – 4; however the degree of reduction seen in r5% was much greater.

The degree to which 'within type' lithological variation accounted for the scatter seen in mean pore-throat size – porosity cross plots was investigated in Section 3.4.3. The majority of samples were shown to behave in consistent manner as illustrated in section 3.4.1. Type 4 samples did show a high degree of scatter; analysis of a number of grain size parameters failed to account for the differing r mean values when porosity was constrained. This result suggests that when grain size and porosity are effectively constrained, other factors not accounted for in this study such as diagenetic history and mineralogy, also play a role in determining the nature of the pore-throat size distributions of mudstones.

The division of the data into two distinct groups comprising types 1 – 4 with unimodal PSD's (corresponding to clay fabric pore space) and types 5 – 6 with bimodal PSD's (corresponding to both clay fabric and lacunar pore space) is largely in agreement with the studies carried out by Dewhurst *et al.*, (1998, 1999a). Dewhurst *et al.*, (1999a) did observe the presence of a sample seemingly intermediate between two these groups (see Figure 3.8, 49% clay sample). Dewhurst *et al.*, (1999a) results illustrated that for samples with clay fractions between 33 and 49% it is not clear whether there is a clay fraction at which the properties change abruptly or that the physical properties of the London Clay vary continuously. It was argued that the potential for an abrupt change in behaviour is real as the decreases in clay content is accompanied by an increase in the amount of silt and/or sand grains. When this component is comprised of relatively coarse rounded grains of quartz and feldspar (with distinct properties to platy clay minerals), if

its proportion reaches some critical value the probability of developing a framework or skeleton is increased which would lead to differing geomechanical properties.

The results of this study imply that there is an abrupt change in behaviours but it is not solely dependent upon the clay content. Unfortunately there are very few samples with clay contents between 33% and 49% in the sample set utilized in this study at similar levels of compaction and therefore further work would be required to investigate the nature of the transition between the two behaviours observed in this study.

3.6 Chapter 3 Conclusions

The work presented here effectively represents a continuum of the work carried out by Fiés(1992) on artificial clay – silt and clay – sand slurries; observation made upon soils by Griffiths and Joshi (1989) and analysis carried upon artificially and naturally compacted geological samples carried out by Dewhurst *et al.*, (1998, 1999a) and Yang and Aplin, (1998) respectively. This study has illustrated that the division of porosity into clay fabric pore space and lacunar pore space is applicable to naturally compacted geological mudstone samples. The samples analysed here clearly exhibited two modes of behaviour, generally marine mudstones types 1 – 4 (typically with clay contents >40%) below porosities of 30% had unimodal pore throat size distributions, here implied to represent porosity within and between clay flocs and silt grains. These distributions are almost entirely composed of pores with throat radii <100nm; modal values decreased from ~50nm to <10nm as porosity decreases from ~30% to <10%. Grain size types 5 – 6 typically have clay contents <40% and exhibit bimodal pore throat size distributions; the smaller diameter mode was comparable to the clay fabric mode characteristic of types 1 – 4, and the second mode comprised pore throats with radii ~ 2 orders of magnitude larger than the clay fabric mode. This second mode is considered to represent pore space created by silt and / or sand grains and corresponds to the lacunar pore space of Fiés(1992). This second mode was seen to decrease both in size and in volume with decreasing porosity and is eventually lost, producing unimodal pore throat size distributions similar to those of types 1 – 4. Overall it has been demonstrated that the

observations made by Fiés(1992) upon artificial slurries are relevant and applicable to naturally compacted geological media.

Examples exhibiting intermediate characteristics between these two characteristic modes of behaviour were not observed in this study implying that these modes of behaviour are distinct, at least in naturally compacted geological samples with less than 30% porosity. There was a paucity of samples with grain size characteristics that are likely to be transitional between the two modes (i.e. clay contents in the 30 – 40% range); the majority of those that did fall into this range were the terrestrial samples from the Zeta Area and were particularly rich in fine silt in the 2 - 10 μm range (cf. Section 3.3). If the loess rich Zeta samples are disregarded then it would seem that the sortable silt content is a key lithological predictor in determining the nature of a mudstones pore-throat size distribution, however further work would be required to further elucidate this statement.

From the results presented in this study an abrupt change in behaviours is favored over a smooth transition; the grain size parameters that dictate this transition are complex, clay content alone is insufficient to account for the behaviour of mudstones because once its drops below ~40% the size distribution of the silt content and the sand content become significant. Sortable silt has the potential to be a useful lithological description for mudstones as it corresponds well with both the clay content and with the nature of the silt content for the majority of samples.

The observation of these two modes of behaviours has significance for the fluid transport properties of such sediments as they are largely dependent upon the pore throat size distribution (cf. Dewhurst *et al.*, 1999a). The distinction in behaviours implies that permeability models should perhaps be calibrated to predict the porosity-permeability relationship of one mode of behaviour or the other as a single model is unlikely to accurately predict the properties of both. Greater understanding of how the grain size distribution influences the pore throat size distributions of mudstones will lead to improved capillary seal risking strategies, and will enable regional seal studies to be

focused upon the distribution and dimensions of grain size GSD types likely to constitute significant seal risk.

Future work could include the integration of more detailed analysis of sedimentary environments and modes of deposition with analysis of the grain and pore-throat size distributions. For example, the Type 2 PSD's are particularly tight containing very few pores with radii $>50\text{nm}$ even at 26.9% porosity. It was proposed in Chapter 2 that type 2 samples represent deposition from high concentrations, for example density flow deposits such as debris flows. The high internal stresses coupled with the likely instantaneous load upon deposition (due to their rapid deposition) characteristic of such deposits may result in particular closely packed textures resulting in the observed tight PSD's such hypotheses could prove valuable in predicting physical properties (flow, acoustic etc) and warrants further investigative studies of well constrained data.

Chapter 4 Combined PCA-cluster analysis based classification of mudstone grain size data

4.0 Introduction

In Chapter 2 a number of mudstone grain size distribution types were proposed to account for the variability and characteristics commonly recorded in the analysis of mudstone grain size data. The six grain size types proposed were defined upon the basis of integrated grain size analysis, including grain size distribution modelling and observations made from thin section and BSEM images. The types were defined arbitrarily and as such this work proved to be time consuming and laborious.

Besides providing a framework in which to understand the depositional processes responsible for the formation of fine grained sedimentary deposits, the definition of a number of mudstone grain size types could facilitate the definition of low permeability flow units or facies for input into large scale geological fluid flow models known as basin models. By proposing a number of mudstone ‘types’ *a priori*, we can simply provide basin modellers with options on how to populate the fine grained section of their models. Additionally, by utilising a classification partially based upon depositional mechanism, grain size fining trends and perhaps more complex sedimentary variations may be included in large fluid flow models.

This work has three purposes. Firstly, to propose the definition of grain size based mudstone types with which to ‘build’ a low permeability facies atlas. Secondly, to discuss classification methodologies and introduce a combined principal component – k mean analysis scheme with which to facilitate the definition of grain size mudstone types. Thirdly, to test a combined PCA-cluster analysis classification technique on four datasets which utilise differing data reductions of grain size data to assess sensitivity of the approach to differing grain size data types. The results are compared to the mudstone types proposed in Chapter 2 and the relationship between grain size type and the petrophysical properties is also discussed.

4.1 Classification and clustering of geological data

The various techniques of multivariate pattern recognition and classification methods were reviewed by Doveton (1994) with regard to their use in relating petrophysical and geological data thus allowing facies and geologically significant variations to be recognised purely from petrophysical data. In this work the aim is to integrate the flow, petrophysical and sedimentological properties of mudstones. Similar approaches have been taken previously by: (1) Driscoll *et al.*, (1985), who used principal component analysis (PCA) to map grain size trends related to zonations of current speeds, water properties and abyssal eddy kinetic energy across the Nova Scotia lower continental rise; (2) Gill *et al.*, (1993), who proposed numerical cluster analysis as a useful tool in the zonation of petrophysical data; (3) Watney *et al.*, (1999), who applied cluster analysis to the petrophysical properties of sandstone reservoirs in a ‘petrofacies’ analysis of the Arroyo Field (Kansas, USA).

Doveton (1994) contrasts “deductive” or top-down approaches which impose a solution with “inductive” or bottom-up approaches that are solely based upon the characteristics of the data; these two approaches can be seen as end-members. In Chapter 2 a number of grain size groups were deduced in a heuristic manner and therefore a solution was imposed upon the dataset. Geological phenomena are typically continuous in nature and thus such classifications can represent a falsehood; however they also allow for greater understanding of the data and provide ways in which it may successfully be used to solve geological problems. Here an inductive approach is taken where classification using a combined PCA-cluster analysis approach is based purely upon the data (although it is presented in comparison to the deductive solution proposed in Chapter 2). Three questions are associated with the combined PCA-cluster analysis approach taken here:

- 1) How well does the PCA extract factors that account for variation present in the dataset?
- 2) How good is the clustering result?
- 3) How well do the clusters correlate to the flow and petrophysical properties of the samples analysed?

The complexity of the relationship between the grain size distribution and the evolution of the pore-throat-throat size distribution with increasing compaction has been illustrated and discussed in Chapter 3. Due to the ambiguous nature of the exact relationship between grain size distribution and

pore-throat-throat size distribution a number of datasets relating to grain size are used here, as the clustering result will only be as good as the significance of the principal components extracted. If the components extracted related to sedimentary parameters, which play a minor role in the evolution of the pore-throat network then the defined clusters will not separate out samples whose pore-throat networks behave in a similar manner. Furthermore the dataset used here is comprised of data of widely varying geological ages and settings, so that factors such as mineralogical content, cementation history etc may perturb any simple relationships.

4.2 Dataset and Data Manipulation

The basic aim of this work was to develop a methodology for the rapid classification of mudstones based on some description of their grain size distributions. Four differing combinations of grain size data were utilised. The same combined PCA – k-means clustering approach is applied to each dataset. The first dataset comprised a range of sedimentary parameters defined below; the second and third dataset comprised the grain size frequency distribution data, and the fourth dataset comprised a combined sedimentary statistic-grain size distribution dataset. The content and manipulation of each dataset is explained below. All data were standardised by scaling to a range between 0 (minimum values) and 1 (maximum value).

4.2.1 Moment statistics and sedimentary parameters dataset

The 8 sedimentary parameters included in the principal component analysis are described below; many of these data types had to be manipulated or standardised prior to input into the principal component analysis, a description of which is also given below:

% Clay: ranges between 0 – 1. Proven lithology – physical property predictor (e.g. Yang and Aplin, 1998, Yang and Aplin, 2004)

% Sand: ranges between 0 – 1 (in reality always <0.3). Plays an increasingly dominant role in the compaction behaviour of fine grained sediments as it increases above 10% (>0.1).

% $>10\mu\text{m}$: ranges between 0 – 1. Was proposed as a ‘palaeocurrent’ proxy by Yokokawa and Franz (2002). May also play an important role in the compaction behaviour of fine grained sediments (Chapter 3).

Mean grain size (μm) (0-63 μm component): records the mean grain size of the ‘mud’ component of the grain size distribution derived by the method of Griffiths (1967). The range of values was scaled to lie between 0 and 1.

Standard deviation (0-63 μm component): Standard deviation of the grain size distribution derived by the method of Griffiths (1967). The range of values was scaled to lie between 0 and 1.

Skew (0-63 μm component): Skew of the grain size distribution derived by the method of Griffiths (1967). Because PCA does not allow negative values the Skewness scale had to be rescaled; this was done by simply adding the maximum absolute skew value to each skew value, shifting the range into an entirely positive range. This led to the range of the skew values and the distance between samples values remaining the same, but simply removed the negative values. The range of values was then scaled to lie between 0 and 1.

Mean grain size of the Sortable Silt fraction (μm) (10-63 μm component): records the mean grain size of the sortable silt component of the grain size distribution, proposed as a ‘palaeocurrent’ proxy by Bianchi *et al.*, (1995) derived by the method of Griffiths (1967).

Skew of the sortable silt fraction (10-63 μm component): Skew of the sortable silt grain size fraction derived by the method of Griffiths (1967). The skewness scale had to be rescaled because PCA does not allow negative values, this was done by simply adding the maximum absolute skew value to each skew value, shifting the range into an entirely positive range. The range of values was scaled to lie between 0 and 1. This parameter was included as an attempt to differentiate: (1,) entirely flocculated (Type 1 and 2, see Chapter 1), (2,) floc - silt mixtures / pure silts (Types 3, 4 and 5 Chapter 1) and (3) truncated distributions (Type 6c Chapter 1). Entirely flocculated distributions will have negative values (or low after manipulation to remove negative values prior to PCA) because the bulk of these distributions lies below 20 μm (Figure 4.1). Mixtures of flocculated and silt material and pure silts will have a proportion of sediment lying between 10 - 63 μm , which will typically approximate a log-

normal distribution and hence skew values will be close to zero (Figure 4.2) Truncated distributions result from the sieving process (at 63 μm) performed prior to Sedigraph analysis to remove the sand component – where the fine sand and silt components form a continuous distribution the sieving will truncate the distribution at the high end, resulting in a positively skewed distribution (Figure 4.3).

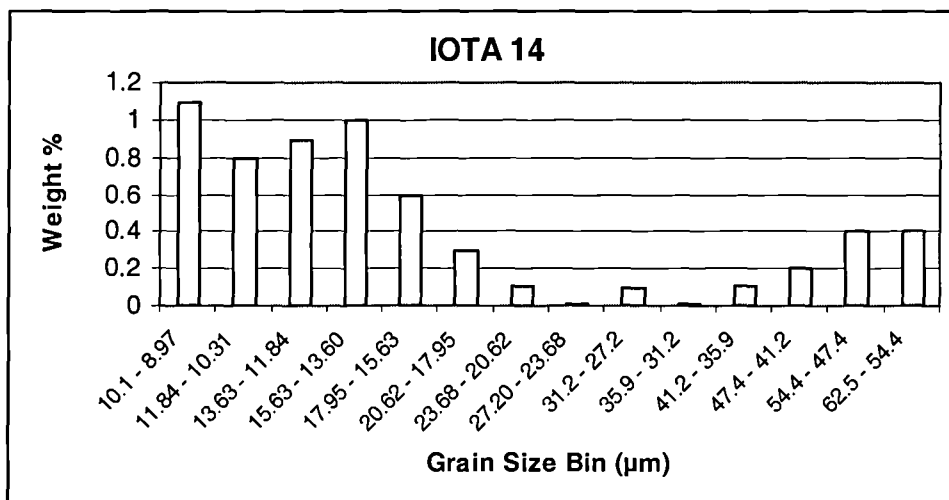


Figure 4.1. The distribution of sediment in the sortable silt range (10-63 μm) for an entirely flocculated sample (Type 2) from the deep water Iota Area (note most grains have a diameter <10 μm). The distribution parameters are as follows: mean grain size 5.79 phi (18.06 μm), standard deviation 0.83phi, skew -0.43 phi.

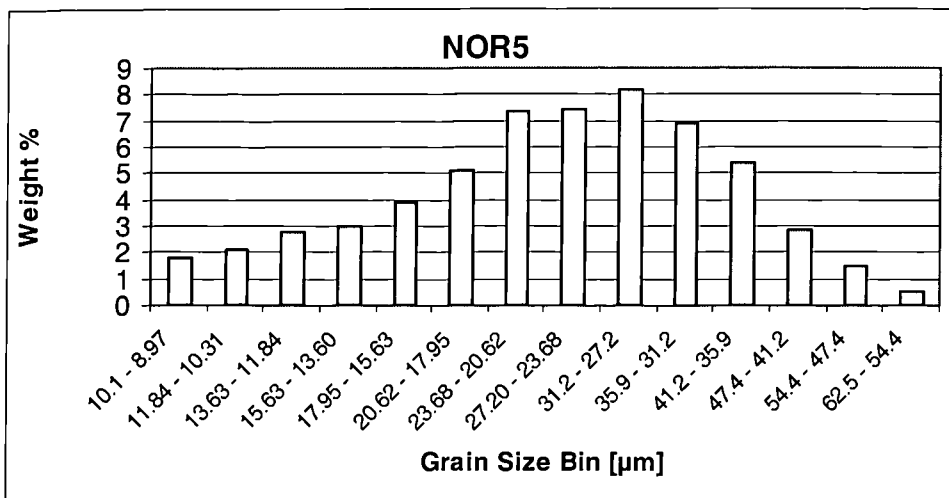


Figure 4.2. The distribution of sediment in the sortable silt range (10-63 μ m) of a floc – silt mixed grain size distribution (Type 5) from the shallow marine Heather Formation (Late Jurassic North Sea). The distribution parameters are as follows: mean grain size 5.27phi (25.95 μ m), standard deviation 0.6phi, skew 0.08phi.

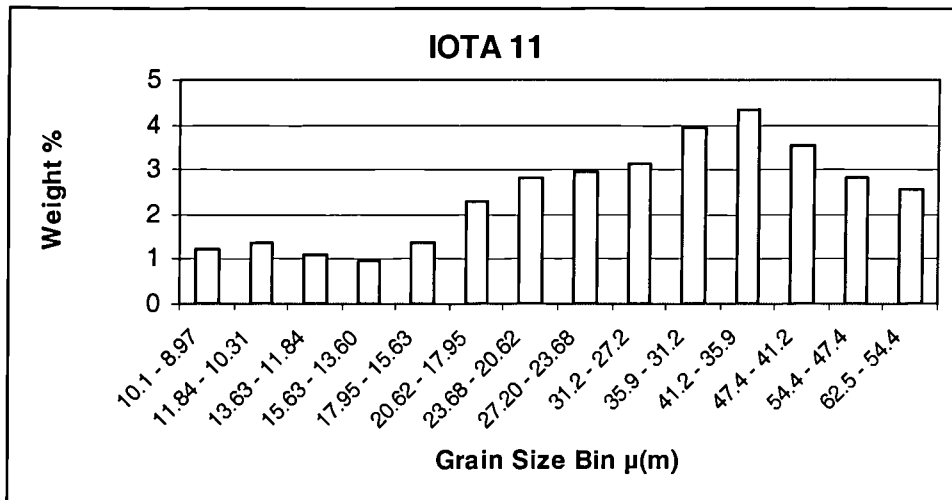


Figure 4.3. The distribution of sediment in the sortable silt range (10-63 μ m) of a floc – silt – sand mixed grain size distribution (Type 6) of a sample from the deep water Iota Area. The distribution parameters are as follows: mean grain size 5.03phi (30.71 μ m), standard deviation 0.71phi, skew 0.16phi.

4.2.2 Whole phi bin dataset

The second dataset consisted of the grain size frequency distribution in the form of weight percent per grain size bin. Bin boundaries were taken at integer phi values (converting grain size class limits in mm to base-2 logarithms and changing the sign) so that each grain size bin represents a smaller size range than the previous one, reflecting the highly skewed nature of these distributions (e.g. Davis, 2002). The sum of each weight percentage value per sample was set to equal 1.

4.2.3 0.2 phi bin dataset

The third data set used was identical to the whole phi bin data set, except that the bin boundaries were set at 0.2 phi values, increasing the resolution of the dataset (with 41 grain size bins as opposed to 9), but also potentially enhancing the significance of small errors present in the dataset. The sum of each weight percentage value per sample was set to equal 1.

4.2.4 Combined dataset

The final dataset combined the dataset defined in 4.2.1 and 4.2.2; each value per sample from each dataset was divided by 2 so that when the datasets were combined, the total value for the sum of the parameters was equal to 1 per sample. Therefore no preferential weighting was given to either dataset or any one parameter. This dataset is referred to as the combined dataset in the text below.

3.3 Methodology: Combined PCA-k-means clustering of mudstone sedimentary parameters

Initially each dataset was subjected to PCA analysis using SPSS; components were extracted from the dataset using the principal component method without rotation. The PCA was carried out for two reasons: (a) to reduce the data prior to input into the k-means cluster routine; (b) to derive a set of orthogonal parameters for use in the cluster analysis routine. This second point is significant as many of the parameters included in the various data sets are highly correlated (see Davis, 2002) which will induce errors in the clustering procedure (see Wishart, 2003a). The extracted components were then classified using cluster analysis. The k-means clustering technique was preferred as other cluster

analysis methodologies typically incorporate a hierarchical ordering of the clusters; the classification of mudstones based on their grain size distribution characteristics is not thought to be structured hierarchically and therefore the k-means approach is utilised.

The cluster analysis procedure forms groups or clusters of maximum homogeneity and thus acts to minimise within-cluster variance. Initially the 162 cases, each described by the significant components (i.e. eigenvalues >1) derived in the PCA analysis were clustered to form a tree by the Increase in Sum of Squares (ISS) method (see Appendix 4.1), also known as Wards method. Subsequently the ‘best cut’ and ‘validation’ options in *ClustanGraphics* were used to estimate the best number of clusters for each dataset. Although the optimum number of clusters may differ between each dataset, having the same number of clusters for each dataset greatly eases comparison between the results obtained for each dataset. Therefore a compromise value best for all datasets was judged to be the best approach to take. Furthermore, because one aim of this work is to assess the degree of correspondence between rapidly classified grain size ‘clusters’ and the pore-throat network (quantified here by r mean), a requirement of this study is that each cluster is sufficiently populated to make such a judgement, thus precluding the definition of a large number of clusters per dataset. As a guide to the optimum number of clusters to use the ‘best cut’ option in *ClustanGraphics* was used. This *ClustanGraphics* module aims to assess how many clusters are present in a dataset by applying a significance test to a series of fusion values in the data tree, the upper tail significance test was utilised; all partitions up to the largest number of clusters significant at the 5% level are given (Wishart, 2003a) i.e. the significance of decreasing the variance by increasing the number of clusters by one was assessed.

Once the number of clusters was specified, each dataset was subjected to the *FocalPoint* k-means clustering analysis procedure in *ClustanGraphics* to refine the cluster model by case relocation. The case relocation procedure allows, at each iteration, every case to be compared with the clusters in the current solution and are either left where they are, assigned to a new cluster or designated as unclassified (i.e. an outlier) (Wishart, 2003b). A case will only be relocated if this reduces the Euclidean Sum of Squares (ESS) (see Appendix 4.1) (Wishart, 2003b). In *ClustanGraphics* both the k-means and *FocalPoint* routines use an ‘exact relocation criteria’ (termed exact assignment test by Wishart, 2003a). A case i from cluster p is assigned to a new cluster if:

$$ESS_p + ESS_q > ESS_{p-i} + ESS_{q-i} \quad (4.1)$$

where ESS_p is the error sum of squares for cluster p, ESS_q is the error sum of squares for cluster q, ESS_{p-i} is the remaining error sum of squares, if case i is moved towards cluster q. ESS_{q-i} is the error sum of squares, if case i is added to cluster q.

Each analysis performed 5000 iterations and the case order was randomised at the start of each iteration as k-means analysis is particularly sensitive to case order (Wishart, 2003b). The starting strategy utilised an initiation of random clusters, after which subsequent steps modify the partition to reduce the sum of the distances for each case from the mean of the cluster to which it belongs. The running means option was used, specifying that the cluster mean is re-calculated every time a case is moved, rather than once every iteration (Wishart, 2003).

4.3.1 Cluster – Pore-throat-throat size distribution (\approx flow properties) linkage

To make an assessment of the relationship between the cluster groups defined and their flow properties, the mean pore-throat-throat size was used as a simple parameter relating to the flow properties of the sediment. The mean pore-throat-throat size is highly correlated with $r10\%$ - the upper tenth percentile of the pore-throat-throat size distribution (Figure 4.4) commonly used to estimate the critical capillary entry pressure of mudstones; furthermore the mean pore-throat-throat size is used as input into porosity-permeability models (Figure 4.5) which have been found to be superior to other model types based on grain size, surface area etc (cf. Yang and Aplin, 1998; Dewhurst *et al.*, 1999a, b).

The principal controls upon the flow properties of mudstones are porosity (compaction state) and grain size distribution (cf. Yang and Aplin, 1998; Dewhurst *et al.*, 1999a, b). By cross plotting the r mean parameter against porosity the degree to which the flow properties of the samples placed into a single group or cluster (accounting for grain size) behaved in a consistent manner was assessed.

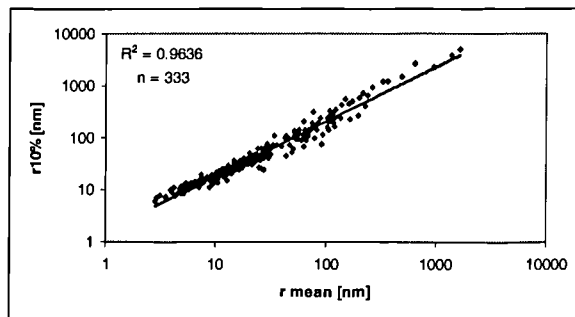


Figure 4.4. r mean [nm] versus $r10\%$ [nm] for mudstone data held at the University of Newcastle (porosity range 4.2% to 36.4%; clay content range 11% - 90%); 'cuttings' samples were removed from this dataset.

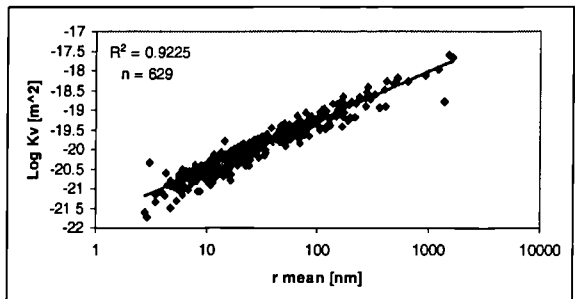


Figure 4.5. r mean [nm] versus K_v [m^2] derived from the Yang and Aplin (1998) permeability model for mudstone data held at the University of Newcastle (porosity range 4.2% to 36.4%; clay content range 11% - 90%).

4.4 Results

4.4.1 Principal Component Analysis

The number of principal components extracted varied for each of the four datasets considered in this study. The scree plots derived from the PCA analysis of each of the datasets are shown in Figure 4.6. A scree plot is a 2-dimensional plot with factors (components) on the x -axis and eigenvalues (an eigenvalue Y for matrix X is the scalar multiple of c , the eigenvector of X , such that $X c = Y c$) on the y -axis. Eigenvalues are derived from PCA and represent the variance accounted for by each extracted component. In SPSS eigenvalues <1 are assumed to represent error variation and therefore are disregarded.

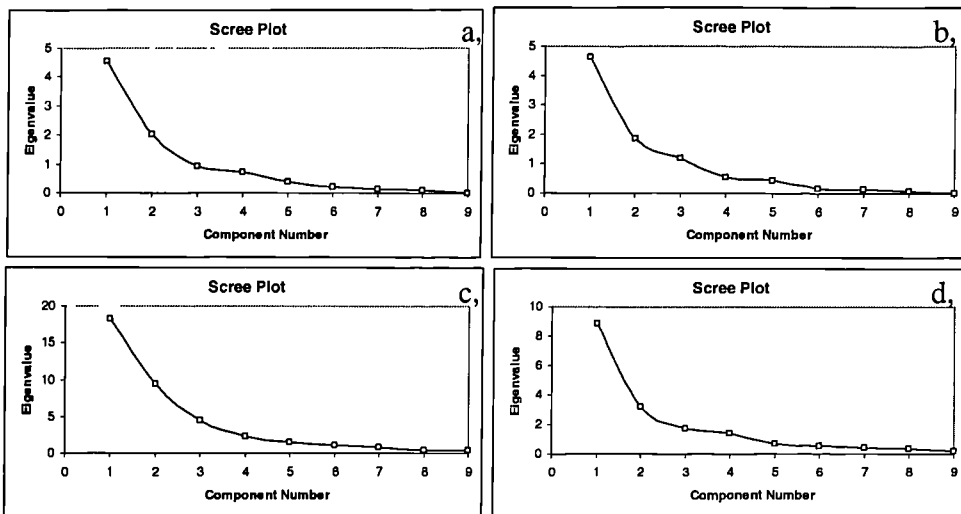


Figure 4.6. Scree plots derived from PCA analysis of: (a) the sedimentary statistic / parameter dataset, (b) the whole phi bin grain distribution dataset, (c) the 0.2 phi bin grain distribution dataset, and (d) the combined dataset.

From Figure 4.6 it can be seen for the sedimentary statistic and parameter data set only the first two components have eigenvalues >1 . Together these two components account for 73.28% of the total variance (Table A4.2.1). For the whole phi bin dataset 3 components are extracted, accounting for 85.38% of the total variance (Table A4.2.2). A total of six factors were extracted accounting for 89.89% of the variance exhibited (Table A4.2.3). Finally, the combined dataset was reduced to 4 components which account for 84.07% of the variance exhibited by the dataset (Table A4.2.4).

4.4.2 *k*-means clustering

The significant components (i.e. eigenvalues >1) derived in the PCA analysis were clustered to form a tree by ISS and a 'best cut' with validation test was performed in *ClustanGraphics* in order to investigate which number of clusters best accounts for the variability of the dataset. Some of the results of these analyses are shown in Figure 4.7, which plots the Cumulative Euclidean Sum of Squares (CESS) (Appendix 4.1) as a function of the number of clusters. The sedimentary statistic and parameter dataset shows the most dramatic drop in cumulative ESS as the cluster number is increased, while the 0.2 phi bin dataset does not exhibit a distinct drop; the other two datasets are intermediate between these two (Fig. 4.7). From this procedure it can be seen that between 6 and 8

clusters will best describe each dataset, while maintaining a sufficiently high number of samples per cluster for them to be adequately populated with data.

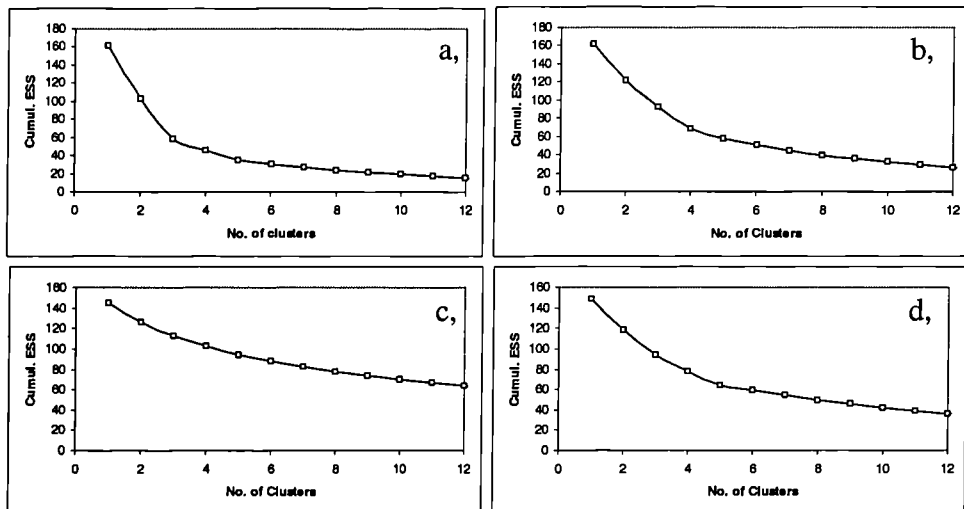


Figure 4.7. Validation of the 'best cut' analysis carried out in *ClustanGraphics* software, plotting Cumulative Euclidean Sum of Squares versus cluster number for: (a) the sedimentary statistic / parameter dataset, (b) the whole phi bin grain distribution dataset, (c) the 0.2 phi bin grain distribution dataset, and (d) the combined dataset.

Focal point clustering was then carried out in order to find the most stable clustering grouping for this dataset; 5000 iterations were performed, the cluster number being allowed to vary between 6 and 8. The statistics relating to the focal point cluster solution are given in Tables A4.3.1 – A4.3.4; the reproducibility for the cluster solutions was consistently low for each of the datasets (<1 – 15% of 5000 iterative trial solutions). The author of the Clustan software expressed surprise at this given that the dataset only comprised two to six variables, suggesting a bug in the software (D. Wishart, 2004, *pers. comm.*); as Clustan are at present the only software vendors offering this type of analysis the cluster solution with the lowest CESS was selected rather than the most reproducible one (Tables A4.3.1 – A4.3.4).

A key aim here is to test the application of rapid techniques for classifying mudstone grain size data and to integrate these with petrophysical and flow property data. No matter how accurate the cluster analysis is, if the dataset is clustered on parameters which have a poor correspondence to petrophysical and flow properties, the ultimate aim of this study is unattainable using these

procedures. For these reasons, the accuracy, dependency and precision of the cluster analysis is of secondary importance compared to the degree to which the grain size clusters correspond to the grain size type and to the pore-throat network (represented by r mean). Emphasis will therefore be placed upon the interpretation of the cluster population.

4.4.3 Cluster Population

Each of the cluster analyses output a set of eight grain size clusters that correspond to the grain size types identified in Chapter 2 to varying degrees. The sedimentary statistic and parameter dataset showed the poorest correspondence to the pore-throat networks and grain size types (Figure 4.8); the majority of the defined clusters correspond to multiple grain size types and the scatter on the porosity – r mean cross plots is typically high. Only clusters 2 and 5 show any degree of constrained correspondence to grain size types 1 / 2 and 5 / 6 respectively. This is reflected by the consistent behaviour seen on the corresponding porosity – r mean cross plots which generally have a lower degree of scatter relative to those for the other clusters (Figure 4.8).

The whole phi bin does slightly better identifying clusters composed of either Types 1 – 4 or Types 5 – 6. Most groups are fairly heterogeneous, however cluster six is composed entirely of Type 5 samples and cluster eight is dominated by Type 1 samples. It is perhaps not surprising that these grain size types represent the end members in the clay-silt mixing spectrum. The r mean – porosity cross plots show reasonable trends with much of the scatter attributable to the inclusion of cuttings in the dataset.

The 0.2 phi bin cluster result has a reasonable correspondence to the grain size types identified in Chapter 1. Cluster one is composed entirely of Type 5 samples and cluster two, three, four, seven and eight are dominated by grain size Types 2, 1, 6b, 6c and 4 respectively. Of the remaining clusters, cluster five is composed of a mix of Types 1,2,3 and 4; the majority of cuttings samples are present in this cluster which is reflected in the r mean – porosity cross plot. Cluster six is predominantly comprised of a mix of Types 2 and 4.

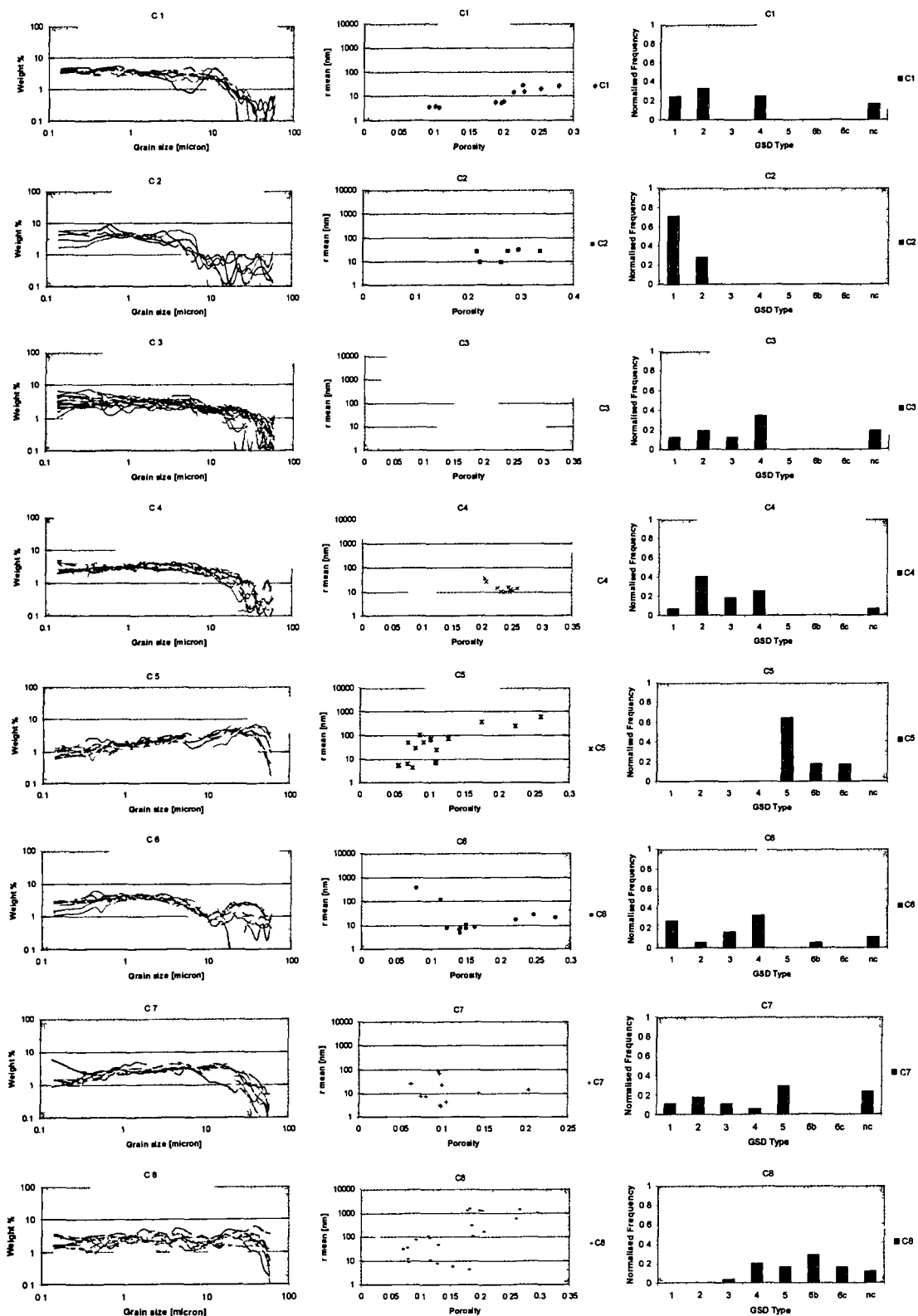


Figure 4.8. Results of the sedimentary statistic and parameter dataset PCA – cluster analysis, showing grain size distributions, r mean – porosity cross plots and grain size type partitions for each cluster (C1 to C8).

The combined dataset also produced satisfactory results; again a single cluster (three) was entirely composed of Type 5 samples. Cluster four mainly comprised of a mix of Types 5,6b and 6c while cluster eight was dominated by grain size Type 6b. Clusters one, two, five, and six were dominated by grain size Types 1 and 4, 3, 4, and 1 respectively; Cluster seven is an approximately equal mix of Types 1,2,3 and 4 with the majority of cuttings samples being present in this cluster which is reflected in the high degree of scatter on the r mean – porosity cross plot. For this dataset the segregation between Types 1 – 4 and 5 – 6 was less clear as Type 5 and Type 6b samples occurred in Type 1 – 4 dominated clusters (see clusters seven, two and one).

Overall the numerical classification methodology used here differentiates grain size Types 1 – 4 from grain size Types 5 – 6 irrespective of the grain size description on which the data is based. The degree of correspondence between the clusters and the grain size types proposed in Chapter 2 increases as the complexity of the description increased. This is illustrated by the observation that the sedimentary statistic and parameter dataset, described by 2 principal components, had the poorest correspondence to the Chapter 2 grain size types; whereas the 0.2 phi bin data, described by 6 principal components had the best correspondence to the grain size typed defined in Chapter 2. Although this is seemingly obvious, it does illustrate that more complex methods of describing mudstone grain size data do not contain redundant data.

The degree to which r mean was correlated to porosity as a function of a specific cluster was generally quantitatively poor. Tables 4.1 – 4.4 describe the cluster population in terms of the grain size types proposed in Chapter 2 and the correlation coefficients obtained from regressing r mean as a function of porosity for each of the datasets used. Generally the correlations are greatest when Types 1 – 4 are segregated from Types 5 – 6 which is consistent with the behaviours observed in Chapter 3. Common to all datasets are clusters composed of Types 1 – 4 which depict a low gradient trend and a cluster or clusters composed of Types 5 – 6c which depict a higher gradient trend illustrating the two modes of behaviour elucidated in Chapter 3. Departures from these trends are typically associated with:

- (a) the inclusion of Type 1 – 4 samples in a dominantly Type 5 – 6 cluster or vice versa,
- (b) the inclusion of cuttings, and
- (c) regional differences.

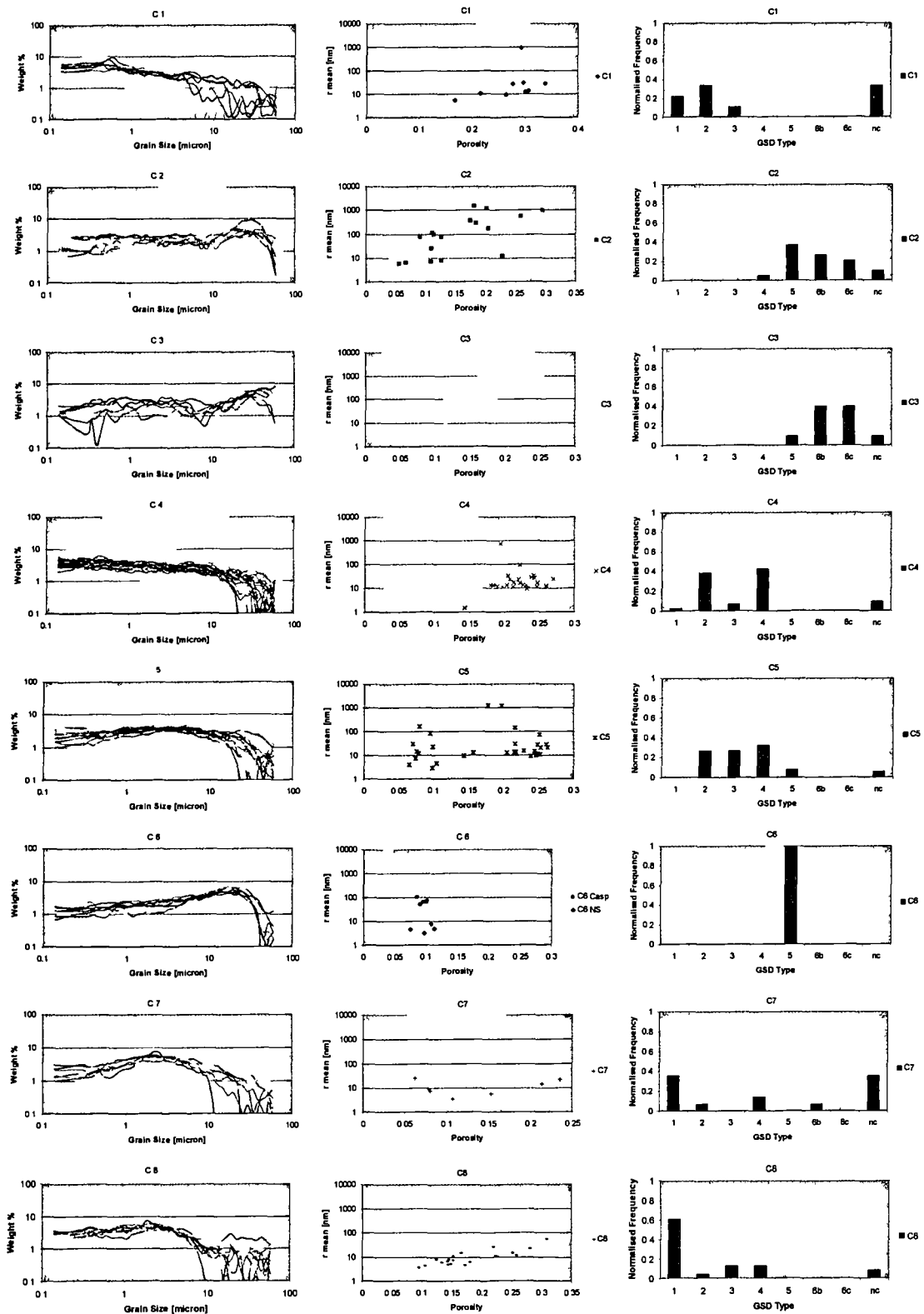


Figure 4.9. Results of the whole phi bin dataset PCA – cluster analysis, showing grain size distributions, r mean – porosity cross plots and grain size type partitions for each cluster.

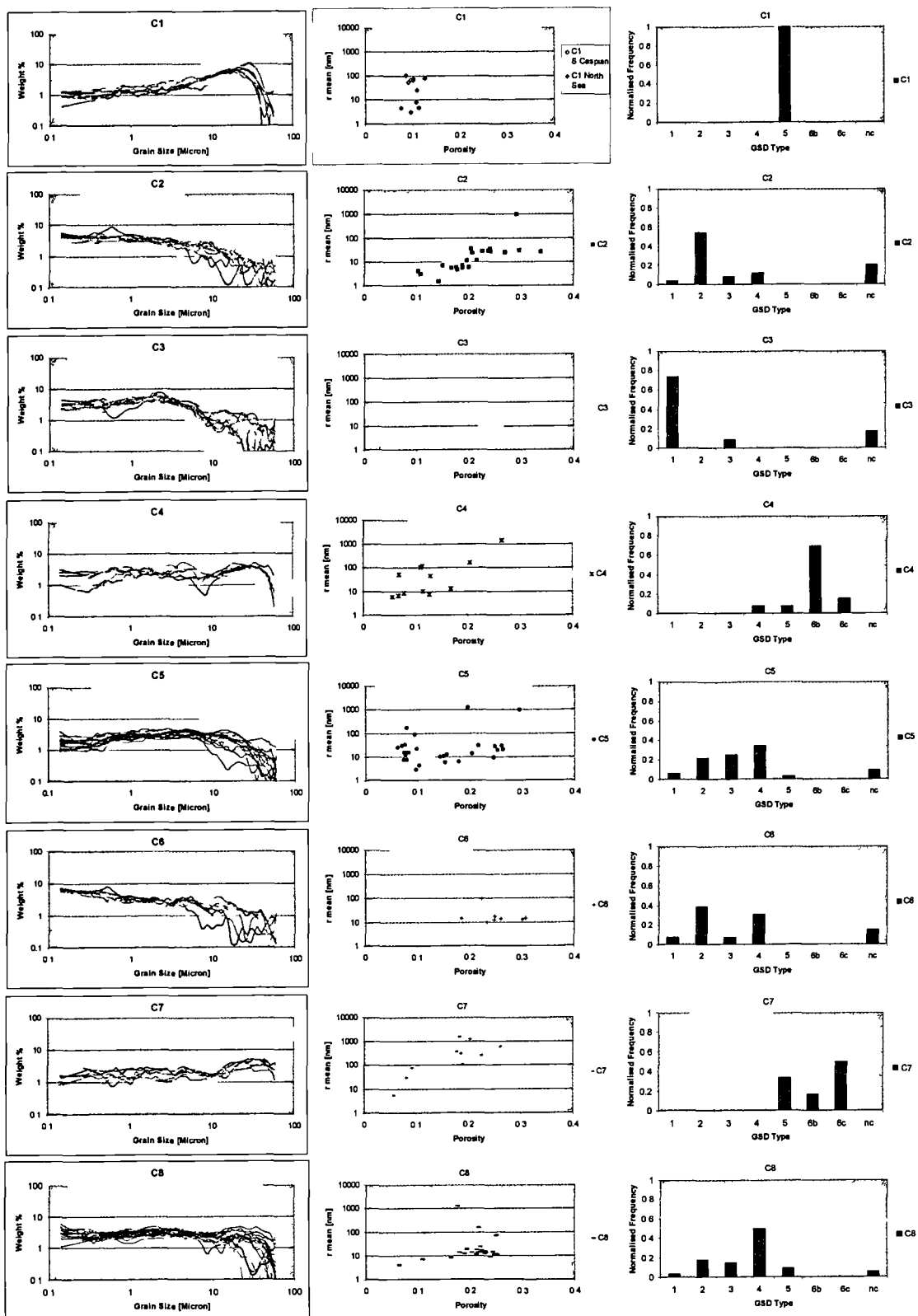


Figure 4.10. Results of the 0.2 phi bin dataset PCA – cluster analysis, showing grain size distributions, r mean – porosity cross plots and grain size type partitions for each cluster.

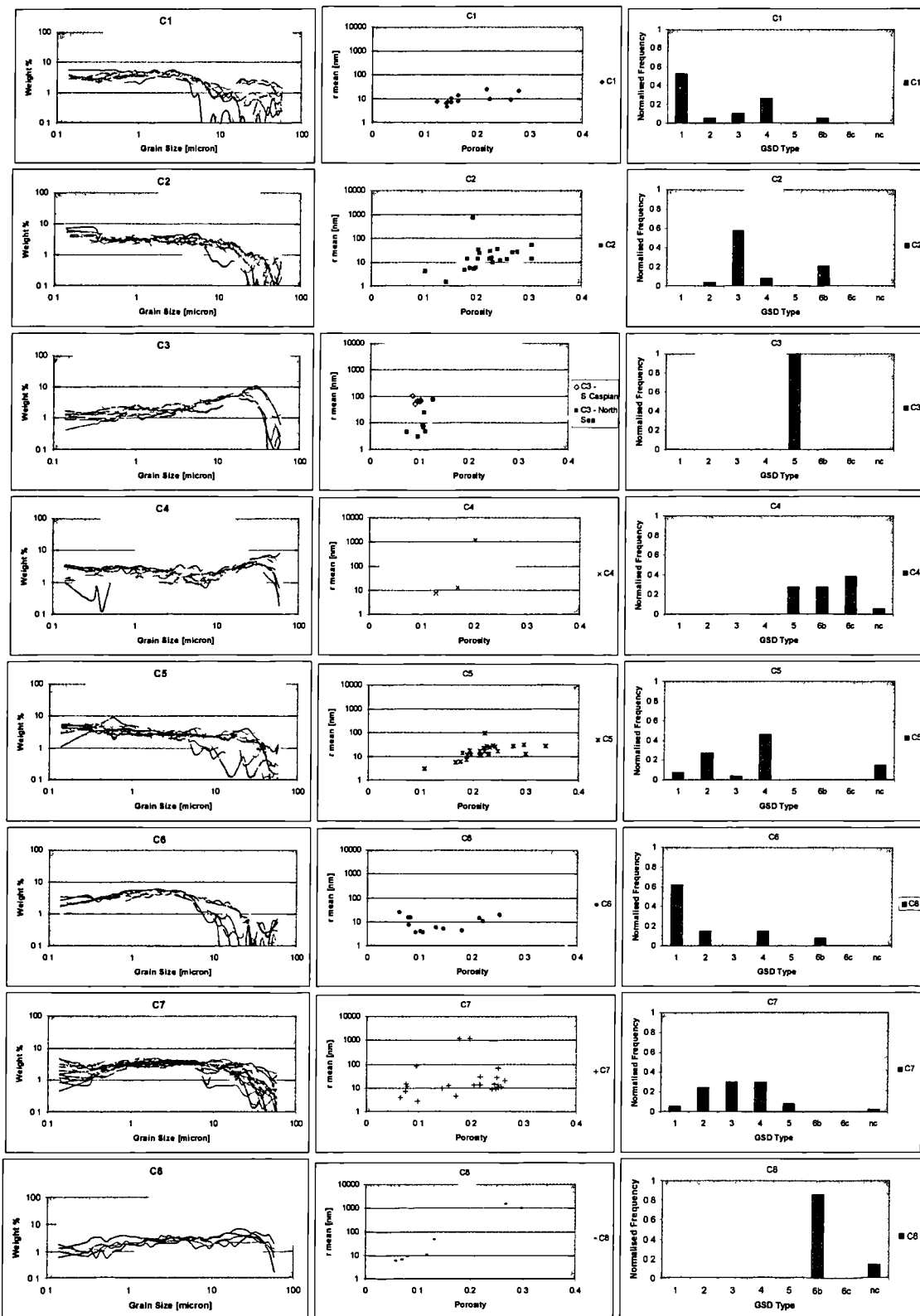


Figure 4.11. Results of the combined dataset PCA – cluster analysis, showing grain size distributions, r mean – porosity cross plots and grain size type partitions for each cluster.

Cluster Number	GSD types	porosity - r mean r^2	Notes
1	1,2,4	0.72	
2	1,2	0.21	Narrow porosity range
3	1,2,3,4	0.42	1 outlier removed from regression [spurious data]
4	1,2,3,4	0.56	
5	5, 6b,6c	0.6	
6	1,2,3,4, 6b	0.14	Inverse relationship i.e. as phi \downarrow r mean \uparrow
7	1,2,3,4, 5	0.03	Mixing framework and matrix supported samples?
8	3,4,5,6b,6c	0.38	Mixing framework and matrix supported samples?

Table 4.1. Sedimentary statistic and parameter dataset: distribution of the grain size types proposed in Chapter 2 as a function of cluster and the corresponding r^2 values for the porosity versus r mean regression [note cuttings were removed from this dataset].

Cluster Number	GSD types	porosity - r mean r^2	Notes
1	1,2,3	0.58	1 outlier removed from regression [spurious data]
2	4,5,6b,6c	0.51	
3	5,6b,6c	0.3	Broad age range (Jurassic to Plio-Pleistocene)
4	1,2,3,4	0.55	1 outlier removed from regression [spurious data]
5	2,3,4,5	0.46	Mixing framework and matrix supported samples?
6	5		Porosity range too narrow for regression to be significant
7	1,2,4,6b	0.05	Mixing framework and matrix supported samples?
8	1,2,3,4	0.68	All IOTA except 1 ZETA area sample

Table 4.2. Whole phi bin dataset: distribution of the grain size types proposed in Chapter 2 as a function of cluster and the corresponding r^2 values for the porosity versus r mean regression [note cuttings were removed from this dataset].

Cluster Number	GSD types	porosity - r mean r^2	Notes
1	5		Porosity range too narrow for regression to be significant
2	1,2,3,4	0.67	
3	1,3	0.71	
4	4,5,6b,6c	0.46	Mixing framework and matrix supported samples?
5	1,2,3,4,5	0.26	Mixing framework and matrix supported samples?
6	1,2,3,4	0.06	Porosity range very narrow
7	5,6b,6c	0.71	
8	1,2,3,4,5	0.001	Mixing framework and matrix supported samples?

Table 4.3. 0.2 phi bin dataset: distribution of the grain size types proposed in Chapter 2 as a function of cluster and the corresponding r^2 values for the porosity versus r mean regression [note cuttings were removed from this dataset].

Cluster Number	GSD types	porosity - r mean r^2	Notes
1	1,2,3,4,6b	0.49	
2	2,3,4,6b	0.49	
3	5		Porosity range too narrow for regression to be significant
4	5,6b,6c	0.49	
5	1,2,3,4	0.63	1 outlier removed from regression [spurious data]
6	1,2,4,6b	0.52	1 outlier removed from regression
7	1,2,3,4,5	0.34	
8	6b	0.92	

Table 4.4. Combined dataset: distribution of the grain size types proposed in Chapter 2 as a function of cluster and the corresponding r^2 values for the porosity versus r mean regression [note cuttings were removed from this dataset].

4.5 Discussion

The results presented here show that the cluster analysis, irrespective of the dataset used, generally segregates grain size Types 1 – 4 from Types 5 – 6, effectively separating those grain size types with low capillary seal risk from those with appreciable capillary seal risk (Chapter 3). The cluster analysis routine was typically unable to partition types 1, 2, 3 and 4, even though Types 1 and 2 have a fully flocculated form while Types 3 and 4 comprise floc-silt mixtures (Chapter 2). This indicates the rather subtle differences in the grain size distributions of type 1 – 4 mudstones. However, differentiation of Type 1 – 4 mudstones is probably of minor importance in terms of flow property modelling and seal prediction as these grain size types typically exhibit very similar pore-throat network properties (see Chapter 3 and Figures 3.7 – 3.10). The whole phi bin, 0.2 phi bin and combined datasets all isolated the bulk of the Type 5 samples into a single cluster, suggesting that these grain size types exhibit some fundamental differences from the others analysed in this study. Similarly, these datasets also all gathered the majority of the cuttings into a single cluster (cluster 5 in the whole phi and 0.2 phi bin datasets and cluster 7 in the combined dataset).

It is interesting that in the case of the 0.2 phi bin dataset, types 1, 2, 5 and even types 6b and 6c were differentiated. Type 6b and Type 6c were loosely defined on the basis of the continuity between the 0-63 μm component and the sand ($>63\mu\text{m}$) component – this definition was used as it was conjectured that when a significant coarse silt ($>10\mu\text{m}$) component was present to ‘bridge’ between the sand and fine silt – clay components the probability of creating and maintaining an effective

framework or skeleton is increased. Type 6b samples had ‘discontinuous’ distributions in that it was interpreted that the grain size distribution was bi-modal with a significant ‘gap’ between the silt and sand components; conversely Type 6c samples were interpreted as having continuous grain size distributions. On this basis Type 6b samples should show greater affinity with Type 3 and 4 samples and Type 6c samples should show greater affinity to Type 5 samples. This is borne out to some degree by clusters 4 and 7 respectively (Figure 4.10). Differentiating such grain size types can potentially have a significant impact on the geometrical arrangement of the grains (sedimentary fabric) and upon the flow properties; these observations and ideas are discussed in Chapters 3 and 5.

The results presented in Chapter 3 illustrate that only grain size Types 5 and 6 have the potential to maintain relatively open, broad pore-throat throat size distributions below porosities of ~20%, so that only they constitute a capillary seal risk. Here, the possibility of segregating these grain size types from other mudstones (i.e. Types 1 – 4) using rapid data reduction and numerical classification techniques has been proven on a number of differing grain size datasets. If the capillary sealing behaviour of mudstones can be placed into a bi-partite partition of ‘good’ and ‘bad’ capillary seals, only 2 grain size clusters may be required. Further investigations would be required to assess the degree to which the segregation between grain size types 1 – 4 and 5 – 6 would be maintained if only two cluster groups were allowed. Furthermore, such a bi-partite partition would not contain enough information with which to make subtle interpretations that can be made in the detailed analysis of mudstone grain size distributions as presented in Chapter 2 when PCA-k-means cluster groups are defined using high resolution frequency distribution data, such as the 0.2 phi bin dataset.

4.5.1 Relationship between clusters and petrophysical data

In this section the relationship between the clusters and their corresponding wireline log data is investigated. The petrophysical data relating to the samples in each of the clusters identified were investigated with regard to assessing the degree to which they could be identified purely from their petrophysical response. The aim was to assess the extent to which grain size data (i.e. the solid matrix) corresponds to the petrophysical response; because most logs respond to both the solid matrix and pore-throat network and its filling fluid the wireline logs were transformed in an attempt to remove the influence of the pore-throat network (cf. Yang *et al.*, (2004). The petrophysical data

assessed included the gamma ray, and the m log, the D log and the Δt_m log defined in Yang et al., (2004):

1). m log: The m log is derived from the resistivity and density logs, m is the coefficient in the Archie's equation and is dependent upon the rock type and texture (Rider, 1996):

$$F = \frac{1}{\phi^m} \quad (4.2)$$

where F is the formation resistivity factor and ϕ is the porosity. The formation resistivity factor is defined as:

$$F = \frac{R_o}{R_w} \quad (4.3)$$

where R_o is the overall rock resistivity ($\text{ohm m}^2 \text{ m}^{-1}$), derived from the deep resistivity log, and R_w is the resistivity of the formation fluid, which is assumed to be $0.1 \text{ ohm m}^2 \text{ m}^{-1}$. Combining equations (2) and (3) gives the equation used to calculate m :

$$m = -\frac{\ln\left(\frac{R_o}{R_w}\right)}{\ln(\phi)} \quad (4.4)$$

2). D log. The D log is derived from the sonic and resistivity logs and is based on the work of Meyer and Nederlof (1984) who used a sonic-resistivity cross-plot to identify petroleum source rocks. Meyer and Nederlof (1984) described a parameter, D , which is related to transit time and resistivity as:

$$D = -6.906 + 3.186 \log(\Delta t) + 0.487(\log(R_{75})) \quad (4.5)$$

Where R_{75} is resistivity at 75°F ($\text{ohm m}^2 \text{ m}^{-1}$) and Δt is transit time ($\mu\text{s ft}^{-1}$). R_{75} is derived from the measured resistivity at the corresponding temperature, T ($^\circ\text{F}$):

$$R_{75} = R_i \frac{T+7}{82} \quad (4.6)$$

3). Δt_m log. The Δt_m log is derived from the sonic and density logs. Δt_m is the transit time of the rock matrix and can be calculated from Wyllie *et al.*'s (1956) relationship between measured velocity and porosity. Their equation can be arranged as:

$$\Delta t_m = \frac{\Delta t - \phi \Delta t_f}{1 - \phi} \quad (4.7)$$

where Δt_f is the transit time of the interstitial fluid, taken here as $200 \mu\text{s ft}^{-1}$.

In Figures 4.12 and 4.13 the range of petrophysical properties for each of the clusters defined for the 0.2 phi bin and combined datasets are presented. Inspection of these figures clearly shows that there is a significant degree of overlap between the clusters and that no one petrophysical parameter would facilitate discrimination of these mudstone GSD type proxies.

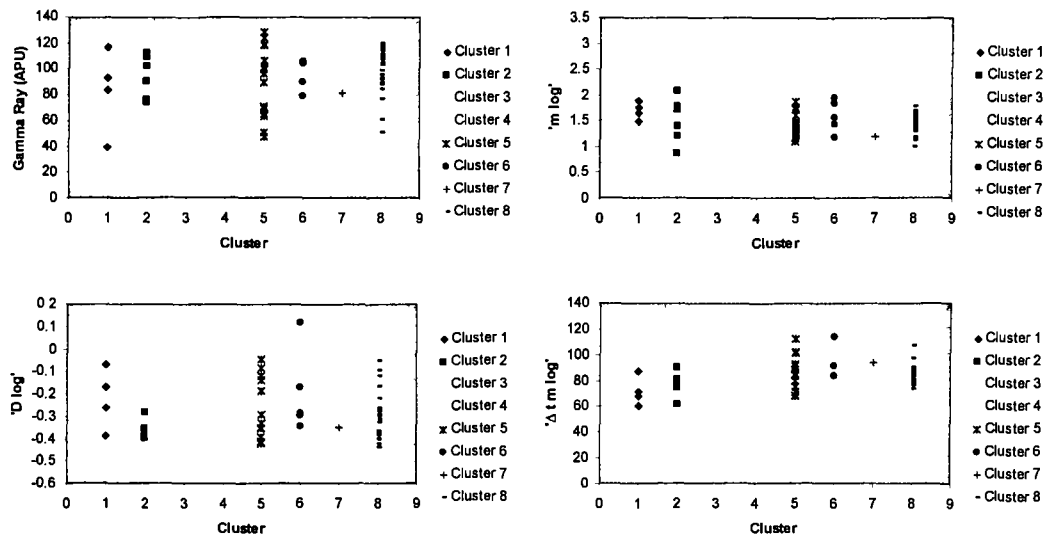


Figure 4.12. Plots illustrating the range of petrophysical responses as a function of cluster derived from the 0.2 phi bin dataset for: (a) Gamma Ray log (APU), (b) m log, (c) D log, and (d) the Δt_m log. See Figure 4.10 for the grain size distribution and r mean – porosity cross plots corresponding to each cluster. Clusters 1, 4 and 7 are dominantly composed of type 5 – 6 samples.

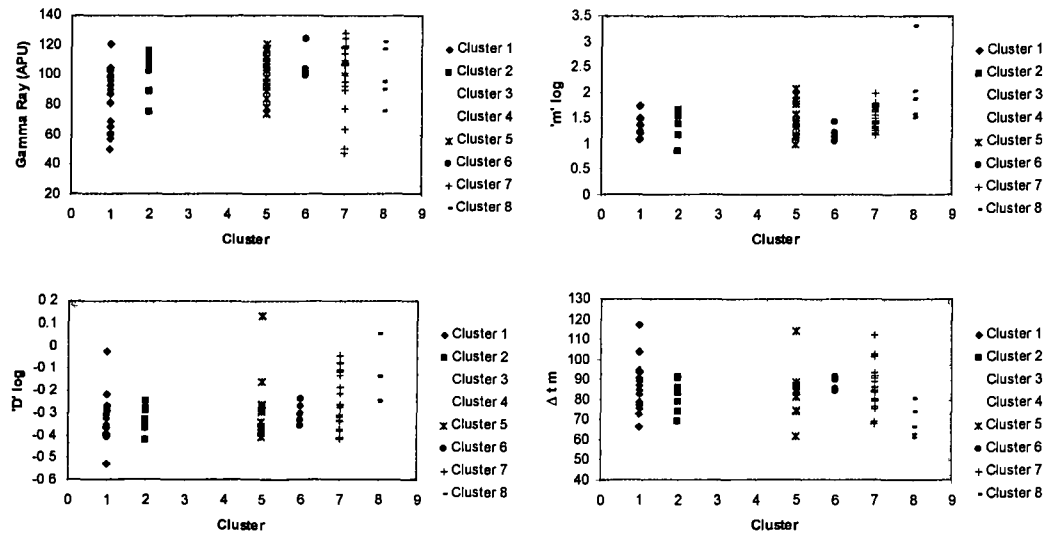


Figure 4.13. Plots illustrating the range of petrophysical responses as a function of cluster derived from the combined dataset for: (a) Gamma Ray log (APU), (b) m log, (c) D log, and (d) the Δt_m log. See Figure 4.11 for the grain size distribution and r mean – porosity cross plots corresponding to each cluster. Clusters 3, 4 and 8 are dominantly composed of Type 5 – 6 samples.

The reasons behind the poor discrimination between what are distinct mudstone lithologies are thought to be three-fold:

- 1) Scaling issues. The analyses upon which the mudstone typing carried out in Chapter 1 were based on samples of the order 1cm^3 in size whereas geophysical logging tools investigate volumes upwards of 50 cm^3 (Rider, 1996) leading to loss in correspondence between tool response and lithology in the presence of any sedimentological heterogeneity.
- 2) Regional effects. The approach taken in this study has been broadly ‘global’ in that location has not been explicitly considered. It is apparent that such an approach fails to extend to defining petrophysically different ranges in a global sense. This is perhaps unsurprising given the common requirement to perform regional calibration of petrophysical data prior to interpretation (for example finding the ‘shale baseline’). It is interesting to note that the gamma ray (Figure 4.12a and 4.13a) fails to discriminate the clusters defined and therefore does not apparently relate to mudstone lithology, as is commonly assumed. These results are in agreement with Yang *et al.*’s (2004) observations. This result is to be expected given that

the gamma ray log measures radioactivity which is strongly influenced by mineralogy rather than grain size (Rider, 1996).

- 3) Porosity – Lithology matrix. The dataset is unbalanced in terms of porosity ('compaction') and lithology (and typically in terms of geological age). The finest samples typically have the highest porosities (and are thus geologically youngest) and vice versa (see Figure 4.14); thus despite efforts made in transforming the logs to remove the effect of porosity, effects associated with geological age are likely to effect tool response.

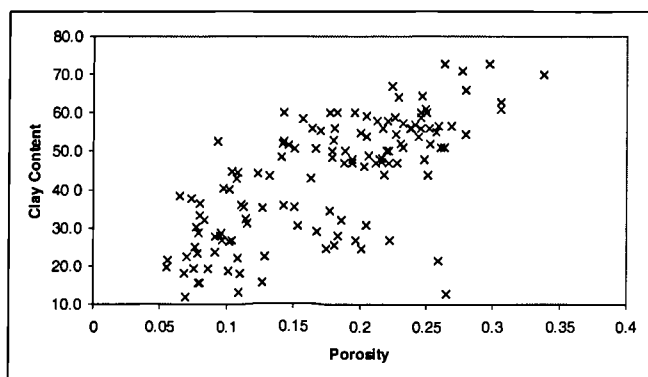


Figure 4.14. Cross plot illustrating the 'lithology (quantified by clay content) – porosity' matrix and the imbalance present in the dataset used in this study.

In his discussion on the challenges facing mudstone sedimentologists, Bohacs (1998) posed the following key questions: (a) 'What are the characteristic responses of mudrock environments on conventional well logs?' and (b) 'Is depositional environment the major control on well-log response – or is it sediment provenance, diagenetic history, tectonic setting?' From these results it would seem that log responses are unlikely to relate to specific depositional settings in a global sense. Similarly, this work indicates that correlating grain size to a single log response would be at the very least problematic. These results stress that multi-variate techniques which are calibrated to regional settings represent the best approach to discriminating mudstone lithologies and hence depositional environments (cf. Yang *et al.*, 2004). Further work, particularly well-constrained laboratory-based investigations upon well characterised mudstone samples, would greatly enhance efforts to link mudstone sedimentology to petrophysics.

4.6 Potential application – defining mudstone ‘flow’ facies as building blocks in geological models

It is a commonly stated fact that the sedimentary fill of the majority of sedimentary basins is dominated by fine grained sediments (e.g. Aplin *et al.*, 1999; Schieber *et al.*, 1998). Therefore attempts to model fluid flow within such environments require a quantitative understanding of these sediment types. Current exploration efforts are largely focussed in deep water, mud rich settings where the reservoirs are embedded in a three-dimensional, low permeability matrix – it is both the interconnectedness of these high- and low-permeability facies (Fogg, 1990) and the bulk properties of the low-permeability sections that is critical to the understanding of large scale fluid flow phenomena. Here, the bulk properties of the low-permeability matrix are considered. In this work flow and petrophysical properties refer to different aspects of a mudstone’s physical properties, “flow properties” embraces features such as porosity, permeability, and capillarity used as inputs to fluid flow models; “petrophysical properties” is used to relate the response of a mudstone to the geophysical techniques used in wireline logging. In reservoir models the flow unit concept provides the framework within which sedimentologically defined architectural elements are integrated with petrophysical (flow) properties to create fluid flow model layers. The flow unit concept was introduced by Ebanks (1987), who defined a flow unit as a volume of rock within which the geological (texture, fabric etc), petrophysical and flow properties (porosity, permeability, capillarity) that affect fluid flow are internally consistent and predictably different from the properties of other rock volumes. Flow units are characterised by Corbett (1997) as:

- 1) Having similar petrophysical and flow properties (particularly porosity and permeability)
- 2) being correlatable between wells

The basic building blocks of reservoir models thus comprise geobodies or architectural units (i.e. stratal, genetic) (cf. Corbett, 1997) which require quantitative data in the form of length scales and geometries. There are a number of difficulties in applying similar concepts to basin models and there are also some important differences between reservoir and basin models that need to be addressed. The fundamental difference between reservoir and basin models is the timescales involved; reservoir models are typically run over their production lifecycles (typically 10 to 20 years); due to the short time scales the flow properties of the sediments involved, with the exception of relative permeability, are static – they generally do not change with time, accept in stress sensitive reservoirs (e.g. chalk); the only parameters to change over time are phase and saturation (which of course effect relative

permeability). In basin modelling geological time scales are involved and therefore not only do saturations and phases change, but also the physical properties of the sediments being modelled. Furthermore, this difference in timescales reflects the differences in the nature and rates of fluid flow phenomenon. Work carried out in the SMACCERS¹ project showed that at realistic oil feeding rates (in mudstones) flow is highly focussed and is controlled by the ratio between buoyancy and capillary forces. In sandstones flow paths become less focussed as the flow regime changes from capillary dominated to viscous dominated (Carruthers, 1998). This work showed that it is the capillary pressure field which ultimately controls migration trajectories in fine-grained sediments. The rates of migration, despite being very low, do vary and are important if dynamic models are to be produced (i.e. if dynamic leakage assessing charge versus leakage for differing trap volumes are to be investigated). Also the capillary pressure field and permeability field are related – both are a function of a sediment's (or flow unit's) pore-throat network and are not static – both will reduce with increasing compaction. Furthermore, if hydrodynamic effects such as overpressure are to be included in modelling studies (which may have significant impact on migration trajectories which invasion percolation based models will miss) then (relative) permeabilities are essential model inputs.

The differences described above do not preclude the application of a flow facies concept in basin model applications. The way that mudstones compact and the range of flow properties that they exhibit is a function of their grain size distribution (Aplin *et al.*, 1995; Yang and Aplin, 1998; Dewhurst *et al.*, 1999b). Therefore facies types delimited in terms of their grain size distribution should have similar flow properties which should evolve with mechanical compaction in a similar fashion. As noted above, establishing flow units within basin models is complicated by a lack of data both in terms of quantitative data describing the geometries and length scales of mudstone units (cf. Bohacs, 1998) and, until recently, in terms of their physical properties. The problems facing basin modellers have been discussed on numerous occasions (Aplin *et al.*, 1999; Duppenbecker and Iliffe 1998); the two most commonly cited issues are the lack of information regarding the geometrical arrangements of various lithologies and facies on the basin scale; and the lack of relevant data for mudstones which dominate the basin fill. Advances in 3D seismic, coupled with advances in our understanding of deep marine sedimentary systems offers an opportunity to begin to address these problems in a truly three dimensional data volume.

¹ An EU sponsored study aimed towards an increased understanding of petroleum migration through fine-grained rock sequences.

4.7 Conclusions

The work presented in this study has illustrated that the PCA – k means technique utilised in this study generally differentiates grain size Types 1 – 4 from grain size Types 5 – 6 irrespective of the description used. The entirely flocculated grain size Types 1 and 2 are not generally differentiated from the floc-silt mixtures of grain size Types 3 and 4. The coarser grain size Types 5 and 6 are in some cases differentiated, but are grouped more often than not.

The segregation between grain size Types 1 – 4 and 5 – 6 was particularly good, especially for the whole phi bin, 0.2 phi bin and combined datasets. In general the degree of partitioning within these two groups improved with the increasing information content of the dataset used; the 0.2 phi bin dataset proved to be most effective at producing clusters with the best correspondence to the grain size types (Table 4.3). In contrast, the combined dataset proved to be most effective at producing clusters with the highest degree of correlation between porosity and r mean (Table 4.4). The sedimentary statistic and parameter dataset proved to have the poorest correspondence to both the grain size types and r mean values (see Table 4.1). Therefore the PCA-k means technique should be applied to the highest resolution data available. Further work would be required to investigate which dataset out of the 0.2 phi bin and combined dataset is best at discriminating mudstone grain size types. Combining sedimentary statistic data with frequency data at the 0.2 phi bin resolution, (rather than at 1 phi bin as in the combined dataset used here) may lead to further improvement in the defined clusters.

While the ‘global’ approach taken in this study seemed to work well in discriminating mudstones into similar grain size types, which exhibit similar ranges of flow properties (such as permeability, critical capillary entry pressure), it is apparent that it cannot be extended to petrophysical properties. This result poses a problem in the practical application of this work, although it is believed that with regional calibration, a similar technique could meet with success.

Overall this study provides a technique with which to rapidly understand, group and model mudstone grain size data and relate it to flow properties. It is ultimately suited to undertaking case studies within areas with significant data coverage and would potentially allow for improved capillary seal prediction and risking.

Chapter 5 Investigation of the statistical distribution of pore-throat network parameters of mudstones as a function of both lithology and porosity

5.0 Introduction

At present the understanding and quantification of the variability of the pore-throat size distributions of mudstones is an area of considerable ignorance. The pore-throat size distribution of a mudstone is the principal control upon fluid flow properties, such as permeability (e.g. Yang and Aplin, 1998) and has been shown to be strongly influenced by both porosity and grain size distribution (e.g. Dewhurst *et al.*, 1999a, b). The pore-throat size distribution as derived from an MICP experiment is commonly reduced to single numerical value such as the mean pore-throat size (herein termed r_{mean}) or some percentile giving an approximation of the values contained within either the lower or upper tails of the pore-throat size distribution. Such pore-throat network parameterizations are typically used to simply describe the pore-throat size distribution, for input into permeability models (e.g. Yang and Aplin, 1998), and for estimating capillary entry pressure (e.g. Schowalter, 1979; Schlömer and Kroos, 1997). In this chapter exploratory data analysis of two numerical descriptions of the pore-throat size distribution r_{mean} and $r_{10\%}$, is performed using standard statistical techniques. The availability of multiple samples of similar lithology and at a similar level of porosity provides the opportunity to make an initial assessment of variability of such parameters, if lithology and porosity are accepted as the principal controls of a mudstones pore-throat size distribution. Such analysis is currently missing from the literature; this is a serious omission given that it is of vital importance if the sensitivity and the level of uncertainty associated with the prediction of properties strongly correlated with pore-throat size distribution (such as permeability and capillary entry pressure) are to be quantified. Why do we want to test distribution type? In reservoir modeling it is nearly always the case that sufficient data have been collected such that histogram transformation procedures alleviate the need for the data to follow a parametric distribution (Deutsch, 2002). Within basin-scale fluid flow models there may be very sparse data to work with. Therefore model population strategies, particularly when downscaling, typically resort to some statistical distribution from which grid cells may be populated. Two parameters used to describe the pore-throat size distribution, the mean pore-throat size and the pore-throat size at the ninetieth percentile of the cumulative pore-

throat size distribution ($r10\%$), are investigated with regard to their respective correspondence to normal and log-normal distributions at constant porosity and ‘support mechanism’ controlled by grain size distribution (Chapter 3).

Greater understanding of how the pore-throat size distributions and their parameterizations vary would provide a greater understanding of the processes operating when mudstones are subjected to burial. Furthering our understanding of these processes would have implications for:

- (a) the prediction of fluid flow properties of mudstones;
- (b) application of petroleum system analysis involving two phase flow through mudstones sequences.

In Chapter 2 of this thesis six mudstone grain size distribution ‘types’ (referred to as GSD types from hereon), were proposed, based upon analysis of the *moment statistic values, application of* the Kranck grain size model, and observations made from thin sections. Analysis of the *influence* of the grain size distribution, and specifically the GSD type, on the nature of the pore-throat size distribution and its evolution with decreasing porosity illustrated that *Types 1 – 4 behaved as* matrix supported sediments, whereas Types 5 and 6 exhibited framework supported behaviour (Chapter 3). Below porosities of 30% Types 1 – 4 (typically with clay contents $>40\%$) had unimodal pore-throat throat size distributions, considered to represent textural porosity within and between clay flocs and silt grains. These distributions were almost entirely composed of pore-throats with throat radii $<100\text{nm}$; modal values decreased from $\sim 50\text{nm}$ to $<10\text{nm}$ with decreasing porosity. Grain size Types 5 – 6 typically had clay contents $<40\%$ and exhibited bimodal pore-throat throat size distributions, a smaller mode comparable to the clay fabric mode characteristic of Types 1 – 4 and a second mode comprising pore-throats with radii \sim two orders of magnitude larger than the clay fabric mode. This second mode was seen to decrease both in size and in volume with decreasing porosity and is eventually lost, producing a unimodal pore-throat size distribution similar to those of Types 1 – 4. It was suggested in Chapter 3 that the pore-throat size distributions of GSD Types 1 – 4 are controlled by the clay fabric and thus relate to a matrix-supported sediment. Conversely the pore-throat size distributions of GSD types 5 and 6 are controlled by both the clay fabric and the structure of the silt and/or sand grains and therefore relate to a framework-supported sediment.

Attempts to derive functions which predict properties of mudstones typically rely on a regression based approach where the property in question (permeability, critical capillary entry pressure etc) is regressed as function of porosity and some lithological parameter such as clay content (e.g. Hildenbrand and Urai, 2003). This technique has been used with some success, but has disregarded the important statistical principle that a point estimate, an interval estimate and a confidence level must be added if the prediction is to be successfully applied. With regard to modeling petrophysical properties such as capillary entry pressure (CEP) and permeability within numerical fluid flow models it is desirable to understand and quantify the statistical distributions from which these parameters are drawn, as functions of both lithology and porosity (as these two variables are important controls upon the pore-throat size distributions of mudstone's (cf. Dewhurst *et al.*, 1999a, b). Furthermore, data analysis techniques such the 'least squares' techniques used in regression assume that data are normally distributed (Kirkup, 2002, p.128, Corbett, 1997). Therefore an attempt to understand which transforms may be applied to result in normality is also of interest.

The hypothesis that mudstones exhibit either a matrix or framework controlled compaction behaviour is tested by analysing the distribution of pore-throat network parameters as a function of porosity and the pore-throat network support type. The assessment of the distribution type represented by the pore-throat network parameters is coupled with statistical tests of variability and sample support commonly applied in a reservoir engineering context (e.g. Jensen *et al.*, 1997). This is done in an attempt to quantify the heterogeneity of the data and to provide reassurance that the number of samples is adequate to accurately quantify the variability exhibited.

The main aim here is thus to test the hypothesis that at r mean and $r10\%$ within a 5% porosity bin are:

- a. Normally distributed
- b. Log-Normally distributed

For two distinct datasets, comprising of a matrix-supported mudstone dataset and a framework-supported mudstone dataset.

5.1. Samples and methods

5.1.1 *Sample selection*

An attempt to replicate the grain size classification framework proposed in Chapter 2 using a combined PCA – k means classification approach illustrated that Types 1 – 4 were generally grouped together, as were Types 5 and 6. This illustrated numerically that GSD Types 1 – 4 and 5 – 6 are essentially indistinguishable in terms of the classification procedure and grain size parameterizations used (Chapter 4).

When data is partitioned the aim is to reduce variability allowing improved understanding of the controls upon the property of interest. The hypothesis proposed in this work is that mudstone pore-throat size distributions and their evolution with increasing compaction exhibits two modes of behaviour dependent upon the nature of the grain size distribution (Dewhurst *et al.*, 1999a). The grain size control upon mudstone pore-throat networks is considered to be reflected principally in how the pore-throats are constructed (which is manifested in the size distribution of the pore-throats). In one mode the clay fabric (i.e. the spatial arrangement and structure of the clay particles $<10\mu\text{m}$) forms the load-bearing phase, whilst in the second mode both the clay fabric and the silt and/or sand grains forms a load-bearing framework (Chapter 3). Similar suggestions have been made in previous studies of artificial slurries (Fiés, 1992) and natural mudstones (Dewhurst *et al.*, 1999a); the clay content at which the mode of behaviour is thought to switch is thought to lie between 30 – 40% (Fiés, 1992; Dewhurst *et al.*, 1999a). Work on artificial slurries performed by Fiés (1992) showed that at clay contents below 30% the modal pore-throat size was directly related to the size of the silt material indicating that the pore-throat network was intimately related to the framework of silt grains (Figure 5.1). As clay contents increased above 30% the size of the modal pore-throat size steadily decreased as the clay sized material began to interact with the framework reflecting the transition from a framework- to matrix-supported regime (Figure 5.1).

In this chapter the sample set is separated into two groups: one is comprised of GSD Types 1 – 4, hypothesized to have a matrix-load bearing structure; and a second comprising GSD Types 5 and

6, hypothesized to have a framework-load bearing structure. This division yields a clay-rich group (clay >40%) termed Group 1 and a silt/sand-rich group (clay <40%) termed Group 2. The clear division of the grain size properties of the groups is shown in Figure 5.2, and is most obvious when the Zeta Area samples are removed owing to the fact that these samples are typically very rich in fine silt (2 – 10 μm) (see Figure 5.2b, d). The division between these two groups was made to reflect both observations made by Fiés (1992) and the observations made on the nature of the grain size distributions (Chapters 2 and 4) and the grain size – pore-throat size relationship (Chapter 3).

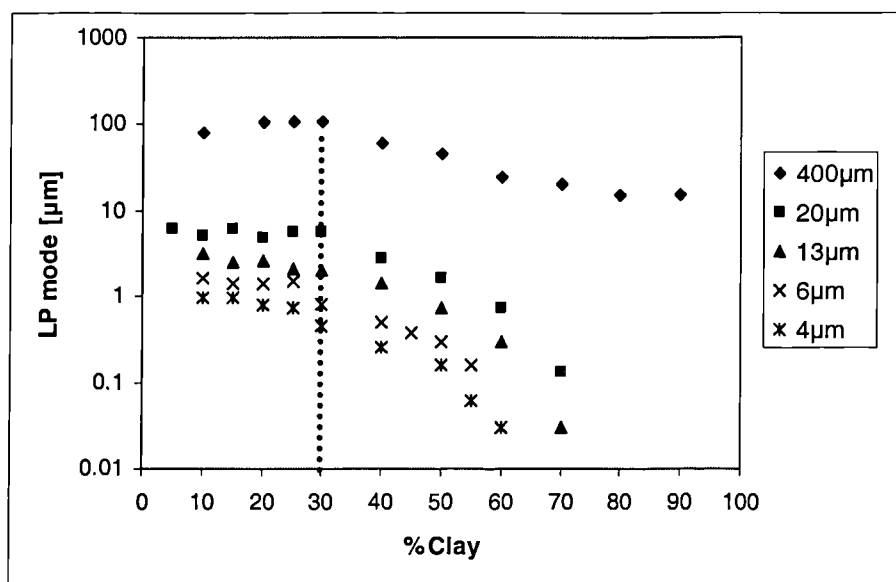


Figure 5.1. Lacunar pore-throat (LP) mode obtained from a volumetric pore-throat density distribution curve as a function of clay content for silt components ranging in diameter from 4 - 400 μm . At any one clay content the size of the LP mode is dependent upon the size of the silt component – with approximately an order of magnitude difference between a silt component size of 20 μm to one at 4 μm . For the sand size material LP remains virtually constant irrespective of clay content; however for the silt-clay mixtures, once clay contents exceed 30%, the LP mode begins to be influenced by the clay sized particles, resulting in the LP reducing as a function of clay content.

To account for the effect of compaction on pore-throat size properties the two groups were divided into 5-10%, 10-15%, 15-20% and 20-25% porosity bins where possible and the distribution of two pore-throat network parameters assessed. The parameters used are the r mean

and $r10\%$, reflecting the mean pore-throat size and the pore-throat radius at the 90th percentile of the relative pore-throat size distribution which is commonly assumed to give the critical threshold pressure from which one estimates seal capacity (e.g. Schowalter, 1979). If these pore network parameters can be shown to be drawn from distinct distributions when constrained by porosity and support regime (matrix- versus framework-supported) then the evidence that these two modes of behaviour are characteristic of the compaction behaviour of mudstones will be strengthened.

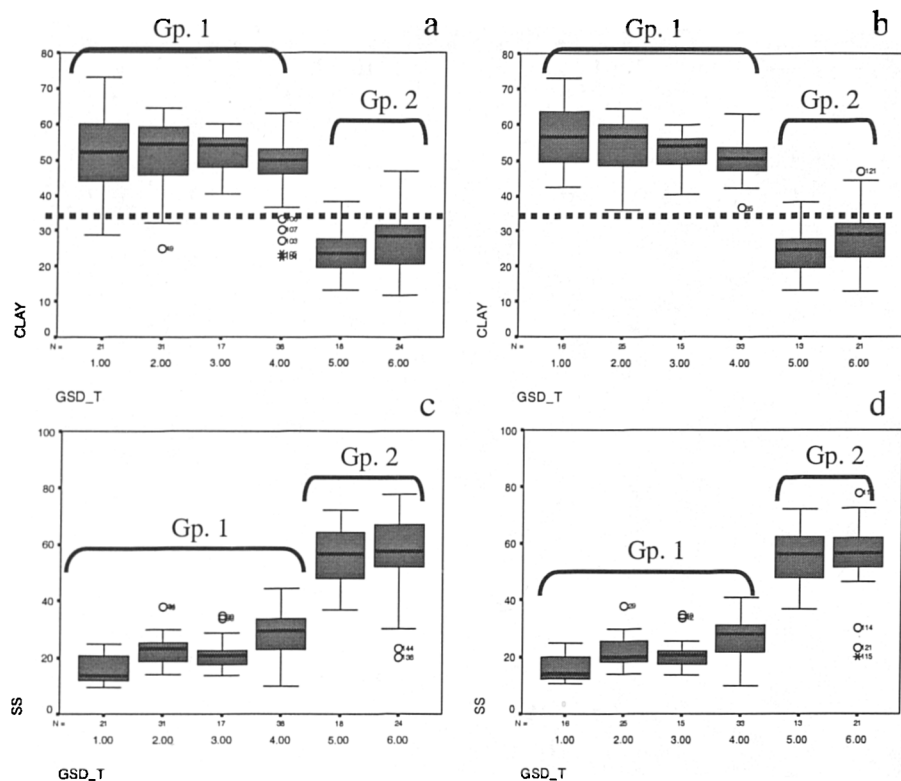


Figure 5.2. Grain size characteristics of the GSD types proposed in Chapter 2 (a) % clay, (b) % clay with the Zeta Area samples removed (c) % sortable silt and (d) % sortable silt with the Zeta Area samples removed.

5.2 Methods

5.2.2 Pore-throat size distribution

Pore-throat throat size distributions were measured by the mercury injection capillary pressure (MICP) technique using a Micrometrics porosimeter. A description of the technique along with a discussion of its advantages and disadvantages is given in Chapter 3.

5.2.1 Statistical analysis

A number of statistical terms are used within this chapter, here they are briefly explained: Testing hypotheses is an essential part of statistical inference, to formulate such a test, usually some theory has been put forward, either because it is believed to be true or because it is to be used as a basis for argument, but has not been proved; here, the suggestions that r mean and $r10\%$ are normally tested or that they are log-normally distributed are tested independently. Thus the null hypothesis is that the data are normally (or log-normally) distributed. A test statistic is a quantity calculated from the sample of data. The value of the test is used to decide whether or not the null hypothesis should be rejected in our hypothesis test. The critical value(s) for a hypothesis test is the threshold to which the value of the test statistic in a sample is compared to determine whether or not the null hypothesis is rejected.

The assumption of normality was tested on both untransformed and log-transformed using the graphical analysis, Anderson-Darling and Ryan-Joiner tests. Due to the small sample numbers (n typically <20) graphical methods were perhaps the most robust method with which to test the assumption of normality. Probability plots and histograms were derived allowing visual inspection of the data. The morphology of the probability plots can be used to interpret the nature of the dataset; Jensen *et al.*, (1997) proposed a series of 'thumb print' forms to aid the interpretation of these plots (Figure 5.4). Bottom truncation results from a situation where the smallest values in the parent population are under sampled; similarly, top truncation results from a situation where the largest values in the parent population are under sampled. Distinct breaks or

changes in slope on the plots result from the presence of two parent populations that may or may not intersect (cf. Figure 5.4).

The details of the Anderson-Darling (AD) and Ryan-Joiner (RJ) tests and their interpretation are described in Appendices A5.1 and A5.2 respectively. Although the basis of the two tests are different both calculate a test statistic, in the AD case the test statistic has to be lower than the critical value (Appendix A5.1); in the RJ case the test statistic has to exceed the critical value (Appendix A5.2). The test statistic for both tests may be used to test the null hypothesis (i.e. that the data have been drawn from a normal distribution). In both tests a *p*-value is also calculated which allows a confidence to be assigned to the result of the statistical test. The interpretation in relation to the *p*-values obtained from the statistical test is given in Table 5.1. It should be noted that with regression the interpretation of *p*-values is not equivalent to that when they are obtained from normality tests. Within regression the derived *p*-values relate to the probability that the correlation obtained is coincidental if *x* and *y* are not in any related. Thus the lower the *p*-value the stronger the evidence that *x* and *y* are related by some underlying process allowing the possibility that the correlation is coincidental to be rejected.

<i>p</i> -value	Interpretation
$p > 0.1$	No evidence against the null hypothesis. The data appear to be consistent with the null hypothesis
$0.05 < p < 0.1$	Weak evidence against the null hypothesis in favour of the alternative
$0.01 < p < 0.05$	Moderate evidence against the null hypothesis in favour of the alternative
$0.001 < p < 0.01$	Strong evidence against the null hypothesis in favour of the alternative
$p < 0.001$	Very strong evidence against the null hypothesis in favour of the alternative

Table 5.1. Interpretation of the *p*-values obtained when perform the AD and RJ test for normality; in both cases the null hypothesis is that the data have been drawn from a normal distribution (or log normal if the data have been transformed).

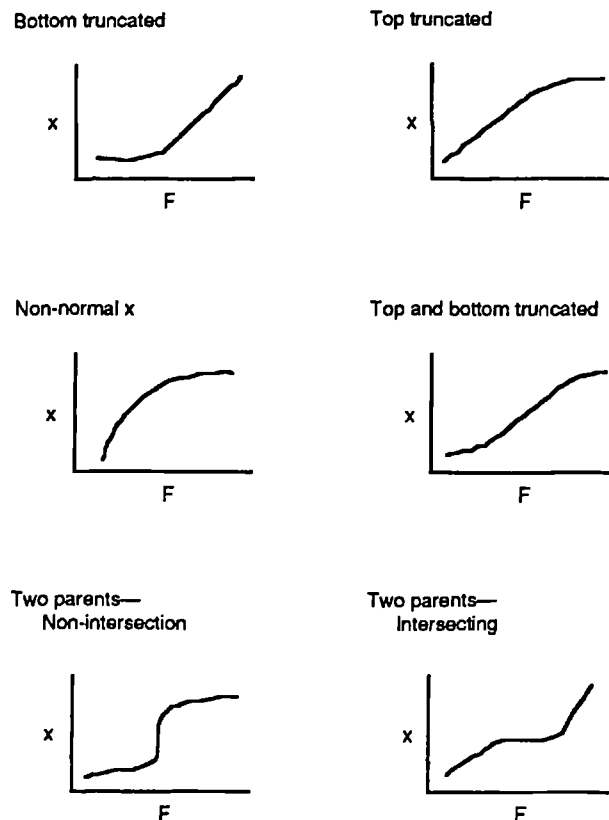


Figure 5.4. Thumb print cumulative distribution function plot morphologies – which can be used in the interpretation of probability plots (x = probability; F = variable) (From Jensen *et al.*, 1997, Figure 4.18).

5.2.2 Variability measures and sample support

In any statistical examination it is important to have an assessment of whether or not your sample size is sufficient to quantify the population you wish to describe. An assessment of the variability and data support (i.e. the number of samples in relation to the exhibited variability) of the two groups identified in this study with regard to their pore-throat network properties was carried out using the co-efficient of variation (C_v) and N-zero (N_0) methods (after Hurst and Rosvoll, 1990; Corbett and Jensen (1992); Jensen *et al.*, (1997)).

The co-efficient of variation (C_v) is a normalised standard deviation:

$$C_v = \frac{\sqrt{\text{var}(k)}}{E(k)} \quad (5.1)$$

and can be estimated by:

$$C_v = \frac{\sigma(k)}{\bar{k}} \quad (5.2)$$

where $\text{var}(k)$ and $E(k)$ are the variance and expectation of k (always estimated!), $\sigma(k)$ and \bar{k} are the standard deviation and mean of the sample population (Ringrose, 2002). When calculating C_v a decision has to be made on which mean to use: here, the arithmetic mean was discounted due to it is sensitive to high values, which were commonly present in this dataset due to the inclusion of cutting data. The harmonic mean was preferred over the geometric mean as it is considered to be appropriate for bed normal (vertical) flow (cf. Corbett, 1997) thought to be the predominant form of flow in mudstones (cf. England *et al.*, 1987). Due to the small sample numbers typically involved in each analysis the standard deviation was multiplied by a correction factor (Corbett, 1997):

$$\left[1 + \frac{1}{4(n-1)} \right] \quad (5.3)$$

The interpretation of C_v values can be guided by the classification proposed by Corbett and Jensen (1992) who used a wide range of petroleum reservoir heterogeneity data to infer that:

- $C_v < 0.5$ implies an effectively homogeneous dataset
- $0.5 < C_v > 1.0$ implies a heterogeneous dataset
- $C_v > 1$ implies a very heterogeneous dataset

The N_0 measure gives an estimate of the sample number required to give an estimate of the true mean with a 20% tolerance:

$$N_0 = \left[\frac{t \cdot C_v \cdot 100}{P} \right]^2 \quad (5.4a)$$

$$N_0 = (10C_v)^2 \quad (5.4b)$$

where t is the critical t -value (taken from standard statistical tables) and varies with size of sample and confidence level. All t -values were taken at the 0.05 level (95%) (note t is sensitive when n is small i.e. varies significantly with low sample numbers); C_v is the coefficient of variation determined from (Eq. 5.2) and P is the % tolerance taken as 20% in this case (Corbett and Jensen, 1992). For large datasets Eq. 5.4a can be approximated by 5.4b (Corbett, 1997). If the actual sample number is significantly less than N_0 then the sample set is insufficient, given the variability exhibited, to be useful statistically (Corbett, 1997). The N_0 estimate was intended originally to maximise sampling programs so that they fully capture the heterogeneity (with effective sample spacing, etc) while remaining cost effective; here it is simply used as a guide to the level of confidence that can be placed in the interpretations and statistics of the datasets presented below.

5.3 Results

The probability plots and related histograms for each of the data partitions are presented in Figures 5.6 – 5.30; the results of the Anderson-Darling and Ryan-Joiner normality tests are presented in Tables 5.2 and 5.5 and the associated Ryan-Joiner probability plots are given in Appendix A5.4. The numerical normality tests may not be particularly robust due to the low sample numbers present in most of the porosity ‘bins’ analysed; the Ryan-Joiner test is more reliable when sample numbers are small (Ryan and Joiner, 1976). The results of the normality tests will be unreliable where data are bi-modal.

5.3.1 Group 1 (matrix-supported samples – GSD Types 1 – 4).

The null hypothesis for both the theory that r mean and $r10\%$ are normally distributed and the theory that r mean and $r10\%$ are log-normally distributed would be rejected on the basis of the

results of the data analysis for the 15 – 20%, 20 – 25% and 20 – 25% Iota Area datasets. This rejection is based on the appearance of probability plots and histograms (Figures 5.10 – 11, 5.12 – 13 and 5.14 – 15); furthermore, these data also failed the test criteria of both the AD and RJ tests strengthening the case to reject the null hypothesis for both theories. This result is believed to be due to the fact that these datasets appear to be bi-modal.

For the 15 - 20% dataset the morphology of the probability plot indicates the presence of two intersecting parent populations (compare Fig. 5.4 and Fig. 5.10); the histograms were also clearly bi-modal (Fig. 5.11). Consideration of the datasets in terms of location, sample type, temperature, and % TOC did not reveal any obvious reason why two populations should be present (see Table A5.3.3 in Appendix A5.3). Both parameters are heterogeneous and sampled insufficiently to quantify the exhibited variability according to the C_v and N_0 estimates (Table 5.2). The data is drawn dominantly from the Iota Area and is comprised of a mix of all 4 GSD Types, mainly in the form of side wall core samples (Fig. 5.5).

The 20 - 25% dataset exhibits similar characteristics to the 15 - 20% dataset; again the morphology of the probability plot indicates the presence of two intersecting parent populations (compare Figs. 5.4 and Fig. 5.12) and the histograms are bi-modal (Fig. 5.13). The rejection of the null hypothesis as indicated by the AD and RJ tests reflects the bi-modal nature of the dataset. Analysis of the porosity values, GSD Types and sample types with regard to the r mean and $r10\%$ values did not reveal any obvious reason why the two populations may be present. It was evident that cuttings have disproportionately larger r mean and $r10\%$ values relative to side wall core samples (Figure 5.12; Table A5.3.4) possibly reflecting the more heterogeneous nature of these sample types (i.e. they sample a much larger volume of rock).

The 20 - 25% dataset included 23 side wall core samples from a single Iota Area well. These samples were used to form a new group and were plotted as probability plots and histograms (Fig. 5.14 and Fig. 5.15) and were subjected to AD and RJ tests (Appendices A5.1 and A5.2, Fig. A5.5). The morphology of the probability plots and the histograms revealed that the data were still bi-modal. The AD and RJ statistics and their associated p -values indicated that this dataset is poorly described by both normal and log normal distributions (Table 5.2 and Appendix A5.4, Fig.

A5.4.5) despite these data being drawn from a single well and thus being particularly well constrained in terms of thermal effects.

The results of the test statistics (Table 5.2) and inspection of the probability plots and histograms (Figures 5.8 and 5.9) are ambiguous and no clear result is apparent. In terms of the AD and RJ test statistics the acceptance criteria is met in all cases (Table 5.2). The absolute values of the test statistics and *p*-values indicate that the hypothesis that *r* mean is log-normally distributed would be accepted with greater confidence. In the case of *r*10% the AD test indicates that normality would be accepted while the RJ test indicates log-normality (Table 5.2). The C_v indicates that both *r* mean and *r*10% are homogeneous, but only *r*10% is sufficiently sampled to quantify the exhibited variability (Table 5.3).

The null hypothesis that the *r* mean and *r*10% values are log-normally distributed for the 5 - 10% and 25 - 30% datasets is accepted; while the theory that they are normally distributed can be rejected given the nature of the probability plots, histograms (Figures 5.6, 5.7 and 5.16, 5.17) and the results of the AD and RJ tests (Table 5.2). In both cases the log transform yields improvement in the approximation to log-normality as indicated by the decrease in the AD values, increase in RJ values and the increase in both *p*-values (i.e. the probability that the data have been drawn from a normal population) and the improved approximations to straight lines on the probability plots relative to the untransformed data. The Ryan-Joiner normality test statistic exceeded the critical value in both cases and thus indicated that the null hypothesis that these datasets are accurately described by a log-normal distribution.

Despite their close approximations to log-normal distributions these two datasets are quite different in many respects. The 5 - 10% porosity dataset is dominated by core plugs and cuttings from the Zeta Area region and represents a mix of all four GSD Types (Figure 5.5). The coefficients of variation indicate that both *r* mean and *r*10% are highly variable (Figure 5.18, Table 5.3). The N_0 estimate indicates that the dataset is significantly under sampled in terms of quantifying the variance (see Table 5.3). The 25 - 30% dataset is largely comprised of side wall core samples from the Iota Area and also represents a mix of all four GSD Types (see Figure 5.5). The untransformed *r* mean is indicated to be heterogeneous according to the coefficient of

variation (C_v) and the dataset is under sampled according to the N_0 estimate (see Table 5.3). The $r10\%$ parameter is homogeneous and is adequately sampled according to the N_0 estimate ($N_0 = n$) (see Table 5.3).

Overall the datasets whose N_0 estimates indicate that there is sufficient data with which to quantify the variability (i.e. the 15 – 20%, 20 -25% and Iota Area 20 – 25% datasets (reference the N_0 values in Table 5.3) the null hypothesis is rejected both in terms of the data being normally distributed and log-normally distributed due to the bi-modal form of the distributions (see Figures 5.11, 5.13 and 5.15). Where the statistical tests pass their respective acceptance criteria, as in the 5 -10% and 25 – 30% datasets, the N_0 estimates indicate that the data are insufficient to accurately quantify the variance exhibited (reference the N_0 values in Table 5.3). In the one example where the sample number is reasonably close to the N_0 estimates and the distributions are not bi-modal an ambiguous picture emerges as both respective hypotheses i.e. that r mean is normally or log normally distributed is accepted given the inspection of the probability plots, histograms and AD and RJ test statistics.

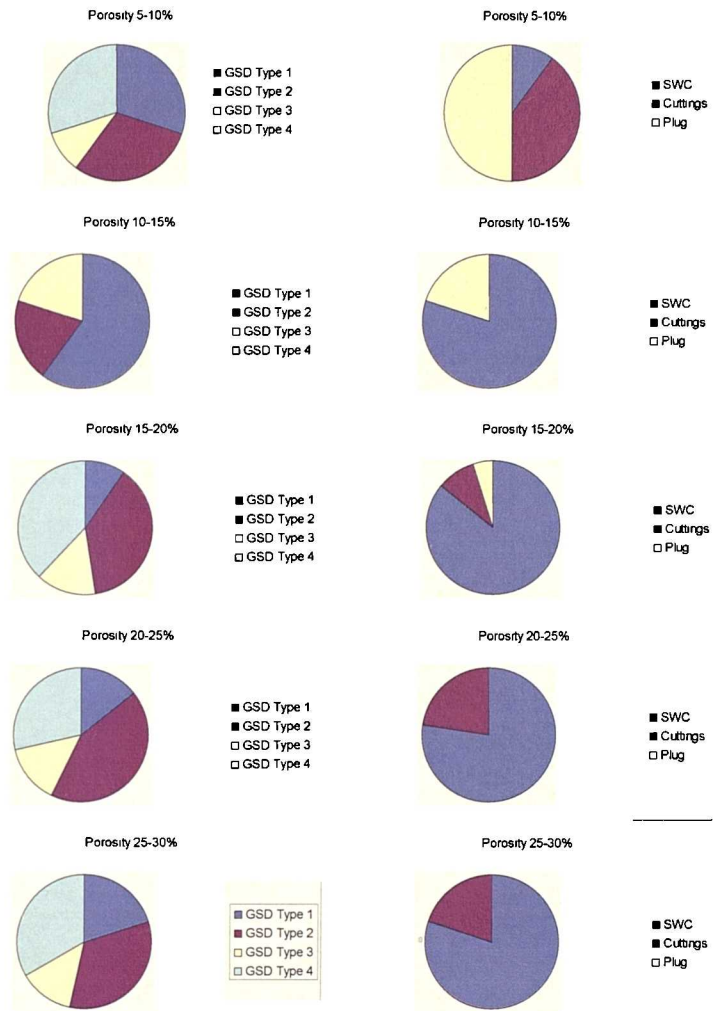


Figure 5.5. Group 1 pie charts illustrating the distribution of grain size distribution type and sample type for each of the five porosity bins comprising GSD Types 1 – 4 defined in this study.

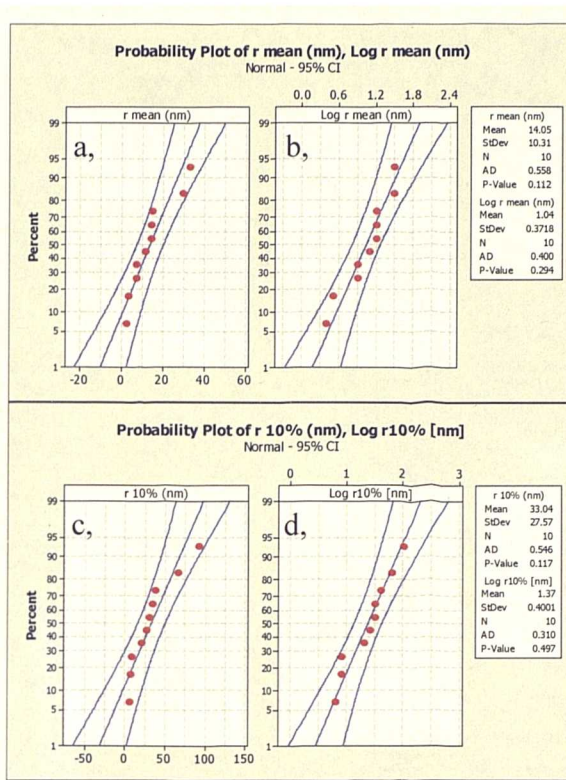


Figure 5.6. Probability plots of: (a) r mean, (b) log r mean, (c) r10%, and (d) log r10% for GSD Type 1 – 4 samples with 5 – 10% porosity (averaging 8.2%). Note that two outliers were removed.

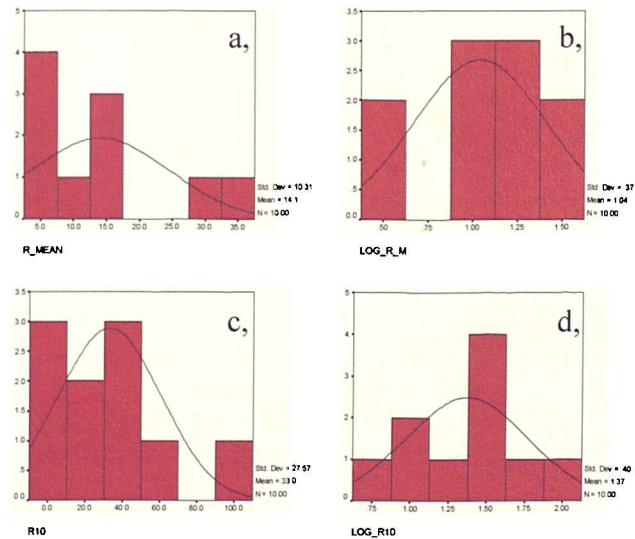


Figure 5.7. Histograms for: (a) r mean, (b) log r mean, (c) r10%, and (d) log r10% for samples with GSD Type 1 – 4 and a 5 – 10% porosity range (averaging 8.2%). Note that two outliers were removed.

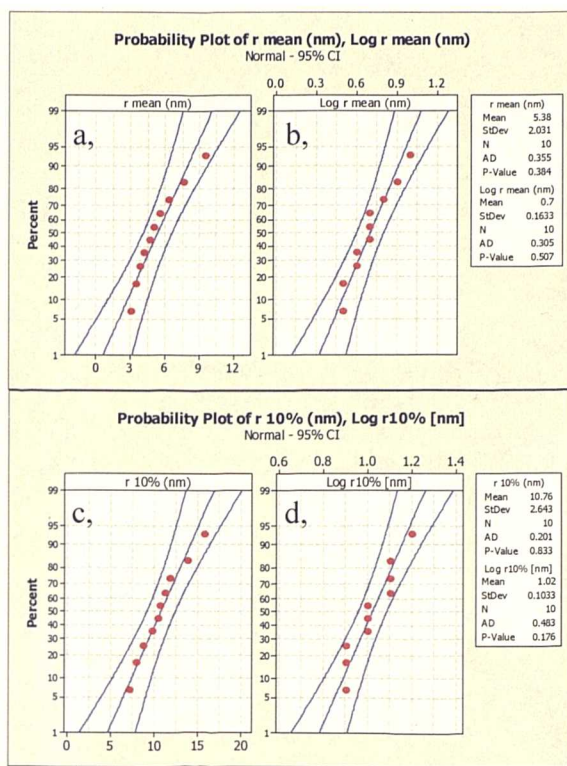


Figure 5.8. Probability plots of: (a) r mean, (b) log r mean, (c) r10%, and (d) log r10% for GSD Type 1 – 4 samples with a porosity range of 10 – 15% (averaging 12.7%).

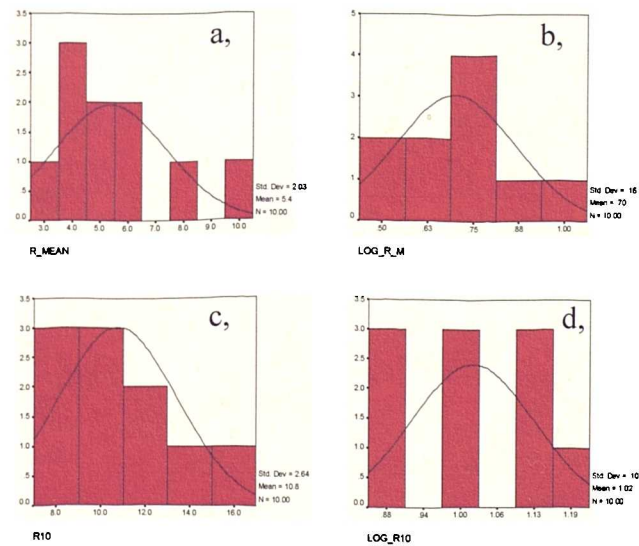


Figure 5.9. Histograms for: (a) r mean, (b) log r mean, (c) r10%, and (d) log r10% for GSD Type 1 – 4 and a porosity range of 10 – 15% (averaging 12.7%).

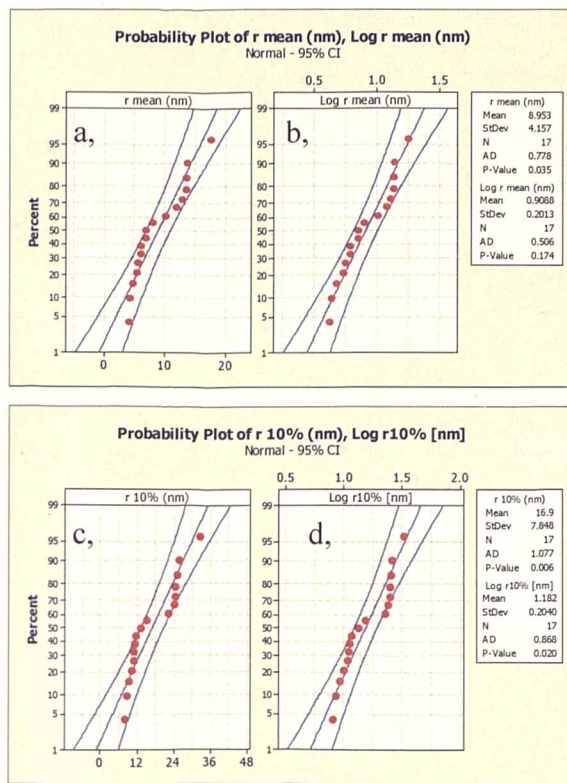


Figure 5.10. Probability plots of: (a) r mean, (b) log r mean, (c) r10%, and (d) log r10% for GSD Type 1 – 4 samples with a porosity range of 15 – 20% (averaging 17.4%).

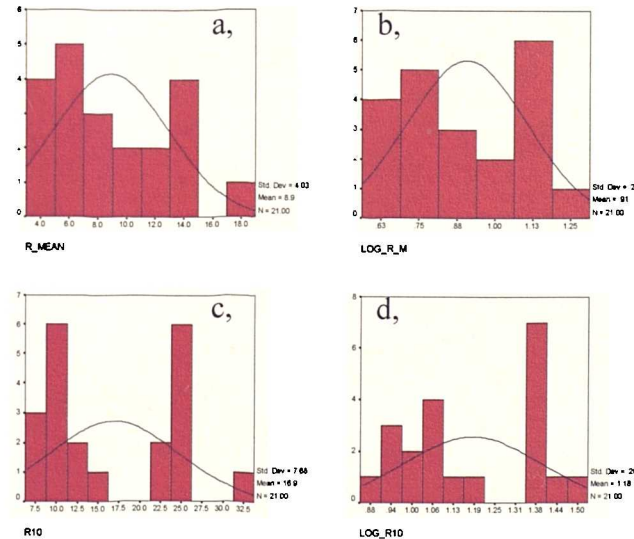


Figure 5.11. Histograms for: (a) r mean, (b) log r mean, (c) r10%, and (d) log r10% for GSD Type 1 – 4 with a porosity range of 15 – 20% (averaging 17.4%).

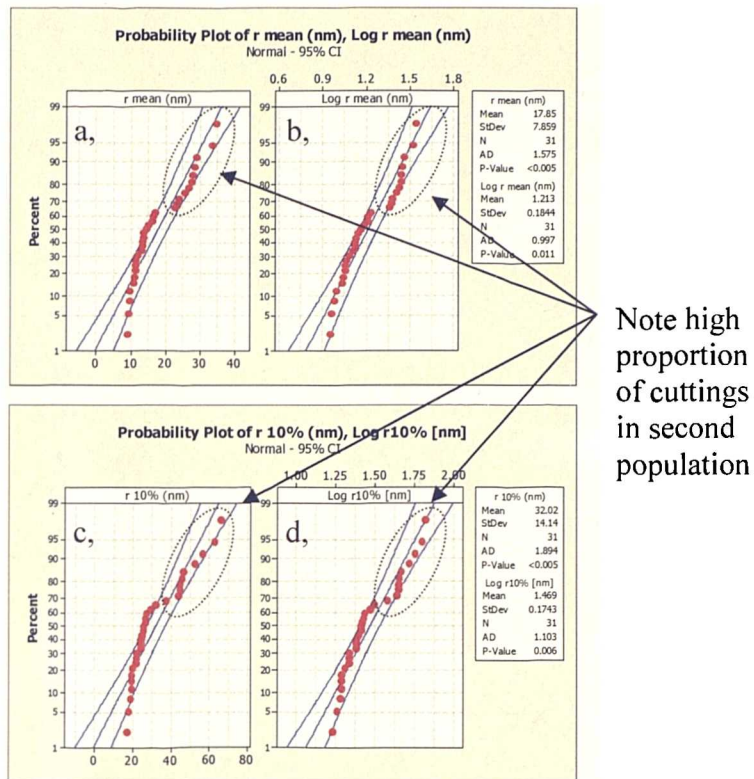


Figure 5.12. Probability plots of: (a) r mean, (b) $\log r$ mean, (c) $r10\%$, and (d) $\log r10\%$ for GSD Type 1 to 4 samples with a porosity range of 20-25% (averaging 22.8%). [Note. The group with larger values incorporates a high proportion of cuttings (see Appendix A5.3., Table A5.3.3)].

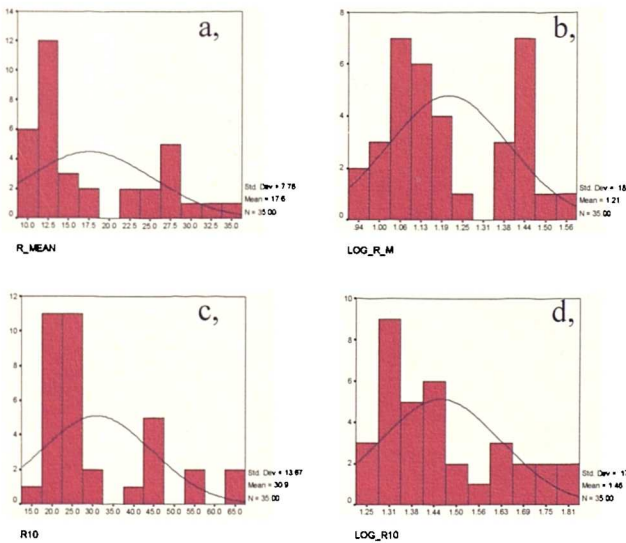


Figure 5.13. Histograms for: (a) r mean, (b) $\log r$ mean, (c) $r10\%$, and (d) $\log r10\%$ for GSD Type 1 to 4 samples with a 20-25% porosity range (averaging 22.8%).

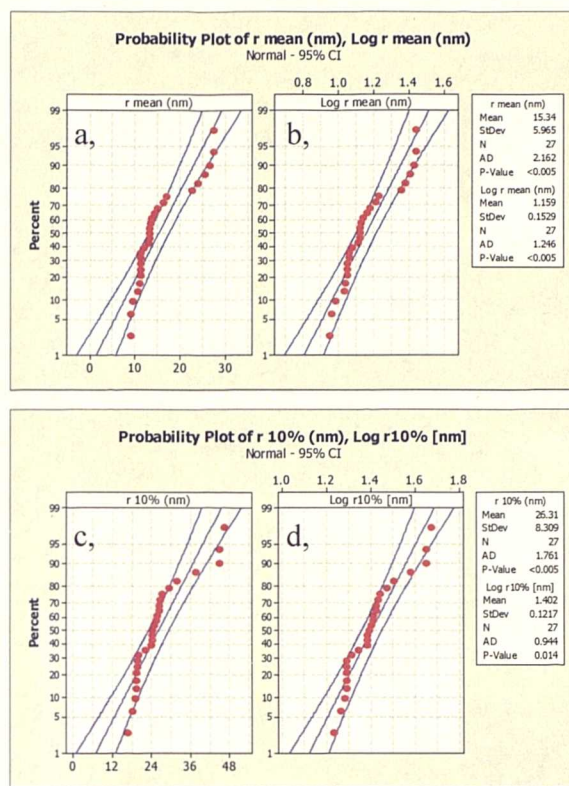


Figure 5.14. Probability plots of: (a) r mean, (b) log r mean, (c) r10%, and (d) log r10% for GSD Type 1 to 4 samples from a single Iota Area well with a 20-25% porosity range (averaging 22.7%).

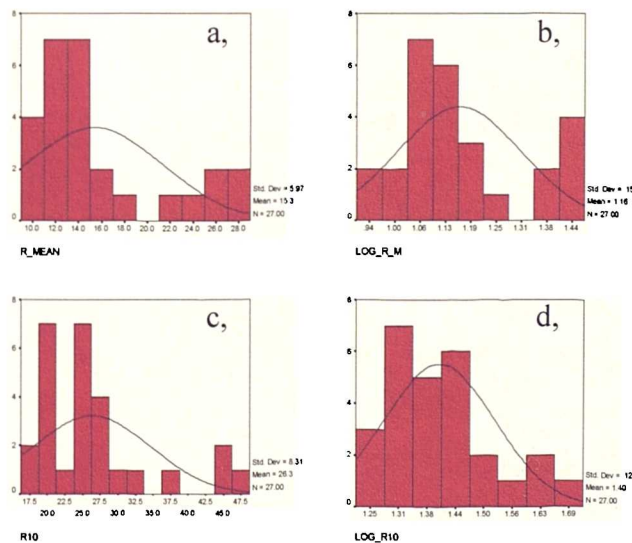


Figure 5.15. Histograms for: (a) r mean, (b) log r mean, (c) r10%, and (d) log r10% for GSD Type 1 to 4 samples from a single Iota Area well with a 20-25% porosity range (averaging 22.7%).

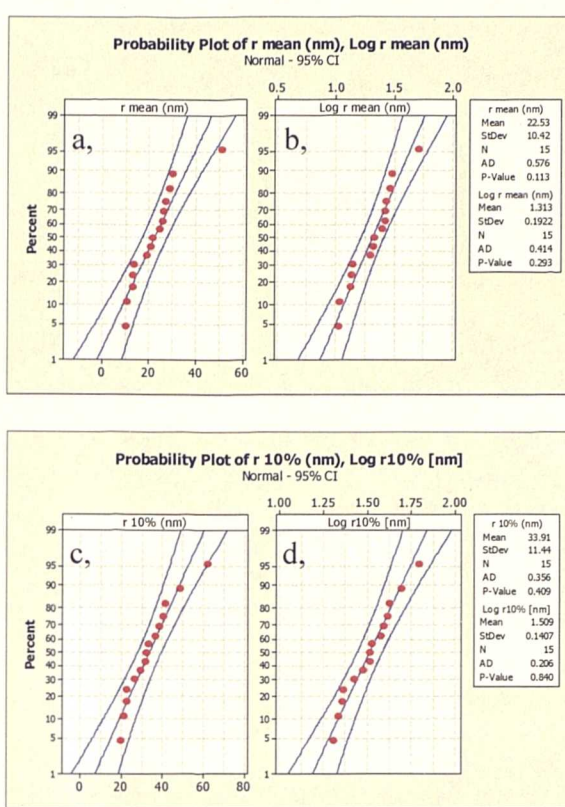


Figure 5.16. Probability plots of: (a) r mean, (b) log r mean, (c) r10%, and (d) log r10% for GSD Type 1 to 4 samples with a 25-30% porosity range (averaging 27.6%).

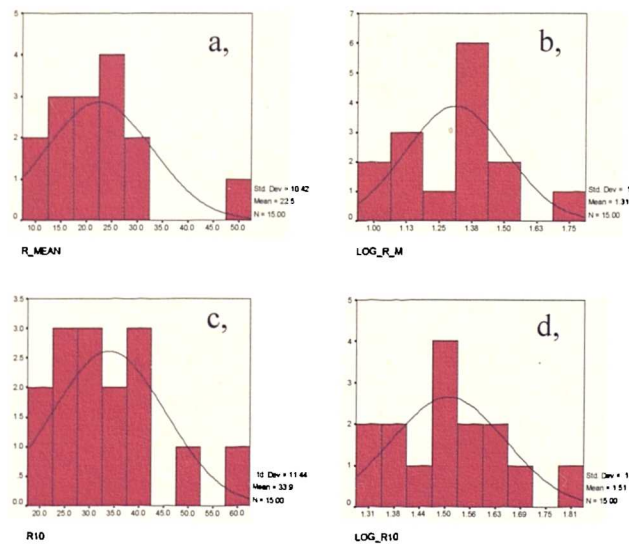


Figure 5.17. Histograms for: (a) r mean, (b) log r mean, (c) r10%, and (d) log r10% for GSD Type 1 to 4 samples with a 25-30% porosity range (averaging 27.6%).

Dataset	Parameter	No.	Critical AD (0.05 - the AD stat. has to be < the critical value)	AD	p-value	Critical RJ (0.05 - the RJ stat. has to be > the critical value)	RJ	p-value
8.20%	r mean	10	0.685	1.806	<0.005	0.918	0.94	>0.1
	r 10%	10	0.685	2.002	<0.006	0.918	0.932	0.091
	log r mean	10	0.685	0.257	0.657	0.918	0.983	>0.1
	log r10%	10	0.685	0.246	0.693	0.918	0.98	>0.1
12.70%	r mean	10	0.685	0.355	0.384	0.918	0.958	>0.1
	r 10%	10	0.685	0.201	0.833	0.918	0.983	>0.1
	log r mean	10	0.685	0.305	0.507	0.918	0.992	>0.1
	log r10%	10	0.685	0.483	0.176	0.918	1	>0.1
17.40%	r mean	17	0.715	0.778	0.035	0.944	0.951	0.082
	r 10%	17	0.715	1.077	0.006	0.944	0.934	0.035
	log r mean	17	0.715	0.506	0.174	0.944	0.973	>0.1
	log r10%	17	0.715	0.868	0.02	0.944	0.951	0.083
22.70%	r mean	31	0.733	1.575	<0.005	0.965	0.941	<0.010
	r 10%	31	0.733	1.894	<0.005	0.965	0.924	<0.011
	log r mean	31	0.733	0.997	0.011	0.965	0.965	0.05
	log r10%	31	0.733	1.103	0.006	0.965	0.96	0.038
22.8% Iota Area	r mean	23	0.725	2.162	<0.005	0.955	0.905	<0.01
	r 10%	23	0.725	1.761	<0.005	0.955	0.908	<0.01
	log r mean	23	0.725	1.246	<0.005	0.955	0.948	0.019
	log r10%	23	0.725	0.944	0.014	0.955	0.956	0.038
27.60%	r mean	15	0.709	0.576	0.113	0.938	0.926	0.033
	r 10%	15	0.709	0.356	0.409	0.938	0.96	>0.1
	log r mean	15	0.709	0.414	0.293	0.938	0.972	>0.1
	log r10%	15	0.709	0.206	0.84	0.938	0.987	>0.1

Table 5.2. Normality test statistics for the pore-throat network parameterizations of the samples with type 1 – 4 grain size distributions partitioned by porosity. The lowest AD values and the highest RJ values greater than the critical value (at 0.05), and their related p-values are in bold.

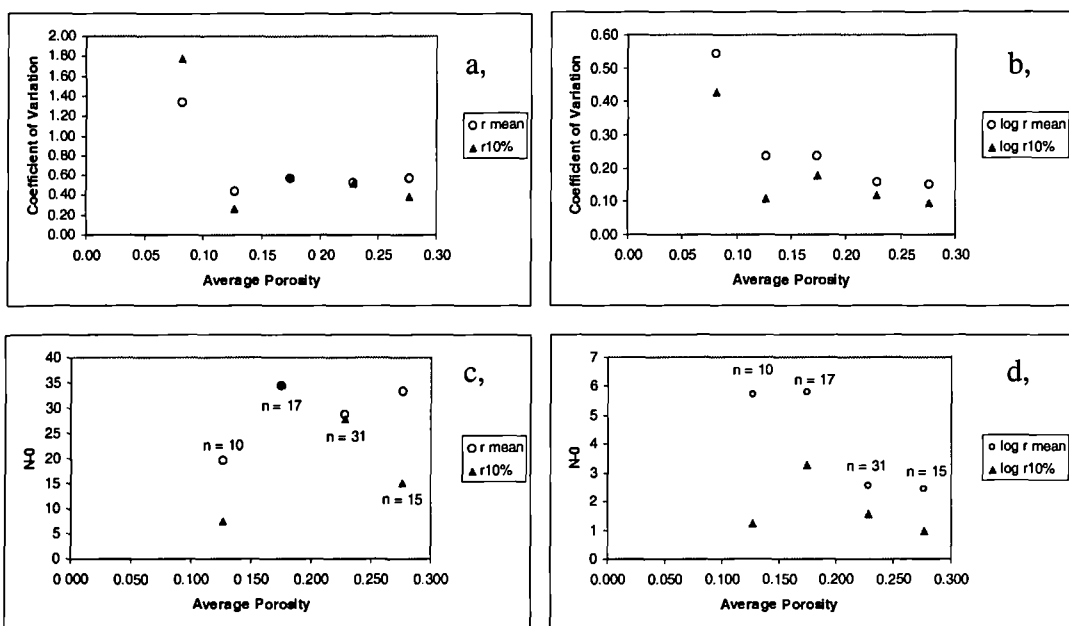


Figure 5.18. Cross plots of average porosity versus: (a) co-efficient of variation for r mean and $r10\%$, (b) co-efficient of variation for $\log r$ mean and $\log r10\%$, (c) N_0 for r mean and $r10\%$ and (d) N_0 for $\log r$ mean and $\log r10\%$. The number of samples is shown on both plots (c) and (d). (Note the 8.2% dataset values were extremely large (Table 5.3) and were thus removed for clarity).

Porosity Range	Av Porosity	No.	r mean CoV	r mean N-0	$r10\%$ CoV	$r10\%$ N-0	$\log r$ mean CoV	$\log r$ mean N-0	$\log r10\%$ CoV	$\log r10\%$ N-0
5-10%	0.082	10	1.34	187	1.77	328	0.41	17	0.33	12
10-15%	0.127	10	0.43	20	0.27	7	0.23	6	0.11	1
15-20%	0.174	17	0.57	34	0.58	35	0.24	6	0.18	3
20-25%	0.228	31	0.53	29	0.52	28	0.16	3	0.12	2
20-25%**	0.227	18	0.43	19	0.36	13	0.13	2	0.09	1
25-30%	0.276	15	0.56	33	0.38	15	0.15	2	0.10	1

Table 5.3. Coefficient of variation and N_0 estimates for the five porosity-based data partitions of Group 1 (GSD Types 1 – 4) for untransformed and log-transformed pore-throat network parameterizations. [** = Iota Area subset].

5.3.2 Group 2 (framework-supported samples – GSD Types 5/6).

Analysis of the probability plots and histograms for the lowest porosity bin (average 7.8%) composed of samples with type 5 or 6 grain size distributions reveals that the pore-throat network parameters have a bi-modal distribution (Figs. 5.20 and 5.21). The two populations identified on the r mean and $r10\%$ probability plots are clearly related to locality, one population corresponding to the Zeta Area samples while the second relates to North Sea samples. Therefore this dataset was further subdivided on the basis of location.

The 5 – 10% Zeta Area dataset's r mean and $r10\%$ values are more closely approximated by a log-normal distribution according to inspection of the probability plots (Fig. 5.22), histograms (Fig. 5.23), AD and RJ (Table 5; Appendix A5.4 Fig. A5.4.8) statistics, and thus the null hypothesis is accepted in this case. However, r mean and $r10\%$ are highly variable and sampled insufficiently to quantify the exhibited variability according to the C_v and N_0 estimates (Table 5.5); it is interesting to note the degree to which this variability is masked by the log-transform (Fig. 5.31; Table 5.5). Conversely the low porosity (average 7.1%) North Sea dataset's r mean and $r10\%$ values seem to be intermediate between a normal and log-normal distribution based on analysis of the probability plots and AD statistics, with the acceptance criteria for the AD and RJ test statistics being met in all cases (Fig. 5.24; Table 5.4). The C_v values indicate that both r mean and $r10\%$ are homogeneous; $r10\%$ is sufficiently sampled to quantify the exhibited variability according to the N_0 estimate (Table 5.5).

Examination of the 10 – 15% porosity dataset again revealed the presence of two intersecting parent populations (Fig. 5.26) and the corresponding histograms are obviously bi-modal (Fig. 4.27). The null hypothesis that the data are normally or log-normally distributed is rejected in both cases in terms of the AD test which fails its test criteria in every case (Table 5.4). The RJ values are only significant for the log r mean and log $r10\%$ parameters (Table 5.4). In contrast to the previous dataset the two populations do not correspond to locality. The group comprising the lower values is dominated by North Sea samples (but includes a Iota Area sample), while the group with larger values includes samples from the North Sea, Iota Area and Zeta Area (Table A5.3.10). As no obvious basis was apparent, this dataset is not further subdivided. The C_v and N_0

estimates indicate that both r mean and $r10\%$ are highly heterogeneous and sampled insufficiently to quantify the exhibited variability (Table 4.5).

The probability plots and histograms for the 15 – 20% dataset (Figs 5.28 and 5.29) both indicate that the null hypothesis, that r mean and $r10\%$ are best described by a log-normal distribution, would be accepted. This assertion is supported by the AD and RJ statistics (see Table 5.4). This dataset was dominated by Type 6 grain size types from the Iota Area, Eta Area and Chi Area in the form of side wall core and plug samples (Fig. 5.19). Both r mean and $r10\%$ are highly variable and are extremely under-sampled to quantify the exhibited variability, according to the C_v and N_0 estimates (Table 5.5). Similarly the null hypothesis that r mean and $r10\%$ are log normally distributed would be accepted for the 20 – 25% porosity dataset as indicated by the probability plots, AD and RJ statistics (Figs 5.30; Table 5.4). A histogram was not plotted since there were only four samples. This dataset was also dominated by Type 6 GSD Types from the Iota Area, Jurassic North Sea and Chi Area in the form of plug and side wall core samples (Fig. 5.19). According to the C_v and N_0 estimates both r mean and $r10\%$ are highly heterogeneous and are extremely under-sampled to quantify the exhibited variability (Table 5.5).

Overall no clear conclusion can be made from this data; location appears to be important in the 5 – 10% porosity dataset, but not in the 10 – 15% dataset, but in both cases the r mean and $r10\%$ values have a bimodal distribution. In terms of the 15 – 20% porosity dataset and the 20 – 25% datasets the null hypothesis that r mean and $r10\%$ are log-normally distributed is accepted, but both datasets are extremely under-represented and exhibit significant variability (Table 5.5).



Figure 5.19. Group 2 pie charts illustrating the distribution of grain size distribution type and sample type for each of the four initial porosity bins comprising GSD Types 5 – 6 utilized in this study.

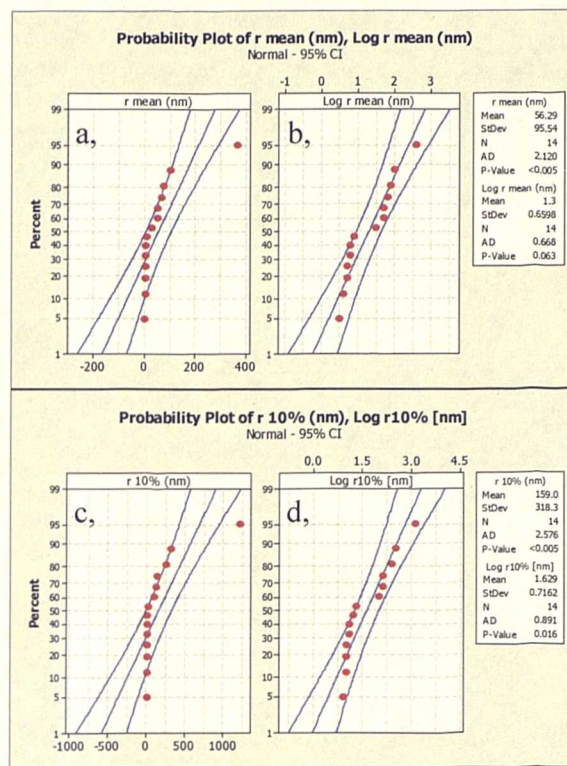


Figure 5.20. Probability plots of: (a) r mean, (b) $\log r$ mean, (c) $r10\%$, and (d) $\log r10\%$ for samples with Type 5 – 6 grain size distributions with a porosity range of 5 – 10% (average 7.8%).

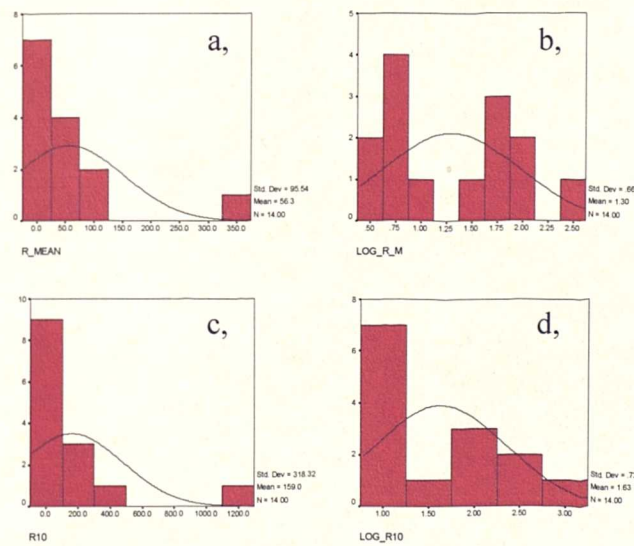


Figure 5.21. Histograms for: (a) r mean, (b) $\log r$ mean, (c) $r10\%$, and (d) $\log r10\%$ for samples with Type 5 – 6 grain size distributions with a porosity range of 5 – 10% (average 7.8%).

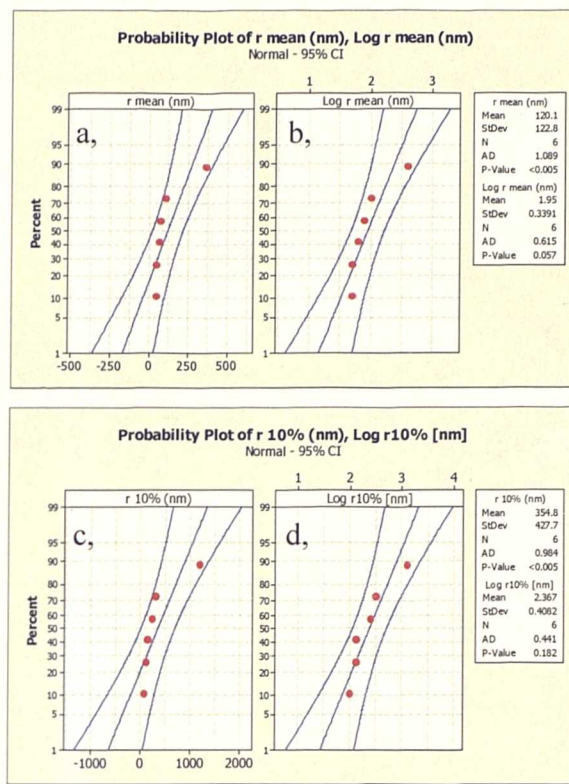


Figure 5.22. Probability plots of: (a) r mean, (b) log r mean, (c) r10%, and (d) log r10% for Zeta Area samples with Type 5 – 6 grain size distributions with a porosity range of 5 – 10% (average 8.5%).

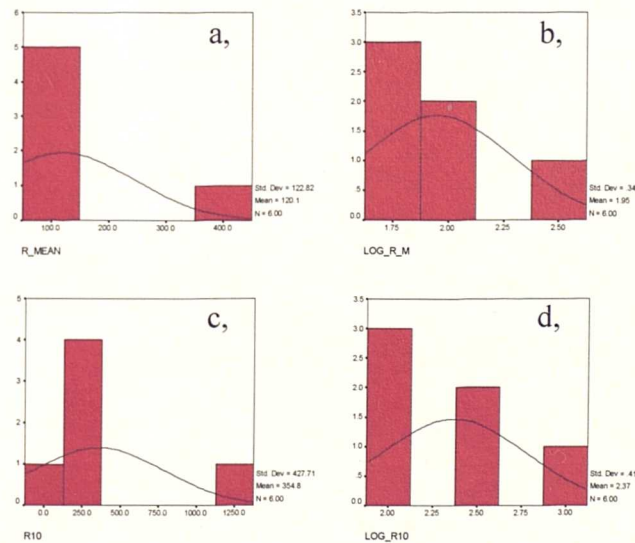


Figure 5.23. Histograms for: (a) r mean, (b) log r mean, (c) r10%, and (d) log r10% for Zeta Area samples with Type 5 – 6 grain size distributions with a porosity range of 5 – 10% (average 8.5%).

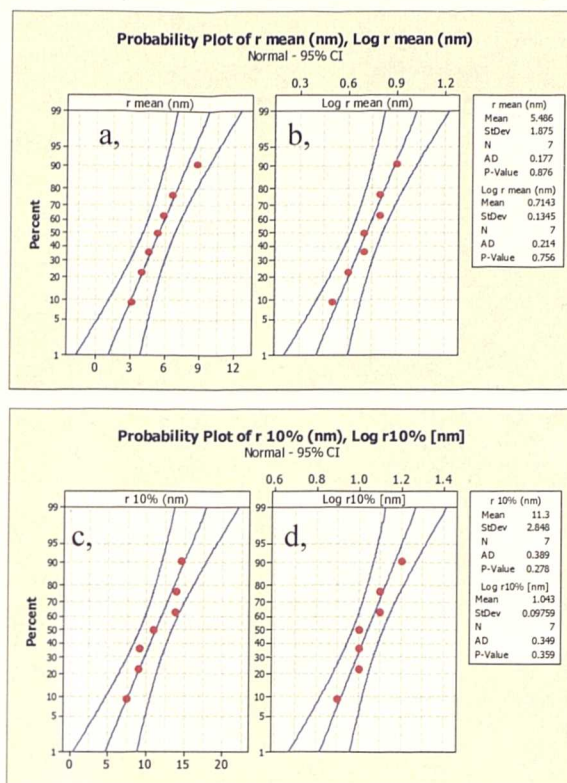


Figure 5.24. Probability plots of: (a) r mean, (b) log r mean, (c) r10%, and (d) log r10% for North Sea samples with Type 5 – 6 grain size distributions with a porosity range of 5 – 10% (average 7.1%).

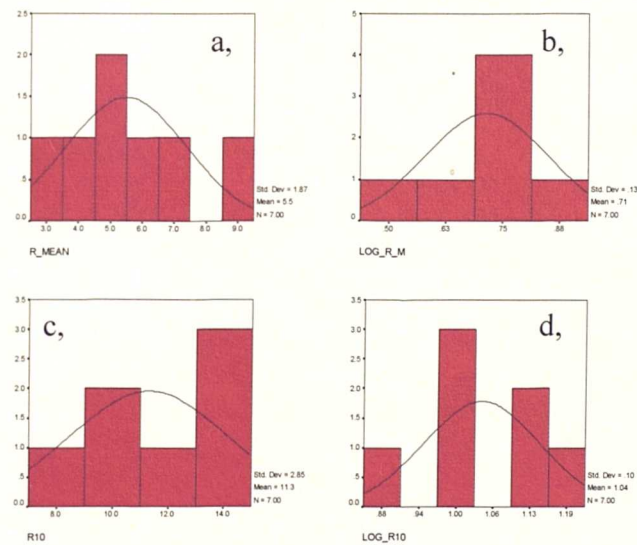


Figure 5.25. Histograms for: (a) r mean, (b) log r mean, (c) r10%, and (d) log r10% for North Sea samples with Type 5 – 6 grain size distributions with a porosity range of 5 – 10% (average 7.1%).

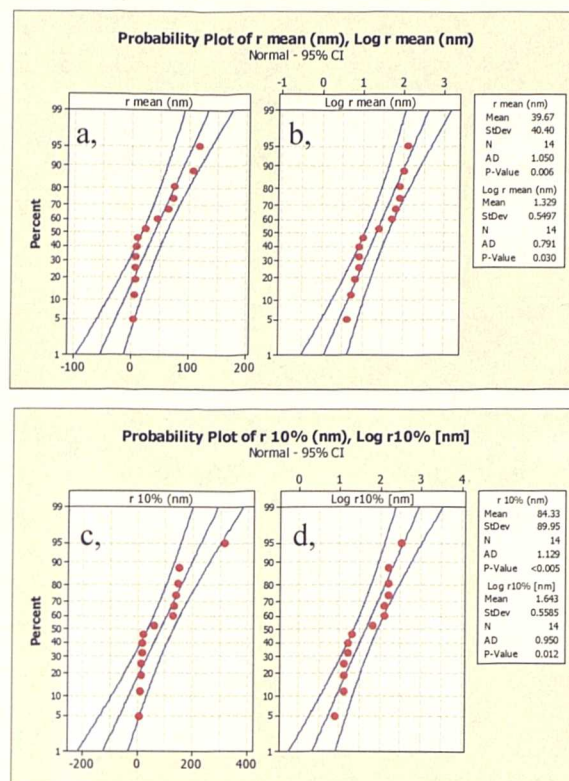


Figure 5.26. Probability plots of: (a) r mean, (b) log r mean, (c) r10%, and (d) log r10% for samples with Type 5 – 6 grain size distributions with a porosity range of 10 – 15% (average 11.4%).

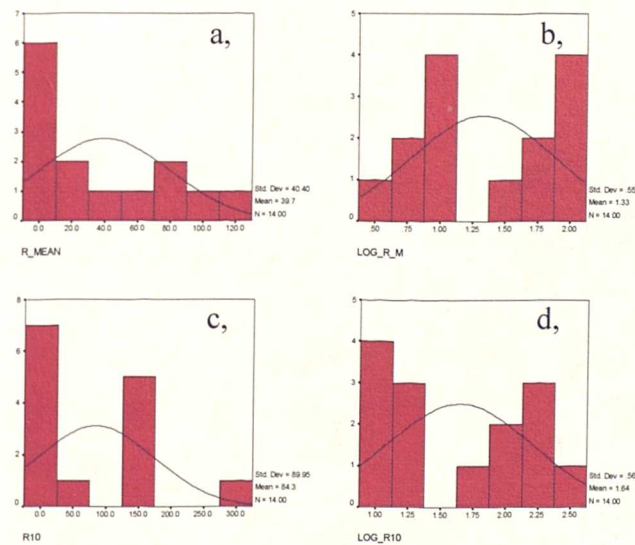


Figure 5.27. Histograms for: (a) r mean, (b) log r mean, (c) r10%, and (d) log r10% for samples with Type 5 – 6 grain size distributions with a porosity range of 10 – 15% (average 11.4%).

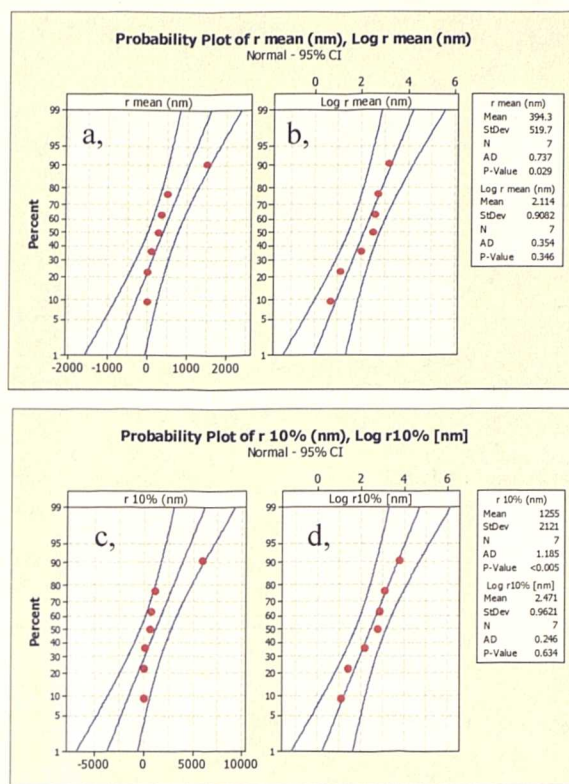


Figure 5.28. Probability plots of: (a) r mean, (b) log r mean, (c) r10%, and (d) log r10% for samples with Type 5 – 6 grain size distributions with a porosity range of 15 – 20% (average 17.5%).

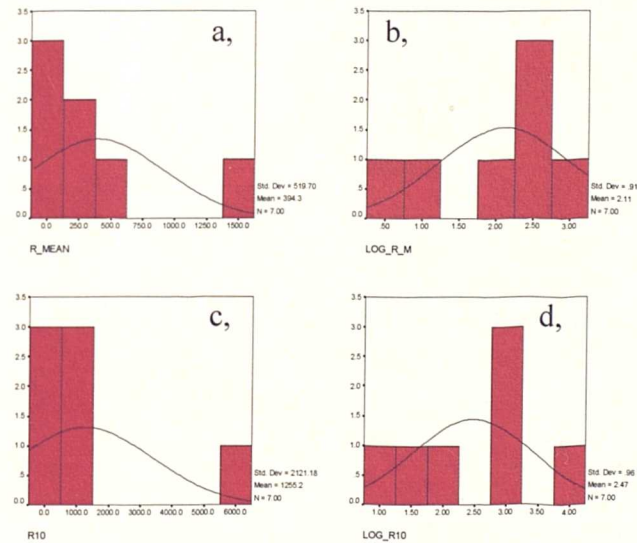


Figure 5.29. Histograms for: (a) r mean, (b) log r mean, (c) r10%, and (d) log r10% for samples with Type 5 – 6 grain size distributions with a porosity range of 15 – 20% (average 17.5%).

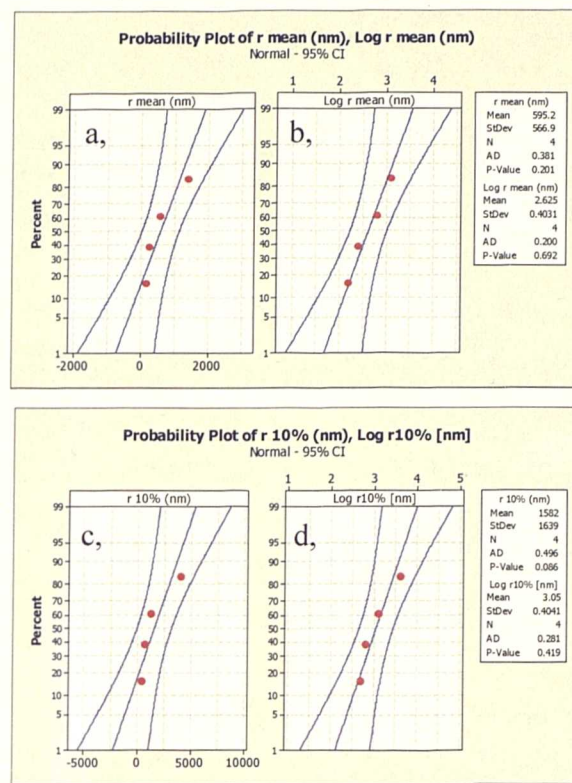


Figure 5.30. Probability plots of: (a) r mean, (b) log r mean, (c) r 10%, and (d) log r 10% for samples with Type 5 – 6 grain size distributions with a porosity range of 20 – 25% (average 23.8%).

Dataset	Parameter	No.	Critical AD (0.05 - the AD stat. has to be < the critical value)	AD	p-value	Critical RJ (0.05 - the RJ stat. has to be > the critical value)	RJ	p-value
7.80%	r mean	14	0.71	2.12	<0.005	0.935	0.748	<0.01
	r 10%	14	0.71	2.576	<0.005	0.935	0.708	<0.01
	log r mean	14	0.71	0.668	0.063	0.935	0.955	>0.1
	log r10%	14	0.71	0.891	0.063	0.935	0.938	0.061
8.5% Zeta Area.	r mean	6	0.63	1.089	<0.005	0.889	0.783	<0.01
	r 10%	6	0.63	0.984	<0.005	0.889	0.804	<0.01
	log r mean	6	0.63	0.615	0.057	0.889	0.907	0.09
	log r10%	6	0.63	0.441	0.182	0.889	0.934	>0.1
7.1% NS	r mean	7	0.65	0.177	0.876	0.898	0.982	>0.1
	r 10%	7	0.65	0.389	0.278	0.898	0.957	>0.1
	log r mean	7	0.65	0.214	0.756	0.898	0.997	>0.1
	log r10%	7	0.65	0.349	0.359	0.898	0.999	>0.1
11.40%	r mean	14	0.71	1.05	0.006	0.935	0.914	0.021
	r 10%	14	0.71	1.129	<0.005	0.935	0.886	<0.01
	log r mean	14	0.71	0.791	0.03	0.935	0.949	>0.1
	log r10%	14	0.71	0.95	0.012	0.935	0.948	0.098
17.50%	r mean	7	0.65	0.737	0.029	0.898	0.865	0.021
	r 10%	7	0.65	1.185	<0.005	0.898	0.784	<0.01
	log r mean	7	0.65	0.354	0.346	0.898	0.961	>0.1
	log r10%	7	0.65	0.246	0.634	0.898	0.979	>0.1
23.80%	r mean	4	0.57	0.381	0.201	0.873	0.923	>0.1
	r 10%	4	0.57	0.496	0.086	0.873	0.887	0.081
	log r mean	4	0.57	0.2	0.692	0.873	0.988	>0.1
	log r10%	4	0.57	0.281	0.419	0.873	0.957	>0.1

Table 5.4. Normality test statistic values for the pore-throat network parameterizations of the samples with type 5 – 6 grain size distributions partitioned by porosity. The lowest AD values and the RJ values greater than the critical value (at 0.05) are in bold.

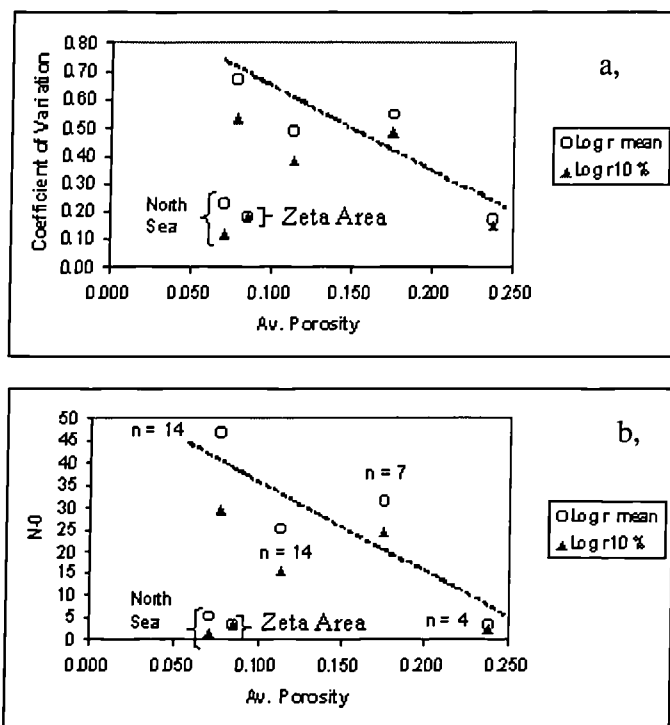


Figure 5.31. Group 2 cross plots of average porosity versus: (a) co-efficient of variation for log r and (b) N_0 for log r mean and log r10%. The number of samples is shown on plot, (b). When location is not considered both C_v and N_0 apparently increase with decreasing porosity; however the significant drop in both C_v and N_0 when samples from the same porosity bin are further divided by location is clearly illustrated. Therefore this increasing heterogeneity may reflect the increasing impact of local factors such as burial history, thermal gradient, etc.

Porosity bin	Av Porosity	No.	r mean CoV	r mean N-0	r10% CoV	r10% N-0	Log r mean CoV	Log r mean N-0	Log r10% CoV	Log r10% N-0
5 - 10%	0.078	14	10.58	11695	17.26	31133	0.67	47	0.53	29
5 - 10%	0.071**	7	0.39	16	0.28	8	0.22	5	0.11	1
5 - 10%	0.085*	6	1.67	293	2.52	665	0.17	3	0.18	3
10 - 15%	0.114	14	3.49	1275	3.90	1590	0.49	25	0.38	15
15 - 20%	0.175	7	21.02	46179	42.22	186332	0.55	31	0.48	24
20 - 25%	0.238	4	1.91	382	2.09	457	0.17	3	0.15	2

Table 5.5. Coefficient of variation and N_0 estimates for the five porosity-based data partitions of Group 2 (GSD Types 5 – 6) for untransformed and log-transformed pore-throat network parameterizations [** = North Sea subset * = Zeta Area subset].

5.4 Discussion

5.4.1 Data distributions and sample support

From the results no clear conclusions can be drawn for Group 1, typically the null hypotheses that r mean and $r10\%$ are normally distributed and that they are log-normally distributed were rejected due to the data were bi-modal in form. This was not the case in two cases, the 5 – 10% and 25 – 30% datasets, and here the null hypothesis that r mean and $r10\%$ values were log-normally distributed was accepted, albeit with the qualifier that the data were highly variable and under sampled (Table 5.3). In one case, the 10 – 15% dataset, the data were not bimodal and was sufficient in terms of accounting for the variability exhibited; however, the results of the statistical tests were ambiguous with neither the hypothesis that the r mean and $r10\%$ values are normally distributed or that the r mean and $r10\%$ values are log-normally distributed being conclusively proven or refuted.

In terms of the C_v and N_0 estimates for the untransformed r mean and $r10\%$ no clear trends are seen with decreasing porosity for Group 1, the 5 - 10% dataset is highly heterogeneous possibly reflecting the large proportion of cuttings in the dataset (Table A5.3.1). According to the N_0 estimate for r mean only the bi-modal 20 - 25% dataset is populated adequately to quantify precisely the variability; for $r10\%$ the 10 - 15%, 20 - 25% and 25 - 30% datasets are all populated sufficiently illustrating that r mean has a higher variance than $r10\%$. It would be expected that the variability of the pore-throat network parameters would decrease as porosity decreases as data from numerous studies has illustrated that the mean pore-throat size and standard deviation of pore-throat size decreases with burial (i.e. increasing effective stress and temperature) e.g. Borst (1982); Griffiths and Joshi (1989, 1990), Katsube and Williamson (1994, 1995); Dewhurst *et al.*, (1998). For the log-transformed r mean C_v is seen to slightly increase with decreasing porosity, this trend is mirrored by the N_0 estimate (Fig. 5.18). No clear trends are apparent for the log-transformed $r10\%$ parameters.

From these results clear conclusions cannot be drawn for Group 2; the 5 – 10% porosity Group 2 dataset was clearly bimodal and was comprised two populations relating to the North Sea and Zeta Area localities. Once partitioned on this basis the Zeta Area 5 – 10% dataset's r mean and $r10\%$ values appeared to conform best to a log-normal distribution and thus the null hypothesis is accepted – although with the qualifier that the data were highly variable and under sampled (Table 5.5). The North Sea 5 – 10% dataset was under sampled for r mean, but sufficiently sampled for $r10\%$ (Table 5.5); however, the results of the statistical tests were ambiguous with neither the hypothesis that the r mean and $r10\%$ values are normally distributed or that the r mean and $r10\%$ values are log-normally distributed being conclusively proven or refuted (refer to AD values, p -values and RF values in Table 5.4).

The 10 – 15% dataset was clearly bimodal, the null hypothesis that the data are normally distributed and that they are log-normally distributed is rejected on the basis of the probability plots, histograms and AD statistical test results. However, in contrast to the previous dataset the underlying cause of this bimodality was not obvious. Furthermore the dataset was significantly under-sampled (Table 5.5). The null hypothesis that r mean and $r10\%$ are log-normality distributed would be accepted for both the 15 – 20% and 20 – 25% datasets as indicated by the probability plots, histograms, Ad and RJ statistical tests. Both datasets are again significantly under sampled.

Initial inspection of the relationship between the coefficient of variation and N_0 to porosity indicates that both these parameters increase with decreasing porosity (Figure 5.31); which as for Group 1 is contrary to what would be expected given the results of previous studies which have illustrated that the mean and standard deviation of pore-throat size distributions decrease with decreasing porosity (e.g. Katsube and Williamson 1994, 1995). If the 5 – 10% dataset is partitioned by location and the 20 – 25% dataset (which only comprises four samples) is disregarded then such a relationship is observed (Figure 5.31). However, to prove conclusively that this was the case many more samples would be required.

As a result of the bimodal and/or heterogeneous nature of the data combined with the low sample numbers per dataset, the degree to which statistically robust statements can be made about the

nature of r mean and $r10\%$ when constrained by porosity and support regime is at best limited. More samples would be required to carry out the initial aims of this work accurately. Below further consideration will be given to the validity of the assumption that the samples segregated into the Group 1 matrix-supported subset and the Group 2 framework-supported subset were truly different. Further consideration is also given to the underlying properties which may have caused the common observation of bimodality seen in the datasets analysed above.

5.4.2 How different are Groups 1 and 2?

To assess how different the distributions are between the two groups proposed in this study datasets of each group corresponding to the same porosity bin were plotted on the same probability plots (Fig. 5.32). It is obvious from the 20-25% porosity bin that the two groups are significantly different, so that establishing the two groups was valid. The 10-15% porosity bin is also plotted (Fig. 5.32 c, d), it is apparent that the Group 2 data is bimodal whereas the Group 1 data is approximately unimodal. Group 2 samples are thought to have a framework-support regime where the load is supported by the interaction of silt and sand grains (minimizing the surface area responsible for bearing the applied load); as compaction proceeds the grains are rearranged until at some point the sediment evolves to a matrix-supported regime (greatly increasing the surface area bearing the load). The controls of this inflection point are unknown but are likely to be at least partly dependent upon the nature of the grain size distribution (Chapter 3). At this transition from framework- to matrix-supported many of the largest pore-throats will be lost and the pore-throat size distribution will evolve to resemble that of an entirely matrix supported sediment type (Fig. 5.32c, d, Chapter 3). The bimodal form of the Group 2 10-15% porosity dataset could simply represent a mix of samples which have maintained a framework and those that have evolved to be matrix-supported. The group of samples from Group 2 with smaller pore-throat network parameters certainly has a distribution which is comparable to that of the Group 1 dataset (Fig. 5.32c, d). The process proposed above would be consistent with the suggestion of a critical compaction point made by Katsube and Williamson (1995) all muds, irrespective of grain size, will evolve to effective zero porosity if subjected to sufficient mechanical and thermal stress.

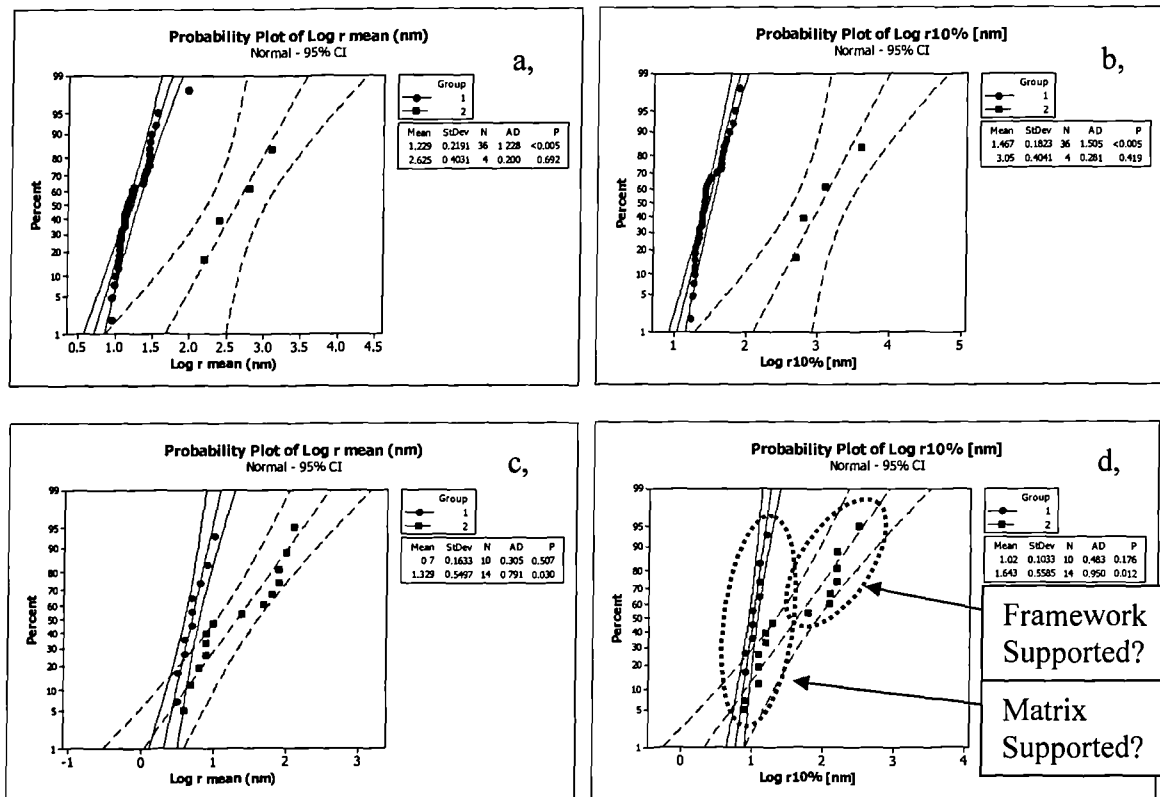


Figure 5.32. Probability plots for Groups 1 and 2 for: (a) r mean from the 20-25% porosity bin, (b) $r10\%$ from the 20-25% porosity bin, (c) r mean from the 10-15% porosity bin, and (d) $r10\%$ from the 10-15% porosity bin.

5.4.3 Bimodality in the r mean and $r10\%$ pore-throat size parameters

The observation that the pore-throat network parameters for a number of the porosity based data partitions are bimodal for both GSD types 1 – 4 and 5 – 6 was not anticipated. It could be suggested that the bimodality is related simply to the low sample number and that increasing the sample population would result in a filling in of the data gap which results in the bi-modal form. However, the Group 1 20 - 25% Iota Area subset was extremely well constrained and still exhibited a bi-modal form. This suggests that, factors other than grain size (and its relation to the support regime) and porosity play a role in determining the nature and behaviour of mudstone pore-throat size distributions.

Group 2 samples with porosity 5 – 10% are clearly derived from two differing parent populations; these populations were shown to relate simply to two differing regions. Further analysis of the two distributions revealed that the Zeta Area dataset had much larger and more variable values of r mean and $r10\%$ and appeared to be best approximated by a log-normal distribution. In contrast the North Sea r mean and $r10\%$ values were much less variable and were closer to a normal distribution. Differences between the Zeta Area and North Sea data may reflect the action of creep closure and/or chemical diagenesis, as the North Sea (Mid to Late Jurassic) samples are significantly older than the Zeta Area samples (Pliocene). Although the Zeta Area samples are actually hotter the North Sea samples would have been exposed to a greater degree of thermal stress as they are much older.

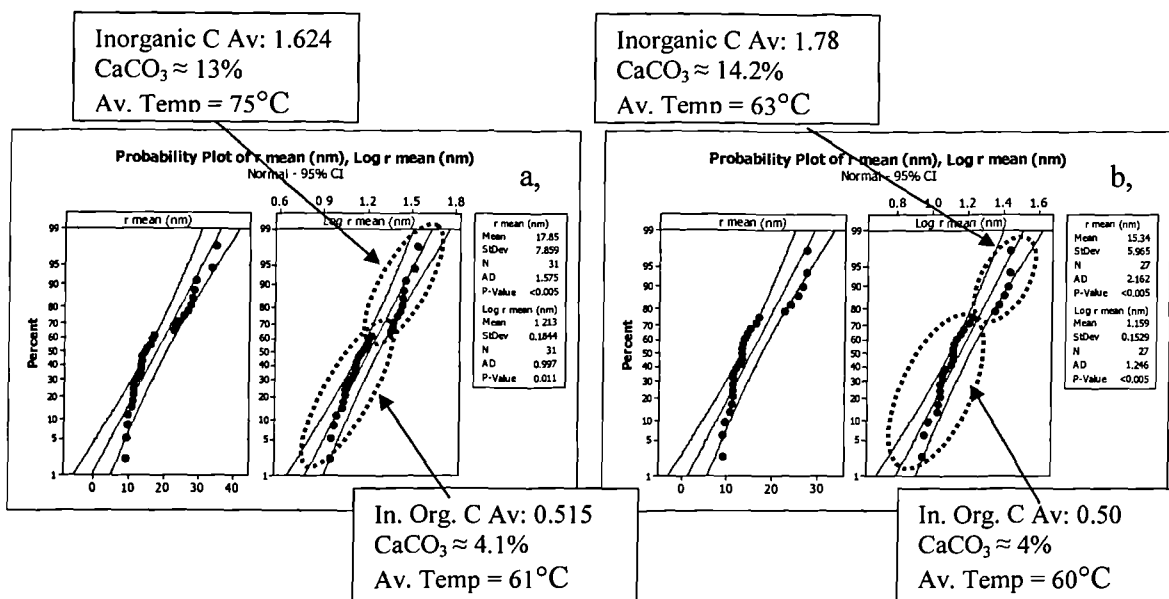


Figure 5.33. Probability plots of r mean and $\log r$ mean for (a) the 20 - 25% grain size type 1 – 4 dataset and (b) the Iota Area well subset illustrating that on average those samples with larger pore-throat size distributions have a higher temperature.

The 20 – 25% porosity partition for samples with Type 1 – 4 grain size distributions are also derived from two differing parent populations. This dataset incorporated 23 side wall core samples from a single Iota Area well, which also show bimodal pore-throat characteristics. In this case the origin of the two populations is less obvious; however, the group with larger pore-throat size parameters has a slightly higher than average CaCO_3 content, both for the full dataset and for

those data drawn exclusively from a single Iota Area well (Fig. 5.33). Also the group with larger pore-throat size values contain a high proportion of cuttings therefore it would seem that these two factors – sample type and carbonate content combine to create the second population with larger pore-throat network parameters.

The dataset comprising only side wall cores from a single Iota Area well showed an even greater contrast in carbonate contents. The group with smaller pore-throat network parameter values (and thus smaller mean pore-throat sizes with lower standard deviations) had an average carbonate content of 4% while the second group, with larger pore-throat network parameters has an average carbonate content of 14.2% (see Fig. 5.33b). In this case, the sample type is identical reducing uncertainty in interpretation; potentially the difference seen in the two pore-throat size modes can be attributed purely to the increased carbonate content. This carbonate content may be in the form of microfossils or cements; microfossils such as coccoliths and foraminifera are two orders of magnitude larger than the majority of grains which make up these sediment types. The fact that the samples with higher pore-throat network values have higher CaCO_3 contents suggests that it is involved in creating and/or maintaining larger pore-throats although further work would be required to understand what mechanisms (i.e. cements, microfossils or a combination?) are actually causing this to be the case.

In some cases the factors leading to bimodality are unclear. For example, the 15 - 20% porosity dataset from samples with Type 1 – 4 GSD's clearly have a bimodal character (Figs 5.10 and 5.11), with the morphology of the probability plots indicating the presence of two intersecting parent populations. Analysis of the location, porosity value, GSD type, CaCO_3 (%), sample type and temperatures did not reveal any obvious basis which could explain the presence of these populations. Similarly, the 10 - 15% porosity dataset from samples with Type 5 – 6 GSD's also have a bimodal character (Fig's 5.26 and 5.27). Again, analysis of the locations, porosity values, GSD types, sample types and temperatures with regard to the r mean and $r10\%$ values did not reveal any obvious basis which could explain the presence of these populations. The group with lower r mean and $r10\%$ values was dominated by North Sea samples, but the presence of North Sea samples in the group with larger values indicates that factors other than locality are of importance. Obviously many factors, such as mineralogy, can potentially vary strongly within a

single locality; further analyses such as quantitative XRD would be required to more fully understand the behaviour of these samples. Overall for these two dataset analysis of the temperature, % carbon and organic carbon data values (which are generally unremarkable) did not reveal any obvious differences between the samples.

5.4.4 Implications for techniques used to predict mudstone flow properties

Basin model population strategies and capillary seal assessment require knowledge of the physical properties of mudstones such as permeability and critical capillary entry pressure, and how they evolve with increasing compaction. The physical properties of mudstones pertinent to fluid flow are intimately related with the nature of the pore-throat size distribution (e.g. Dewhurst *et al.*, 1999a, b). Previous studies have illustrated that the pore-throat size distribution is controlled principally by the porosity (compaction state) and grain size distribution (e.g. Yang and Aplin, 1998; Dewhurst *et al.*, 1998; Chapter 3). The sealing capacity of a mudstone is quantified by the critical capillary entry pressure (CEP), sometimes termed the displacement pressure, and is defined as the pressure at which the seal is penetrated by sufficient volume of non-wetting phase fluid to allow flow of the non-wetting phase (e.g. Hildenbrand *et al.*, 2002).

The data presented in this chapter were unable to validate the hypothesis that at approximately constant porosity and support regime the r mean and $r10\%$ pore-throat network parameters are normally or log-normally distributed. These hypotheses were neither proven nor refuted due to the insufficient samples numbers. This result highlights the requirement for further analysis of well characterized mudstones. Despite this result an attempt at deriving a predictive equation for capillary entry pressure (CEP) using regression techniques will be made; previous work will be introduced briefly and the implications of the choice of predictive parameters, and those inherent in the use of regression used to estimate CEP will be discussed.

Regression techniques are typically employed to estimate a parameter over a continuous range of an independent parameter or parameters; in carrying out such analysis several assumptions are made, including the assumption that the variables are normally distributed (e.g. Kirkup, 2002). The detailed analysis carried out in Section 5.3 has highlighted the impact of both differing

localities and sample types (Figures 5.14 and 5.20) upon the range, absolute values and potential distributions of the r mean and $r10\%$ pore-throat network parameters. This work highlights the dangers of performing regressions on datasets unconstrained in terms of lithology, location, sample types etc; without taking into account the subtleties outlined in this work regressions will be degraded both in regard to their degree of fit and predictive ability. The results in this suggest that a ‘global’ approach is unlikely to be successful and that regional calibration is a vital procedure if physical property prediction is to be successful.

Although numerous studies have reported on the sealing properties of mudstones (e.g. Krushin (1997); Schrömer and Krooss (1997)) the only function which has been published describing the relationship between critical entry pressure (displacement pressure), clay content and porosity is that of Hildenbrand and Urai (2003):

$$CEP_{Hg} = -10.24 + 0.47C - 0.15\phi \quad (5.5)$$

where CEP_{Hg} is the mercury-air displacement pressure in MPa, C = fractional clay content and ϕ = porosity. The r^2 value determined for the Hildenbrand and Urai (2003) dataset equals 0.88 after it was screened for high clay content and calcareous samples. This dataset comprised 19 mudstone samples taken from outcrops ranging in age from Pliocene to Eocene; Hg-derived (‘effective’) porosities ranged between 14.6 and 32.7%. Clay contents ranged between 24 and 95% while sand content ranged between 0 and 32% (Tables 1 and 2, Hildenbrand and Urai, 2003). A relationship between critical entry pressure (displacement pressure), clay content and sand content is also published by these authors, but is not considered here as it has been illustrated that porosity is a fundamental control upon the nature and evolution of pore-throat throat distributions in mudstones (e.g. Yang and Aplin, 1998; Dewhurst *et al.*, 1999a,b).

In the previous section an attempt to characterize the distribution of r mean and $r10\%$ at approximately constant porosity and support regime was made; in the light of the inconclusive result obtained an assumption on the distribution has to be made if regression techniques are to be employed. From inspection of cross plots of porosity versus $r10\%$ [nm] and CEP_{Hc} [MPa] made for each Group (Fig. 5.34) it is clear that: (a) the two groups are different, and (b) that a normal

distribution could not account for the variance exhibited (particularly for Group 2), however, the clear scatter within the data plots indicates clearly that other factors are of significance in agreement with the work above.

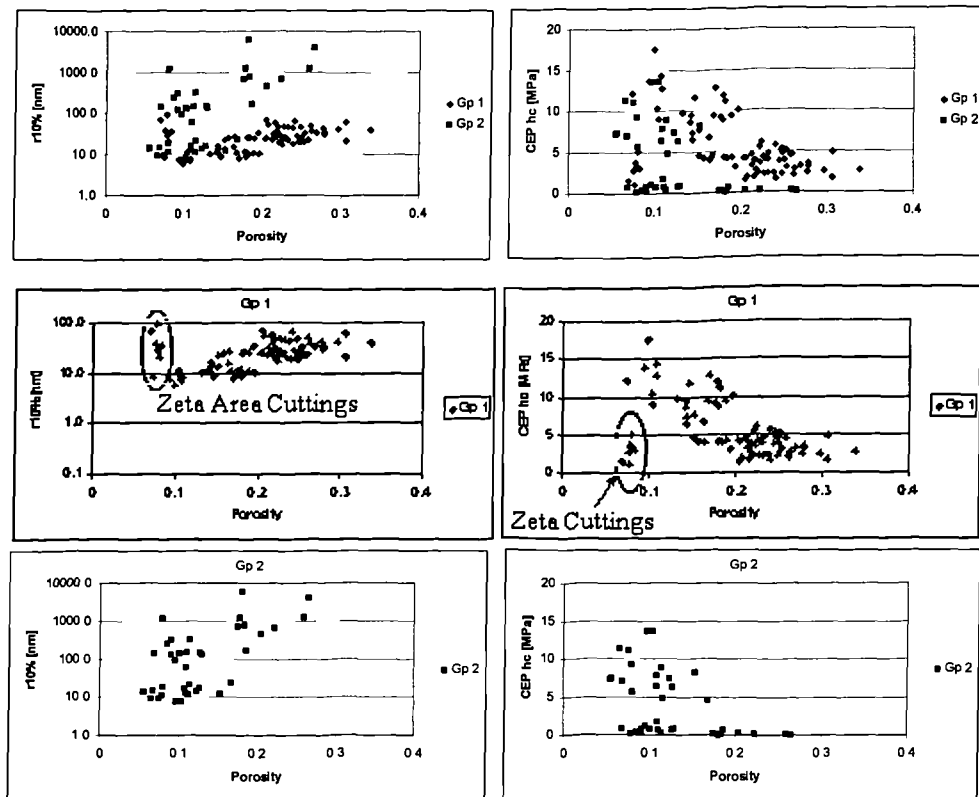


Figure 5.34. Porosity versus $r10\%$ [nm] (a) and CEP_{hc} [MPa] (converted to an oil-water system using an oil-water interfacial tension of 0.051N/m and a wetting angle of 0°) for both Groups collectively (a, b) and for Group 1 (c, d) and Group 2 (e, f) individually.

Lithological variation within the two groups could potentially play a significant role in contributing to this observed variance in $r10\%$ for the two groups. From these plots the assumption is made that $r10\%$ is log-normally distributed. The untransformed CEP value was regressed as a function of the porosity and lithological parameter (Fig. 5.35). Due to the exponential form of the relationship between natural logarithm of the critical pore-throat radius and the CEP when mean Log- $r10\%$ is large (i.e. > 2.3 ($\approx 200\text{nm}$)) the entry pressure will be small and due to the exponential form of the relationship its potential spread (variance) is small (Figure

5.35). Conversely, when the mean Log-r10% is small (i.e. 1.9 (\approx 80nm)) the entry pressure will be large and so will its potential spread (variance). Due to of the exponential relationship between Log-r10% [nm] and CEP_{Hg} [MPa], if Log-r10% is normally distributed for a particular data partition then CEP should also be normally distributed - its variance will be dependent upon the mean and spread of the Log-r10% population (Fig. 5.35).

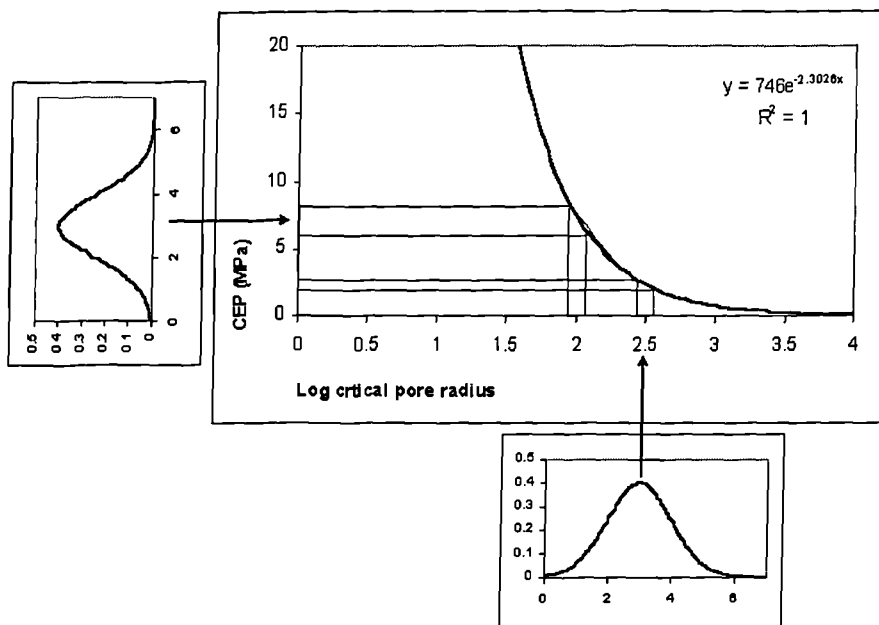


Figure 5.35. Plot of the exponential relationship between critical pore radius and capillary pressure (with constant wetting angle and interfacial tension) illustrating the inter-relationship between statistical distributions used to represent these parameters (see text for discussion).

The CEP_{Hg} was regressed using the following equation:

$$CEP_{Hg} = a + bx_1 + cx_2 \quad (5.6)$$

where CEP_{Hg} is the mercury – air CEP, x_1 is the fractional porosity, x_2 is a lithological parameter (either clay content or sortable silt) and a , b , and c are regression coefficients to be determined (reported as Intercept, X Variable 1 and X Variable 2 in Appendices A5.5 – 8). This equation was regressed on to a Group 1 dataset and a Group 2 dataset. The Group 1 dataset was further divided

into a dataset which comprised all the data, a second in which cuttings were removed, a third dataset where all the Zeta Area samples were removed, and a fourth where both cuttings and Zeta Area samples were removed. The Group 2 dataset was further divided into one set which comprised of all the data, and a second where the Zeta Area samples were removed (no Type 5 – 6 GSD's corresponded to cutting samples).

The initial analysis correlates mercury – air entry pressure (CEP_{Hg}) to porosity and to one of two lithological parameters, the clay content (% $<2\mu m$) and the sortable silt content (% $>10\mu m$) to test which parameter has the greatest correspondence to CEP. This analysis was carried out on both Group 1 and Group 2 sample sets. A second series of regressions was performed on two regional data sets: a Group 1 (GSD Types 1 – 4) Iota Area subset and a Group 2 (GSD Types 5 – 6) Jurassic North Sea subset; in these analyses porosity, clay, sortable silt and temperature are assessed.

5.4.4.1 Group 1 Porosity – grain size correlations

The regression tables are given in Appendix A5.5-6 and a summary of these results is given in Table 5.6. From the correlation coefficients and the error estimates it can be seen that the degree of correlation is generally poor. The error estimates vary from 20MPa for all the data to ~ 16 MPa for the datasets which exclude the Zeta Area and cuttings samples; this range corresponds to a significant range of ~ 1.9 – 1.5 MPa for an oil-water system (assuming an oil-water interfacial tension of 0.035 N/m and an oil-water contact angle of 0°). Recalling the interpretation of p -values: within regression the derived p -values relate to the probability that the correlation obtained is coincidental if x and y are not in any related. Thus the lower the p -value the stronger the evidence that x and y are related by some underlying process allowing the possibility that the correlation is coincidental to be rejected. The p -values for porosity are consistently lower than those for either of the lithological parameters; the lower the p -value the more evidence there is to reject the null hypothesis that the parameter is insignificant in explaining the variance in y . Therefore from the results given in Table 5.6 it can be stated that for Group 1 samples (GSD types 1 – 4) porosity is the most significant variable in predicting CEP. This result is contrary to that of Hildenbrand and Urai (2003) who suggested that clay content was most significant.

Inspection of their data reveals that after they removed two outliers clay content and porosity were weakly negatively correlated, i.e. clay content increased with decreasing porosity, which leads to autocorrelation and an overstatement of the importance of the clay content. For this dataset the clay content and porosity are weakly positively correlated and the sortable silt and porosity are uncorrelated (Fig. 5.36). This correlation may lead to a slight underestimation of the clay content which is reflected in the generally lower *p*-values for clay relative to the sortable silt parameter.

Dataset	n	Regression weights								R^2	Standard Error in y estimate (CEP _{Hg} (MPa))
		Intercept	<i>p</i> -value	Porosity	<i>p</i> -value	Clay	<i>p</i> -value	Sortable Silt	<i>p</i> -value		
All - Φ - clay	83	32.75	7.08E-03	-391.87	2.31E-10	163.21	7.31E-06			0.40	20.28
All - Φ - Sortable Silt	83	119.11	5.74E-15	-257.57	4.35E-09			-130.18	8.76E-05	0.37	20.89
No cuttings - Φ - clay	66	58.01	1.16E-04	-402.99	4.83E-10	125.41	1.29E-03			0.49	19.19
No cuttings - Φ - Sortable Silt	66	125.66	6.76E-15	-308.75	2.11E-10			-97.58	4.00E-03	0.48	19.51
No Zeta Area - Φ - clay	71	90.88	3.31E-08	-392.01	2.15E-11	59.53	8.82E-02			0.55	16.70
No Zeta Area - Φ - Sortable Silt	71	138.04	1.19E-16	-380.69	3.88E-14			-81.15	8.51E-03	0.57	16.21
No Cuttings No Zeta Area - Φ - clay	60	89.67	1.31E-07	-395.84	2.29E-10	65.40	7.10E-02			0.57	16.66
No Cuttings No Zeta Area - Φ - Sortable Silt	60	137.57	9.94E-15	-379.18	2.40E-12			-76.37	1.73E-02	0.59	16.30

Table 5.6. Summary table of the results obtained from regressing porosity and clay content or sortable silt content onto CEP_{Hg} for the four Group 1 (GSD types 1 – 4) datasets.

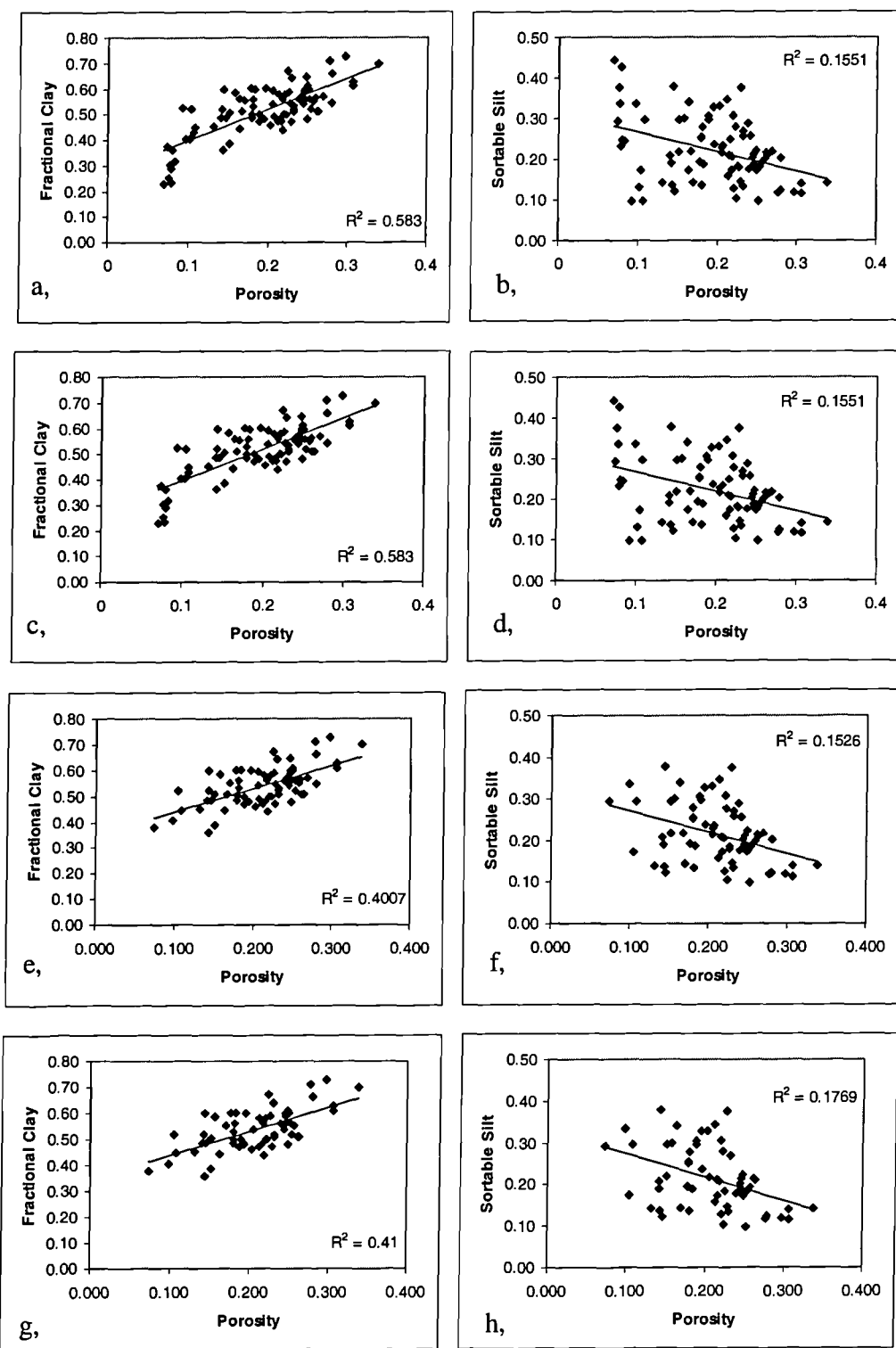


Figure 5.36. Cross plots of clay content and sortable silt against porosity for the complete dataset (a, b), the cuttings screened dataset (c, d), the Zeta Area screened dataset (e, f) and the cuttings and Zeta Area screened dataset (g, h) for Group 1. The extremely low correlation coefficients allows autocorrelation to be discounted when interpreting the regression results.

5.4.4.2 Group 2 Porosity – grain size correlations

Analysis of the correlations between CEP_{Hg} , porosity and the lithological parameters indicates that the regressions for Group 2 samples are of low quality. The regression tables are given in Appendix A5.6 and a summary of these results is given in Table 5.7. As for Group 1, the porosity p -values are lower than those for either of the lithological parameters for Group 2; this indicates that the porosity is more significant in accounting for the variance exhibited by y . In terms of the lithological parameters inclusion of sortable silt as a predictor variable results in an increase in the r^2 , a decrease in the standard error and has lower p -values than the clay content suggesting that this lithological parameter is of more use in predicting CEP (Table 5.7). In Group 2 neither of the lithological parameters shows any degree of correlation with porosity (Fig. 5.37). In terms of the error estimates, the values vary from 27MPa for all the data to ~22MPa from the dataset that exclude the Zeta Area samples; this range corresponds to a significant range of ~2.59 – 2.08MPa for an oil-water system. The highest correlation was obtained for the dataset where the Zeta Area samples were removed and porosity and sortable silt were used as the predictor variables (Table 5.7).

Dataset	n	Regression weights								R^2	Standard Error in y estimate (CEP_{Hg} (MPa))
		Intercept	p -value	Porosity	p -value	Clay	p -value	Sortable Silt	p -value		
All - Φ - clay	39	37.26	4.34E-02	-287.69	1.65E-03	106.46	8.21E-02			0.27	27.61
All - Φ - Sortable Silt	39	133.07	4.33E-06	-273.10	1.14E-03			-122.56	2.89E-03	0.38	25.43
No Zeta Area - Φ - clay	31	75.95	4.76E-01	-396.08	2.82E-05	43.43	4.57E-01			0.48	24.46
No Zeta Area - Φ - Sortable Silt	31	139.30	1.22E-06	-378.17	1.48E-05			-96.04	1.53E-02	0.57	22.20

Table 5.7. Summary table of the results obtained from regressing porosity and clay content or sortable silt content onto CEP_{Hg} for the four Group 2 (GSD types 5 – 6) datasets.

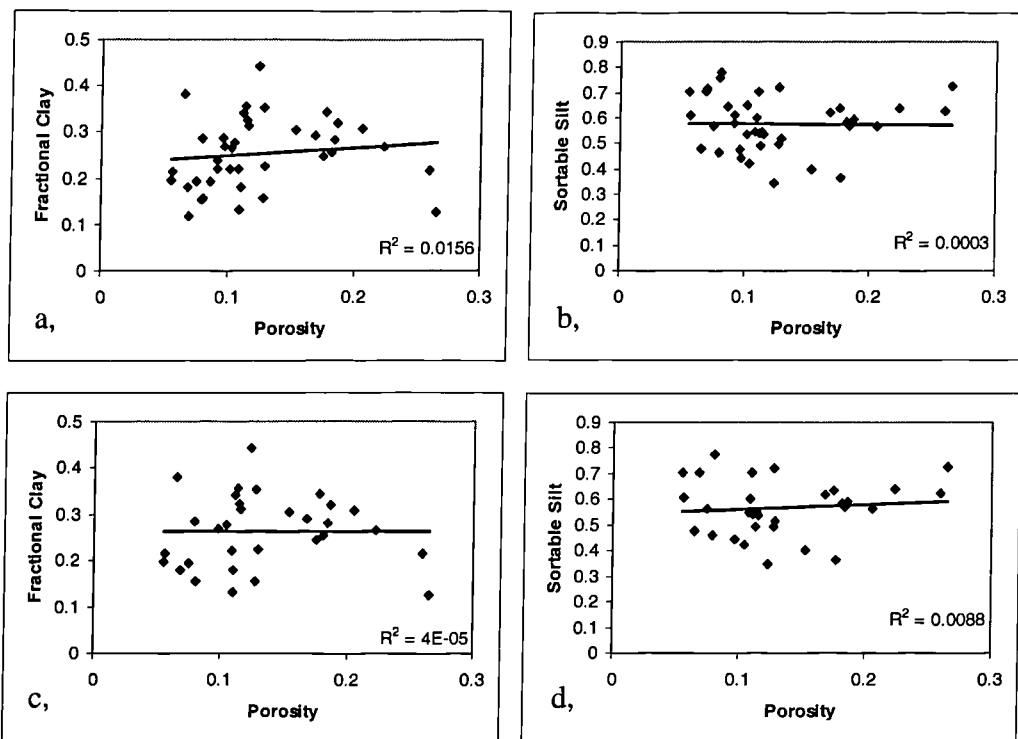


Figure 5.37. Cross plots of clay content and sortable silt against porosity for the complete dataset (a,b) and the Zeta Area screened dataset (c,d), for Group 2 samples. The extremely low correlation coefficients allows autocorrelation to be discounted when interpreting the regression results.

5.4.4.3 Porosity – grain size – temperature

The results presented above illustrate that despite porosity and grain size being important controls upon a mudstone's pore-throat size distribution (Chapter 3; Yang and Aplin, 1998; Dewhurst et al., 1998, 1999a), these parameters yield poor predictions. When the data were partitioned by location, in addition to porosity and support regime, the variability was seen to decrease significantly (e.g. Table 5.5). The reduction of variability is thought to reflect the impact of differing burial histories and mineralogies. In an effort to improve the CEP prediction a Group 1 Iota Area dataset and a Group 2 Jurassic North Sea dataset were further analysed. The regressions were performed as before (see Equation 5.5), but in also included temperature, in an attempt to test for a chemical compaction effect. For these regressions the form of the equation was:

$$CEP_{Hg} = a + bx_1 + cx_2 + dx_3 \quad (5.6)$$

where CEP_{Hg} is the mercury – air CEP, x_1 is the porosity, x_2 is a lithological parameter - either clay content or sortable silt, x_3 is the temperature (°C) and a , b , c and d are regression coefficients to be determined (reported as Intercept, X Variable 1, X Variable 2 and X Variable 3 in the Appendix tables).

5.4.4.3.1 Iota Area subset (Group 1)

The results of the regressions carried out upon the Group 1 Iota Area subset are given in Appendix 6 and summarized in Table 5.8. The degree of fit was improved as evidenced by the modest increase in r^2 values relative to the ‘global’ Group 1 dataset (Table 5.6). The inclusion of temperature is seen to improve the degree of fit of the regressions with the porosity – sortable silt – temperature dataset having the highest r^2 , the lowest standard error and has lower p -values than the clay content suggesting that this lithological parameter is of more use in predicting CEP (Table 5.8).

Dataset	n	Regression weights										R ²	Standard Error in y estimate (CEP Hg (MPa))
		Intercept	p-value	Porosity	p-value	Clay	p-value	Sortable Silt	p-value	Temperature (°C)	p-value		
Iota Area - ϕ - clay	50	68.97	6.80E-06	-318.36	4.26E-09	65.23	3.26E-02					0.54	12.67
Iota Area - ϕ - Sortable Silt	50	122.66	2.40E-16	-306.06	9.44E-12			-101.75	6.90E-05			0.64	11.22
Iota Area - ϕ - clay - Temp.	50	18.71	4.16E-01	-160.39	3.18E-02	48.00	1.00E-01			0.37	1.05E-02	0.80	11.91
Iota Area - ϕ - Sortable Silt - Temp.	50	74.86	2.71E-03	-189.73	3.66E-03			-86.44	5.95E-04	0.28	3.19E-02	0.68	10.78

Table 5.8. Summary table of the results obtained from regressing porosity, temperature and clay content or sortable silt content onto CEP_{Hg} for an Iota Area subset comprising of Group 1 samples (GSD types 1 – 4).

The weighting for temperature is positive indicating that as it increases in value the CEP_{Hg} value also increases (i.e. pore-throat size decreases). This possibly reflects a chemical compaction effect, but may simply reflect the positive correlation between porosity and temperature (Fig. 5.38) both of which are partly dependent upon burial depth which could mask the true relationship. The temperature for these samples ranges from 35.8°C to 108.6°C, according to Aplin *et al.*, (2003) the smectite to illite (I-S) transition occurs at 120°C in similar Iota Area wells. Therefore the temperature effect seen in these samples is unlikely to be related to the I-S transition and suggests that some other temperature mediated reaction may be taking place. For the effect of the mechanically reduced and chemically reduced porosity to be fully assessed uncorrelated parameters would be required.

Some parameter which is sensitive to temperature but less correlated with porosity would potentially improve the ability to assess the relative importance of mechanical and chemical effects; by assessing the *p*-values the significance of each predictor variable could be gauged. In this case the *p*-values for porosity change radically when temperature is included. The *p*-values obtained from regressions performed without temperature indicate that porosity is overwhelming the most significant parameter (see Table 5.8). When temperature is included the *p*-values for porosity significantly increase, and increases by about an order of magnitude for the lithological parameter. This increase will reflect partly that the variance is now being accounted for by three rather than two predictor variables. Further work would be required to fully explore which predictor variables are of most use in predicting CEP_{Hg} . For example the $CaCO_3$ content (%) could be utilized as a predictor variable in the Iota Area as it seemed to have a role in controlling the nature of the mudstones pore-throat size distributions in this area (5.4.3, Fig. 5.33).

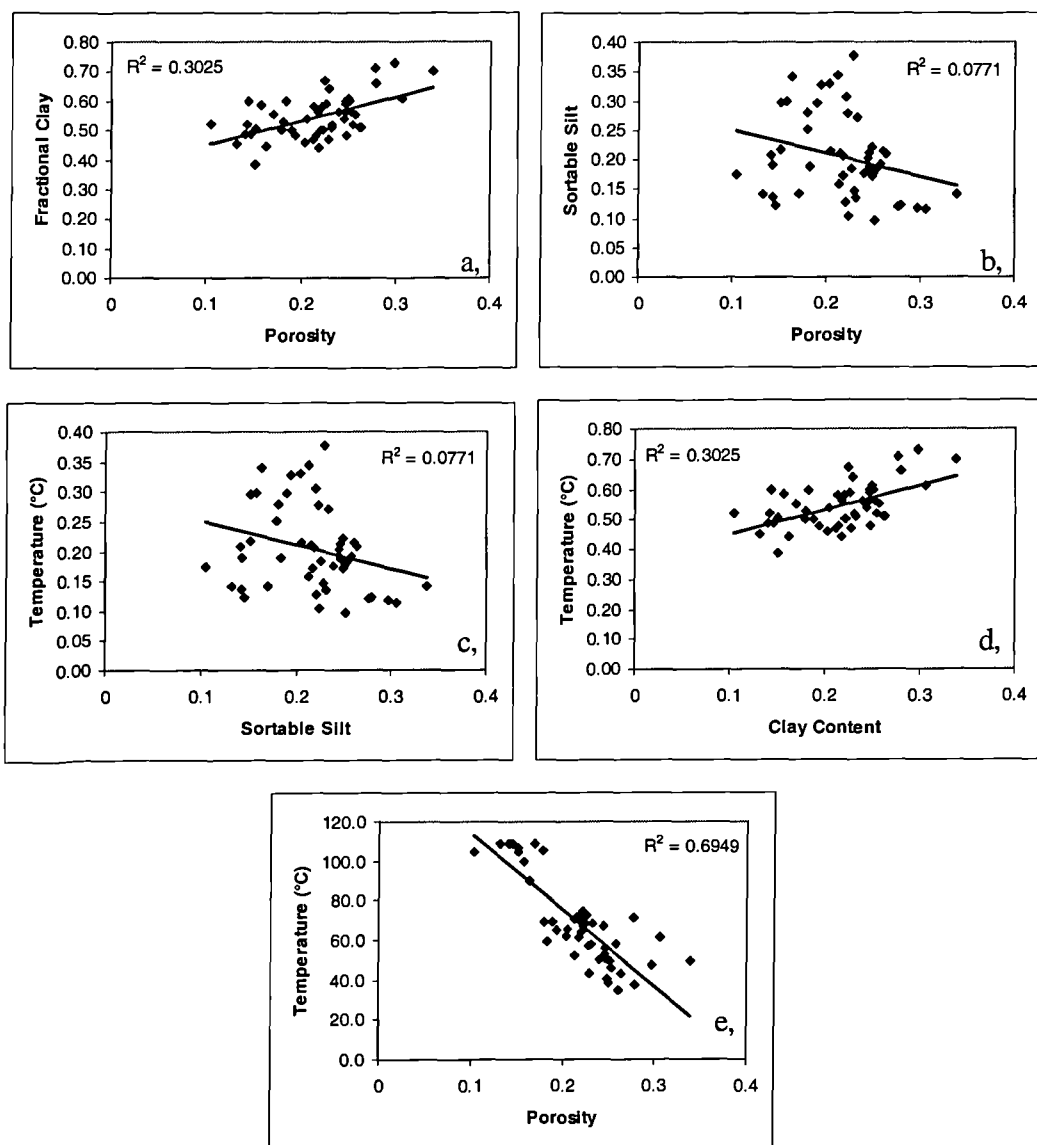


Figure 5.38. Cross plots of clay content and sortable silt against porosity (a, b), clay content and sortable silt against temperature (c, d), and temperature and porosity (e) for the Group 1 Iota Area dataset. The significant correlation between porosity and temperature prohibits the distinct of porosity and temperature driven effects upon the evolution of pore networks using regression analysis.

5.4.4.3.2 North Sea Subset (Group 2)

The results of the regressions carried out upon the Group 2 Jurassic North Sea subset are given in Appendix A5.8 and summarized in Table 5.9. The degree of fit was improved as evidenced by the increase in r^2 values relative to that of the 'global' Group 2 dataset (Table 5.7). The inclusion of temperature is seen to improve the degree of fit of the regressions; again the porosity – sortable silt – temperature dataset has the highest r^2 , the lowest standard error and has lower p -values than the clay content which again suggests that the sortable silt (% $>10\mu\text{m}$) is of more use in predicting CEP (Table 5.8). For the North Sea subset a number of samples also have significant sand contents – which will be reflected by the sortable silt value, but not by the clay content value. The degree of improvement (quantified by r^2) when temperature is included is greater than that seen for the Group 1 Iota Area subset suggesting that temperature is more significant in predicting CEP for the older, hotter Jurassic North Sea samples (compare Fig. 5.37e and Fig. 5.38e). For the sample set the temperature ranges from 59.9°C to 140.4°C and therefore is likely to encompass the range over which the I-S transition takes place which probably accounts for the increased significance of temperature for this dataset relative to the Group 1 Iota Area subset.

Regression weights													
Dataset	N	Intercept	p -value	Porosity	p -value	Clay	p -value	Sortable Silt	p -value	Temperature ($^\circ\text{C}$)	p -value	R^2	Standard Error in y estimate (CEP Hg (MPa))
NS - Φ - clay	18	62.63	2.60E-02	-374.68	6.08E-03	111.91	1.73E-01					0.48	24.92
NS - Φ - Sortable Silt	18	178.00	1.36E-05	-335.24	3.26E-03			-161.98	4.64E-03			0.66	20.16
NS - Φ - clay - Temp.	18	23.66	8.02E-01	-266.32	3.16E-01	116.64	2.10E-01			0.20	7.30E-01	0.53	25.25
NS - Φ - Sortable Silt - Temp.	18	105.94	1.55E-01	-52.60	8.11E-01			-195.74	1.26E-02	0.49	3.00E-01	0.71	19.79

Table 5.9. Summary table of the results obtained from regressing porosity, temperature and clay content or sortable silt content onto CEP_{Hg} for the Jurassic North Sea subset investigated comprising of Group 2 samples (GSD Types 5 – 6).

The results for this dataset are similar to those obtained for the Group 1 data; the weighting for temperature is positive indicating that as it increases in value the CEP_{Hg} also increases. Again this possibly reflects the positive correlation between porosity and temperature (Fig. 5.39) both of which are partly dependent upon burial depth. The error estimate was again slightly reduced to that of global Group 2 dataset, ranging between 24.92MPa and 19.79MPa corresponding to a significant range of $\sim 2.33 - 1.85$ MPa for an oil-water system (again assuming an oil-water interfacial tension of 0.035 N/m and an oil-water contact angle of 0°).

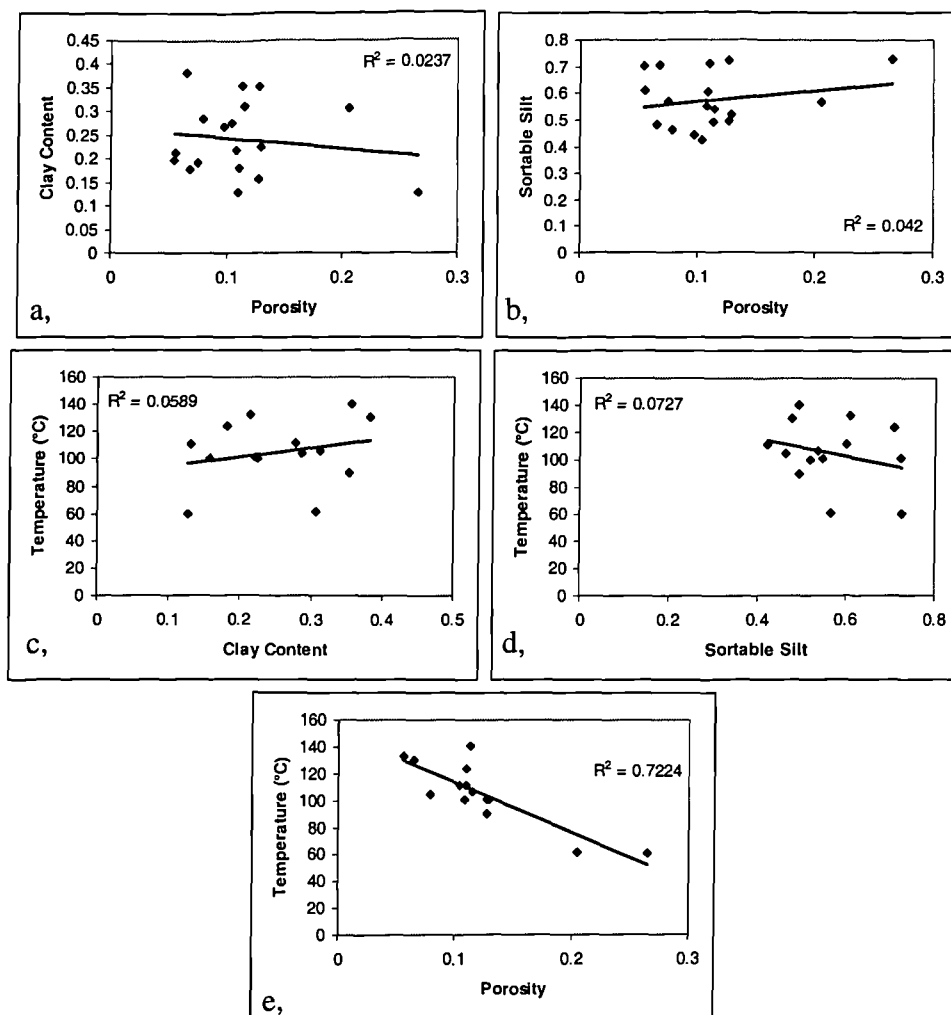


Figure 5.39. Cross plots of clay content and sortable silt against porosity (a, b), clay content and sortable silt against temperature (c, d), and temperature and porosity (e) for the Group 2 Jurassic North Sea dataset. The significant correlation between porosity and temperature prohibits the distinct of porosity and temperature driven effects upon the evolution of pore networks using regression analysis.

5.5 Conclusions

The two groups investigated in this study were formed in an attempt to capture variation observed in terms of grain size distribution (Chapters 2 and 4) and in terms of the pore-throat size distribution characteristics observed in Chapter 3. It was proposed that GSD Types 1 – 4 relate to matrix supported sediments where the pore-throat network is formed by the clay fabric, these sediments formed Group 1; GSD Types 5/6 had framework supported pore-throat networks formed by both the clay fabric and the interaction of silt/sand grains, where the latter collapse preferentially upon compaction. The analysis carried out in this study attempted to (a) characterize the statistical distribution of two pore-throat network parameters, r mean and $r10\%$, when porosity and support regime is accounted for, and (b) capture the behaviours observed in Chapter 3.

The results obtained were largely inconclusive, with the datasets derived either exhibiting a bimodal character unrelated to porosity or support range, or exhibiting a high degree of variability which degraded the confidence of the results of the statistical tests. Therefore the overall result that the hypothesis that r mean and $r10\%$ can be described by a normal distribution when porosity and support regime are accounted for is neither confirmed or refuted; similarly the hypothesis that r mean and $r10\%$ can be described by a log-normal distribution when porosity and support regime are accounted for is neither confirmed or refuted. Robust statements about the nature of the r mean and $r10\%$ distributions cannot be made on the basis of the results obtained here.

Despite the inclusive result it is believed the two groups established in this study are different. This statement is supported by Figures 5.32 and 5.34, both of which illustrate that Group 2 samples typically exhibit higher variability and have larger r mean and $r10\%$ values relative to Group 1 samples at any one porosity level. The degree of difference is most significant at high porosities and decreases as compaction proceeds, as the larger lacunar pore-throats of the Group 2 samples are preferentially lost.

The results of this work indicate that when constrained by porosity and grain size distribution and its relationship to support regime the pore-throat network parameters of mudstones are

appropriately described by a log-normal distribution. A clearer inference could be made from the Group 2 data as they were more closely described by log-normal distributions according to the AD and RJ statistical tests. The Group 1 dataset exhibited more subtleties and in some cases exhibited bi-modal distributions. The pore-throat network properties were shown to be sensitive to a number of factors, other than porosity and grain size distribution, including location (Sedimentary basin), sample type, CaCO₃ (%) content, etc.

In terms of the parameters themselves, the r mean parameter was shown to exhibit a higher degree of variability relative to the $r10\%$ parameter for both Groups 1 and 2. Both groups were shown to be inadequately populated and therefore efforts should be made to analyse mudstones from a range of porosities.

The regressions illustrated that a global approach taken to predict CEP solely using porosity and a lithological parameter is likely to meet with limited success. This is thought due to the sensitivity of this parameter to factors other than porosity and grain size distribution. For the global Group 2 dataset, the Iota Area Group 1 subset and the Jurassic North Sea subset, the sortable silt parameter was found to show a greater degree of correspondence to the CEP value than the clay content as indicated by the r^2 values. Including temperature as a predictor variable was seen to slightly increase the degree of correlation; however, temperature's negative correlation with porosity complicates interpretation.

The results of the regressions obtained in this study illustrate that despite the high values for error in the CEP estimate, the transition from poor capillary seals is extremely rapid (due to the form of the relationship between $r10\%$ - and CEP and thus column height (Fig. 5.35). For example for the Group 1 dataset screened for cuttings and Zeta Area samples the follow equation was obtained (Table 5.6):

$$\text{CEP}_{\text{Hg}} = 137.57 - 379.18\phi - 76.37ss \quad (5.7)$$

where CEP_{Hg} is mercury-air capillary entry pressure, ϕ is fractional porosity and ss is fractional sortable silt content. If the CEP is converted to an oil-water system using an oil-water interfacial

tension of 0.051N/m and a wetting angle of 0° and a oil column height is calculated, assuming a water density of 1030kg and an oil density of 800kg, it can be seen that if sortable silt is held constant at 0.5 (50%) then column height increases from 48m at 26% porosity to 1429m at 20% porosity.

Similarly, for the Group 2 dataset screened for Zeta Area samples the following equation was obtained (Table 5.7):

$$CEP_{Hg} = 139.30 - 378.17\phi - 96.04ss \quad (5.8)$$

where CEP_{Hg} is mercury-air capillary entry pressure, ϕ is fractional porosity and ss is fractional sortable silt content. Again converting to an oil-water system and calculating an oil column height using the parameters given above, it can be seen that if sortable silt is held constant at 0.82 (82%) then column height increases from 2m at 16% porosity to 1379m at 10% porosity. These results illustrate that the transition from poor seals (which would be of high risk) to quality seals (which essentially cease to be a risk) occurs extremely rapidly over narrow porosity ranges, and therefore in assessing capillary seal failure it is of vital importance to constrain the range over which this transition occurs.

Further work is required in terms of simply collecting relevant data which should lead to greater understanding of the bimodality seen in the datasets utilized in this study. Furthermore the addition of further data would lead to a greater robustness in the statistics and definition of statistical distributions for these data types. For both groups 1 and 2 the inclusion of temperature in the regression was seen to improve the correlation, especially for the North Sea data set where the temperature ranges between $<60^{\circ}\text{C}$ to $>130^{\circ}\text{C}$ thus encompassing the I-S transition. The inclusion of data, such as mineralogy (e.g. % I-S) may allow greater appreciation of the interplay of mechanical and chemical effects operating when mudstones are compacted.

Chapter 6 Conclusions and future work

6.0 Conclusions and future work

The data presented within this thesis provides an outstanding dataset of mudrocks collected from a diverse range of settings, representing a wide range of geological ages, tectonic, and sedimentary settings, etc. The key aim was to evaluate similarities and characteristics which were apparently of ‘global’ significance rather than consider factors likely to be of local importance, which are poorly constrained in this dataset.

In Chapter 2 a generic mudstone typing framework was described; the dataset utilized in this study was separated into six mudstone ‘types’ based upon analysis of the grain size spectra, observations from petrographic and SEM images and standard grain size descriptions (% sortable silt; moment statistics). This work presents a novel approach and integrates grain size analysis and microscopy methods (to mudstones) for the first time. The potential of combining the Kranck grain size model with theory on suspended sediment behaviour was recognized. Such an approach has the potential to provide insight into the hydrodynamic conditions present at the time of deposition, making detailed quantitative interpretations of the sedimentological genesis of mudstones a reality for the first time. The scheme proposed in Chapter 2 is not a ‘silver bullet’ and should not be seen as a stand alone methodology; combining it with the scheme of Macquaker and Adam’s (2003) and the bedding form / association scheme proposed by Pickering *et al.*, (1986) would provide a generic, process based, descriptive methodology and classification scheme for mudstones which, particularly in a case study context, would provide a level of detail allowing significant interpretations of mudstone sequences to be made. The GSD types proposed in Chapter 2 prove a starting point and reference for the subsequent analyses undertaken within this study.

In Chapter 3 the relationship between grain size ‘type’ as defined in Chapter 2 and pore size distribution at a range of porosities was investigated. The findings of previous studies of the interplay between grain size and compaction in controlling the pore size

distributions of artificial slurries, soils and geological materials were summarized and integrated into this work; this work, on naturally compacted geological materials, essentially completes a continuum from work on artificial slurries (Fiés, 1992), to work on artificially compacted soils (Griffiths & Joshi, 1989)) to work on artificially compacted mudstone material (Dewhurst *et al.*, 1998, 1999a.b). It was illustrated that the work of Fiés(1992) carried out on artificial slurries had relevance for naturally compacted geological materials. The GSD types defined were found to divide into two groups which exhibited distinct pore size distribution characteristics. Types 1 – 4 (typically with clay contents >40%), with porosities below 30%, had unimodal pore throat size distributions, here implied to represent porosity within and between clay flocs and silt grains (clay fabric pores), and were hypothesized to be ‘matrix’ supported. Grain size types 5 – 6 (typically clay contents <40%) exhibited bimodal pore throat size distributions; the smaller diameter mode was comparable to the clay fabric mode characteristic of types 1 – 4, and the second mode (lacunar pores) comprised pore throats with radii ~ 2 orders of magnitude larger than the clay fabric mode. This second mode was observed to collapse preferentially, in agreement with Dewhurst *et al.*, (1998), decreasing both in size and in volume as porosity is lost. The lacunar pores eventually disappear, either becoming either ‘blind’ pores only accessible through clay fabric pores and/or the larger pores themselves are compacted to an equivalent size to that of the clay fabric pores, producing unimodal pore throat size distributions similar to those of types 1 – 4. Types 5 -6 were hypothesized to be framework-supported. Dewhurst *et al.*, (1999a) hypothesized that at some ‘intermediate’ grain size there may be either a smooth continuation of variation in pore properties or an abrupt transition between ‘matrix’ and ‘framework’ behaviours. Unfortunately, there was a paucity of samples with grain size characteristics that are likely to be transitional between the two modes (i.e. clay contents in the 30 – 40% range). The data presented in Chapter 3 favour an abrupt change in behaviours rather than a smooth transition. The grain size parameters that dictate this transition are complex, and clay content alone is insufficient to account for the behaviour of mudstones because once it drops below ~40% the size distribution of both the silt and the sand components become significant. The sortable silt content is a likely key lithological predictor in determining the nature of mudstone pore size distributions as it corresponds well with the

clay content, with the size distribution of the range silt and with the sand content for the majority of samples. However, further work is required to investigate the influence of detailed grain size upon the pore properties of mudstones.

In Chapter 4 the degree of robustness of the six mudstone GSD types proposed in Chapter 2 was assessed using a numerical classification technique. For the first time a combined PCA-cluster analysis classification methodology was applied to the grain size based classification of mudstones. As the results of any classification will be partly dependent upon the input data, four different datasets encompassing different grain size data were assessed. The results illustrated that irrespective of input data Types 1 – 4 were typically segregated from Types 5 – 6; however, the technique was unable to make any consistent segregations below this level. The clusters derived from this analysis were assessed with regard to the extent to which they corresponded to petrophysical data. Each cluster exhibited a high degree of overlap, and could not be identified from petrophysical measurements alone. While the ‘global’ approach taken in this study seemed to work well in discriminating mudstones into similar GSD types, it was apparent that it cannot easily be extended to petrophysical properties.

Based on the results obtained in Chapter 3 and 4, GSD types 1 – 4 and types 5 – 6 were amalgamated into two groups in Chapter 5. These groups were then further divided into 5% porosity intervals prior to carrying out an analysis of the statistical distribution of two pore parameters - the mean pore size (r mean) and the pore size at the ninetieth percentile of the cumulative pore size distribution ($r10\%$). Due to their common occurrence in ‘natural’ datasets, the normal and log-normal distributions were tested for. Unfortunately, due to insufficient sample numbers and complexities within the data neither the hypothesis that these parameters were normally distributed, nor the hypothesis that the parameters were log-normally distributed could be confidently validated or refuted. However, it was illustrated that even when accounting for porosity and support regime (i.e. matrix versus framework), the r mean and $r10\%$ parameters were often highly variable and it was clear other factors were playing a role. In the discussion of this work a regression based approach was considered for predicting critical capillary entry pressure

(commonly calculated from $r10\%$). It was suggested that due to the exponential form between $\log-r10\%$ and critical capillary entry pressure, the transition from a poor capillary seal to a very good capillary seal was extremely rapid and occurred over a narrow porosity range, indicating that if capillary seal assessment is to be successful capturing this range is of fundamental importance.

The work carried out in this study has highlighted several potentially fruitful avenues of future research. The application of the mudstone typing methodology and mudstone ‘types’ proposed in Chapter 2 require testing within a case study context in order to assess their true practical value. Consideration of the interplay between the grain size characteristics of mudstones and their relationship to depositional mechanisms and conditions highlights the need for further studies in this area. Laboratory analysis of the interplay between flocculated and ‘autonomous’ grain size populations under controlled hydrodynamic conditions will constrain how the grain size spectra of muds and mudstones relate to conditions in the water column at the time of deposition. Such findings will enhance the process-based interpretation of mudstones, particularly where both grain size and petrographic data are available.

Further detailed descriptions of mudstones, in particular those which combine grain size, petrographic and MICP analyses on samples recovered from known tectonic and sedimentological settings, is encouraged. It remains unclear whether or not mudstones exhibit a smooth or abrupt transition between matrix- and framework-supported behaviours. Indeed, it may well be the case that these two possibilities are not mutually exclusive, but rather form the two end-members of the spectrum which describes mudstone behavior. Further work, in particular laboratory based compaction studies of well characterized mudstones spanning the behaviours identified in this work could further resolve the evolution of mudstone pore networks as compaction proceeds, and the influence of grain size upon this evolution.

From the observation of matrix-supported and framework-supported behaviours revealed in Chapter 3 to be typical of the compaction characteristics of mudstones, a clear parallel

can be drawn with the work of Yin *et al.*, (1993) and Pirmez *et al.*, (1997) which investigated the inter-relationships between porosity, grain size and P-wave velocity (V_p). Laboratory analysis of simple sand-clay mixtures have made similar findings to those presented in Chapter 3. Two idealised modes of behaviour of the sound velocity-porosity-lithology relationship were revealed (Marion *et al.*, 1992; Yin, 1993). The two characteristic domains, according to Yin *et al.*, (1993) are matrix-supported (isostress) or framework supported (isostrain); the behaviour of these two types differs because when an acoustic wave propagates through a matrix-supported rock all the sediment grains are exposed to the same degree of stress, conversely when such an event occurs in a framework-supported sediment, only those grains forming the framework are exposed to the stress (Pirmez *et al.*, 1997; Yin *et al.*, 1993). The terms used by Yin *et al.* (1993) to describe matrix- and framework-supported sediments are isostress and isostrain respectively, they are derived from composite mechanics. Isostrain¹ relates to where both framework (i.e. the largest grains in contact) and matrix grains (such as clay flocs within a dominantly silt mixture) are subject to the same strains; while isostress² relates to a composite where both matrix- and framework ‘grains’ are subject to the same stress. Within the structure established by Pirmez *et al.*, (1997), which was based on Yin *et al.*’s (1993) work, the behavior of the physical properties such as V_p and porosity change abruptly between these two domains, where the transition between domains occurs as a function of grain size distribution, at some critical clay content (V_{crit}). Where $V_{clay} > V_{crit}$ the sediment is matrix supported, where an increase in clay content results in a decrease of V_p , and bulk modulus and an increase in porosity. When $V_{clay} < V_{crit}$ the sediment is framework supported, as clay is increased it fills the pore spaces increasing the bulk modulus, which results in a decrease in porosity and an increase in V_p . However, Yin *et al.*, (1993) utilized simple clay-sand mixtures, and it has been shown in this work that in reality the more complex grain size spectra of natural sediments is matched by more complex behaviours. Laboratory based studies of materials with more realistic grain size distribution investigating the relationships between grain size, support regime, porosity, pore size distribution, V_p , and V_s would provide potentially an integration of grain size,

¹ Strain is the change in length per unit length.

² Stress is defined as force per unit area.

pore size (and thus flow property) and acoustic properties of mudstones within a single framework. Combined studies of grain and pore size distribution and their corresponding acoustic properties and may well lead to a point where the extraction of mudstone grain and pore properties from seismic data is possible. The isostrain–isostress regime theory may be invoked to explain how the pore networks of fine grained sediments evolve with increasing compaction. For example, those sediments (typically coarser) that maintain ‘open’ pore networks and thus may define the weak points in a petroleum system are likely to be in the isostrain regime (GSD types 5 – 6); while GSD types 1 – 4 are likely to be in the isostrain regime. It would seem that there is a potentially high degree of overlap between the pore and acoustic properties of mudstones which both relate to the nature of the grain size distribution and how it is structured.

References:

Agrawal, Y.C., McCave, I.N. & Riley, J.B., 1991. Sedigraph techniques, In: Syvitski, J.P.M. (Ed.), *Principles, Methods, & Application of Particle Size Analysis*: Cambridge Univ. Press, New York, 119-128.

Aplin, A.C., Yang, Y. & Hansen, S., 1995. Assessment of β , the compression coefficient of mudstones & its relationship with detailed lithology. *Marine & Petroleum Geology*, **12**, 955 – 963.

Aplin, A.C., Fleet, A.J. & MacQuaker, J.H.S., 1999. Muds & Mudstones: Physical and Fluid Flow Properties. In: Aplin, A.C., Fleet, A.J. & MacQuaker, J.H.S. (eds) 1999. *Muds & Mudstones: Physical & Fluid Flow Properties*. Geological Society, Special Publications, **158**, 1-8.

Aplin, A.C., Matenaar, I.F., & Van der Pluijm, B., 2003. Influence of mechanical compaction & chemical diagenesis on the microfabric & fluid flow properties of Gulf of Mexico mudstones. *Journal of Geochemical Exploration*, **78 – 79**, 449 – 451.

Ashley, G.M. 1978. Interpretation of polymodal sediments. *Journal of Geology*, **86**, 411 – 421.

Baas, J.H., & Best, J.L., 2002. Turbulence modulation in clay-rich sediment laden flows & some implications for sediment deposition. *Journal of Sedimentary Research*, **72**, 336 – 340.

Berhane, I., Sternberg, R.W., Kineke, G.C., Milligan, T.G. & Kranck, K., 1997. The variability of suspended aggregates on the Amazon Continental Shelf. *Continental Shelf Research*, **17**, 267 – 285.

Blatt, H., Middleton, G.V. & Murray, R.C., 1980. *Origin of Sedimentary Rocks*, (2nd Edition), Prentice-Hall, Englewood Cliffs, NY.

Blatt, H. & Totten, M.W., 1981. Detrital quartz as an indicator of distance from shore in marine mudrocks. *Journal of Sedimentary Petrology*, **51**, 1259–1266.

Bohacs, K.M., 1998. Contrasting expressions of depositional sequences in mudrocks from marine to non-marine environs. In: Schieber, J., Zimmerle, W., & Sethi, P.S. (eds) *Shales & Mudstones: Part 1 Basin studies, sedimentology and palaeontology*. Schweizerbart'sche Verlagsbuchhandlung, 33–78.

Borst, R.L., 1982. Some effects of compaction & geological time on the pore parameters of argillaceous rocks. *Sedimentology*, **29**, 291 – 298.

Bulfinch, D.L. & Ledbetter, M.T. 1984. Deep Western boundary undercurrent delineated by sediment texture at base of North American continental rise. *Geo-Marine Letters*, **3**, 31 – 36.

Burland, J.B. 1990. On the compressibility and shear strength of natural clays. *Geotechnique*, **40**, 329 – 378.

Carruthers, D.J.F., 1998. Transport modelling of secondary oil migration using gradient-driven invasion percolation techniques. PhD Thesis, Heriot-Watt University, Edinburgh.

Chang, T.S., Flemming, B.W. & Bartholomä, A., 2004, Distinction between sortable silts & aggregated particles in muddy intertidal sediments of the southern North Sea. From Particle Size to Sediment Dynamics, International Workshop HWK, Delmenhorst.

Christiansen, C. & Hartman, D., 1991. The hyperbolic distribution. In: Syvitski, J.P.M. (ed.) *Principles, Methods, & Application of Particle Size Analysis*. Cambridge University Press, New York, 237 – 248.

Coakley, J.P., & Syvitski, J.P.M., 1991, Sedigraph techniques. In: Syvitski, J.P.M. (ed.) *Principles, Methods, & Application of Particle Size Analysis*. Cambridge University Press, New York, 129-142.

Corbett, P.M.W. & Jensen, J.L. 1992., Variation of Reservoir Statistics According to Sample Spacing & Measurement Type for Some Intervals in the Lower Brent Group. *Log Analyst*, **33**, 22 – 41.

Corbett, P.M.W., 1997. An Introduction to Geoengineering. Lecture notes. MSc Petroleum Geochemistry, University of Newcastle.

Curran, K.J., Hill, P.S., Schell, T.M., Milligan, T.G. & Piper, D.J.W., 2004. Inferring the mass fraction of floc-deposited mud: application to fine grained turbidites. *Sedimentology*, **51**, 927 – 944.

Davis, J.C., 2002. *Statistics & Data Analysis in Geology*, (3rd Edition), John Wiley, New York, 638pp.

Deutsch, C.V., 2002. *Geostatistical Reservoir Modeling*. Applied Geostatistics Series. Oxford University Press, New York, 376pp.

Dewhurst, D.N., Aplin, A.C., Sarda, J-P. & Yang, Y., 1998. Compaction-driven evolution of porosity & permeability in natural mudstones: An experimental study. *Journal of Geophysical Research*. **103**(B1), 651 – 661.

Dewhurst, D.N., Aplin, A.C., & Yang, Y., 1999a. Permeability & fluid flow in natural mudstones. In: Aplin, A.C., Fleet, A.J. & Macquaker, J.H.S. (eds) *Muds & Mudstones: Physical & Fluid Flow Properties*. Geological Society, Special Publications, **158**, 23-43.

Dewhurst, D.N., Aplin, A.C., & Sarda, J., 1999b. Influence of clay fraction on pore-scale properties & hydraulic conductivity of experimentally compacted mudstones. *Journal of Geophysical Research*, **104**(B12), 29,261-29,274.

Dewhurst, D.N., Cartwright, J.A. & Lonergan, L., 1999c. The development of polygonal fault systems by syneresis of colloidal sediments. *Marine & Petroleum Geology*, **16**, 793 – 810.

Doveton, J.H. 1994. *Geologic Log Analysis Using Computer Methods*. American Association of Petroleum Geologists, Computer Applications, No. 2, Tulsa, 169 pp.

Drake, D.E. & Caccione, D.A. 1986. Field observations of bed shear stress and sediment resuspension on continental shelves, Alaska and California. *Continental Shelf Research*, **6**, 415 – 429.

Driscoll, M.L., Tucholke, B.E. & McCave, I.N., 1985. Seafloor zonation in sediment texture on the Nova Scotian Lower Continental Rise. *Marine Geology*, **66**, 25 – 41.

Duppenbecker, S.J. & Iliffe, J.E., (eds) 1998. *Basin Modelling: Practice & Progress*. Geological Society Special Publication, London, **141**, 245pp.

Ebanks, W.J., Jr., 1987. Flow Unit Concept – Integrated Approach to Reservoir Description for Engineering Projects. *American Association of Petroleum Geologists Bulletin*, **551** – 552.

Ehrlich, R., 1983. Editorial: Size Analysis Wears No Clothes, or Have Moments Come & Gone? *Journal of Sedimentary Petrology*, **53**, p2.

Einsele, G., 1991. Submarine Mass Flow Deposits and Turbidites. In: Einsele, G., Ricken, W., & Seilacher, A. (eds) *Cycles and Events in Stratigraphy*, Springer-Verlag, Berlin, 313 – 339.

Eisma, D. 1993. *Suspended sediment in the aquatic environment*. Springer-Verlag.

England W.A., Mackenzie, A.S., Mann, D.M., Quigley, T.M. 1987. Movement and entrapment of fluids in the subsurface. *Journal of the Geological Society*, **144**, 327 – 347.

Fies, J.C. 1984. Analyse de la repartition du volume des pores dans les assemblages argile-squelettes: comparaison entre un modele d'espace poral textural et les donnees fournies par la porosimetre au mercury. *Agronomie*, **4**, 891 – 899.

Fies, J.C. 1992., Analysis of soil textural porosity relative to skeleton particle size using mercury porosimetry. *Soil Science Society of America Journal*, **56**, 1062 – 1067.

Fies, J.C. & Bruand, A., 1990. Textural porosity analysis of silty clay soil using pore volume balance estimation, mercury porosimetry and quantified backscattered electron scanning image (BESI). *Geoderma*, **47**, 209 – 219.

Fies, J.C. & Bruand, A., 1998. Particle packing & organisation of the textural porosity in clay-silt-s& mixtures. *European Journal of Soil Science*, **49**, 557 – 567.

Flemming, B.W. 2000. A revised textural classification of gravel-free muddy sediments on the basis of ternary diagrams. *Continental Shelf Research*, **20**, 1125 – 1137.

Fogg, G. E., 1990. Architecture and interconnectedness of geologic media: Role of the low-permeability facies in flow & transport. In: S. P. Neuman & Neretrieck I., (eds.) *Hydrogeology of Low Permeability Environments*, Verlag Heinz Heise, Hannover, Germany, 19 – 40.

Gibbs, R.J., Matthews, M.D., & Link, D.A., 1971. The relationship between sphere size and settling velocity. *Journal of Sedimentary Petrology*, **41**, 7-18.

Gill, D., Shomrony, A. & Fligelman, H., 1993. Numerical zonation of log suites and logfacies recognition by multivariate clustering. *American Association of Petroleum Geologists Bulletin*, **77**, 1781 – 1791.

Gorsline, D.S., 1984. A review of fine-grained sediment origins, characteristics, transport, & deposition. In: Stow, D.A.V., & Piper, D.J.W. (eds.) *Fine-grained sediments: deep sea processes & facies*. Geological Society Special Publication, **15**, 17 – 34.

Griffiths, J.C., 1967. *Scientific method in analysis of sediments*. McGraw-Hill. 508pp.

Griffiths, F.J. & Joshi, R.C., 1989. Change in pore size distribution due to consolidation of clays. *Geotechnique*, **39**, 159 – 167.

Hamilton, E.L., 1971, Prediction of in-situ acoustic and elastic properties of marine sediments., *Geophysics*, **36**, 266-284.

Hamilton, E.L., 1980, Geoacoustic modeling of the sea floor; *Journal of the Acoustic Society of America*, **68**, 313-1340.

Hampton, M.A., Lee. H.J., & Locat, J., 1996. Submarine Landslides. *Reviews of Geophysics*, **34**, 33 – 59.

Hein, F.J. & Gorsline, D.S., 1981. Geotechnical aspects of fine-grained mass flow deposits: California Continental Borderland. *Geo-Maine Letters*, **1**, 1 -5.

Hein, F.J., 1991. The need for grain size analyses in marine geotechnical studies. In: Syvitski, J.P.M. (ed.) *Principles, Methods, & Application of Particle Size Analysis*, Cambridge University Press, New York, 346-362.

Hildenbrand, A. & Urai, J.L., 2003. Investigation of the morphology of pore space in mudstones – first results. *Marine and Petroleum Geology*, **20**, 1185-1200.

Hurst, A. & Rosvoll, K., 1991. Permeability variations in sandstones & their relationship to sedimentary structures. In: Lake, L.W., Carroll, H.B. Jr & Wesson, T.C. (eds) *Reservoir Characterisation II*, Academic Press, San Diego, California, 66 – 196.

Jensen, J.L., Lake, L.W., Corbett, P.M.W. & Goggin, D.J., 1997. *Statistics for Petroleum Engineers & Geoscientists*. Prentice-Hall, New Jersey, 390pp.

Jones, K.P.N., McCave, I.N., & Weaver, P.P.E., 1992. Textural and dispersal patterns of thick mud turbidites from the Madeira Abyssal Plain, *Marine Geology*, **107**, 149 – 173.

Katsube, T.J. & Williamson, M.A., 1994. Effects of diagenesis on clay nanopore structure and implications for sealing capacity, *Clay Minerals*, **29**, 451 – 461.

Katsube, T.J. & Williamson, M.A., 1995. Critical depth of burial of subsiding shales and its effect on abnormal pressure development. In: Bell, J.S., Bird, T.D., Hillier, T.L. & Greener, P.L. (eds) *Proceedings of the Oil & Gas Forum '95, Energy from Sediments*. Geological Survey of Canada Open File, **3058**.

Kirkup, L. 2002. *Data Analysis with Excel®: An Introduction for Physical Scientists*, Cambridge University Press, Cambridge, 446pp.

Kranck, K., 1975. Sediment Deposition from flocculated suspensions, *Sedimentology*, **22**, 111-123.

Kranck, K., 1980. Experiments on the significance of flocculation in the settling of fine-grained sediment in still water, *Canadian Journal of Earth Science*, **17**, 1517 - 1526.

Kranck, K. 1984., Grain-size characteristics of fine turbidites. In: Stow, D.A.V., & Piper, D.J.W. (eds.) *Fine-grained sediments: deep sea processes and facies*, Geological Society of London Special Publication, **15**, 83 – 94.

Kranck, K & Milligan, T.G., 1985. Origin of grain size spectra of suspension deposited sediment, *Geo-Marine Letters*, **5**, 61 – 66.

Kranck, K & Milligan, T.G., 1991. Grain size in oceanography, In: Syvitski, J.P.M. (ed.) *Principles, Methods, & Application of Particle Size Analysis*, Cambridge University Press, New York, 332-345.

Kranck, K., Smith P.C., & Milligan, T.G., 1996a. Grain size characteristics of fine grained unflocculated sediments I: "One-round" distributions, *Sedimentology*, **43**, 589-596.

Kranck, K., Smith, P.C., & Milligan, T.G., 1996b. Grain size characteristics of fine grained unflocculated sediments II - "Multi-round" distributions", *Sedimentology*, **43**, 597-606.

Krushin, J.T., 1997. Seal capacity of non-smectite clays. In: Surdam, R.C. (ed) *Seals, traps and the petroleum system*. AAPG Memoir 67, 31 – 47.

van Leussen, W., 1988. Aggregation of particles, settling velocity of mud flocs – a review. In: Dronkers, J. & van Leussen, W. (eds) *Physical Processes in Estuaries*. Springer-Verlag, New York, 348 – 403.

Lindsay, J.F., Prior, D.B., & Coleman, J.M. 1984. Distributary-mouth bar development & role of submarine l&slides in delta-growth, South pass, Mississippi-delta, *American Association of Petroleum Geologists*, **68**, 1732 – 1743.

Macquaker J.H.S. & Gawthorpe R.L., 1993. Mudstone lithofacies in the Kimmeridge Clay Formation, Wessex Basin, southern England: Implications for the origin and controls of the distribution of mudstones, *Journal of Sedimentary Petrology*, **63**, 1129-1143.

Macquaker J.H.S. & Taylor, K.G., 1996. A sequence stratigraphic interpretation of a mudstone-dominated succession: the Lower Cleveland Ironstone Formation, UK. *Journal of the Geological Society of London*, **153**, 759 – 770.

Macquaker J.H.S. & Howell J.K., 1999. Small-scale (< 5.0 m) vertical heterogeneity in mudstones: Implications for high resolution stratigraphy in siliciclastic mudstone successions, *Journal of the Geological Society of London*, **156**, 105 – 112.

Macquaker, J.H.S. & Adams, A.E., 2003. Maximising information from fine-grained sedimentary rocks: An inclusive nomenclature for mudstones. *Journal of Sedimentary Research*, **73**, 735 – 744.

Marion, D., Nur, A., Yin, H. & Han, D., 1992. Compressional velocity and porosity in s&-clay mixtures. *Geophysics*, **57**, 554 – 563.

McCave, I.N., 1984. Erosion, transport & deposition of fine grained marine sediments. In: Stow, D.A.V. & Piper, D.J.W. (eds.) *Fine-grained sediments: deep sea processes and facies*, Geological Society of London Special Publication, **15**, 35-69.

McCave, I.N. & Jones, K.P.N., 1988. Deposition of ungraded muds from non-turbulent turbidity currents, *Nature*, **333**, 250 – 252.

McCave, I.N., & Syvitski, J.P.M., 1991. Principles and methods of geological particle size analysis. In: Syvitski, J.P.M. (ed) *Principles, Methods, & Application of Particle Size Analysis*, Cambridge University Press, Cambridge, 3-21.

McCave, I.N., Manighetti, B., & Robinson, S.G., 1995. Sortable silt and fine sediment size/composition slicing: parameters for palaeocurrent speed and palaeoceanography, *Paleoceanography*, **10**, 593-610.

Meyer, B.L. & Nederlof, M.H., 1984. Identification of source rocks from wireline logs by density/resistivity & sonic transit time/resistivity crossplots, *American Association of Petroleum Geologists Bulletin*, **68**, 121 – 129.

Middttømme, K. & Roaldset, E., 1999. Thermal conductivity of sedimentary rocks: uncertainties in measurement & modelling. In: Aplin, A.C., Fleet, A.J. & Macquaker, J.H.S. (eds) *Muds & Mudstones: Physical & Fluid-Flow Properties*, Geological Society of London Special Publication, **158**, 45 – 60.

Miller, M.C., McCave, I.N. & Komar, P.D., 1977. Threshold of sediment motion under unidirectional currents, *Sedimentology*, **24**, 507 – 527.

Milligan, T.G. & Loring, D.H., 1997. The effect of flocculation on the size distributions of bottom sediment in coastal inlets: implications for contaminant transport, *Water Air Soil Pollution*, **99**, 33-42.

Milliman, J.D. & Syvitski, J.P.M., 1992. Geomorphic/tectonic control of sediment discharge to the ocean: the importance of small mountainous rivers, *Journal of Geology* **100**, 525 – 544.

Mulder, T & Alexander, J., 2001. The physical character of subaqueous sedimentary density flows & their deposits, *Sedimentology*, **48**, 296 – 299.

Nagaraj, T.S., Vatsala, A. & Srinivasa Murthy, B.R., 1990. Discussion: Change in pore size distribution due to consolidation of clays, *Geotechnique*, **40**, 303 – 309.

O'Brien, N.R. & Slatt, R.M., 1990. *Argillaceous rock atlas*. Springer-Verlag. 141pp.

Newsham, K.E., Rushing, J.A., Lasswell, P.M., Cox, J.C. & Blasingame, T.A., 2004. A comparative study of laboratory techniques for measuring capillary pressures in tight gas sands, *Society of Petroleum Engineers*, 89866.

Pickering, K.T., Stow, D.A.V., Watson, M.P. & Hiscott, R.N. 1986. Deep-water facies, processes & models: a review & classification scheme for modern and ancient sediments, *Earth Science Reviews*, **23**, 75 – 174.

Piper, D.J.W., 1978. Turbidite muds & silts on deep-sea fans & abyssal plains. In: Stanley, D.J. & Kelling, G. (eds) *Sedimentation in Submarine Canyons, Fans & Trenches*, Dowden, Hutchinson & Ross, Stroudsburg, Pa., 163 – 176.

Piper, D.J.W & Stow, D.A.V., 1991. Fine-Grained Turbidites. In: Einsele, G., Ricken, W., & Seilacher, A. (eds) *Cycles & Events in Stratigraphy*, Springer-Verlag, Berlin, 360 – 376.

Pirmez, C., Flood, R.D., Baptiste, J., Yin, H.Z. & Manley, P.L., 1997. Clay content, porosity & velocity of Amazon Fan sediments determined from ODP Leg 155 cores and wireline logs, *Geophysical Research Letters*, **24**, 317-320.

Richardson, J.F. & Zaki, W.N., 1958. Sedimentation and fluidization, *Transactions of the Institute of Chemical Engineering*, **32**, 35 – 53.

Rider, M. 1996. *The Geological Interpretation of Well Logs*. (3rd Edition), Caithness (Whittles Publishing).

Ryan, T.A. & Joiner, B.L. 1976. Minitab: A statistical computing system for student researchers. *The American Statistician*, **27**, 222 – 225.

Schieber, J., Zimmerle, W. & Sethi, P.S., 1998. (eds) *Shales & Mudstones I. Basin Studies, Sedimentology, & Palaeontology*. E. Schweizerbart'sche Verlagsbuchhandlung, Stuttgart, 384pp.

Schieber, J., 1998. Deposition of fine-grained sediments. In: Schieber, J., Zimmerle, W. & Sethi, P.S., 1998. (eds) *Shales & Mudstones I. Basin Studies, Sedimentology, & Palaeontology*. E. Schweizerbart'sche Verlagsbuchhandlung, Stuttgart, 384pp.

Schieber, J., 1999. Distribution and deposition of mudstone facies in the Upper Devonian Snye Group of New York, *Journal of Sedimentary Research*, **69**, 909-92.

Schlömer, S. & Krooss, B. M., 1997. Experimental characterisation of the hydrocarbon sealing efficiency of caprocks, *Marine and Petroleum Geology*, **14**, 565 – 580.

Schowalter, T. T. 1979. Mechanics of secondary hydrocarbon migration and entrapment. *American Association of Petroleum Geologists*, **63**, 723 – 760.

Slatt, R.M., 2003. Importance of shales and mudrocks in oil and gas exploration & reservoir development, *In: Scott, E.D., A. H. Bouma, & W.R. Bryant (eds) Siltstones, mudstones & shales: depositional processes & characteristics*, SEPM/GCAGS Special Publication, Society of Economic Paleontologists and Mineralogists, 1-22.

Sorby, H.C., 1908. On the application of quantitative methods to the study of the structure and history of rocks, *Quarterly Geological Society of London*, **64**. 171 – 233.

Stevens, R.L., Bengtsson, H. & Lepland, A., 1996. Textural provinces and transport interpretations with fine-grained sediments in the Skagerrak, *Journal of Sea Research*, **35**, 99 – 110.

Stow, D.A.V. & Bowen, A.J., 1980. A physical model for transport and sorting of fine grained sediments by turbidity currents, *Sedimentology*, **26**, 31 – 46.

Stow, D.A.V., & Piper, D.J.W., 1984. Deep-water fine-grained sediments: facies models. *In: Stow, D.A.V., & Piper, D.J.W. (eds) Fine-Grained Sediments: Deep-Water Processes & Facies*, Geological Society of London Special Publication, **15**, 611-645.

Stow, D.A.V. & Shanmugam, G. 1980. Sequence of structures in fine-grained turbidites: comparison of recent deep-sea & ancient flysch sediments, *Sedimentary Geology*, **25**, 23 – 42.

Sutherland, R.A. & Lee, C.T., 1994. Discrimination between coastal sub-environments using textural characteristics, *Sedimentology*, **41**, 1133 – 1145.

Talling, P.J., 2001. On the frequency distribution of turbidite thickness, *Sedimentology*, **48**, 1297 – 1329.

Tanner, W.F., 1991a. Suite statistics: The hydrodynamic evolution of the sediment pool, *In: Syvitski, J.P.M. (Ed) Principles, Methods, & Application of Particle Size Analysis*, Cambridge University Press, New York, 225-236.

Tanner, W.F., 1991b. Application of suite statistics to stratigraphy & sea level changes, *In: Syvitski, J.P.M. (ed.) Principles, Methods, & Application of Particle Size Analysis*, Cambridge University Press, New York, 282-293.

Underhill, J.R., 1998. Jurassic. *In: Glennie, K.W. (ed) Petroleum Geology of the North Sea*, Blackwell Science. 245 – 293.

Unsold, G., 1982. Der Transportbeginn rolligen Sohlmaterials in gleichformigen turbulenten Stromungen: eine kritische Uberprufung der Shields-Funktion und ihre experiemntelle Erweiterung auf feinstkörnige, nicht-bindige Sedimente, Doctoral Dissertation, University of Kiel, Germany, 145pp.

Waples, D.W. 1998. Basin Modelling: how well have we done? *In: Duppenbecker, S.J. & Iliffe, J.E. (eds) Basin Modelling: Practices and Progress*. Geological Society of London Special Publication, **141**, 1 – 14.

Wateney, W.L., *et al.* 1999. Petrofacies analysis – a petrophysical tool for geologic/engineering reservoir characterisation. *In: Schatzinger, R. & Jordan, J. (eds) Reservoir characterization- Recent Advances*. AAPG Memoir, **71**, 73 – 90.

Weaver, C.E., 1989. *Clays, Muds, & Shales*. Developments in Sedimentology 44, Amsterdam, Elsevier, 819pp.

Weltje, G.J. & Prins, Maarten, P.A., 2003. Muddled or mixed? Inferring palaeoclimate from size distributions of deep-sea clastics, *Sedimentary Geology*, **162**, 39-62.

Wetzel, A., 1987. Sedimentological significance of strain and sonic velocity anisotropy in fine-grained turbiditic & hemipelagic deep-sea sediments an example from the Mississippi Fan, *Marine Geology*, **74**, 191-207.

Wetzel, A. & Balson, P., 1992. Sedimentology of fine-grained turbidites inferred from continuously recorded physical properties data, *Marine Geology*, **103**, 165-178.

Wishart, D., 2003a. *ClustanGraphics Primer: A Guide to Cluster Analysis*, (2nd Edition), Edinburgh, 64pp.

Wishart, D., 2003b. *Focal Point Clustering User Guide*, Edinburgh, 32pp.

Wyllie, M.R.J., Gregor, A.R. & Gardener, L.W., 1956. Elastic wave velocities in heterogeneous & porous media, *Geophysics*, **21**, 41 – 70.

Wunderlich, F., 1969. Studien zur Sedimentbewegung 1. Transportformen und Schlichtbildung im Gebeit der Jade. *Senckenbergiana maritime*, **10**, 257 – 267.

Yang, Y. & Aplin, A.C., 1997. A method for the disaggregation of mudstones. *Sedimentology*, **44**, 559 – 562.

Yang, Y., & Aplin, A.C., 1998. Influence of lithology and compaction on the pore size distribution and modelled permeability of some mudstones from the Norwegian margin, *Marine & Petroleum Geology*, **15**, 163-175.

Yang, Y., Aplin, A.C. & Later, S.R., 2004. Quantitative assessment of mudstone lithology using geophysical wireline logs & artificial neural networks, *Petroleum Geoscience*, **10**, 141 – 152.

Yang, Y., & Aplin, A.C., 2004. Definition and practical application of mudstone porosity-effective stress relationships, *Petroleum Geoscience*, **10**, 153 – 162.

Yin, H.Z. 1993. Acoustic velocity and attenuation in rocks: isotropy, intrinsic anisotropy and stress induced anisotropy. Unpublished PhD thesis. Stanford University.

Yin, H.Z., Nur, A., & Mavko, G., 1993. Critical porosity - a physical boundary in poroelasticity, *International journal of rock mechanics and mining sciences and geomechanics abstracts*, **30**, 805 – 808.

Yokokawa, M. & Franz, S.O., 2002. Changes in grain size and magnetic fabric at Blake-Bahama Outer Ridge during the late Pleistocene (marine isotope stages 8-10), *Marine Geology*, **189**, 123 – 144.

Appendix A2.1: Moment Statistics (after Griffiths, 1967)

X = midpoint in each class

f^a = frequency

\bar{X} = arithmetic mean

\bar{X}' = assumed mean

C = class interval = 1 phi

$$d = \frac{X - \bar{X}'}{c} \quad \text{A2.1.1}$$

Moments around the arbitrary origin are calculated as:

$$n_1 = \frac{\sum fd}{\sum f} \quad \text{A2.1.2}$$

$$n_2 = \frac{\sum fd^2}{\sum f} \quad \text{A2.1.3}$$

$$n_3 = \frac{\sum fd^3}{\sum f} \quad \text{A2.1.4}$$

$$n_4 = \frac{\sum fd^4}{\sum f} \quad \text{A2.1.5}$$

The Moments around the true man corrected for group data are then calculated as:

$$m_1 = \bar{X} = \bar{X}' + cn_1 \quad \text{A2.1.6}$$

$$m_2 = \hat{\sigma}^2 = c^2(n_2 - n_1^2) \quad \text{A2.1.7}$$

$$\hat{\sigma} = \sqrt{\hat{\sigma}^2} \quad \text{A2.1.8}$$

$$m_3 = c^3(n_3 - 3n_2n_1 + 2n_1^3) \quad \text{A2.1.9}$$

$$\sqrt{b_1} = \frac{m_3}{\hat{\sigma}^{\frac{3}{2}}} \quad \text{A2.1.10}$$

$$Sk = \frac{\sqrt{b_1}}{2} \quad \text{A2.1.11}$$

$$m_4 = c^4(n_4 - 4n_3n_2 + 6n_1^2n_2 - 3n_1^4) \quad \text{A2.1.12}$$

$$b_2 = \frac{m_4}{\hat{\sigma}^4} \quad \text{A2.1.13}$$

$$K = b_2 - 3 \quad \text{A2.1.14}$$

Thus the summary statistics of the mean, standard deviation, skewness and kurtosis of grouped grain size data are:

m_1 , $\hat{\sigma}$, Sk and K .

Appendix A4.1. Euclidean Sum of Squares (ESS), Cumulative Euclidean Sum of Squares (CESS) and Increase in Sum of Squares (ISS).

The Euclidean Sum of Squares (ESS) E_p for a cluster p is given by:

$$E_p = \frac{\sum_{i \in p} c_i \sum_j w_j (x_{ij} - \mu_{pj})^2}{\sum_j w_j}$$

where: x_{ij} is the value of variable j in case i within cluster p

c_i is an optional differential weight for case i

w_j is an optional differential weight for variable j

μ_{pj} is the mean of variable j for cluster p

The total ESS for all clusters p (i.e. the cumulative ESS) is thus $E = \sum_p E_p$ and the increase in the Euclidean Sum of Squares $I_{p \cup q}$ (ISS) at the union of two clusters p and q is:

$$I_{p \cup q} = E_{p \cup q} - E_p - E_q \Rightarrow \text{Minimum}$$

In *ClustanGraphics* k-means has been implemented to minimize the total Euclidean Sum of Squares E . This is equivalent to minimizing the sum of the weighted squared Euclidean distances d_{ip}^2 between each case i and the mean μ_p of the cluster p to which it belongs.

Appendix A4.2 – PCA results

		Initial Eigenvalues			Extraction Sums of Squared Loadings		
Component		Total	% of Variance	Cumulative %	Total	% of Variance	Cumulative %
1	4.57	50.83	50.83	50.83	4.57	50.83	50.83
2	2.02	22.44	73.28	73.28	2.02	22.44	73.28
3	0.92	10.23	83.51				
4	0.70	7.72	91.23				
5	0.36	3.98	95.20				
6	0.19	2.14	97.34				
7	0.14	1.58	98.92				
8	0.09	1.01	99.92				
9	0.01	0.08	100.00				
Extraction Method: Principal Component Analysis.							

Table A4.2.1. % total variance accounted for from the principal component analysis of the sedimentary statistic and parameter dataset.

Total Variance Explained					Extraction Sums of Squared Loadings		
Component		Total	% of Variance	Cumulative %	Total	% of Variance	Cumulative %
1	4.63	51.41	51.41	51.41	4.63	51.41	51.41
2	1.87	20.78	72.19	72.19	1.87	20.78	72.19
3	1.19	13.20	85.38	85.38	1.19	13.20	85.38
4	0.53	5.84	91.22				
5	0.43	4.76	95.99				
6	0.17	1.92	97.90				
7	0.13	1.43	99.33				
8	0.06	0.67	100.00				
9	0.00	0.00	100.00				
Extraction Method: Principal Component Analysis.							

Table A4.2.2. % total variance accounted for from the principal component analysis of the grain size distribution (1 phi bin) dataset.

Total Variance Explained		Initial Eigenvalues	% of Variance	Cumulative %	Extraction Sums of Squared Loadings		
Component	Total				Total	% of Variance	Cumulative %
1	18.29	44.6	44.6	44.6	18.29	44.6	44.6
2	9.36	22.83	67.43	67.43	9.36	22.83	67.43
3	4.47	10.89	78.32	78.32	4.47	10.89	78.32
4	2.29	5.59	83.91	83.91	2.29	5.59	83.91
5	1.44	3.52	87.43	87.43	1.44	3.52	87.43
6	1.01	2.46	89.89	89.89	1.01	2.46	89.89
7	0.79	1.93	91.82	91.82			
8	0.43	1.04	92.86	92.86			
9	0.4	0.97	93.83	93.83			
10	0.38	0.92	94.75	94.75			
11	0.28	0.68	95.43	95.43			
12	0.24	0.59	96.02	96.02			
13	0.19	0.45	96.47	96.47			
14	0.15	0.38	96.85	96.85			
15	0.13	0.33	97.17	97.17			
16	0.11	0.28	97.45	97.45			
17	0.1	0.25	97.7	97.7			
18	0.09	0.23	97.93	97.93			
19	0.08	0.21	98.14	98.14			
20	0.08	0.19	98.33	98.33			
21	0.07	0.18	98.51	98.51			
22	0.07	0.16	98.66	98.66			
23	0.06	0.14	98.8	98.8			
24	0.05	0.13	98.93	98.93			
25	0.05	0.11	99.04	99.04			
26	0.04	0.11	99.15	99.15			
27	0.04	0.1	99.25	99.25			
28	0.04	0.09	99.34	99.34			
29	0.04	0.09	99.43	99.43			
30	0.03	0.07	99.5	99.5			
31	0.03	0.07	99.57	99.57			
32	0.03	0.07	99.63	99.63			
33	0.03	0.06	99.7	99.7			
34	0.02	0.05	99.75	99.75			
35	0.02	0.05	99.8	99.8			
36	0.02	0.04	99.84	99.84			
37	0.02	0.04	99.88	99.88			
38	0.01	0.03	99.91	99.91			
39	0.01	0.03	99.95	99.95			
40	0.01	0.03	99.97	99.97			
41	0.01	0.03	100	100			
Extraction Method: Principal Component Analysis.							

Table A4.2.3. % total variance accounted for from the principal component analysis of the grain size distribution (0.2 phi bin) dataset.

Total Variance Explained		Initial Eigenvalues			Extraction Sums of Squared Loadings		
Component	Total						
1	8.85	49.18	49.18	8.85	49.18	49.18	49.18
2	3.18	17.68	66.86	3.18	17.68	66.86	
3	1.71	9.48	76.34	1.71	9.48	76.34	
4	1.39	7.73	84.07	1.39	7.73	84.07	
5	0.70	3.90	87.97				
6	0.51	2.81	90.79				
7	0.43	2.39	93.18				
8	0.35	1.97	95.15				
9	0.21	1.17	96.32				
10	0.17	0.93	97.25				
11	0.13	0.73	97.98				
12	0.11	0.63	98.61				
13	0.09	0.48	99.10				
14	0.07	0.38	99.48				
15	0.06	0.32	99.79				
16	0.03	0.17	99.96				
17	0.01	0.04	100.00				
18	0.00	0.00	100.00				
Extraction Method: Principal Component Analysis.							

Table A4.2.4. % total variance accounted for from the principal component analysis of the combined sedimentary statistic / parameter and grain size distribution (1 phi bin) dataset.

Appendix A4.3 – k-means cluster statistics

Solution: 1 Frequency: 39 Reproducibility: 0.26%. ESS = 21.58936310 [+0.0%]										
Cluster	All	Cluster:	1	2	3	4	5	6	7	8
	162	Number:	12	7	40	27	17	18	17	24
Cluster Means										
nr factor 1	0		-0.844	-1.177	-0.573	-0.701	2.043	-0.248	0.569	0.871
nr factor 2	-0		-1.719	2.239	0.119	-0.741	-0.275	1.411	-0.781	0.519
Deviations from the Means										
nr factor 1	0		-0.848	-1.181	-0.577	-0.705	2.039	-0.252	0.565	0.867
nr factor 2	-0		-1.717	2.241	0.121	-0.739	-0.273	1.413	-0.779	0.521
Cluster Standard Deviations										
nr factor 1	1		0.325	0.397	0.347	0.313	0.386	0.405	0.49	0.351
nr factor 2	1		0.318	0.67	0.281	0.235	0.549	0.429	0.288	0.436
t-Tests on Cluster Means										
nr factor 1			-0.846	-1.179	-0.576	-0.704	2.035	-0.251	0.564	0.865
nr factor 2			-1.713	2.235	0.12	-0.737	-0.272	1.409	-0.777	0.52
F-Tests on Cluster Variances										
nr factor 1			0.105	0.157	0.12	0.098	0.149	0.163	0.24	0.123
nr factor 2			0.101	0.446	0.079	0.055	0.3	0.183	0.082	0.189

Table A4.3.1. Focal point cluster statistics for the cluster analysis performed upon the principal components extracted from the sedimentary statistic / parameter dataset.

Solution: 2 Frequency: 75 Reproducibility: 15.00%. ESS = 36.66257858 [+0.1%]										
Cluster	All	Cluster:	1	2	3	4	5	6	7	8
	163	Number:	9	19	10	42	37	9	14	23
Cluster Means										
fac1_nr	0		0.969	-1.442	-1.635	0.31	0.157	-1.536	0.543	0.976
fac2_nr	0		-1.485	-0.53	-1.737	-0.237	0.92	1.58	0.891	-0.433
fac3_nr	0		-1.5	0.138	1.412	-0.802	0.17	-1.28	1.406	0.694
Deviations from the Means										
fac1_nr	0		0.969	-1.442	-1.635	0.31	0.157	-1.536	0.543	0.976
fac2_nr	0		-1.485	-0.53	-1.737	-0.237	0.92	1.58	0.891	-0.433
fac3_nr	0		-1.5	0.138	1.412	-0.802	0.17	-1.28	1.406	0.694
Cluster Standard Deviations										
fac1_nr	1		0.463	0.514	0.685	0.347	0.437	0.522	0.658	0.464
fac2_nr	1		0.761	0.467	0.664	0.402	0.469	0.367	0.517	0.395
fac3_nr	1		0.601	0.522	0.94	0.504	0.308	0.529	0.471	0.485
t-Tests on Cluster Means										
fac1_nr			0.969	-1.442	-1.635	0.31	0.157	-1.536	0.543	0.976
fac2_nr			-1.485	-0.53	-1.737	-0.237	0.92	1.58	0.891	-0.433
fac3_nr			-1.5	0.138	1.412	-0.802	0.17	-1.28	1.406	0.694
F-Tests on Cluster Variances										
fac1_nr			0.215	0.265	0.469	0.121	0.191	0.272	0.433	0.215
fac2_nr			0.579	0.218	0.441	0.162	0.22	0.135	0.267	0.156
fac3_nr			0.361	0.272	0.883	0.254	0.095	0.28	0.222	0.235

Table A4.3.2. Focal point cluster statistics for the cluster analysis performed upon the principal components extracted from the whole phi bin dataset.

Solution: 1 Frequency: 198 Reproducibility: 1.32%. ESS = 58.86563873 [+0.0%]									
Cluster	All	1	2	3	4	5	6	7	8
	162	11	24	23	13	32	13	12	34
Cluster Means									
Fac_1_nr	0.043	-1.907	0.7	1.303	-0.897	0.113	0.411	-1.665	0.112
Fac_2_nr	-0.163	0.397	-0.686	-0.172	-0.612	0.763	-0.453	-1.382	-0.13
Fac_3_nr	0.016	1.112	0.893	-1.068	-0.639	-0.272	1.435	-1.192	0.179
Fac_4_nr	0.122	1.949	0.126	0.651	-0.046	0.225	-1.359	-0.938	0.077
Fac_5_nr	0.111	0.285	-0.205	0.179	-1.409	0.068	0.349	1.158	0.395
Fac_6_nr	0.025	-0.702	0.9	-0.522	0.011	0.631	-0.982	0.767	-0.43
Deviations from the Means									
Fac_1_nr	0.043	-1.95	0.658	1.26	-0.939	0.07	0.368	-1.708	0.069
Fac_2_nr	-0.163	0.56	-0.523	-0.009	-0.449	0.927	-0.289	-1.219	0.034
Fac_3_nr	0.016	1.097	0.878	-1.084	-0.655	-0.288	1.42	-1.208	0.163
Fac_4_nr	0.122	1.827	0.004	0.529	-0.168	0.103	-1.481	-1.06	-0.045
Fac_5_nr	0.111	0.173	-0.316	0.068	-1.52	-0.044	0.237	1.047	0.283
Fac_6_nr	0.025	-0.727	0.875	-0.547	-0.014	0.606	-1.007	0.742	-0.455
Cluster Standard Deviations									
Fac_1_nr	1.04	0.582	0.385	0.359	0.608	0.5	0.488	0.436	0.556
Fac_2_nr	0.851	0.781	0.557	0.671	0.846	0.475	0.699	0.531	0.544
Fac_3_nr	1.029	0.942	0.659	0.543	0.619	0.571	0.612	0.73	0.511
Fac_4_nr	0.981	0.628	0.568	0.614	1.051	0.572	0.623	0.977	0.569
Fac_5_nr	0.723	0.529	0.324	0.396	0.447	0.451	0.298	1.055	0.349
Fac_6_nr	1.015	1.036	0.888	1.113	0.659	0.439	1.142	0.881	0.379
t-Tests on Cluster Means									
Fac_1_nr		-1.874	0.632	1.212	-0.903	0.067	0.354	-1.642	0.067
Fac_2_nr		0.659	-0.615	-0.01	-0.528	1.09	-0.34	-1.433	0.039
Fac_3_nr		1.066	0.853	-1.053	-0.636	-0.28	1.379	-1.174	0.158
Fac_4_nr		1.863	0.005	0.54	-0.171	0.105	-1.51	-1.081	-0.046
Fac_5_nr		0.24	-0.437	0.094	-2.102	-0.06	0.328	1.447	0.392
Fac_6_nr		-0.716	0.862	-0.539	-0.013	0.597	-0.992	0.731	-0.448
F-Tests on Cluster Variances									
Fac_1_nr		0.313	0.137	0.119	0.342	0.231	0.22	0.176	0.285
Fac_2_nr		0.843	0.429	0.622	0.989	0.312	0.675	0.39	0.408
Fac_3_nr		0.838	0.41	0.279	0.361	0.308	0.354	0.503	0.246
Fac_4_nr		0.41	0.336	0.392	1.148	0.34	0.404	0.992	0.337
Fac_5_nr		0.535	0.201	0.3	0.381	0.388	0.17	2.127	0.232
Fac_6_nr		1.042	0.766	1.202	0.422	0.187	1.265	0.754	0.139

Table A4.3.3. Focal point cluster statistics for the cluster analysis performed upon the principal components extracted from the 0.2 phi bin dataset.

A4.3.3

Solution: 1 Frequency: 58 Reproducibility: 0.39%. ESS = 45.59243393 [+0.0%]									
Cluster	All	1	2	3	4	5	6	7	8
	162	19	24	12	18	28	13	39	9
Cluster Means									
fac1_nr	0.004	0.6	0.674	-1.82	-1.383	0.574	0.707	0.143	-1.23
fac2_nr	0.019	-1.166	0.587	1.131	-1.095	-0.405	0.748	0.612	-0.551
fac3_nr	-0.025	0.516	-0.685	-0.619	-0.391	-1.044	1.627	0.364	1.212
fac4_nr	-0.033	-1.226	1.012	-0.81	0.195	0.044	0.006	-0.33	1.26
Deviations from the Means									
fac1_nr	0.004	0.597	0.67	-1.824	-1.387	0.57	0.703	0.139	-1.234
fac2_nr	0.019	-1.185	0.568	1.112	-1.115	-0.424	0.729	0.593	-0.57
fac3_nr	-0.025	0.541	-0.66	-0.594	-0.366	-1.019	1.653	0.389	1.237
fac4_nr	-0.033	-1.193	1.045	-0.776	0.229	0.077	0.04	-0.296	1.293
Cluster Standard Deviations									
fac1_nr	1.002	0.497	0.38	0.535	0.548	0.476	0.472	0.536	0.688
fac2_nr	0.973	0.609	0.472	0.696	0.645	0.607	0.666	0.495	0.654
fac3_nr	0.95	0.587	0.611	0.428	0.443	0.476	0.617	0.355	0.59
fac4_nr	0.907	0.877	0.523	0.358	0.866	0.439	0.462	0.449	0.565
t-Tests on Cluster Means									
fac1_nr		0.595	0.669	-1.821	-1.384	0.569	0.702	0.139	-1.232
fac2_nr		-1.218	0.584	1.143	-1.146	-0.436	0.749	0.61	-0.586
fac3_nr		0.569	-0.695	-0.625	-0.386	-1.072	1.74	0.41	1.302
fac4_nr		-1.315	1.153	-0.856	0.252	0.085	0.044	-0.326	1.426
F-Tests on Cluster Variances									
fac1_nr		0.246	0.144	0.285	0.299	0.226	0.222	0.286	0.472
fac2_nr		0.392	0.236	0.511	0.44	0.389	0.468	0.258	0.452
fac3_nr		0.382	0.414	0.203	0.217	0.251	0.422	0.14	0.386
fac4_nr		0.936	0.333	0.156	0.913	0.234	0.26	0.246	0.388

Table A4.3.4. Focal point cluster statistics for the cluster analysis performed upon the principal components extracted from the combined dataset.

Appendix A5.1 The Andersen-Darling Test Statistic

The Andersen-Darling test is classed as a ‘Goodness of fit’ test based on the cumulative distribution function. The workings of the test are illustrated in Figure A1; essentially the data are standardized, ordered from largest to smallest prior to the degree to which the empirical CDF (from the data) matches the theoretical CDF (the parametric distribution you are testing against). Within the A-D test the null hypothesis that the true distribution was drawn from the theoretical CDF with its assumed parameters is rejected if the AD statistic value is greater than the critical value (CV). The rejection rule is defined as:

$$AD > CV = 0.752 / (1 + 0.75/n + 2.25/n^2) \quad \text{A5.1.1}$$

where AD is the measured Andersen-Darling test statistic, CV is the critical value and n is the sample number.

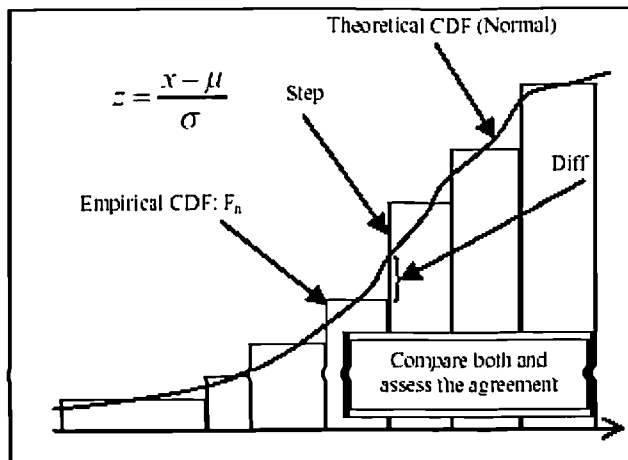


Figure A5.1.1 Illustration of the concept behind the distance of Goodness of Fit Tests such as the Andersen-Darling test.

The larger the AD value the stronger the indication of non-normality, if the p -value is less than your desired level (0.05 – 95%) then there is evidence against the null hypothesis and hence against normality for the variable. The Anderson-Darling test is considered an empirical cumulative distribution function based test and uses the squared difference

from normality, where normality is based on the normal cumulative density function for a mean and standard deviation from your dataset (Figure A5.1).

Appendix A5.2 The Ryan-Joiner (RJ) Test Statistic.

In addition to the probability plots, AD tests and their associated p -values, Ryan-Joiner tests were also performed (see Ryan and Joiner, 1976). As the normal distribution plot as straight lines on probability plots one obvious way to judge the near linearity of any plot is to compute its "correlation coefficient." When this is done for normal probability plots, a formal test can be obtained termed the Ryan-Joiner (RJ) test. The RJ values needs to exceed some critical value, dependent upon the number of samples, to be significant. Critical values for the Ryan-Joiner normality test were calculated from Eq. A2.1 for significance at the 95% level (0.05) (Ryan and Joiner, 1976):

$$cv(n) \approx 1.0063 - \frac{0.1288}{\sqrt{n}} - \frac{0.6118}{n} + \frac{1.3505}{n^2}, \text{ for } \alpha = 0.05 \quad \text{A5.2.1}$$

The reader is referred to the White paper by Ryan and Joiner (1976) available at <http://www.minitab.com/resources/whitepapers/normprob.aspx> for further details. In the case of normality tests p -values need to be greater than some value (usually 0.1) for the assumption that the data is normally distributed to be supported.

Appendix A5.3 Group 1 data tables.

Sample	KB Depth (m)	gsd type	Sample type	Corrected Porosity	r mean (nm)	Log r mean (nm)	r 10% (nm)	Log r10% [nm]	CEP [MPa]	Temperature (C)	Total C (%)	TOC (%)	Measured Gs (g/cm^3)
NOR_1	4435.7	3	Plug	0.098	2.8	0.4	5.8	0.8	12.1	142.0	1.5	1.5	2.833
SCB_5	5211.1	1	RSW core	0.093	3.5	0.5	7.4	0.9	9.5	123.0	1.2	0.4	2.786
TRIN_4	4254.8	2	Core	0.074	7.3	0.9	8.4	0.9	8.3				
SCB_23	6618.6	1	Core	0.08	7.4	0.9	20.2	1.3	3.5	168.0	0.7	0.2	2.775
SCB_11	5590.0	4	Cuttings	0.078	11.8	1.1	27.4	1.4	2.6	132.5	1.9	1.0	2.738
SCB_25	6623.5	2	Core	0.076	14.6	1.2	37.4	1.6	1.9	168.2	1.0	0.3	2.79
SCB_27	6633.7	2	Core	0.083	14.6	1.2	34.2	1.5	2.0	168.4	0.9	0.4	2.75
SCB_8	5500.0	1	Cuttings	0.079	15.3	1.2	30.8	1.5	2.3	130.3	1.9	0.9	2.705
SCB_10	5560.0	4	Cuttings	0.07	29.9	1.5	66.9	1.8	1.0	131.8	2.6	1.5	2.677
SCB_19	5680.0	4	Cuttings	0.077	33.3	1.5	91.9	2.0	0.8	134.8	2.4	1.3	2.719
			Arith Mean	0.081	14.050	1.031	33.040	1.368	4.388				
			Geo Mean	0.080	10.733	0.966	23.357	1.309	2.997				
			Har Mean	0.080	7.902	0.892	15.952	1.247	2.118				
			SD	0.009	10.568	0.364	28.256	0.414	4.115	r10% CoV	1.77	r10% N-0	328
			Min	0.070	2.800	0.447	5.800	0.763	0.762	r mean CoV	1.34	r mean N-0	187
			Max	0.098	33.300	1.522	91.900	1.963	12.068	Log r mean CoV	0.41	Log r mean N-0	17
			Skew	1.130	1.002	-0.334	1.250	-0.237	1.104	Log r10% CoV	0.33	Log r10% N-0	12
			Kurtosis	0.747	0.159	-0.584	1.215	-1.002	-0.322	CEP CoV	1.94	CEP N-0	395

Table A5.3.1. Physical property data and statistical data reductions for the 5 – 10% porosity bin Group 1 subset.

Sample	KB Depth (m)	gsd type	Sample type	Corrected Porosity	r mean (nm)	Log r mean (nm)	r 10% (nm)	Log r10% [nm]	CEP [MPa]	Temperature (C)	Total C (%)	TOC (%)	Measured Gs (g/cm^3)
SCB_17	5631.4	1	RSW core	0.102	3.9	0.6	9.8	1.0	7.1	133.5	1.4	0.2	2.818
TRIN_3	4234.2	2	Core	0.108	3.1	0.5	8.0	0.9	8.8				
SCB_7	5235.2	1	RSW core	0.107	3.5	0.5	7.1	0.9	9.9	123.6	1.1	0.4	2.808
GOM_58	6690.4	3	SWC	0.104	4.2	0.6	11.3	1.1	6.2	104.5	1.2	0.8	2.746
GOM_68	6882.6	1	SWC	0.142	4.7	0.7	10.7	1.0	6.5	108.6	1.5	0.7	2.770
GOM_70	6883.7	1	SWC	0.146	5.1	0.7	8.7	0.9	8.0	108.6	2.2	0.6	2.782
GOM_67	6882.3	3	SWC	0.132	5.6	0.7	10.5	1.0	6.7	108.6	1.4	0.7	2.778
GOM_69	6882.8	1	SWC	0.141	6.4	0.8	11.8	1.1	5.9	108.6	1.4	0.7	2.770
GOM_66	6881.9	1	SWC	0.143	7.7	0.9	13.9	1.1	5.0	108.6	2.1	0.7	2.774
NOR_10	2288.8	2	Plug	0.143	9.6	1.0	15.8	1.2	4.4	84.2	2.7	2.3	2.763
			Arith Mean	0.127	5.380	0.705	10.760	1.020	6.860				
			Geo Mean	0.125	5.073	0.690	10.476	1.015	6.681				
			Har Mean	0.124	4.807	0.676	10.203	1.010	6.505				
			SD	0.019	2.082	0.158	2.710	0.108	1.699	r10% CoV	0.27	r10% N-0	7
			Min	0.102	3.100	0.491	7.100	0.851	4.430	r mean CoV	0.43	r mean N-0	20
			Max	0.146	9.600	0.982	15.800	1.199	9.858	Log r mean CoV	0.23	Log r mean N-0	6
			Skew	-0.396	1.077	0.464	0.605	0.085	0.423	Log r10% CoV	0.11	Log r10% N-0	1
			Kurtosis	-2.149	0.707	-0.464	0.130	-0.312	-0.221	CEP CoV	0.26	CEP N-0	7

Table A5.3.2. Physical property data and statistical data reductions for the 10 – 15% porosity bin Group 1 subset.

Sample	KB Depth (m)	gsd type	Sample type	Corrected Porosity	r mean (nm)	Log r mean (nm)	r 10% (nm)	Log r10% [nm]	CEP [MPa]	Temperature (C)	Total C (%)	TOC (%)	Measured Gs (g/cm^3)
GOM_63	6802.8	1	SWC	0.151	7.0	0.85	13.3	1.12	5.3	106.9	1.3	1.2	2.801
TRIN_14	3207.7	3	Core	0.181	4.2	0.62	9.2	0.96	7.6				
GOM_71	6884.2	1	SWC	0.17	4.4	0.64	8.0	0.90	8.7	108.6	1.7	0.7	2.812
ANG_10	3231.0	2	SW core	0.179	4.8	0.68	8.6	0.93	8.1	91.5	1.3	1.2	2.737
ANG_9	3039.0	4	SWC	0.196	5.4	0.73	10.1	1.00	6.9	82.9	1.2	0.5	2.784
ANG_7	3019.0	3	cuttings	0.167	5.6	0.75	10.8	1.03	6.5	82.0	1.1	0.7	2.717
ANG_4	2983.0	2	SW core	0.177	6.1	0.79	11.2	1.05	6.2	80.4	1.6	1.4	2.682
GOM_62	6719.0	3	SWC	0.179	6.1	0.79	11.6	1.06	6.0	105.1	2.3	1.8	2.802
ANG_5	2995.0	4	SWC	0.188	7.0	0.85	10.9	1.04	6.4	80.9	2.0	1.4	2.688
GOM_52	5992.4	4	SWC	0.163	8.0	0.90	15.1	1.18	4.6	89.7	1.2	0.9	2.759
GOM_59	6702.9	2	SWC	0.151	10.2	1.01	22.2	1.35	3.2	104.8	1.3	1.1	2.746
GOM_42	4720.7	4	SWC	0.189	11.9	1.08	24.2	1.38	2.9	69.4	0.9	0.7	2.762
GOM_54	6470.6	4	SWC	0.157	12.9	1.11	24.4	1.39	2.9	99.9	2.4	1.2	2.777
GOM_41	4706.1	4	SWC	0.18	13.6	1.13	24.5	1.39	2.9	69.1	1.4	1.3	2.682
GOM_28	4197.7	2	SWC	0.183	13.6	1.13	25.0	1.40	2.8	59.1	2.4	2.0	2.643
SCB_4	4570-4580	3	Cuttings	0.164	13.8	1.14	25.7	1.41	2.7	112.5	3.1	1.4	2.734
GOM_34	4496.4	4	SWC	0.194	17.6	1.25	32.5	1.51	2.2	65.0	1.1	0.7	2.693
Arith Mean 0.175 8.953 0.908 16.900 1.184 5.056 Geo Mean 0.174 8.095 0.887 15.258 1.167 4.587 Har Mean 0.174 7.353 0.867 13.843 1.151 4.142 SD 0.014 4.218 0.204 7.963 0.206 2.219 r10% CoV 0.58 r10% N-0 35 Min 0.151 4.200 0.623 8.000 0.903 2.154 r mean CoV 0.57 r mean N-0 34 Max 0.196 17.600 1.246 32.500 1.512 8.749 Log r mean CoV 0.24 Log r mean N-0 6 Skew -0.301 0.623 0.179 0.517 0.185 0.163 Log r10% CoV 0.18 Log r10% N-0 3 Kurtosis -0.876 -0.888 -1.430 -1.231 -1.649 -1.471 CEP CoV 0.54 CEP N-0 30													

Table A5.3.3. Physical property data and statistical data reductions for the 15 – 20% porosity bin Group 1 subset.

Sample	KB Depth (m)	gsd type	Sample type	Corrected Porosity	r mean (nm)	Log r mean (nm)	r 10% (nm)	Log r10% [nm]	CEP [MPa]	Temperature (C)	Total C (%)	TOC (%)	Measured Gs (g/cm^3)
GOM_18	3758.8	4	SWC	0.239	9.0	0.95	18.1	1.26	3.9	50.4	1.1	0.5	2.798
GOM_19	3777.7	4	SWC	0.246	9.2	0.96	20.2	1.31	3.5	50.8	0.7	0.6	2.767
GOM_40	4669.5	1	SWC	0.224	9.5	0.98	16.8	1.23	4.2	68.4	2.1	0.8	2.776
ANG_2	2805.0	4	cuttings	0.232	9.7	0.99	21.9	1.34	3.2	72.4	3.2	2.2	2.622
GOM_37	4614.7	1	SWC	0.221	10.6	1.03	19.0	1.28	3.7	67.3	1.3	0.7	2.784
GOM_20	3867.9	4	SWC	0.212	11.0	1.04	22.1	1.34	3.2				
GOM_23	4029.5	3	SWC	0.246	11.3	1.05	19.5	1.29	3.6	55.8	1.1	0.6	2.761
GOM_17	3750.0	2	SWC	0.249	11.3	1.05	19.6	1.29	3.6	50.3	0.6	0.3	2.79
GOM_21	3891.7	2	SWC	0.246	11.4	1.06	19.7	1.29	3.6	53.1	1.2	0.4	2.921
GOM_24	4094.7	4	SWC	0.228	11.9	1.08	25.8	1.41	2.7	57.1	1.0	0.5	2.787
GOM_35	4535.1	3	SWC	0.205	13.0	1.11	24.4	1.39	2.9	65.7	1.3	0.7	2.735
GOM_46	4843.0	2	SWC	0.215	13.2	1.12	26.6	1.42	2.6	71.8	1.4	0.7	2.8
GOM_25	4133.7	4	SWC	0.231	13.3	1.12	25.6	1.41	2.7	57.8	1.6	0.8	2.765
GOM_31	4335.5	4	SWC	0.203	13.5	1.13	24.0	1.38	2.9	61.8	0.9	0.4	2.792
GOM_29	4315.4	3	SWC	0.217	13.7	1.14	26.7	1.43	2.6	61.4	1.2	0.9	2.739
GOM_36	4582.4	3	SWC	0.244	14.4	1.16	27.3	1.44	2.6	66.7	0.9	0.4	2.784
GOM_9	3400.7	1	SWC	0.229	15.1	1.18	24.9	1.40	2.8	43.4	1.4	1.0	2.666
ANG_1	2670.0	2	cuttings	0.247	16.2	1.21	21.8	1.34	3.2	66.3	2.6	2.3	2.607
GOM_50	4992.9	4	SWC	0.222	16.3	1.21	29.4	1.47	2.4	74.8	1.0	0.5	2.805
GOM_43	4767.1	1	SWC	0.213	17.0	1.23	31.9	1.50	2.2	70.3	0.7	0.6	2.770
GOM_32	4455.6	4	SWC	0.22	22.7	1.36	45.1	1.65	1.6	64.2	1.2	0.8	2.776
ANG_11	3340.0	2	Cuttings	0.207	23.4	1.37	52.6	1.72	1.3	96.4	3.6	2.8	2.551
GOM_39	4655.8	4	SWC	0.232	23.9	1.38	44.9	1.65	1.6	68.1	2.0	1.9	2.779
GOM_44	4794.5	1	SWC	0.218	25.5	1.41	37.8	1.58	1.9	70.9	7.4	0.2	2.378
GOM_6	3258.3	3	SWC	0.248	26.7	1.43	46.6	1.67	1.5	40.6	1.7	0.8	2.702
GOM_48	4896.9	2	SWC	0.226	27.4	1.44	24.2	1.38	2.9	72.9	1.2	0.9	3.019
ANG_17	3145.0	2	Cuttings	0.227	27.8	1.44	46.1	1.66	1.5	81.2	4.9	3.5	2.493
ANG_18	3190.0	2	Cuttings	0.238	28.3	1.45	43.8	1.64	1.6	83.2	4.1	2.8	2.544
SCB_2	2690-2700	2	Cuttings	0.216	29.0	1.46	57.1	1.76	1.2		3.1	0.1	2.754
ANG_19	3235.0	2	Cuttings	0.241	33.4	1.52	63.1	1.80	1.1	85.3	4.7	3.5	2.53
ANG_20	3355.0	2	Cuttings	0.205	34.6	1.54	66.0	1.82	1.1	90.7	3.9	2.5	2.582
Arith Mean													
Geo Mean													
Har Mean													
SD													
Min													
Max													
Skew													
Kurtosis													
r10% CoV													
r mean CoV													
Log r mean CoV													
Log r10% CoV													
CEP CoV													

Table A5.3.4. Physical property data and statistical data reductions for the 20 –25% porosity bin Group 1 subset.

Sample	KB Depth (m)	gsd type	Sample type	Corrected Porosity	r mean (nm)	Log r mean (nm)	r 10% (nm)	Log r10% [nm]	CEP [MPa]	Temperature (C)	Total C (%)	TOC (%)	Measured Gs (g/cm ³)
GOM_18	3758.8	4	SWC	0.239	9.0	0.95	18.1	1.26	3.9	50.4	1.1	0.5	2.798
GOM_19	3777.7	4	SWC	0.246	9.2	0.96	20.2	1.31	3.5	50.8	0.7	0.6	2.767
GOM_40	4669.5	1	SWC	0.224	9.5	0.98	16.8	1.23	4.2	68.4	2.1	0.8	2.776
GOM_37	4614.7	1	SWC	0.221	10.6	1.03	19.0	1.28	3.7	67.3	1.3	0.7	2.784
GOM_20	3867.9	4	SWC	0.212	11.0	1.04	22.1	1.34	3.2				
GOM_23	4029.5	3	SWC	0.246	11.3	1.05	19.5	1.29	3.6	55.8	1.1	0.6	2.761
GOM_17	3750.0	2	SWC	0.249	11.3	1.05	19.6	1.29	3.6	50.3	0.6	0.3	2.79
GOM_21	3891.7	2	SWC	0.246	11.4	1.06	19.7	1.29	3.6	53.1	1.2	0.4	2.921
GOM_24	4094.7	4	SWC	0.228	11.9	1.08	25.8	1.41	2.7	57.1	1.0	0.5	2.787
GOM_35	4535.1	3	SWC	0.205	13.0	1.11	24.4	1.39	2.9	65.7	1.3	0.7	2.735
GOM_46	4843.0	2	SWC	0.215	13.2	1.12	26.6	1.42	2.6	71.8	1.4	0.7	2.8
GOM_25	4133.7	4	SWC	0.231	13.3	1.12	25.6	1.41	2.7	57.8	1.6	0.8	2.765
GOM_31	4335.5	4	SWC	0.203	13.5	1.13	24.0	1.38	2.9	61.8	0.9	0.4	2.792
GOM_29	4315.4	3	SWC	0.217	13.7	1.14	26.7	1.43	2.6	61.4	1.2	0.9	2.739
GOM_36	4582.4	3	SWC	0.244	14.4	1.16	27.3	1.44	2.6	66.7	0.9	0.4	2.784
GOM_9	3400.7	1	SWC	0.229	15.1	1.18	24.9	1.40	2.8	43.4	1.4	1.0	2.666
GOM_50	4992.9	4	SWC	0.222	16.3	1.21	29.4	1.47	2.4	74.8	1.0	0.5	2.805
GOM_43	4767.1	1	SWC	0.213	17.0	1.23	31.9	1.50	2.2	70.3	0.7	0.6	2.770
GOM_32	4455.6	4	SWC	0.22	22.7	1.36	45.1	1.65	1.6	64.2	1.2	0.8	2.776
GOM_39	4655.8	4	SWC	0.232	23.9	1.38	44.9	1.65	1.6	68.1	2.0	1.9	2.779
GOM_44	4794.5	1	SWC	0.218	25.5	1.41	37.8	1.58	1.9	70.9	7.4	0.2	2.378
GOM_6	3258.3	3	SWC	0.248	26.7	1.43	46.6	1.67	1.5	40.6	1.7	0.8	2.702
GOM_48	4896.9	2	SWC	0.226	27.4	1.44	24.2	1.38	2.9	72.9	1.2	0.9	3.019
Arith Mean 0.228 15.257 1.157 26.965 1.412 2.820 Geo Mean 0.227 14.356 1.148 25.801 1.406 2.713 Har Mean 0.227 13.618 1.140 24.823 1.401 2.596 SD 0.014 5.875 0.152 8.865 0.129 0.763 r10% CoV 0.36 r10% N-0 13 Min 0.203 9.000 0.954 16.800 1.225 1.502 r mean CoV 0.43 r mean N-0 19 Max 0.249 27.400 1.438 46.600 1.668 4.166 Log r mean CoV 0.13 Log r mean N-0 2 Skew 0.089 1.099 0.696 1.237 0.749 -0.206 Log r10% CoV 0.09 Log r10% N-0 1 Kurtosis -1.071 -0.094 -0.598 0.655 -0.149 -0.617 CEP CoV 0.29 CEP N-0 9													

Table A5.3.5 Physical property data and statistical data reductions for the 20 – 25% porosity bin Gulf of Mexico Group 1 subset.

Sample	KB Depth (m)	gsd type	Sample type	Corrected Porosity	r mean (nm)	Log r mean (nm)	r 10% (nm)	Log r10% [nm]	CEP [MPa]	Temperature (C)	Total C (%)	TOC (%)	Measured Gs (g/cm^3)
GOM_16	3706.4	4	SWC	0.252	10.5	1.02	20.0	1.30	3.5	49.4	1.1	0.4	2.795
GOM_26	4146.5	3	SWC	0.257	10.8	1.03	22.9	1.36	3.1	58.1	1.7	0.7	2.832
ANG_14	2525.0	2	Cuttings	0.259	13.1	1.12	22.5	1.35	3.1	53.3	4.0	3.2	2.518
GOM_4	3148.6	3	SWC	0.25	13.5	1.13	26.4	1.42	2.7	38.4	1.5	0.7	2.741
ANG_12	2374.5	2	SW core	0.306	13.9	1.14	21.3	1.33	3.3	46.5	2.5	1.3	2.655
GOM_10	3538.1	4	SWC	0.253	19.3	1.29	33.2	1.52	2.1	46.1	1.2	0.5	2.75
GOM_8	3380.8	4	SWC	0.263	20.7	1.32	36.9	1.57	1.9	43.0	1.7	0.8	2.746
GOM_3	3104.7	1	SWC	0.279	21.6	1.33	29.6	1.47	2.4	37.6	1.4	0.5	2.762
ANG_16	2955.0	2	Cuttings	0.269	24.6	1.39	32.2	1.51	2.2	72.7	4.4	3.2	2.512
ANG_15	2670.0	4	Cuttings	0.279	26.1	1.42	32.1	1.51	2.2	59.8	4.7	3.5	2.521
GOM_15	3700.6	2	SWC	0.338	26.3	1.42	38.5	1.59	1.8	49.3	4.9	0.1	2.894
GOM_45	4817.7	1	SWC	0.277	27.1	1.43	41.5	1.62	1.7	71.3	4.5	0.9	2.764
GOM_1	2987.0	4	SWC	0.261	28.8	1.46	48.9	1.69	1.4	35.2	1.3	0.5	2.75
GOM_13	3616.5	2	SWC	0.297	30.3	1.48	40.6	1.61	1.7	47.6	5.2	0.2	2.686
GOM_30	4330.0	1	SWC	0.306	51.3	1.71	62.0	1.79	1.1	61.7	10.0	2.0	2.441
		Arith Mean	0.276	22.527	1.313	33.907	1.509	2.275					
		Geo Mean	0.275	20.552	1.300	32.263	1.503	2.169					
		Har Mean	0.274	18.804	1.286	30.773	1.497	2.064					
		SD	0.026	10.598	0.195	11.629	0.143	0.722	r10% CoV	0.38	r10% N-0	15	
		Min	0.250	10.500	1.021	20.000	1.301	1.129	r mean CoV	0.56	r mean N-0	33	
		Max	0.338	51.300	1.710	62.000	1.792	3.500	Log r mean CoV	0.15	Log r mean N-0	2	
		Skew	1.166	1.392	0.118	1.012	0.269	0.314	Log r10% CoV	0.10	Log r10% N-0	1	
		Kurtosis	0.931	3.223	-0.248	1.219	-0.399	-0.875	CEP CoV	0.35	CEP N-0	13	

Table A5.3.6. Physical property data and statistical data reductions for the 25 – 30% porosity bin Group 1 subset.

Group 2 data tables.

Sample	KB Depth (m)	gsd type	Sample type	Corrected Porosity	r mean (nm)	Log r mean (nm)	r 10% (nm)	Log r10% [nm]	CEP [MPa]	Temperature (C)	Total C (%)	TOC (%)	Measured Gs (g/cm³3)	
NOR_7	3484.6	5	Plug	0.097	3.1	0.5	7.5	0.9	9.3		1.7	1.3	2.769	
NOR_6	3005.45	5	Plug	0.065	4.0	0.6	9.0	1.0	7.8	130.2	1.8	1.5	2.764	
NOR_28	3861.82	5	Plug	0.075	4.6	0.7	9.2	1.0	7.6		1.9	1.6	2.747	
NOR_29	4133.39	6	Plug	0.055	5.4	0.7	14.0	1.1	5.0		0.1	0.1	2.756	
NOR_9	3517.3	6	Plug	0.056	5.9	0.8	13.8	1.1	5.1	132.8	1.6	1.3	2.737	
NOR_27	3550.92	6	Plug	0.068	6.6	0.8	14.6	1.2	4.8		1.2	1.1	2.867	
NOR_24	2798.5	6	Plug	0.079	8.8	0.9	11.0	1.0	6.4	104.6	3.4	2.4	2.696	
TRIN_5	3812.1	6	Core	0.080	29.2	1.5	18.1	1.3	3.9					
SCB_15	5620.26	5	RSW core	0.091	52.1	1.7	127.5	2.1	0.5	133.3	1.3	0.1	2.758	
SCB_24	6619.17	6	Core	0.069	52.3	1.7	139.5	2.1	0.5	168.1	1.5	0.2	2.709	
SCB_6	5227.35	5	RSW core	0.096	67.1	1.8	92.1	2.0	0.8	123.4	1.5	0.2	2.756	
SCB_22	6507.18	6	Core	0.091	76.4	1.9	310.8	2.5	0.2	165.3	0.9	0.3	2.766	
SCB_13	5615.45	5	RSW core	0.086	105.0	2.0	247.1	2.4	0.3	133.1	1.4	0.2	2.715	
SCB_26	6627.1	6	Core	0.079	367.6	2.6	1211.6	3.1	0.1	168.3	1.2	0.2	2.656	
				Arith Mean	0.078	56.293	1.301	158.986	1.623	3.728				
				Geo Mean	0.076	20.020	1.144	42.000	1.488	1.667				
				Har Mean	0.075	9.195	1.003	18.776	1.374	0.440				
				SD	0.014	97.247	0.669	324.001	0.730	3.356	r10% CoV	17.26	r10% N-0	31133
				Min	0.055	3.100	0.491	7.500	0.875	0.058	r mean CoV	10.58	r mean N-0	11695
				Max	0.097	367.600	2.565	1211.600	3.083	9.333	Log r mean CoV	0.67	Log r mean N-0	47
				Skew	-0.224	3.021	0.397	3.185	0.718	0.250	Log r10% CoV	0.53	Log r10% N-0	29
				Kurtosis	-0.962	10.032	-1.117	10.844	-0.791	-1.461	CEP CoV	7.62	CEP N-0	6075

Table A5.3.7. Physical property data and statistical data reductions for the 5 – 10% porosity bin Group 2 subset.

Sample	KB Depth (m)	gsd type	Sample type	Corrected Porosity	r mean (nm)	Log r mean (nm)	r 10% (nm)	Log r10% [nm]	CEP [MPa]	Temperature (C)	Total C (%)	TOC (%)	Measured Gs (g/cm³3)	
SCB_15	5620.26	5	RSW core	0.091	52.1	1.7	127.5	2.1	0.5	133.3	1.3	0.1	2.758	
SCB_24	6619.17	6	Core	0.069	52.3	1.7	139.5	2.1	0.5	168.1	1.5	0.2	2.709	
SCB_6	5227.35	5	RSW core	0.096	67.1	1.8	92.1	2.0	0.8	123.4	1.5	0.2	2.756	
SCB_22	6507.18	6	Core	0.091	76.4	1.9	310.8	2.5	0.2	165.3	0.9	0.3	2.766	
SCB_13	5615.45	5	RSW core	0.086	105.0	2.0	247.1	2.4	0.3	133.1	1.4	0.2	2.715	
SCB_26	6627.1	6	Core	0.079	367.6	2.6	1211.6	3.1	0.1	168.3	1.2	0.2	2.656	
				Arith Mean	0.085	120.083	1.955	354.767	2.364	0.396				
				Geo Mean	0.085	90.217	1.936	231.123	2.337	0.303				
				Har Mean	0.084	76.384	1.919	176.683	2.313	0.197				
				SD	0.010	127.938	0.333	445.530	0.419	0.265	r10% CoV	2.52	r10% N-0	665
				Min	0.069	52.100	1.717	92.100	1.964	0.058	r mean CoV	1.67	r mean N-0	293
				Max	0.096	367.600	2.565	1211.600	3.083	0.760	Log r mean CoV	0.17	Log r mean N-0	3
				Skew	-0.952	2.316	1.817	2.254	1.303	0.141	Log r10% CoV	0.18	Log r10% N-0	3
				Kurtosis	0.272	5.462	3.475	5.228	1.775	-0.840	CEP CoV	1.34	CEP N-0	188

Table A5.3.8. Physical property data and statistical data reductions for the 5 – 10% porosity bin South Caspian Basin Group 2 subset.

Sample	KB Depth (m)	gsd type	Sample type	Corrected Porosity	r mean (nm)	Log r mean (nm)	r 10% (nm)	Log r10% [nm]	CEP [MPa]	Temperature (C)	Total C (%)	TOC (%)	Measured Gs (g/cm^3)
NOR_7	3484.6	5	Plug	0.097	3.1	0.5	7.5	0.9	9.3		1.7	1.3	2.769
NOR_6	3005.45	5	Plug	0.065	4.0	0.6	9.0	1.0	7.8	130.2	1.8	1.5	2.764
NOR_28	3861.82	5	Plug	0.075	4.6	0.7	9.2	1.0	7.6		1.9	1.6	2.747
NOR_29	4133.39	6	Plug	0.055	5.4	0.7	14.0	1.1	5.0		0.1	0.1	2.756
NOR_9	3517.3	6	Plug	0.056	5.9	0.8	13.8	1.1	5.1	132.8	1.6	1.3	2.737
NOR_27	3550.92	6	Plug	0.068	6.6	0.8	14.6	1.2	4.8		1.2	1.1	2.867
NOR_24	2798.5	6	Plug	0.079	8.8	0.9	11.0	1.0	6.4	104.6	3.4	2.4	2.696
Arith Mean													
Geo Mean													
Har Mean													
SD													
Min													
Max													
Skew													
Kurtosis													

Table A5.3.9. Physical property data and statistical data reductions for the 5 – 10% porosity bin Jurassic North Sea Group 2 subset.

Sample	KB Depth (m)	gsd type	Sample type	Corrected Porosity	r mean (nm)	Log r mean (nm)	r 10% (nm)	Log r10% [nm]	CEP [MPa]	Temperature (C)	Total C (%)	TOC (%)	Measured Gs (g/cm^3)
NOR_12	3044.9	5	Plug	0.104	4.3	0.6	7.5	0.9	9.3	111.4	1.3	1.3	2.723
NOR_2	4386.4	5	Plug	0.113	4.8	0.7	11.5	1.1	6.1	140.4	2.3	2.2	2.812
NOR_26	3040.6	5	Plug	0.109	7.0	0.8	13.0	1.1	5.4	111.2	3.6	2.8	2.726
GOM_65	6881.0	6	SWC	0.123	7.6	0.9	13.8	1.1	5.1	108.6	1.2	0.6	2.77
NOR_23	2589.8	6	Plug	0.127	7.7	0.9	16.2	1.2	4.3	89.6	1.2	1.1	2.738
NOR_8	2705.9	5	Plug	0.108	8.0	0.9	16.0	1.2	4.4	101.0	0.2	0.2	2.754
NOR_25	2801.6	6	Plug	0.115	10.6	1.0	21.1	1.3	3.3	106.3	1.0	0.8	2.757
NOR_5	2860.9	5	Plug	0.11	24.2	1.4	62.0	1.8	1.1	123.6	0.9	0.8	2.789
NOR_22	2412.9	6	Plug	0.129	45.4	1.7	130.0	2.1	0.5	100.2	2.2	1.9	2.788
SCB_12	5602.1	5	RSW core	0.101	64.3	1.8	141.6	2.2	0.5	132.8	1.3	0.3	2.738
SCB_16	5627.5	5	RSW core	0.102	72.1	1.9	134.8	2.1	0.5	133.4	1.3	0.1	2.755
NOR_3	2657.8	5	Plug	0.127	74.6	1.9	150.0	2.2	0.5	100.7	1.4	1.4	2.76
GOM_55	6579.7	6	SWC	0.111	106.9	2.0	146.3	2.2	0.5	102.2	1.1	1.1	2.662
GOM_72	6884.3	6	SWC	0.114	117.9	2.1	316.8	2.5	0.2	108.6	0.5	0.3	2.702
Arith Mean													
Geo Mean													
Har Mean													
SD													
Min													
Max													
Skew													
Kurtosis													

Table A5.3.10. Physical property data and statistical data reductions for the 10 – 15% porosity bin Group 2 subset.

Sample	KB Depth (m)	gsd type	Sample type	Corrected Porosity	r mean (nm)	Log r mean (nm)	r 10% (nm)	Log r10% [nm]	CEP [MPa]	Temperature (C)	Total C (%)	TOC (%)	Measured Gs (g/cm^3)
GOM_56	6673.6	6	SWC	0.153	5.6	0.7	12.4	1.1	5.6	104.2	1.5	0.8	2.721
ANG_23	2444.0	6	SWC	0.168	13.1	1.1	22.8	1.4	3.1				
GOM_11	3559.5	6	SWC	0.186	103.4	2.0	163.7	2.2	0.4	46.5	1.2	0.5	2.599
ANG_22	4142.0	6	Core	0.183	285.8	2.5	741.2	2.9	0.1				
TRIN_7	3835.0	6	Core	0.175	358.5	2.6	676.0	2.8	0.1				
TRIN_8	3872.9	5	Core	0.177	496.7	2.7	1209.5	3.1	0.1				
TRIN_12	3993.9	6	Core	0.181	1497.0	3.2	5960.5	3.8	0.01				
Arith Mean 0.175 394.311 2.109 1255.149 2.460 1.345 Geo Mean 0.174 128.537 1.904 288.633 2.270 0.243 Har Mean 0.174 25.611 1.662 52.040 2.062 0.056 SD 0.012 538.252 0.911 2196.937 0.998 2.272 r10% CoV 42.22 r10% N-0 186332 Min 0.153 5.600 0.748 12.400 1.093 0.012 r mean CoV 21.02 r mean N-0 46179 Max 0.186 1497.000 3.175 5960.500 3.775 5.645 Log r mean CoV 0.55 Log r mean N-0 31 Skew -1.341 1.998 -0.668 2.414 -0.334 1.670 Log r10% CoV 0.48 Log r10% N-0 24 Kurtosis 1.737 4.387 -0.834 6.045 -0.975 1.904 CEP CoV 40.73 CEP N-0 173480													

Table A5.3.11. Physical property data and statistical data reductions for the 15 – 20% porosity bin Group 2 subset.

Sample	KB Depth (m)	gsd type	Sample type	Corrected Porosity	r mean (nm)	Log r mean (nm)	r 10% (nm)	Log r10% [nm]	CEP [MPa]	Temperature (C)	Total C (%)	TOC (%)	Measured Gs (g/cm^3)
NOR_21	2090.6	6	Plug	0.205	163.8	2.2	453.7	2.7	0.154	61.2	1.5	1.5	2.767
GOM_75	5697.0	5	SWC	0.223	242.7	2.4	652.2	2.8	0.107				
TRIN_9	3873.4	5	Core	0.259	571.0	2.8	1231.9	3.1	0.057				
NOR_11	2047.9	6	Plug	0.265	1403.4	3.1	3990.3	3.6	0.018	59.9	1.0	1.0	2.752
Arith Mean 0.238 595.224 2.626 1582.028 3.041 0.084 Geo Mean 0.237 422.470 2.602 1098.201 3.020 0.064 Har Mean 0.235 315.224 2.578 833.374 3.001 0.044 SD 0.031 602.336 0.441 1741.559 0.440 0.063 r10% CoV 2.09 r10% N-0 457 Min 0.205 163.800 2.214 453.700 2.657 0.018 r mean CoV 1.91 r mean N-0 382 Max 0.265 1403.400 3.147 3990.300 3.601 0.154 Log r mean CoV 0.17 Log r mean N-0 3 Skew -0.279 1.477 0.564 1.769 1.011 0.147 Log r10% CoV 0.15 Log r10% N-0 2 Kurtosis -4.018 1.884 -1.543 3.134 0.401 -1.640 CEP CoV 1.43 CEP N-0 214													

Table A5.3.12. Table A3.11. Physical property data and statistical data reductions for the 20 – 27% porosity bin Group 2 subset.

Appendix A5.4 – Ryan-Joiner normality test results.

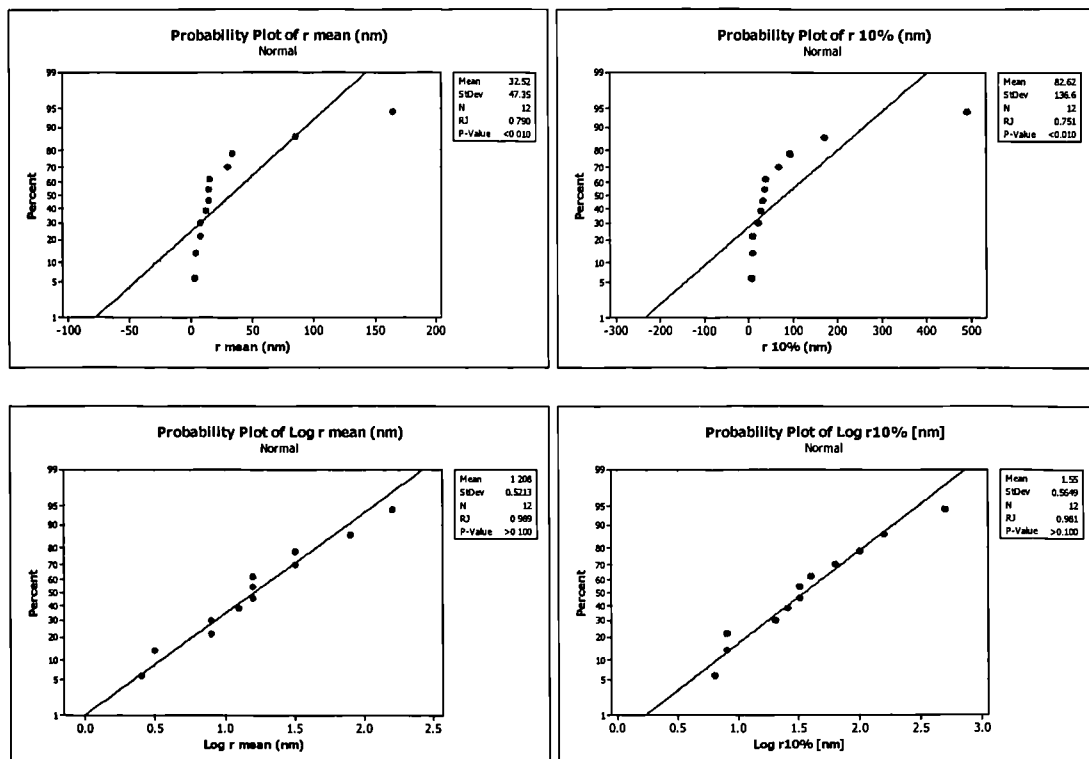


Figure A5.4.1. Probability plots generated from the Ryan-Joiner normality test for (a) log r mean (b) log r 10% (c) log r mean and (d) log r 10% for samples with type 1 – 4 gsd's and an average porosity 8.2% (range 7 – 9.8%). The critical value at the 0.05 level is equal to 0.927 for $n = 12$ and is exceeded for both log r mean and log r 10%.

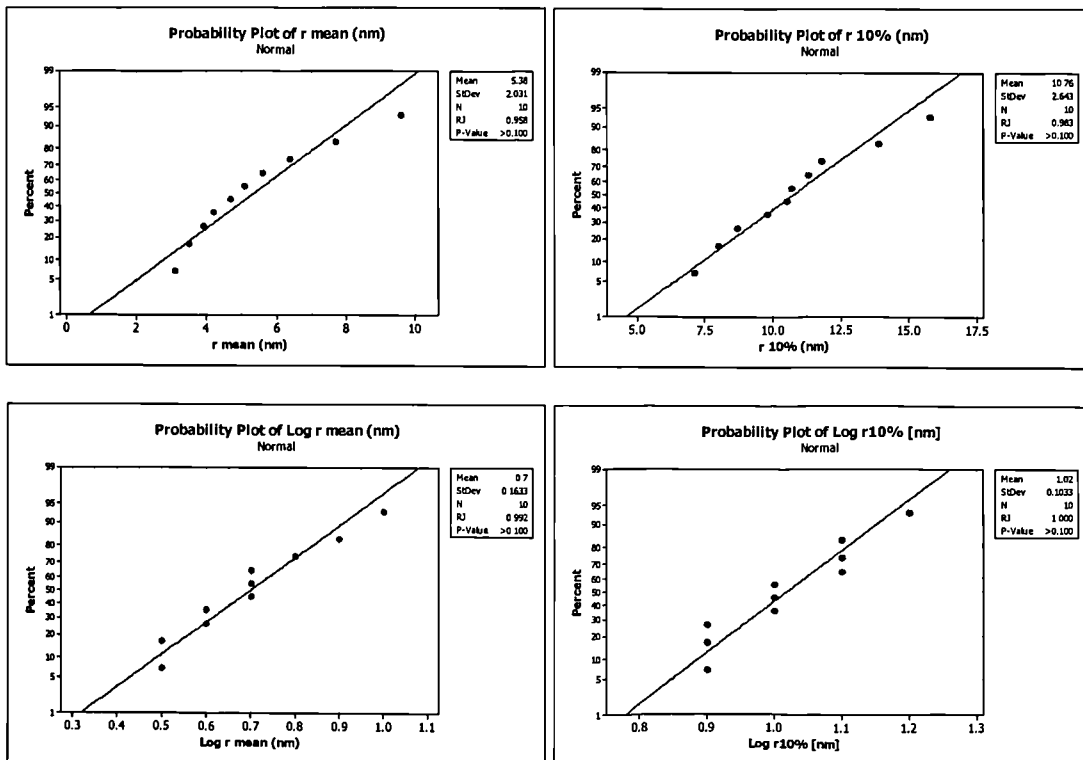


Figure A5.4.2. Probability plots generated from the Ryan-Joiner normality test for (a) log r mean (b) log $r 10\%$ (c) log r mean and (d) log $r 10\%$ for samples with type 1 – 4 gsd's and an average porosity 12.7% (range 10.2 – 14.6%). The critical value at the 0.05 level is equal to 0.917 for $n = 10$ and is exceeded for both r mean and $r 10\%$.

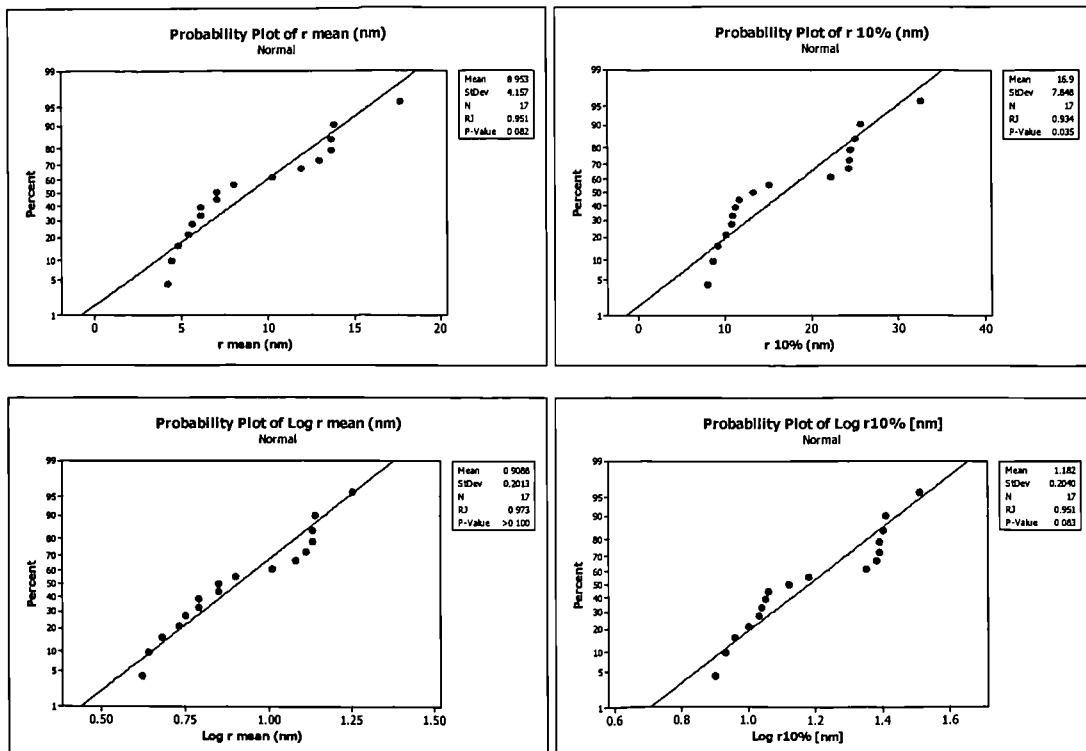


Figure A5.4.3. Probability plots generated from the Ryan-Joiner normality test for (a) log r mean (b) log r10% (c) log r mean and (d) log r10% for samples with type 1 – 4 gsd's and an average porosity 17.4% (range 15.1 – 19.6%). The critical value at the 0.05 level is equal to 0.944 for $n = 17$ and is exceeded for all but r10%.

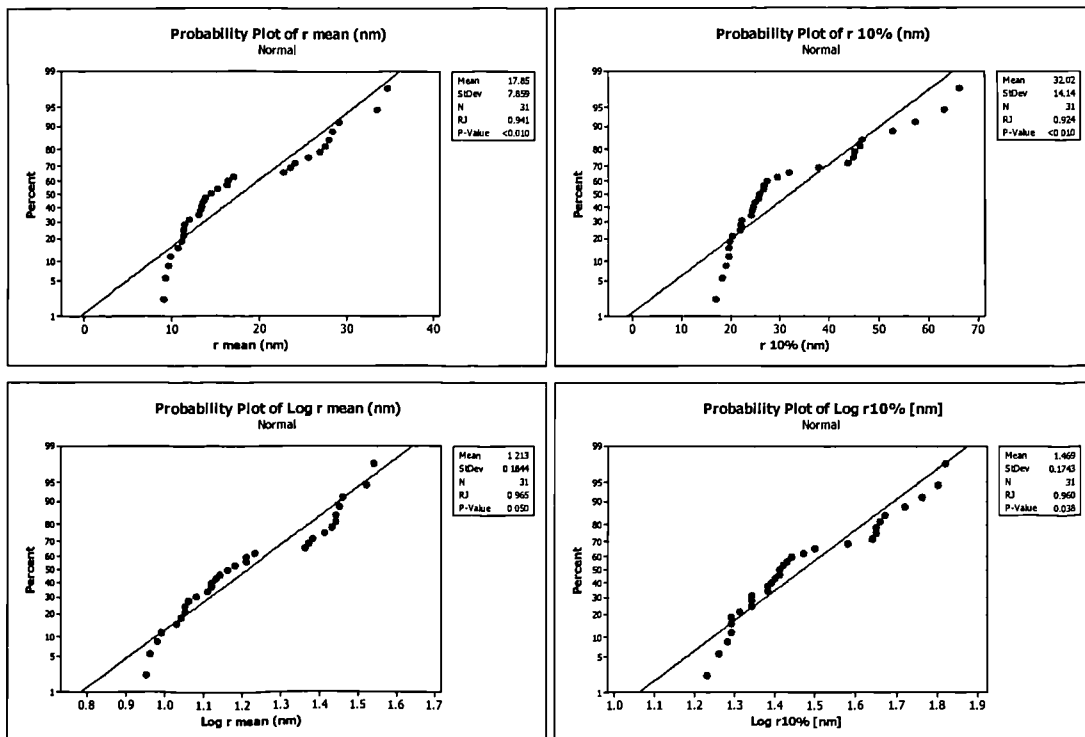


Figure A5.4.4. Probability plots generated from the Ryan-Joiner normality test for (a) log r mean (b) log r10% (c) log r mean and (d) log r10% for samples with type 1 – 4 gsd's and an average porosity 22.7% (range 20.3 – 24.9%). The critical value at the 0.05 level is equal to 0.965 for $n = 31$ and exceeds the values obtained for r mean and r10% and log r10% indicating strong evidence against normality.

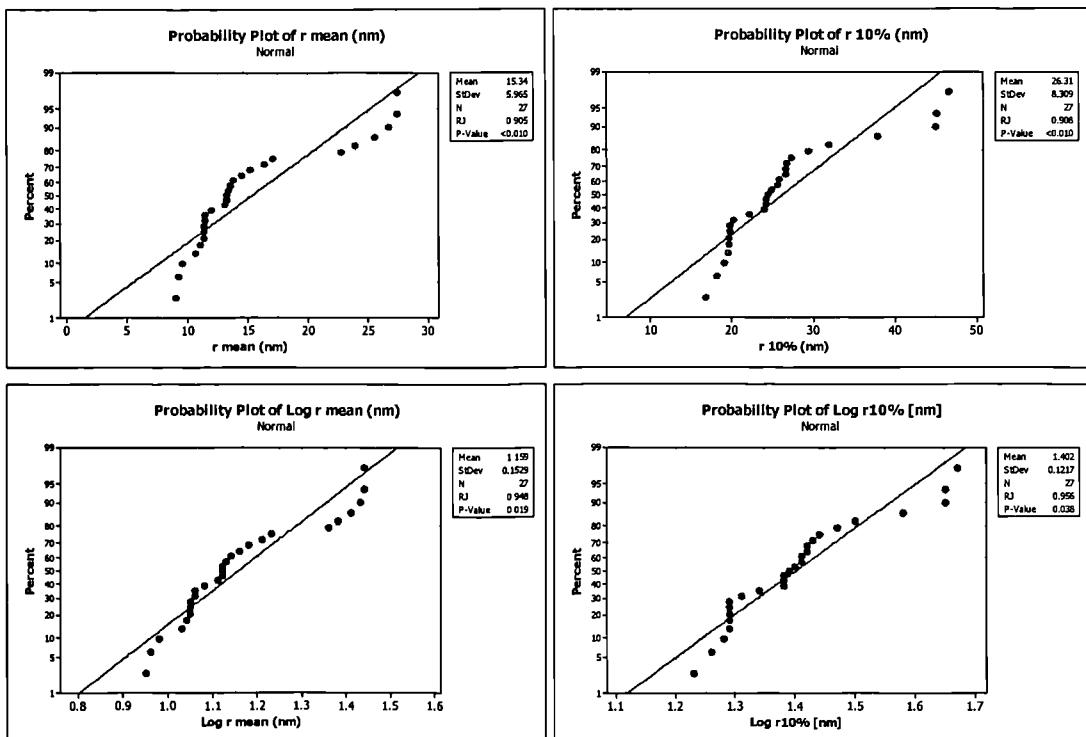


Figure A5.4.5. Probability plots generated from the Ryan-Joiner normality test for (a) log r mean (b) log r10% (c) log r mean and (d) log r10% for samples with type 1 – 4 gsd's from a single Iota Area well and an average porosity of 22.8% porosity (range 20.3 – 24.9%). The critical value at the 0.05 level is equal to 0.955 for $n = 23$ and exceeds all the values except log r10%.

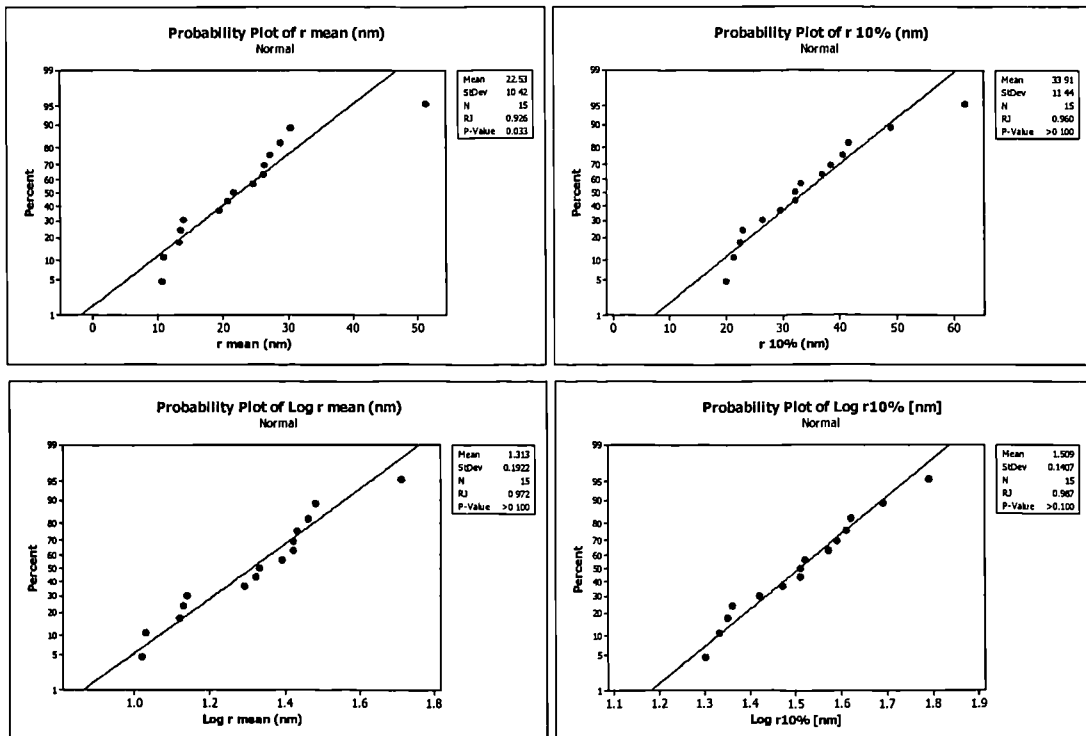


Figure A5.4.6. Probability plots generated from the Ryan-Joiner normality test for (a) log r mean (b) log r10% (c) log r mean and (d) log r10% for samples with type 1 – 4 gsd's and an average porosity 27.6% (range 25 – 33.8%). The critical value at the 0.05 level is equal to 0.938 for $n = 15$ and is exceeded by all but r mean.

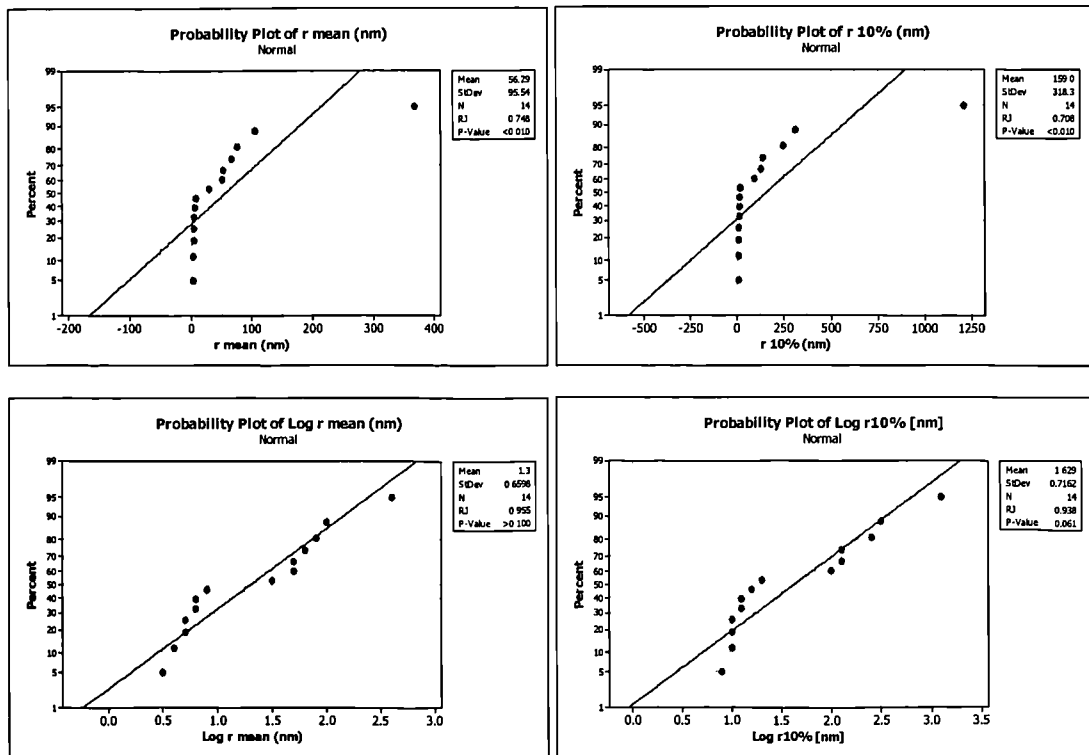


Figure A5.4.7. Probability plots generated from the Ryan-Joiner normality test for (a) log r mean (b) log r10% (c) log r mean and (d) log r10% for samples with type 5 – 6 gsd's and an average porosity 7.8% (range 5.5 – 9.7%). The critical value at the 0.05 level is equal to 0.935 for $n = 14$ and is only exceeded for by log r mean.

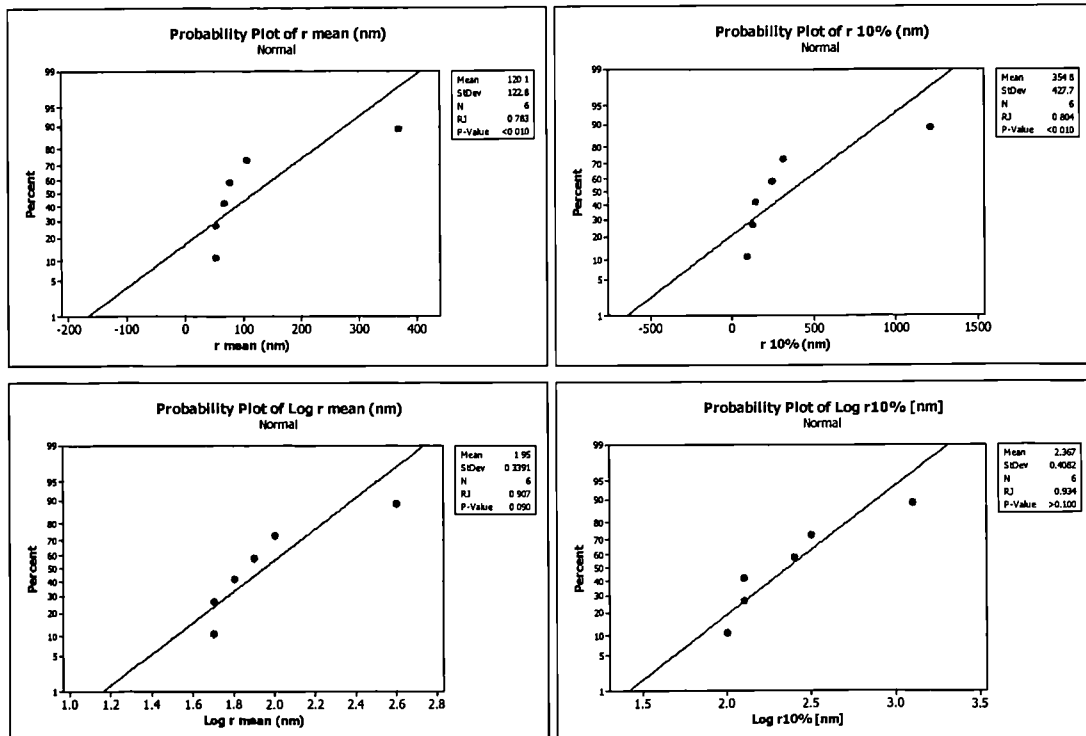


Figure A5.4.8. Probability plots generated from the Ryan-Joiner normality test for (a) log r mean (b) log r10% (c) log r mean and (d) log r10% for Zeta Area samples with type 5 – 6 gsd's and an average porosity 8.5% (range 6.9 – 9.6%). The critical value at the 0.05 level is equal to 0.889 for $n = 6$ and is only exceeded by log r mean and log r10%.

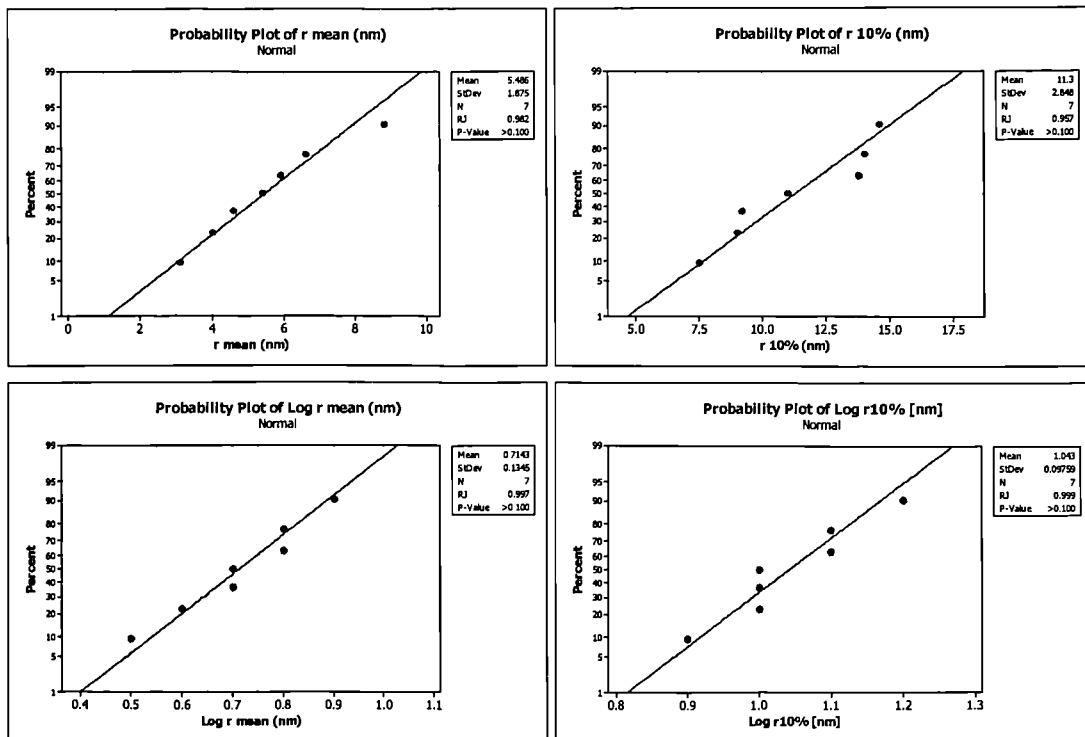


Figure A5.4.9. Probability plots generated from the Ryan-Joiner normality test for (a) log r mean (b) log r10% (c) log r mean and (d) log r10% for Jurassic North Sea samples with type 5 – 6 gsd's and an average porosity 7.1% (range 5.5 – 9.7%). The critical value at the 0.05 level is equal to 0.898 for $n = 7$ and is exceeded all the parameters.

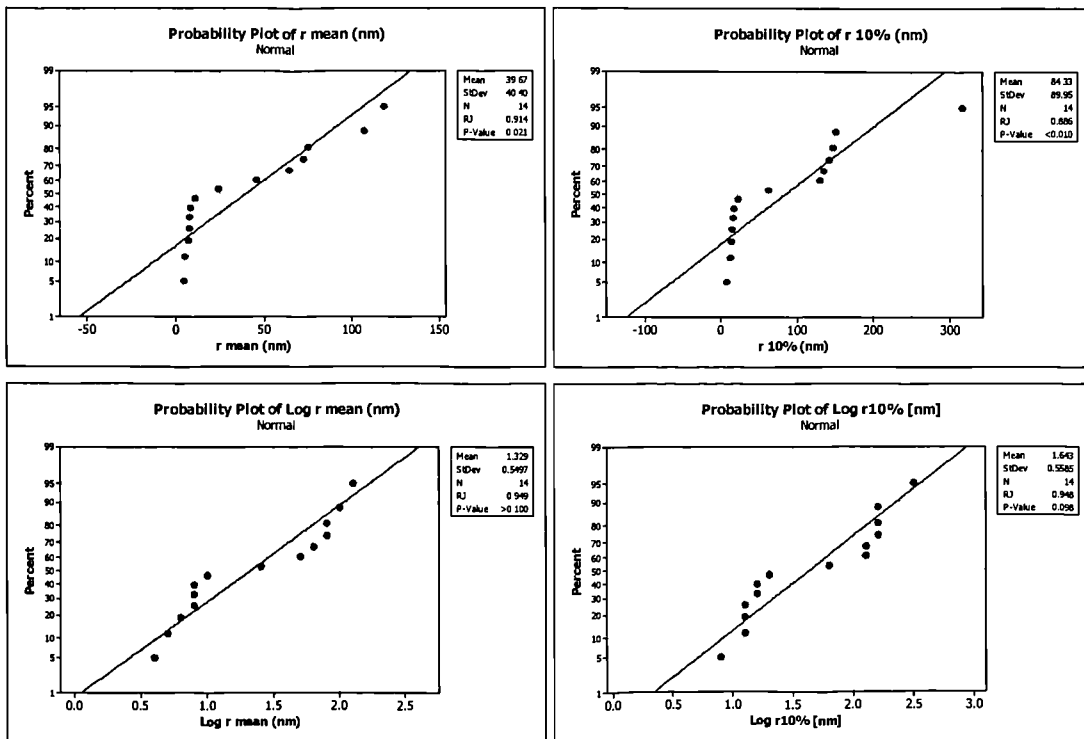


Figure A5.4.10. Probability plots generated from the Ryan-Joiner normality test for (a) log r mean (b) log r10% (c) log r mean and (d) log r10% for samples with type 5 – 6 gsd's and an average porosity 11.4% (range 10.1 – 12.9%). The critical value at the 0.05 level is equal to 0.935 for $n = 14$ and is only exceeded by log r mean and log r10%.

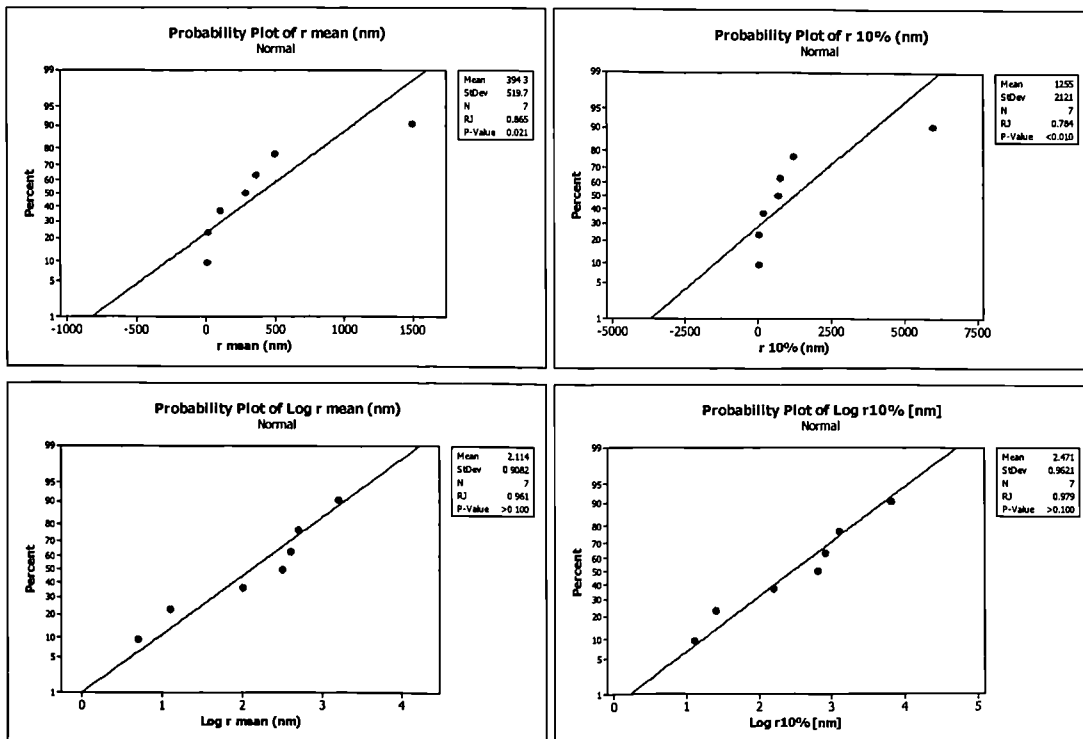


Figure A5.4.11. Probability plots generated from the Ryan-Joiner normality test for (a) log r mean (b) log r 10% (c) log r mean and (d) log r 10% for samples with type 5 – 6 gsd's and an average porosity 17.5% (range 15.3 – 18.6%). The critical value at the 0.05 level is equal to 0.898 for $n = 7$ and is only exceeded by log r mean and log r 10%.

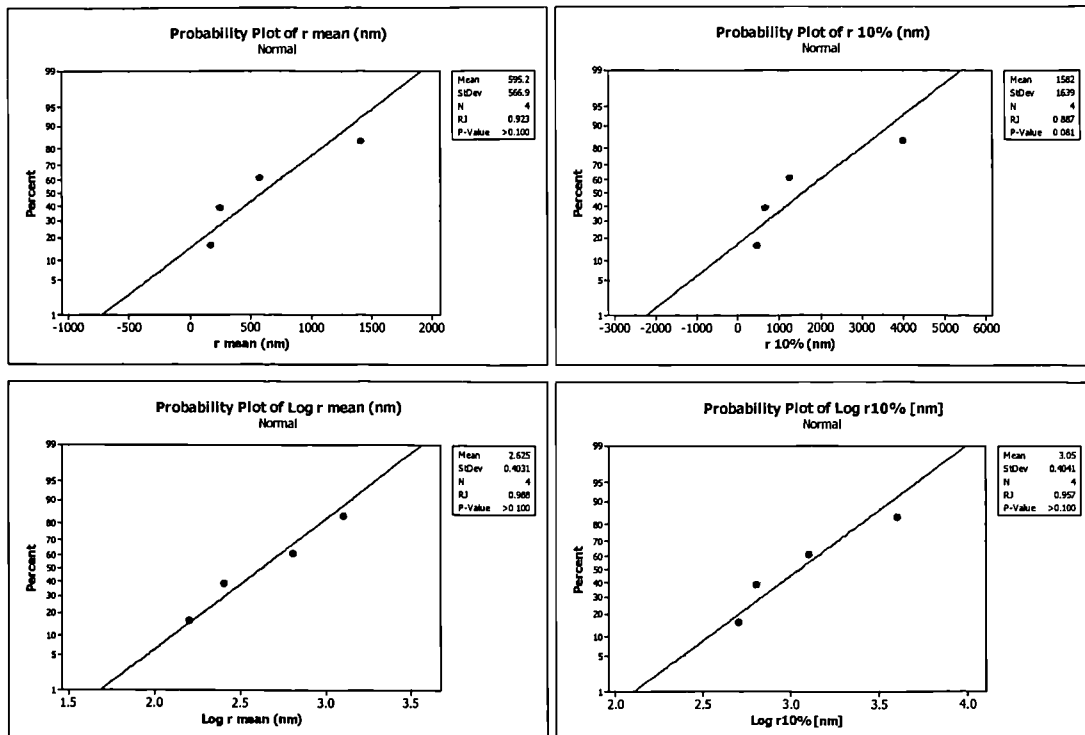


Figure A5.4.12. Probability plots generated from the Ryan-Joiner normality test for (a) log r mean (b) log r10% (c) log r mean and (d) log r10% for samples with type 5 – 6 gsd's and an average porosity 23.8% (range 20.5 – 26.5%). The critical value at the 0.05 level is equal to 0.873 for $n = 4$ and is exceeded by all the parameters.

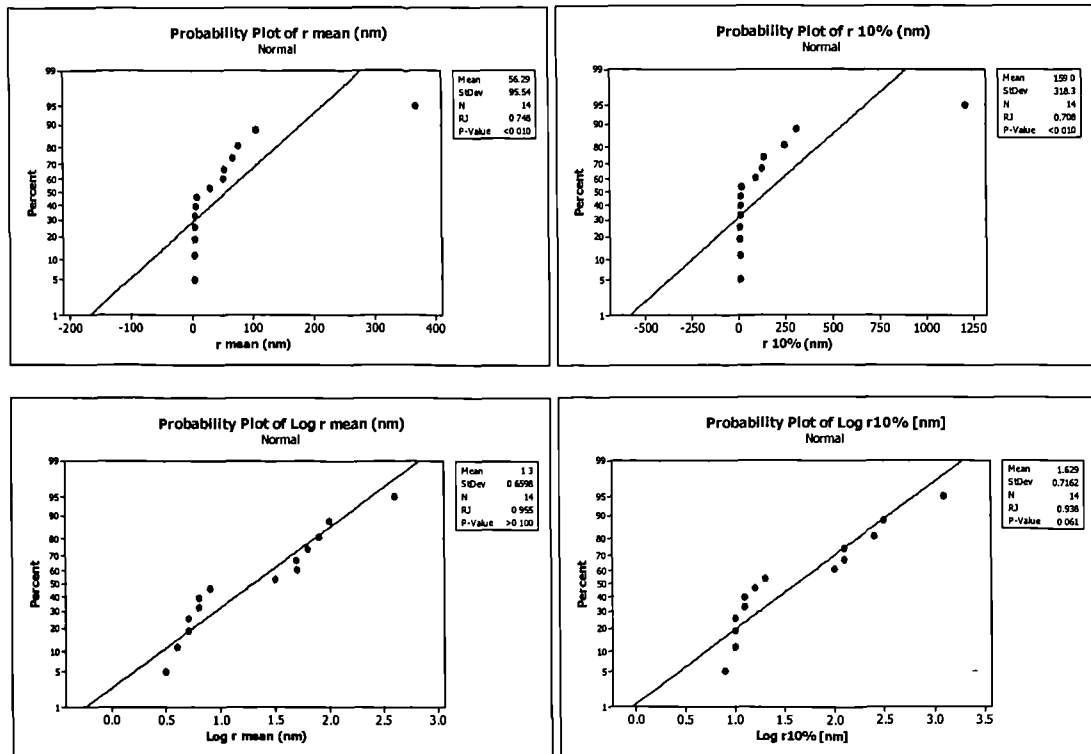


Figure A5.4.7. Probability plots generated from the Ryan-Joiner normality test for (a) log r mean (b) log r10% (c) log r mean and (d) log r10% for samples with type 5 – 6 gsd's and an average porosity 7.8% (range 5.5 – 9.7%). The critical value at the 0.05 level is equal to 0.935 for $n = 14$ and is only exceeded for by log r mean.

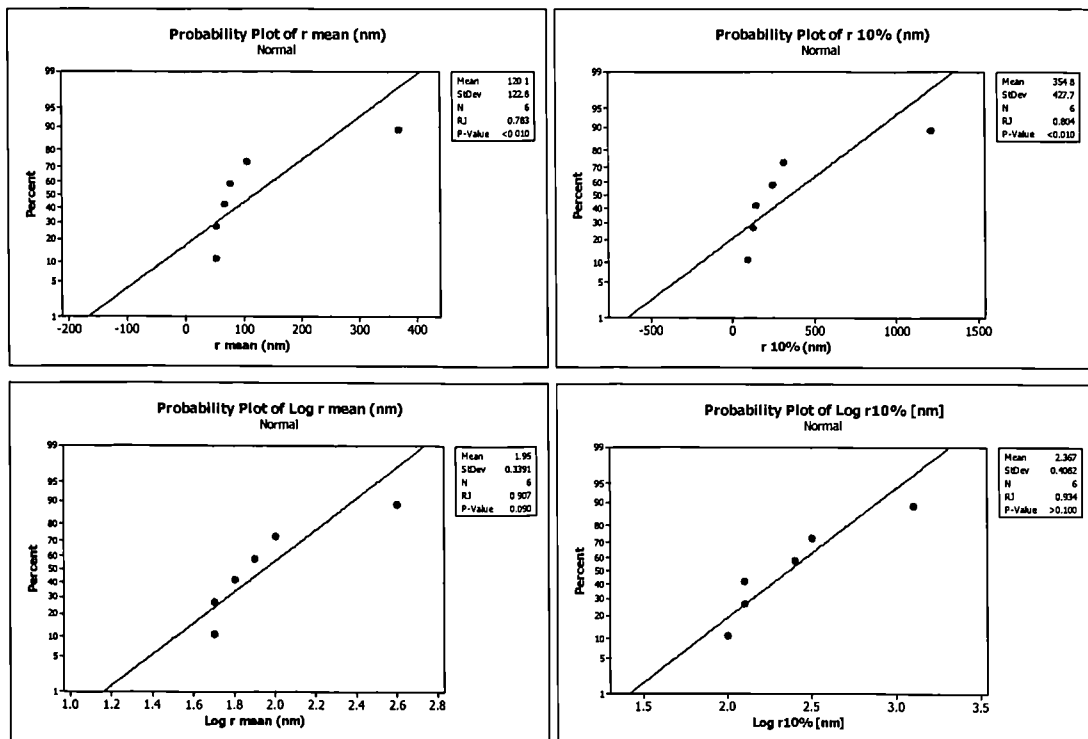


Figure A5.4.8. Probability plots generated from the Ryan-Joiner normality test for (a) log r mean (b) log r10% (c) log r mean and (d) log r10% for Zeta Area samples with type 5 – 6 gsd's and an average porosity 8.5% (range 6.9 – 9.6%). The critical value at the 0.05 level is equal to 0.889 for $n = 6$ and is only exceeded by log r mean and log r10%.

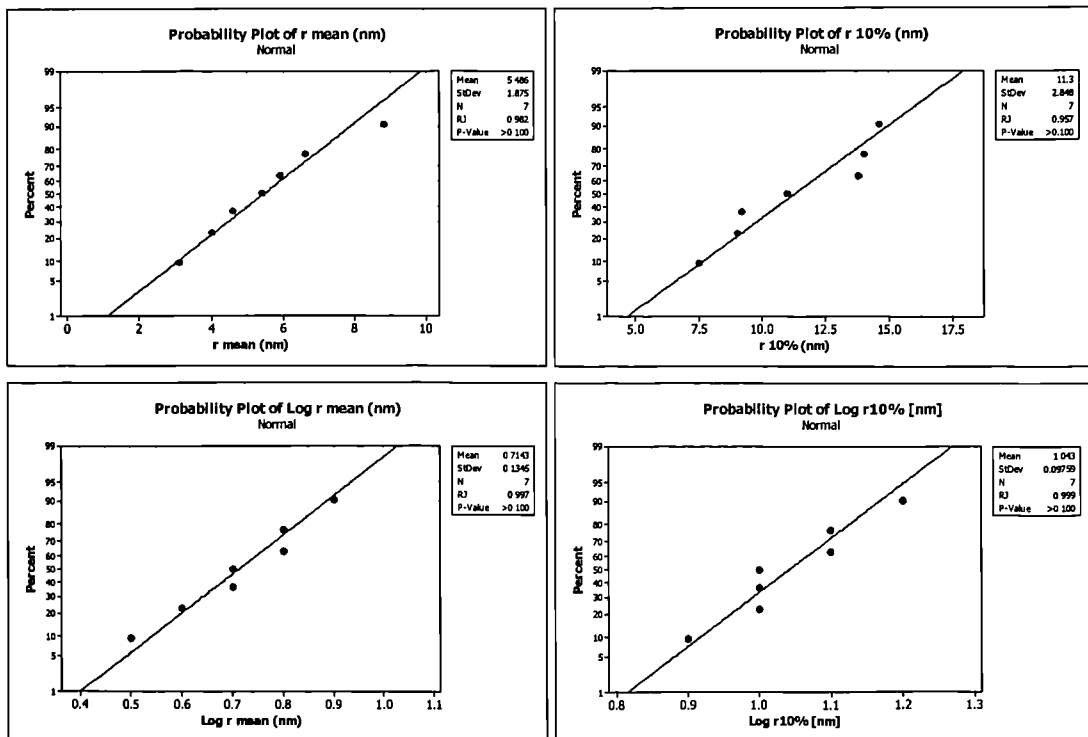


Figure A5.4.9. Probability plots generated from the Ryan-Joiner normality test for (a) log r mean (b) log r10% (c) log r mean and (d) log r10% for Jurassic North Sea samples with type 5 – 6 gsd's and an average porosity 7.1% (range 5.5 – 9.7%). The critical value at the 0.05 level is equal to 0.898 for $n = 7$ and is exceeded all the parameters.

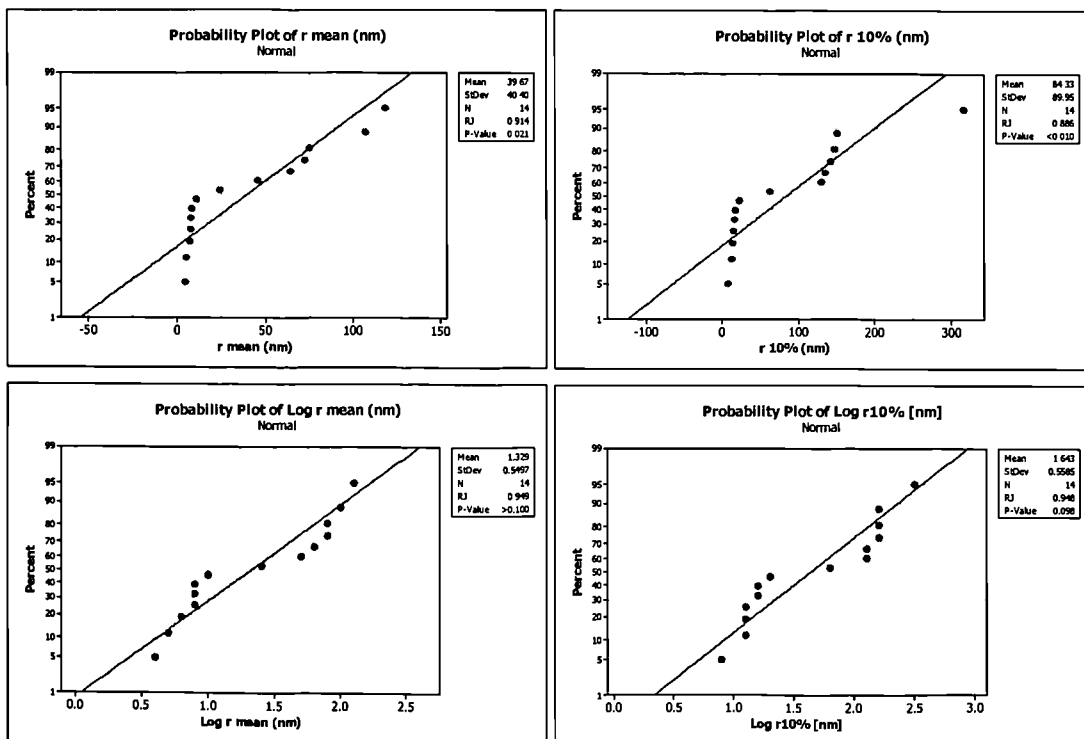


Figure A5.4.10. Probability plots generated from the Ryan-Joiner normality test for (a) log r mean (b) log r10% (c) log r mean and (d) log r10% for samples with type 5 – 6 gsd's and an average porosity 11.4% (range 10.1 – 12.9%). The critical value at the 0.05 level is equal to 0.935 for $n = 14$ and is only exceeded by log r mean and log r10%.

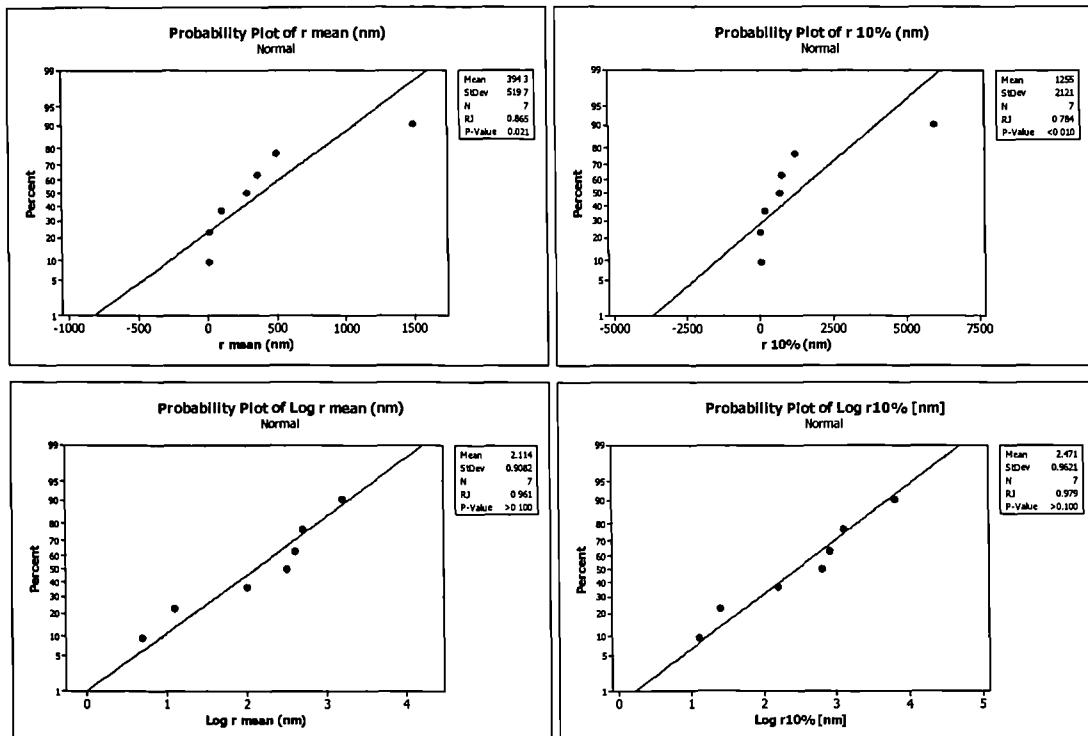


Figure A5.4.11. Probability plots generated from the Ryan-Joiner normality test for (a) log r mean (b) log r10% (c) log r mean and (d) log r10% for samples with type 5 – 6 gsd's and an average porosity 17.5% (range 15.3 – 18.6%). The critical value at the 0.05 level is equal to 0.898 for $n = 7$ and is only exceeded by log r mean and log r10%.

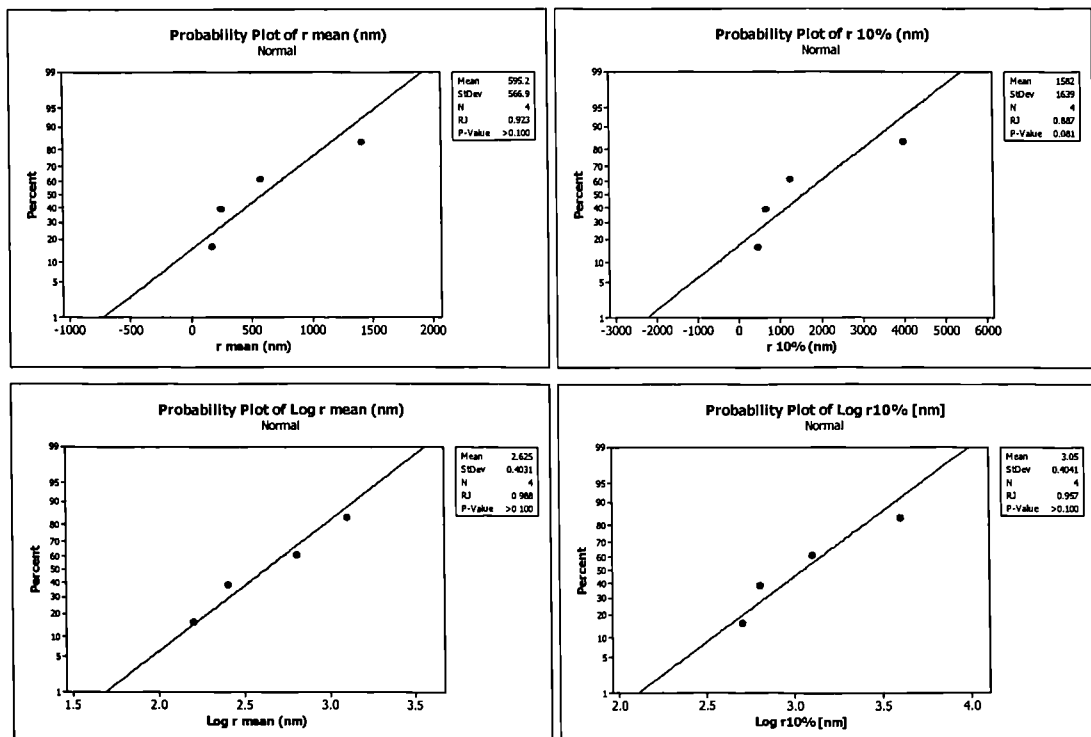


Figure A5.4.12. Probability plots generated from the Ryan-Joiner normality test for (a) log r mean (b) log r10% (c) log r mean and (d) log r10% for samples with type 5 – 6 gsd's and an average porosity 23.8% (range 20.5 – 26.5%). The critical value at the 0.05 level is equal to 0.873 for $n = 4$ and is exceeded by all the parameters.

Appendix A5.5 – Group 1 Regression Tables

SUMMARY OUTPUT

<i>Regression Statistics</i>	
Multiple R	0.634537
R Square	0.402638
Adjusted R Square	0.387704
Standard Error	20.28083
Observations	83

ANOVA

	<i>df</i>	<i>SS</i>	<i>MS</i>	<i>F</i>	<i>Significance F</i>
Regression	2	22178.79	11089.4	26.96102	1.12E-09
Residual	80	32904.97	411.3121		
Total	82	55083.76			

	<i>Coefficients</i>	<i>Standard Error</i>	<i>t Stat</i>	<i>P-value</i>	<i>Lower 95%</i>	<i>Upper 95%</i>	<i>Lower 95.0%</i>	<i>Upper 95.0%</i>
Intercept	32.74527	11.84642	2.764148	0.007081	9.170114	56.32043	9.170114	56.32043
X Variable 1	-391.874	54.02818	-7.25315	2.31E-10	-499.394	-284.355	-499.394	-284.355
X Variable 2	163.2118	34.01571	4.79813	7.31E-06	95.5183	230.9053	95.5183	230.9053

Table A5.5.1. Regression statistics obtained from a multiple linear regression of CEP_{Hg} on porosity (Variable 1) and clay content (Variable 2) on the unscreened Group 1 (gsd types 1 – 4) dataset.

SUMMARY OUTPUT

<i>Regression Statistics</i>	
Multiple R	0.605046
R Square	0.36608
Adjusted R Square	0.350232
Standard Error	20.89219
Observations	83

ANOVA

	<i>df</i>	<i>SS</i>	<i>MS</i>	<i>F</i>	<i>Significance F</i>
Regression	2	20165.09	10082.54	23.09949	1.21E-08
Residual	80	34918.67	436.4834		
Total	82	55083.76			

	<i>Coefficients</i>	<i>Standard Error</i>	<i>t Stat</i>	<i>P-value</i>	<i>Lower 95%</i>	<i>Upper 95%</i>	<i>Lower 95.0%</i>	<i>Upper 95.0%</i>
Intercept	119.1052	12.40192	9.603774	5.74E-15	94.4246	143.7859	94.4246	143.7859
X Variable 1	-257.566	39.0983	-6.58764	4.35E-09	-335.374	-179.757	-335.374	-179.757
X Variable 2	-130.184	31.4994	-4.13291	8.76E-05	-192.87	-67.4983	-192.87	-67.4983

Table A5.5.2. Regression statistics obtained from a multiple linear regression of CEP_{Hg} on porosity (Variable 1) and sortable silt content (Variable 2) on the unscreened Group 1 (gsd types 1 – 4) dataset.

SUMMARY OUTPUT

<i>Regression Statistics</i>	
Multiple R	0.703148
R Square	0.494417
Adjusted R Square	0.478367
Standard Error	19.18697
Observations	66

ANOVA

	<i>df</i>	<i>SS</i>	<i>MS</i>	<i>F</i>	<i>Significance F</i>
Regression	2	22680.63	11340.32	30.80436	4.67E-10
Residual	63	23192.82	368.14		
Total	65	45873.45			

	<i>Coefficients</i>	<i>Standard Error</i>	<i>t Stat</i>	<i>P-value</i>	<i>Lower 95%</i>	<i>Upper 95%</i>	<i>Lower 95.0%</i>	<i>Upper 95.0%</i>
Intercept	58.00555	14.11056	4.110792	0.000116	29.80784	86.20327	29.80784	86.20327
X Variable 1	-402.994	54.80376	-7.35341	4.83E-10	-512.511	-293.478	-512.511	-293.478
X Variable 2	125.4109	37.2303	3.368517	0.001293	51.01201	199.8097	51.01201	199.8097

Table A5.5.3. Regression statistics obtained from a multiple linear regression of CEP_{Hg} on porosity (Variable 1) and clay content (Variable 2) on the Group 1 (gsd types 1 – 4) dataset screened for cuttings.

SUMMARY OUTPUT

<i>Regression Statistics</i>	
Multiple R	0.690944
R Square	0.477403
Adjusted R Square	0.460813
Standard Error	19.50715
Observations	66

ANOVA

	<i>df</i>	<i>SS</i>	<i>MS</i>	<i>F</i>	<i>Significance F</i>
Regression	2	21900.12	10950.06	28.7759	1.33E-09
Residual	63	23973.32	380.5289		
Total	65	45873.45			

	<i>Coefficients</i>	<i>Standard Error</i>	<i>t Stat</i>	<i>P-value</i>	<i>Lower 95%</i>	<i>Upper 95%</i>	<i>Lower 95.0%</i>	<i>Upper 95.0%</i>
Intercept	125.6566	12.36982	10.15832	6.76E-15	100.9375	150.3758	100.9375	150.3758
X Variable 1	-308.751	40.84809	-7.55851	2.11E-10	-390.379	-227.122	-390.379	-227.122
X Variable 2	-97.58	32.66053	-2.9877	0.004002	-162.847	-32.3131	-162.847	-32.3131

Table A5.5.4. Regression statistics obtained from a multiple linear regression of CEP_{Hg} on porosity (Variable 1) and sortable silt content (Variable 2) on the Group 1 (gsd types 1 – 4) dataset screened for cuttings.

SUMMARY OUTPUT

<i>Regression Statistics</i>						
Multiple R	0.740689					
R Square	0.54862					
Adjusted R Square	0.535344					
Standard Error	16.69647					
Observations	71					

<i>ANOVA</i>						
	<i>df</i>	<i>SS</i>	<i>MS</i>	<i>F</i>	<i>Significance F</i>	
Regression	2	23040.26	11520.13	41.32453	1.8E-12	
Residual	68	18956.51	278.7722			
Total	70	41996.76				

	<i>Coefficients</i>	<i>Standard Error</i>	<i>t Stat</i>	<i>P-value</i>	<i>Lower 95%</i>	<i>Upper 95%</i>	<i>Lower 95.0%</i>	<i>Upper 95.0%</i>
Intercept	90.87858	14.57909	6.233489	3.31E-08	61.78648	119.9707	61.78648	119.9707
X Variable 1	-392.005	48.97386	-8.00438	2.15E-11	-489.731	-294.279	-489.731	-294.279
X Variable 2	59.52727	34.40996	1.729943	0.088177	-9.13669	128.1912	-9.13669	128.1912

Table A5.5.5. Regression statistics obtained from a multiple linear regression of CEP_{Hg} on porosity (Variable 1) and clay content (Variable 2) on the Group 1 (gsd types 1 – 4) dataset screened for Zeta Area samples.

SUMMARY OUTPUT

<i>Regression Statistics</i>						
Multiple R	0.758077					
R Square	0.57468					
Adjusted R Square	0.562171					
Standard Error	16.20732					
Observations	71					

<i>ANOVA</i>						
	<i>df</i>	<i>SS</i>	<i>MS</i>	<i>F</i>	<i>Significance F</i>	
Regression	2	24134.72	12067.36	45.93988	2.38E-13	
Residual	68	17862.05	262.6772			
Total	70	41996.76				

	<i>Coefficients</i>	<i>Standard Error</i>	<i>t Stat</i>	<i>P-value</i>	<i>Lower 95%</i>	<i>Upper 95%</i>	<i>Lower 95.0%</i>	<i>Upper 95.0%</i>
Intercept	138.0368	12.60885	10.94761	1.19E-16	112.8762	163.1974	112.8762	163.1974
X Variable 1	-380.689	39.97817	-9.52243	3.88E-14	-460.465	-300.914	-460.465	-300.914
X Variable 2	-81.1523	29.9485	-2.70973	0.008514	-140.914	-21.3911	-140.914	-21.3911

Table A5.5.6. Regression statistics obtained from a multiple linear regression of CEP_{Hg} on porosity (Variable 1) and sortable silt content (Variable 2) on the Group 1 (gsd types 1 – 4) dataset screened for Zeta Area samples.

SUMMARY OUTPUT

<i>Regression Statistics</i>	
Multiple R	0.754126
R Square	0.568706
Adjusted R Square	0.553573
Standard Error	16.65581
Observations	60

ANOVA

	<i>df</i>	<i>SS</i>	<i>MS</i>	<i>F</i>	<i>Significance F</i>
Regression	2	20850.75	10425.37	37.58028	3.9E-11
Residual	57	15812.72	277.4161		
Total	59	36663.47			

	<i>Coefficients</i>	<i>Standard Error</i>	<i>t Stat</i>	<i>P-value</i>	<i>Lower 95%</i>	<i>Upper 95%</i>	<i>Lower 95.0%</i>	<i>Upper 95.0%</i>
Intercept	89.66704	14.88491	6.024024	1.31E-07	59.86051	119.4736	59.86051	119.4736
X Variable 1	-395.839	51.50323	-7.68571	2.29E-10	-498.972	-292.705	-498.972	-292.705
X Variable 2	65.40113	35.54145	1.840136	0.070957	-5.76944	136.5717	-5.76944	136.5717

Table A5.5.7. Regression statistics obtained from a multiple linear regression of CEP_{Hg} on porosity (Variable 1) and clay content (Variable 2) on the Group 1 (gsd types 1 – 4) dataset screened for both cuttings and Zeta Area samples.

SUMMARY OUTPUT

<i>Regression Statistics</i>						
Multiple R	0.765959					
R Square	0.586693					
Adjusted R Square	0.572191					
Standard Error	16.3048					
Observations	60					

<i>ANOVA</i>						
	<i>df</i>	<i>SS</i>	<i>MS</i>	<i>F</i>	<i>Significance F</i>	
Regression	2	21510.22	10755.11	40.45609	1.16E-11	
Residual	57	15153.25	265.8465			
Total	59	36663.47				

	<i>Coefficients</i>	<i>Standard Error</i>	<i>t Stat</i>	<i>P-value</i>	<i>Lower 95%</i>	<i>Upper 95%</i>	<i>Lower 95.0%</i>	<i>Upper 95.0%</i>
Intercept	137.5745	13.27301	10.36498	9.94E-15	110.9958	164.1533	110.9958	164.1533
X Variable 1	-379.183	42.68582	-8.88311	2.4E-12	-464.66	-293.706	-464.66	-293.706
X Variable 2	-76.37	31.14136	-2.45237	0.017277	-138.729	-14.0105	-138.729	-14.0105

Table A5.5.8. Regression statistics obtained from a multiple linear regression of CEP_{Hg} on porosity (Variable 1) and sortable silt content (Variable 2) on the Group 1 (gsd types 1 – 4) dataset screened for both cuttings and Zeta Area samples.

Appendix A5.6 – Group 2 Regression Tables

SUMMARY OUTPUT

<i>Regression Statistics</i>	
Multiple R	0.521796
R Square	0.272271
Adjusted R Square	0.231842
Standard Error	27.61379
Observations	39

ANOVA

	<i>df</i>	<i>SS</i>	<i>MS</i>	<i>F</i>	<i>Significance F</i>
Regression	2	10270.39	5135.196	6.734493	0.003277
Residual	36	27450.78	762.5216		
Total	38	37721.17			

	<i>Coefficients</i>	<i>Standard Error</i>	<i>t Stat</i>	<i>P-value</i>	<i>Lower 95%</i>	<i>Upper 95%</i>	<i>Lower 95.0%</i>	<i>Upper 95.0%</i>
Intercept	37.25891	17.79941	2.093266	0.043433	1.160071	73.35774	1.160071	73.35774
X Variable 1	-287.689	84.54642	-3.40274	0.001649	-459.157	-116.221	-459.157	-116.221
X Variable 2	106.4625	59.51966	1.788695	0.082082	-14.2488	227.1738	-14.2488	227.1738

Table A5.6.1. Regression statistics obtained from a multiple linear regression of CEP_{Hg} on porosity (Variable 1) and clay content (Variable 2) on the unscreened Group 2 (gsd types 5 – 6) dataset.

SUMMARY OUTPUT

<i>Regression Statistics</i>	
Multiple R	0.618738
R Square	0.382837
Adjusted R Square	0.34855
Standard Error	25.4297
Observations	39

ANOVA

	<i>df</i>	<i>SS</i>	<i>MS</i>	<i>F</i>	<i>Significance F</i>
Regression	2	14441.06	7220.531	11.16572	0.000169
Residual	36	23280.11	646.6696		
Total	38	37721.17			

	<i>Coefficients</i>	<i>Standard Error</i>	<i>t Stat</i>	<i>P-value</i>	<i>Lower 95%</i>	<i>Upper 95%</i>	<i>Lower 95.0%</i>	<i>Upper 95.0%</i>
Intercept	133.0682	24.61649	5.405655	4.33E-06	83.14376	182.9927	83.14376	182.9927
X Variable 1	-273.103	77.26257	-3.53474	0.001142	-429.799	-116.408	-429.799	-116.408
X Variable 2	-122.562	38.33431	-3.1972	0.002889	-200.308	-44.8169	-200.308	-44.8169

Table A5.6.2. Regression statistics obtained from a multiple linear regression of CEP_{Hg} on porosity (Variable 1) and sortable silt content (Variable 2) on the unscreened Group 2 (gsd types 5 – 6) dataset.

SUMMARY OUTPUT

<i>Regression Statistics</i>	
Multiple R	0.69006
R Square	0.476183
Adjusted R Square	0.438767
Standard Error	24.45724
Observations	31

<i>ANOVA</i>					
	<i>df</i>	<i>SS</i>	<i>MS</i>	<i>F</i>	<i>Significance F</i>
Regression	2	15225.32	7612.661	12.72687	0.000117
Residual	28	16748.38	598.1565		
Total	30	31973.7			

	<i>Coefficients</i>	<i>Standard Error</i>	<i>t Stat</i>	<i>P-value</i>	<i>Lower 95%</i>	<i>Upper 95%</i>	<i>Lower 95.0%</i>	<i>Upper 95.0%</i>
Intercept	75.94775	18.94851	4.008113	0.000411	37.13345	114.7621	37.13345	114.7621
X Variable 1	-396.082	79.32049	-4.99344	2.82E-05	-558.563	-233.601	-558.563	-233.601
X Variable 2	43.43242	57.59765	0.754066	0.457105	-74.5511	161.416	-74.5511	161.416

Table A5.6.3. Regression statistics obtained from a multiple linear regression of CEP_{Hg} on porosity (Variable 1) and clay content (Variable 2) on the Group 2 (gsd types 5 – 6) dataset screened for Zeta Area samples.

SUMMARY OUTPUT

<i>Regression Statistics</i>	
Multiple R	0.753987
R Square	0.568497
Adjusted R Square	0.537675
Standard Error	22.19778
Observations	31

ANOVA

	<i>df</i>	<i>SS</i>	<i>MS</i>	<i>F</i>	<i>Significance F</i>
Regression	2	18176.95	9088.475	18.44472	7.76E-06
Residual	28	13796.76	492.7413		
Total	30	31973.7			

	<i>Coefficients</i>	<i>Standard Error</i>	<i>t Stat</i>	<i>P-value</i>	<i>Lower 95%</i>	<i>Upper 95%</i>	<i>Lower 95.0%</i>	<i>Upper 95.0%</i>
Intercept	139.3006	22.64407	6.151748	1.22E-06	92.91626	185.6849	92.91626	185.6849
X Variable 1	-378.169	72.30905	-5.2299	1.48E-05	-526.288	-230.051	-526.288	-230.051
X Variable 2	-96.0422	37.15853	-2.58466	0.015252	-172.158	-19.9264	-172.158	-19.9264

Table A5.6.4. Regression statistics obtained from a multiple linear regression of CEP_{Hg} on porosity (Variable 1) and sortable silt content (Variable 2) on the Group 2 (gsd types 5 – 6) dataset screened for Zeta Area samples.

Appendix A5.7 Group 1 Iota Area Subset Regression Tables

SUMMARY OUTPUT

<i>Regression Statistics</i>	
Multiple R	0.737485
R Square	0.543884
Adjusted R Square	0.524475
Standard Error	12.66566
Observations	50

<i>ANOVA</i>					
	<i>df</i>	<i>SS</i>	<i>MS</i>	<i>F</i>	<i>Significance F</i>
Regression	2	8990.503	4495.251	28.02196	9.73E-09
Residual	47	7539.686	160.4189		
Total	49	16530.19			

	<i>Coefficients</i>	<i>Standard Error</i>	<i>t Stat</i>	<i>P-value</i>	<i>Lower 95%</i>	<i>Upper 95%</i>	<i>Lower 95.0%</i>	<i>Upper 95.0%</i>
Intercept	68.96928	13.62231	5.062966	6.8E-06	41.56476	96.3738	41.56476	96.3738
X Variable 1	-318.362	44.29757	-7.18691	4.26E-09	-407.478	-229.247	-407.478	-229.247
X Variable 2	65.23202	29.6187	2.202393	0.032579	5.646939	124.8171	5.646939	124.8171

Table A5.7.1. Regression statistics obtained from a multiple linear regression of CEP_{Hg} on porosity (Variable 1) and clay content (Variable 2) on the Gulf of Mexico Group 1 (gsd types 1 – 4) data subset.

SUMMARY OUTPUT

<i>Regression Statistics</i>	
Multiple R	0.801256
R Square	0.642011
Adjusted R Square	0.626777
Standard Error	11.22083
Observations	50

ANOVA

	<i>df</i>	<i>SS</i>	<i>MS</i>	<i>F</i>	<i>Significance F</i>
Regression	2	10612.56	5306.281	42.14446	3.28E-11
Residual	47	5917.627	125.907		
Total	49	16530.19			

	<i>Coefficients</i>	<i>Standard Error</i>	<i>t Stat</i>	<i>P-value</i>	<i>Lower 95%</i>	<i>Upper 95%</i>	<i>Lower 95.0%</i>	<i>Upper 95.0%</i>
Intercept	122.6596	9.942565	12.33681	2.4E-16	102.6577	142.6614	102.6577	142.6614
X Variable 1	-306.056	34.11664	-8.97087	9.44E-12	-374.69	-237.422	-374.69	-237.422
X Variable 2	-101.749	23.30421	-4.36613	6.9E-05	-148.631	-54.8673	-148.631	-54.8673

Table A5.7.2. Regression statistics obtained from a multiple linear regression of CEP_{Hg} on porosity (Variable 1) and sortable silt content (Variable 2) on the Gulf of Mexico Group 1 (gsd types 1 – 4) data subset.

SUMMARY OUTPUT

<i>Regression Statistics</i>	
Multiple R	0.777798
R Square	0.60497
Adjusted R Square	0.579207
Standard Error	11.91448
Observations	50

ANOVA

	<i>df</i>	<i>SS</i>	<i>MS</i>	<i>F</i>	<i>Significance F</i>
Regression	3	10000.26	3333.421	23.48225	2.29E-09
Residual	46	6529.927	141.9549		
Total	49	16530.19			

	<i>Coefficients</i>	<i>Standard Error</i>	<i>t Stat</i>	<i>P-value</i>	<i>Lower 95%</i>	<i>Upper 95%</i>	<i>Lower 95.0%</i>	<i>Upper 95.0%</i>
Intercept	18.71389	22.7874	0.821239	0.415746	-27.1547	64.5825	-27.1547	64.5825
X Variable 1	-160.391	72.42019	-2.21472	0.031772	-306.165	-14.6164	-306.165	-14.6164
X Variable 2	47.99555	28.60179	1.678061	0.100118	-9.5768	105.5679	-9.5768	105.5679
X Variable 3	0.369483	0.138535	2.667066	0.010527	0.090626	0.64834	0.090626	0.64834

Table A5.7.3. Regression statistics obtained from a multiple linear regression of CEP_{Hg} on porosity (Variable 1), clay content (Variable 2) and temperature (Variable 3) on the Gulf of Mexico Group 1 (gsd types 1 – 4) data subset.

SUMMARY OUTPUT

<i>Regression Statistics</i>							
Multiple R	0.822479						
R Square	0.676472						
Adjusted R Square	0.655372						
Standard Error	10.78241						
Observations	50						

<i>ANOVA</i>							
	<i>df</i>	<i>SS</i>	<i>MS</i>	<i>F</i>	<i>Significance F</i>		
Regression	3	11182.21	3727.404	32.06082	2.44E-11		
Residual	46	5347.978	116.2604				
Total	49	16530.19					

	<i>Coefficients</i>	<i>Standard Error</i>	<i>t Stat</i>	<i>P-value</i>	<i>Lower 95%</i>	<i>Upper 95%</i>	<i>Lower 95.0%</i>	<i>Upper 95.0%</i>
Intercept	74.85554	23.61514	3.169812	0.002713	27.32078	122.3903	27.32078	122.3903
X Variable 1	-189.726	61.94067	-3.06303	0.003655	-314.406	-65.0463	-314.406	-65.0463
X Variable 2	-86.445	23.4367	-3.68844	0.000595	-133.621	-39.2694	-133.621	-39.2694
X Variable 3	0.282931	0.127818	2.213543	0.031859	0.025647	0.540215	0.025647	0.540215

Table A5.7.3. Regression statistics obtained from a multiple linear regression of CEP_{Hg} on porosity (Variable 1), sortable silt content (Variable 2) and temperature (Variable 3) on the Gulf of Mexico Group 1 (gsd types 1 – 4) data subset.

Appendix A5.8 Group 2 Jurassic North Sea Subset Regression Tables

SUMMARY OUTPUT

<i>Regression Statistics</i>	
Multiple R	0.694367
R Square	0.482146
Adjusted R Square	0.413099
Standard Error	24.91509
Observations	18

ANOVA

	<i>df</i>	<i>SS</i>	<i>MS</i>	<i>F</i>	<i>Significance F</i>
Regression	2	8669.359	4334.679	6.982839	0.007187
Residual	15	9311.426	620.7618		
Total	17	17980.79			

	<i>Coefficients</i>	<i>Standard Error</i>	<i>t Stat</i>	<i>P-value</i>	<i>Lower 95%</i>	<i>Upper 95%</i>	<i>Lower 95.0%</i>	<i>Upper 95.0%</i>
Intercept	62.6267	25.34991	2.47049	0.025973	8.594609	116.6588	8.594609	116.6588
X Variable 1	-374.681	117.4332	-3.19059	0.00608	-624.984	-124.378	-624.984	-124.378
X Variable 2	111.9106	78.21478	1.430811	0.172987	-54.8004	278.6215	-54.8004	278.6215

Table A5.8.1. Regression statistics obtained from a multiple linear regression of CEP_{Hg} on porosity (Variable 1) and clay content (Variable 2) on the Jurassic, North Sea Group 2 (gsd types 5 – 6) data subset.

SUMMARY OUTPUT

<i>Regression Statistics</i>	
Multiple R	0.813004
R Square	0.660976
Adjusted R Square	0.615773
Standard Error	20.15923
Observations	18

ANOVA

	<i>df</i>	<i>SS</i>	<i>MS</i>	<i>F</i>	<i>Significance F</i>
Regression	2	11884.86	5942.432	14.62232	0.0003
Residual	15	6095.921	406.3947		
Total	17	17980.79			

	<i>Coefficients</i>	<i>Standard Error</i>	<i>t Stat</i>	<i>P-value</i>	<i>Lower 95%</i>	<i>Upper 95%</i>	<i>Lower 95.0%</i>	<i>Upper 95.0%</i>
Intercept	177.9962	28.13776	6.325883	1.36E-05	118.0219	237.9705	118.0219	237.9705
X Variable 1	-335.239	95.9195	-3.495	0.003257	-539.686	-130.791	-539.686	-130.791
X Variable 2	-161.983	48.75254	-3.32255	0.004639	-265.897	-58.0693	-265.897	-58.0693

Table A5.8.2. Regression statistics obtained from a multiple linear regression of CEP_{Hg} on porosity (Variable 1) and sortable silt content (Variable 2) on the Jurassic, North Sea Group 2 (gsd types 5 – 6) data subset.

SUMMARY OUTPUT

<i>Regression Statistics</i>	
Multiple R	0.72835
R Square	0.530494
Adjusted R Square	0.389642
Standard Error	25.25342
Observations	14

ANOVA

	<i>df</i>	<i>SS</i>	<i>MS</i>	<i>F</i>	<i>Significance F</i>
Regression	3	7205.765	2401.922	3.766329	0.048118
Residual	10	6377.355	637.7355		
Total	13	13583.12			

	<i>Coefficients</i>	<i>Standard Error</i>	<i>t Stat</i>	<i>P-value</i>	<i>Lower 95%</i>	<i>Upper 95%</i>	<i>Lower 95.0%</i>	<i>Upper 95.0%</i>
Intercept	23.65709	91.79453	0.257718	0.801851	-180.874	228.1881	-180.874	228.1881
X Variable 1	-266.324	252.14	-1.05625	0.315702	-828.127	295.4794	-828.127	295.4794
X Variable 2	116.6358	87.04381	1.339967	0.209908	-77.3099	310.5816	-77.3099	310.5816
X Variable 3	0.198536	0.560383	0.354286	0.730481	-1.05008	1.447148	-1.05008	1.447148

Table A5.8.3. Regression statistics obtained from a multiple linear regression of CEP_{Hg} on porosity (Variable 1), clay content (Variable 2) and Temperature (Variable 3) on the Jurassic, North Sea Group 2 (gsd types 5 – 6) data subset.

SUMMARY OUTPUT

<i>Regression Statistics</i>	
Multiple R	0.843641
R Square	0.71173
Adjusted R Square	0.625249
Standard Error	19.7879
Observations	14

ANOVA

	<i>df</i>	<i>SS</i>	<i>MS</i>	<i>F</i>	<i>Significance F</i>
Regression	3	9667.51	3222.503	8.22989	0.004696
Residual	10	3915.61	391.561		
Total	13	13583.12			

	<i>Coefficients</i>	<i>Standard Error</i>	<i>t Stat</i>	<i>P-value</i>	<i>Lower 95%</i>	<i>Upper 95%</i>	<i>Lower 95.0%</i>	<i>Upper 95.0%</i>
Intercept	105.9394	68.85663	1.538551	0.154933	-47.4827	259.3616	-47.4827	259.3616
X Variable 1	-52.6045	214.7612	-0.24494	0.811453	-531.122	425.9132	-531.122	425.9132
X Variable 2	-195.739	64.49358	-3.03502	0.012569	-339.44	-52.0387	-339.44	-52.0387
X Variable 3	0.493872	0.452067	1.092475	0.300244	-0.5134	1.501139	-0.5134	1.501139

Table A5.8.4. Regression statistics obtained from a multiple linear regression of CEP_{Hg} on porosity (Variable 1), sortable silt content (Variable 2) and Temperature (Variable 3) on the Jurassic, North Sea Group 2 (gsd types 5 – 6) data subset.